Theory, Analysis, and Applications of Multidimensional, Multiconductor Transmission-Line Metamaterials

by

Stuart Barth

A thesis submitted in partial fulfillment of the requirements for the degree of

Doctor of Philosophy

in

Electromagnetics and Microwaves

Department of Electrical and Computer Engineering

University of Alberta

© Stuart Barth, 2021

Abstract

The past few decades have seen incredible growth in the interest of using periodic structures to improve the efficacy of microwave-frequency devices, since they provide access to dispersion-engineered phenomena such as bandgaps, group- and phase-velocity control, and advanced resonance behaviors. Metamaterials – periodic, composite structures which may support novel wave phenomena not possible with natural materials – hold the promise of enabling many next-generation electromagnetic technologies in a broad array of fields, ranging from imaging to communications to wireless power transfer, among others. One of the more promising technologies for realizing metamaterials are those created using transmission-line techniques – i.e., those designed to interface with transmission-line modes. The use of these modes is highly desirable due to their ability to be manipulated with standard electronic components, their inherent ease of analysis, and their capacity to effect strong miniaturization.

However, there are some serious analytical challenges facing systems which support multiple, coupled, transmission-line modes – as may be found in modern devices employing metamaterials, for example antennas, filters, and sensors. Multiconductor transmission-line theory provides a framework for analyzing these systems, but the theory is incomplete in at least one important aspect: it cannot predict all of the properties of a given set of transmission-line modes. Owing to this uncertainty, the theory has found limited use in the development of more elaborate networks, such as those required to enable advanced metamaterial phenomena.

This thesis contributes to the completion of multiconductor transmission-line theory by providing a path forward for the computation of the modal properties of coupled transmission lines. It is demonstrated that transmission-line modes are ideally normal modes, and that as such their definitions in terms of sets of voltages and currents may be expressed as entirely real quantities. It is postulated that total charge (or, in the frequency domain, current) carried by the coupled lines is basis-invariant, which allows for expressions that uniquely determine the voltages and currents of the modes to within a sign – which, in turn, allows the modal properties to be uniquely determined.

Having a process for determining multiconductor transmission-line modal properties, the work then develops novel processes with which to analyze more elaborate, multidimensional networks of multiconductor

transmission-lines loaded with discrete circuit elements. A set of network parameters – M-Parameters – is rigorously defined and used throughout the work to assist with various derivations. A process for computing the dispersive properties of generalized, multidimensional networks is proposed and validated, along with a numerically-efficient process for assembling networks from their sub-components of multiconductor transmission line and other circuit elements.

Applications of the theory and analyses explored in this work are given in the final chapter. A novel, fully-printed, dual-band quadrature hybrid coupler is designed and experimentally validated using new understandings of bandgap phenomena. Using knowledge of the underlying transmission-line modal properties, an electromagnetic bandgap structure is designed with inherent impedance matches and mismatches, to produce a fully printed common-mode filter that does not require a defected ground plane. The proposed multidimensional analysis is used to model and investigate the canonical uniplanar compact electromagnetic bandgap structure, where its dispersive properties are predicted to a much higher degree of agreement with full-wave solvers than previously proposed models. Lastly, various multidimensional metamaterial unit cells – a two-dimensional variant of a bandgap structure previously only modelled in one dimension, a two-dimensional hexagonal structure, and an isotropic primitive cubic lattice-based unit cell – are modelled, where it is found that various Bloch modal properties are in agreement with those predicted by full-wave solvers.

Preface

This thesis is an original work. However, some figures and data have been included from several published articles by this author, including:

1. S. Barth and A. K. Iyer, "A dual-band quadrature hybrid coupler using embedded MTM-EBGs," in *Proceedings of the IEEE International Symposium on Antennas and Propagation and USNC/URSI Radio Science Meeting*, Boston, MA, Jul. 2018, pp. 199 – 200.

   - Used in section 4.1.3

2. S. Barth and A. K. Iyer, "A novel scaling process for the computation of multiconductor transmission-line modal properties using the basis invariance of total current and power," *IEEE Access*, vol. 8, 2020.

   - Used in section 3.1

3. S. Barth, B. P. Smyth, J. A. Brown, and A. K. Iyer, "Theory and design of dual-band microstrip networks using embedded metamaterial-based electromagnetic bandgap structures (MTM-EBGs)," *IEEE Trans. Antennas Propag.*, vol. 68, no. 3, pp. 1761 – 1772, 2020.

   - Used in sections 4.1.1 and 4.1.2

4. S. Barth and A. K. Iyer, "A compact MTM-EBG-enabled common-mode filter without a defected ground," in *Proceedings of the IEEE International Symposium on Antennas and Propagation and North American Radio Science Meeting*, Montreal, QC, Canada, Jul. 2020, pp. 801 – 802.

   - Used in section 4.1.4

Small portions of these texts may have been reproduced in this thesis with little or no editing. Data given in item 3 may have been obtained by Mr. B. P. Smyth, or Mr. J. A. Brown, otherwise it was directly obtained by the author through discussion with Dr. A. K. Iyer. Experimental design and ideas presented in these works were generally collaborative efforts among all the authors.

Additionally, the subject matter of section 4.2, along with various specific figures and portions of the text have been submitted for publication to the *IEEE Trans. Antennas Propag.* as "The MTM-EBG as a Rigorous Multiconductor Model of the UC-EBG and Approaches for Miniaturization" by S. Barth and A. K. Iyer. The ideas presented in this section were generally a collaborative effort by the authors.

Dedication

There is a mine for silver and a place where gold is refined. Iron is taken from the earth, and copper is smelted from ore. Man puts an end to the darkness; he searches the farthest recesses for ore in the blackest darkness. Far from where people dwell he cuts a shaft, in places forgotten by the foot of man; far from men he dangles and sways.

The earth, from which food comes, is transformed below as by fire; sapphires come from its rocks, and its dust contains nuggets of gold. No bird of prey knows that hidden path, no falcon's eye has seen it. Proud beasts do not set foot on it, and no lion prowls there.

Man's hand assaults the flinty rock and lays bare the roots of the mountains. He tunnels through the rock; his eyes see all its treasures. He searches the sources of the rivers and brings hidden things to light.

But where can wisdom be found? Where does understanding dwell? Man does not comprehend its worth; it cannot be found in the land of the living. The deep says, 'It is not in me'; the sea says, 'It is not with me.' It cannot be bought with the finest gold, nor can its price be weighed in silver. It cannot be bought with the gold of Ophir, with precious onyx or sapphires. Neither gold nor crystal can compare with it, nor can it be had for jewels of gold. Coral and jasper are not worthy of mention; the price of wisdom is beyond rubies. The topaz of Cush cannot compare with it; it cannot be bought with pure gold.

Where then does wisdom come from? Where does understanding dwell? It is hidden from the eyes of every living thing, concealed even from the birds of the air. Destruction and Death say, 'Only a rumour of it has reached our ears.'

God understands the way to it and he alone knows where it dwells, for he views the ends of the earth and sees everything under the heavens. When he established the force of the wind and measured out the waters, when he made a decree for the rain and a path for the thunderstorm, then he looked at wisdom and appraised it; he confirmed it and tested it. And he said to man, 'The fear of the Lord - that is wisdom, and to shun evil is understanding.'

(Job 28)

S·D·G I·D·E

Acknowledgements

I would like to acknowledge first and foremost my supervisor, Professor Ashwin K. Iyer, for his myriad of supports throughout my time as a doctoral student. Funding of fundamental research as he did for a number of years is a bold decision; I am very grateful for the privilege of being able to contribute to this field of research, along with the many other opportunities he provided to teach, manage his laboratory, and to attend and present at numerous conferences. Over the past several years, I have deeply appreciated his compassion and understanding of personal circumstances, and for how he would expend great effort in order to improve working conditions for his students.

My fellow groupmates and many peers in W3-030 over the years deserve special recognition for making graduate school the great experience it has been. My groupmates helped flush out many challenging concepts over long periods of time (e.g., complex power), and I'm grateful in particular to Mitchell Semple and David Sawyer for always being willing to discuss a variety of technical topics in detail. Mitchell specifically helped with several ideas on linear algebra operations that were used in this work.

I could not have completed this endeavour without the support of my family. I would like to thank my amazing wife Carly for putting up with my working many late nights and holidays, and occasionally spending more time with a certain laser than I would with her. I would also like to thank my parents for their many supports over the years, and my brother for the occasional comedic break and chance to air my frustrations.

With so much time spent with my colleagues at the University of Alberta, I think it is inevitable that I would call some of them my friends. I would like to thank in particular Mitchell Semple, Thomas Jones, Sanghamitro Das, and the amazing couple Navid and Arezoo Hosseini for the many good times both on and off campus. It has been a privilege to know such amazing people, and I wish you all the best of success in the years to come.

Finally, I would also like to acknowledge funding of this work from the IEEE Antennas and Propagation Society, Alberta Innovates, and KP Performance Antenna (an Infinite Electronics Group company). Their contributions made this work possible.

Contents

List of Acronyms

UHF	Ultra-High Frequency
SHF	Super-High Frequency
EHF	Extremely-High Frequency
SAR	Synthetic Aperture Radar
EMI	Electro-Magnetic Interference
EMC	Electro-Magnetic Compatibility
WPT	Wireless Power Transfer
PT	Parity-Time
RADAR	Radio Detection and Ranging
TEM	Transverse Electromagnetic
TL	Transmission Line
MTL	Multiconductor Transmission Line
MTM	Metamaterial
MTS	Metasurface
TL-MTM	Transmission-Line Metamaterial
1D	One-Dimensional
2D	Two-Dimensional
3D	Three-Dimensional
MS	Microstrip
VI	voltage and current
PI	power and current
PV	power and voltage
CMT	Coupled-Mode Theory
NRI	Negative Refractive Index
PBG	Photonic Bandgap Structure
EBG	Electromagnetic Bandgap Structure
SW	Surface Wave
CBCPW	Conductor-Backed Coplanar Waveguide
CPW	Coplanar Waveguide
PEC	Perfect Electric Conductor
PMC	Perfect Magnetic Conductor
PPW	Parallel Plate Waveguide
CSL	Coupled Slotline
HFSS	High Frequency Structural Simulator
CBCPS	Conductor-Backed Coplanar Stripline
CPS	Coplanar Stripline
VNA	Vector Network Analyzer
SMA	Sub-Miniature 'A'
PCB	Printed Circuit Board
SL	Slotline
GPS	Global Positioning System

MU-MIMO	Multi-User Multiple-Inputs Multiple-Outputs
MTL-MTM	Multiconductor Transmission-Line Metamaterial
MTM-EBG	Metamaterial Electromagnetic Bandgap Structure
SCBCPW	Shielded Conductor-Backed Coplanar Waveguide
UC-EBG	Uniplanar Compact Electromagnetic Bandgap Structure

List of Tables

List of Figures

List of Assumption Sets

Chapter 1

Introduction

1.1 Motivation

The use of electromagnetic waves for a variety of novel purposes in modern life has expanded into both critical and trivial applications, and shows no signs of abating. As these technologies mature, a greater need for intricate manipulation of these electromagnetic fields has elucidated many new research directions. A number of key application areas stand out: communications, imaging, sensing, absorbing and cloaking, and Wireless Power Transfer (WPT) are some of the main fields which may benefit from advanced field control mechanisms, although of course there are others [1].

1.1.1 Communications

Wireless communications have become integral to everyday life in our society. The need for increasingly large bandwidths not only force communications bands upwards in frequency out of the Ultra-High Frequency (UHF) (i.e., microwaves, or the sub-S, S, and L bands) and into the Super-High Frequency (SHF) and Extremely-High Frequency (EHF) (i.e., millimeter-waves, or the L to Y bands), but also necessitate the use of next-generation technologies such as targeted beamforming and Multi-User Multiple-Inputs Multiple-Outputs (MU-MIMO) communications channels [2–5]. The latter technologies require the development and widespread adoption of robust and dynamic electronically-steered, frequency-agile antennas – which themselves must also perform these operations while keeping stringent limits on radiated power density, polarization purity, and maximum side lobe levels, among other parameters [6–11]. Such systems have arguably not yet been completely developed, due to the massive challenges of satisfying all of these requirements and operations simultaneously.

1.1.2 Imaging

A number of imaging applications have arisen over the past few decades with advancements in higher-frequency microwave and millimeter-wave systems, but also in the numerical processing of data needed to produce useful results. These applications include security (for the detection of concealed objects), health (for the imaging of various biological tissues *in vivo*), and earth monitoring (typically for environmental

events such as forest fires, earthquakes, or flooding) [12, 13]. One of the largest obstacles in imaging is achieving adequate resolution – since fields must be sampled over electrically large apertures in order to properly reconstitute features – as well as problems associated with the diffraction limit [14, 15], which limits the electrical size of the images to be resolved. While these issues my be mitigated in large part by moving to higher frequencies (for example, in the EHF band), one of the more attractive features of electromagnetic-based imaging is that lower frequencies (such as those in the UHF band) have substantially larger penetration capability into a larger range of materials [16]. Therefore, it is of interest to develop technologies which may perform imaging with relatively low frequencies, which remain electrically small and yet are capable of resolving images in the near field of scatterers.

1.1.3 Sensing

With the advent of low-power computational devices and ubiquitous wireless connectivity, information regarding physical processes and parameters may be gathered from a variety of environments, and transmitted elsewhere for real-time or bulk statistical analysis. The sensing of constitutive medium parameters of materials is useful in process control, such as in the production of microwave dielectrics – which in modern applications require extremely low tolerances [17]. Digitization and the desire for continuous, real-time monitoring of concentration levels in fluids for process control and health applications has opened a market for a plethora of low-cost, low-energy sensors [18]. Biological molecules and processes have been found to exhibit unique and determinable ionic and molecular resonance frequencies, many of which lie in the microwave frequency range [19, 20] – sensing of these processes could have large impact for health monitoring and research. Modern technologies have paved the way for sensing of forces in mechanical systems, where the monitoring of the material integrity of various infrastructure such as buildings, bridges, and roads has become of interest as a mechanism of improving construction reliability and saving maintenance costs [21–23]. However, classical methods of sensing suffer from noticeable drawbacks. The physical sizes of the sensors preclude them from being included in various environments, while similarly arrays of these sensors lack the resolution for many demanding surface applications. Therefore, processes for miniaturization and ruggedization of these sensors is highly desired.

1.1.4 Absorbing and Cloaking

Many modern measurement methodologies require extremely sensitive data acquisition devices that exhibit very low signal-to-noise ratios, for example in applying ETSI 302 [24] or ITU-R F.699-6 [25] which recommend up to 80 dB of main-to-side lobe levels. In order to gauge such large differences in signal level, radiators must be measured in enclosed anechoic environments – the boundaries of which must provide reflection levels that are well below this value. Therefore, increasingly absorbent materials are desired to effect field suppression, often over increasingly small distances – which may not be feasibly achieved with natural materials.

Noise, interference, and/or cross-talk (generally, Electro-Magnetic Interference (EMI)) are increasingly becoming issues of concern in Printed Circuit Board (PCB) environments as the density and complexity of components – often with several embedded wireless technologies – are regularly increasing. As system

voltages decrease in an effort to reduce power consumption, there are increasingly smaller tolerances for unwanted EMI in electronic devices. On-board absorbers (so-called *reflectionless filters*) are desired to suppress the EMI, but their layout may be complex and difficult to implement [26, 27].

Reducing Radio Detection and Ranging (RADAR) cross-sections is key for the defence industry, by implementing stealth technologies such as microwave absorbers or cloaks [28, 29]. Currently, absorbing solutions which operate over narrow frequency bands exist, but challenges remain in creating broadband devices with large absorbing angles, which remain thin and light – as is typically desired by the defence community.

1.1.5 Wireless Power Transfer

Along with the increased demand for wireless communications, the demand for WPT for the wireless powering or charging of electrical devices is also growing at a rapid rate. While the physical processes of WPT are relatively well-understood, various restrictions and guidelines limit the electromagnetic field strengths used, typically for health and safety reasons [30–32]. These limits conflict with the desire for increased power transfer, for supporting multiple devices or faster charging time of batteries. Additionally, resonantly coupled systems generally possess strong correlations between transfer efficiency, distance between source and receiver, frequencies of optimal transfer, and load impedance of the receiver – all of which may vary in realistic scenarios. As such, solutions must be found in which high levels of power may be efficiently directed to distributed, arbitrary loads, while maintaining safely low power densities.

1.2 Solutions

The manipulation of electromagnetic waves for the aforementioned purposes began with the use of various materials, where it was determined that different materials may exhibit a variety of interesting effects [33]. Although the use of composite materials have been demonstrated to give rise to a larger variety of behaviors than uniform materials on their own [34], physicists and engineers have been increasingly looking to novel wave phenomena in order to meet the challenges of modern systems.

1.2.1 Novel Wave Phenomena

Time-modulated waves and materials are increasingly being studied as mechanisms with which to overcome fundamental limits imposed on devices and systems by classical materials. Examples include non-reciprocity in circuits without the use of magnetic materials [35–43], which allow the the development of novel, miniaturized electronic components; wideband absorption in electrically thin materials [44, 45], allowing for applications such as RADAR absorption in lightweight and low-profile surfaces; performance increases in WPT efficiency through the use of coherent excitations [46, 47]; or electromagnetic cloaking [48, 49].

Electromagnetic scattering phenomena which may be described with non-Hermitian Hamiltonians have been shown to exhibit novel wave behaviors. After it was first demonstrated that Parity-Time (PT)-symmetric systems also exhibited the real eigenvalue spectra required by physical processes [50], it was

shown that systems comprised of balanced gains and losses (the source of the broken charge symmetry) could also be used to realize devices such as unidirectional couplers [51, 52], imagers [53], sensors [54, 55], and cloaks [56]. Related to the study of non-Hermitian systems is the study of *exceptional points*, at which both the eigenvalues and eigenvectors of a system coalesce, and about which the system becomes much more sensitive to perturbations [57–59]. This behavior has been utilized to develop more sensitive sensor systems, among other applications [60, 61].

Topological insulators – purposefully designed junctions between two disparate periodic structures – have been shown to support wave propagation, while the bulk materials themselves impede propagation at the same frequencies [62, 63]. Due to a configuration of carefully selected symmetries, electromagnetic waves are strictly confined to the interface between the two materials, and may propagate energy efficiently around arbitrarily shaped surfaces. This concept has been generalized to the theory of so-called "line waves" [64], and both have been shown to have applications in WPT through the guiding of power along a surface in a controllable beam [65].

Moire physics involves the study of the product of overlapping planar periodic patterns, which typically produces a novel pattern with a period differing from those which created it [66]. Moreover, the properties of the final pattern may be modified to a relatively large extent through small offsets in the originating patterns. Applications of these effects have included various mechanisms for imaging (interferometry) [67, 68]. In recent years, the field of "twistronics" has studied the interaction of two-dimensional semiconducting materials, which create Moire patterns. It has been determined that when the sheets are rotated relative to each other at a so-called "magic angle", superconductivity may be achieved under certain conditions for certain combinations of materials [69–71]. Moreover, by adjusting this angle, the material can change its properties from conducting to insulating, thereby allowing strong control of the materials' properties with only very minor changes. This mechanism has been proposed as a means by which to control field canalization for power transfer applications [72].

Periodic structures exhibiting symmetries have been demonstrated to possess controllable dispersion properties – in particular, lower dispersion, which finds use in the design of waveguides [73–75]. One particular type of higher symmetry is *glide* symmetry, which results from the combination of multiple mirroring operations. Glide symmetry has been used to design low-dispersion, high-power waveguides, as well as antennas and lenses for high-frequency communications systems [76–81].

The implementation of these novel forms of wave physics (among others) often require functionalities that cannot be found in natural materials. Therefore, in order to best realize these novel phenomena, researchers have turned to *artificial* materials to produced the desired wave-manipulation capabilities.

1.2.2 Artificial Materials

The core concept of artificial materials is related to that of composites: that the combinations of materials with disparate properties may be combined to yield a single object, which under some forms of examination may be considered a "material", and which possesses properties differing from those of its constituent materials. Of course, even natural materials themselves are composites, being composed of microscopic molecules and atoms, themselves comprised of structured fields – akin to what early Greek

atomist philosophers referred to as *substance and void* [82] – such that strictly speaking, there exists no homogenous material (not even a vacuum [83, 84]). The analysis of such composites is known as *effective medium theory* [85], and from the perspective of electromagnetics it places limits on the probing wavelengths (and hence frequency range) in which the substance may be considered a "material". Generally speaking, if the composite is periodic in nature, the probing wavelength must be significantly larger than the periodicity – in this case the composite may be considered a single, corporate, "artificial material" with its own unique set of properties.

Periodic composites are most often used in the creation of artificial electromagnetic materials due to their inherent ease of analysis and understanding, and moreover in most functional designs, the disparate materials used are conductors and dielectrics [86]. Combinations of these materials were first used for electromagnetic wave manipulation in the middle of the 20^{th} century, in an effort to produce artificial dielectrics with designable permittivities [87–89]. In the absence of suitable natural materials, researchers used these composites to develop lenses for microwave applications, including communications and imaging [90–96].

However, only a limited number of novel wave-manipulating phenomena could be achieved with these classical composites, which were mainly developed to increase the selection of materials available for use in engineering design. With the rapid introduction of many new low-loss materials in the later half of the 20^{th} century, the need for (and interest in) artificial materials gradually reduced with time. However, in the same time period, new types of composites which had not been considered previously were starting to be investigated, owing to the fact that they might produce responses that these classical composites fundamentally could not: metamaterials.

1.2.3 Metamaterials

Metamaterials (MTMs) are synthetic, periodic, composites which embody a simple idea: media which propagate electromagnetic waves in manners not found in natural materials [97–99]. Critically, along with effective-medium theory's requirement that the periodicity of the media's composite inclusions must be much smaller than the probing wavelength, causality [100,101] and the Kramers-Kronig relations [102,103] require that the more unnatural waves travelling through these media always exhibit dispersion (along with other effects), thus limiting the types of wave behaviors that may be developed – but, even still, many fascinating effects may be realized. From the perspective of canonical constitutive parameters, unnatural wave propagation means that the effective permittivity and permeability of the media are not simultaneously positive. Other perspectives may be taken on the definition of MTMs, such as media which exhibit left-handed propagation, negative refractive index, or negative phase velocity – however, it has been a matter of some debate as to which of these properties are related to negative constitutive medium parameters, and which may be found in natural materials [104–106]. Regardless of the specific definitions, modern vernacular has extended the terminology of MTMs to include any kind of medium, the constitutive parameters of which are deliberately tailored for a specific purpose, regardless of their signs or whether or not the media support unnatural wave propagation effects.

While concepts such as negative refractive index and negative phase velocity were investigated after

the dawn of the 20$^{\text{th}}$ century [107], it wasn't until Veselago published his seminal consolidating work [108] in the 1960s that these ideas were linked to concepts of constitutive medium parameters. However, owing to a lack of natural materials which exhibited these properties, their study was rendered a mere curiosity. Simultaneously, work was being completed on study of artificial plasmas (which were understood to possess an effective permittivity less than unity) [109,110], although this work did not lead to any substantial consideration of novel media. These ideas were revisited by Pendry and Sievenpiper/Yablonovitch independently just before the turn of the 21$^{\text{st}}$ century [111–114], and critically, Pendry went on to apply the idea to develop artificial media which exhibited negative permeability [115]. Smith's experimental combination of Pendry's ideas lead to what is generally agreed to be the first realized MTM [116].

Since that time, numerous MTMs have been proposed with which to develop a variety of devices for a variety of applications. One of the original applications was in the development of flat lenses for imaging applications, which also possessed the ability to amplify evanescent near-field waves, a property known as superlensing [117–119]. Modern imaging systems use commonplace imaging modalities such as Synthetic Aperture Radar (SAR), in which one or more transmitting or receiving antennas are combined to yield the effects of a single, larger aperture via the application of signal processing algorithms [120–122]. One particular class of SAR: multistatic imaging – in which multiple sources are used to illuminate a target, and multiple receivers are used in the computation of the properties of the imaged object using the received scattered fields – has become prevalent due to its use of non-moving antennas, which can significantly reduce imaging errors, as well as produce real-time images [123–126]. However, these systems are often large and non-portable (especially at low frequencies), and are not easily integrated with other devices. Lenses, along with the use of multiple antennas and signal processing algorithms, may be used to advance imaging technologies to focus electromagnetic waves from the far-field to or from nearby sources or receivers. While SHF volumetric lenses have been used for some time, the development of superlenses and their ability to resolve sub-wavelength features beyond the classical diffraction limit could satisfy the need to resolve images in the extreme near-field [127–131]. These and other types of negative-refracting lenses abilities to be implemented in a flat form allows them to be easily integrated with other technologies, unlike traditional lenses that always require curved surfaces.

In short order, MTMs were applied to communications systems. It has been demonstrated that MTMs may be used to miniaturize antennas [132–139], develop dual-band [140–145], multi-band [146–151], or wideband [152–154] antennas, or enact more exotic functionalities such as decoupling adjacent antennas [155–158] or shaping their radiation patterns [159–164]. Similarly, they have been demonstrated to find use in miniaturizing circuits [165–169], effecting dual-band [170–176] or multi-band [177,178] operation, or implementing novel effects such as broadband impedance matching [179, 180]. In general, MTMs possess advantages over a multitude of other methods by which these effects may be realized, such as compact forms, low-cost or low-profile realization, or models exhibiting higher levels of accuracy [181, 182].

While many differing techniques have been applied to sensor technologies – such as non-contact fluid sensing [183–191], sensing of mechanical forces [192–195] or temperatures [196–199] – the implementation of these sensors with MTMs has enabled enhanced sensitivities, miniaturized sensing platforms, and increased precision of results [200–209].

Electromagnetic absorbers find use in anechoic environment and stealth applications [210–212]. Through the integration of MTMs, absorbers have been developed which exhibit low-profile thicknesses, wideband operation, or even tunable frequency ranges [213–216]. Similarly, MTMs have been used to develop a multitude of various clocking technologies for defence or communications applications [217–221].

The placement of resonant coils or other elements that exhibit resonances in between the transmitter(s) and receiver(s) of WPT systems has been demonstrated to increase coupling efficiency, increase bandwidth, or increase power transfer efficiency [222–226]. However, these solutions often take up large amounts of space, and are limited in the range of effects they may provide. MTMs exhibiting extreme parameters, such as when the constitutive parameters are near zero or possess very large values, have been demonstrated to greatly enhance this coupling with much smaller resonators, and greater choice of design over the specific benefits they provide to the power transfer system [227–235].

The two-dimensional equivalents of MTMs – Metasurfaces (MTSs) – have been shown to demonstrate many of the same advantages that MTMs possess over other solutions, while possessing flat profiles or designed to be conformal to arbitrary surfaces [236–250]. However, these advantages can come with a few associated drawbacks, most notably limited bandwidths, efficiencies, and antenna gains [251–253].

1.2.4 Transmission-Line Metamaterials

One particular noteworthy class of MTMs is Transmission Line (TL)-MTMs. TL-MTMs have been noted for their ease of analysis, accurate equivalent-circuit models, capacity for miniaturization, and ease of producing wideband and/or impedance-matched performance [181, 182]. TL-MTMs are also composite media, however, the constituent disparate elements used are: a) TL sections and, b) circuit elements such as capacitors or inductors. TL-MTMs draw their strengths from the fact that using the analysis of TLs, the per-unit-length admittance and impedance quantities may be readily determined, and therefore, by homogenizing the composite TL network as warranted by effective medium theory, the effective per-unit-length properties of the network may be relatively simply obtained as well.

The development of MTMs using TL networks came about as a result of the observation that in certain combinations of loading components (notably, series capacitors and shunt inductors), the per-unit-length admittance and impedance of the networks could be made simultaneously negative over certain frequency ranges [254, 255]. Since these quantities are proportional to the effective constitutive medium parameters, novel wave behaviors such as left-handed propagation, negative phase velocity, and negative refractive index are expected to be supported as well. While the analysis of One-Dimensional (1D) networks allowed for simple observations to be made in rapid succession, these were mostly used to verify properties of the more elaborate Two-Dimensional (2D) networks which were developed to validate wave behaviors such as negative refractive index and to realize devices such as superlenses, antennas, or microwave circuits – most of which originated from the research group of Eleftheriades just after the turn of the 20^{th} century [256–263].

The analysis of these 2D TL networks may be implemented in closed form, with a minimum of approximation [257] – a direct consequence of the consideration of only a single propagating mode in the MTM networks. However, it shortly became apparent that the complex networks of conductors present

in modern devices would support multiple such modes, as indicated by Multiconductor Transmission Line (MTL) Theory [264, 265]. Early analysis of such systems in 1D indicated a rich variety of wave-manipulation capability [266–276], but unfortunately due to the complexity of analyses of such systems, little work has been completed on the extension of these multi-modal networks into high-dimensional arrays [277, 278].

Such analyses are necessary if MTMs are to fulfill their promise as designer media which have the capacity to strongly manipulate electromagnetic waves – since in realistic systems, these waves may readily exist in multiple modes and travel in multiple dimensions. One key challenge preventing further developments in this field is the determination of whether the properties of TL modes may be determined in multi-modal systems, some of which surprisingly the leading experts in the field have deemed not possible [264, 265, 279].

1.3 Contributions

This thesis aims to expand the understanding of MTL-based MTMs (MTL-MTMs) through investigation of their modal properties. In order to achieve this goal, several discrete investigations are completed to bring understanding from the fundamentals of TL modes, to the dispersion analysis of the Brillouin zone contours of several novel and complex MTL-MTMs:

1. Modal properties of MTLs are derived, and it is shown that contrary to current understanding the properties may be uniquely determined under the typical assumptions employed for TL analysis. It is revealed that the missing information that has prevented this conclusion is the fact that TL modes are *normal* modes – and that moreover, by postulating that total charge of the system is basis-invariant, the mode's eigenvectors (distributions of currents and voltages) may be scaled to a unique quantity.

2. A generalized dispersion analysis is derived in order to allow for the study of MTL-MTMs in a variety of configurations. This analysis derives the Bloch modal properties such as propagation constants, as well as other properties such as impedance and constitutive medium parameters, for periodic MTL-based networks based on Bravais lattice shapes in an arbitrary number of dimensions.

3. Supporting network analysis methods are developed in order for this dispersion analysis to be implemented in a computationally-efficient manner. A new set of network parameters is developed – referred to as $[M]$-parameters – which represent sets of underdetermined, homogenous equations expressed on a basis of voltages and currents observed at the network's ports. Additionally, a generalized process for concatenation of these networks under arbitrary combinations of connected or unconnected terminals is developed in order to rapidly assemble expressions for these complicated, multidimensional MTL networks.

4. Applications of the previously developed analyses are exhibited through the development of novel MTM-based devices. A dual-band coupler, a common-mode filter, and a 2D model of a canonical

periodic structure are all proposed and validated. The multidimensional network analysis developed in this work is partially verified through comparison of the predicted dispersion data with the results of full-wave simulations. Lastly, the computation of various modal properties of several novel, multidimensional MTL-MTMs are validated numerically, where it is shown that modal properties predicted by full-wave simulators are in good agreement with those predicted through the use of the MTL-based dispersion analysis.

1.4 Outline

The outline of this thesis is as follows: Chapter 2 presents a number of analytical derivations in order to provide the necessary rigour for understanding the novelty of the work. It begins with fundamental electromagnetic theory, but quickly works up to the periodic analyses of MTL-MTMs in order to guide the reader through the relevant details in an expedited manner. The chapter gives a thorough analysis of TL theory, detailing the necessary assumptions required for a medium to support TL modes. The coupling of various modes is then studied through the introduction of coupled-mode theory, where examples are presented to illustrate the various types of coupling observed in multi-modal systems. The effects of coupling on the resulting eigenmodes and eigenvectors are investigated as a lead-in to the more complicated MTL theory, and the products of bandgaps and complex modes are briefly investigated. MTL theory is introduced as an extension of TL theory to the case of multiple conductors. The properties of the various supported modes are then derived, and lastly, a 1D periodic analysis is introduced by which the Bloch modal properties of simple 1D MTL networks may be determined.

Chapter 3 builds upon the fundamentals presented in the previous chapter by deriving the novel analytical tools used by this thesis. The chapter begins by introducing the postulate which allows for the determination of modal properties: that total charge in MTL systems is invariant to the bases it may be expressed on. This allows for the scaling ambiguity of the modal system's eigenvectors to be removed, and the properties of the modes (within the typical assumptions made for TLs) uniquely determined. Validation of the postulate is given with respect to both numerically-determined characteristic impedances from full-wave simulators as well as experimentally-determined quantities. $[M]$-parameters are introduced with which to describe networks in arbitrary, sourceless configurations – including cases that cannot be modelled with conventional $[Z]$, $[Y]$, or $[ABCD]$ parameters. Processes for computationally-efficient determination of similar Bloch modal properties in MTL-MTM networks are then introduced. A general expression for the propagation of TL modes in a periodic lattice is derived, with arbitrary boundary conditions applied to any of the unit-cells' axes. The process of determining the $[M]$-parameter description of this network from its constituent components – generalized network concatenation – is developed.

Chapter 4 uses these novel analytical processes to develop novel MTM devices. A dual-band, fully-printable quadrature hybrid coupler is developed and experimentally validated in which the proposed layout does not use any more space that the canonical single-band equivalent. A full-printable common-mode filter is proposed and experimentally verified, which does not make use of a defected conductor backing – allowing its integration into low-noise multilayer circuitry. It is shown that a canonical 2D

device – the uniplanar compact electromagnetic bandgap structure – may be reasonably well-modelled as a two-dimensional intersection of previously introduced one-dimensional MTL-based structures. The modal analysis of multidimensional MTL-MTMs is validated through comparison of the numerically-produced data with those extracted from equivalent structures simulated in full-wave simulation. Three cases are studied to illustrate the applicability of the processes to various MTL configurations and Bravais lattice types: a 2D, rectangular, anisotropic, MTM; a 2D hexagonal, isotropic, MTM; and a 3D primitive cubic, isotropic, MTM.

The thesis is concluded in Chapter 5, with a summary of results and unfinished, future work.

Chapter 2

Background

2.1 Transmission-Line Theory

2.1.1 History of Transmission-Line Theory

The study of the propagation of voltages and currents along TLs historically arose from the increasing use of electrical wires and cables for telegraphy (and later on, telephony) in the mid-19$^{\text{th}}$ century [280, 281]. The increasing lengths of the individual lines exaggerate the effects of dispersion (that is, the frequency-dependent behavior of the lines) to a point where communication was strongly inhibited. This dispersion could only be overcome through thorough understanding of the propagation effects of the lines, which lead to the first analyses in the 1850s with the work of Lord Kelvin [282] – although his work was somewhat rudimentary; understandably so, since of course the existence of electromagnetic waves had yet to be postulated! The more convenient mathematical forms presently used were formulated by Heaviside [283, 284], who applied Maxwell's relatively new theory of electromagnetic waves to the propagation of voltages and currents in telegraph cables [285]. Further explanatory work can also be attributed to Mie [286] and even Schelkunoff [287], among others.

2.1.2 Transmission Line Modes

TL theory deals with the study of two parallel conductors, which are assumed or approximated to possess a longitudinally-invariant cross-sectional profile. These structures possess an infinite number of propagating modes, however, a pair of conductors will only support one mode which is predominantly Transverse Electromagnetic (TEM) – that is, both the electric and magnetic fields of the mode possess an insignificant longitudinal component. In general, TEM modes are considered to possess zero longitudinal field components, while those which possess small, but negligible longitudinal field components are referred to as *quasi*-TEM. These TEM or quasi-TEM modes supported by two or more conductors are referred to in this work as TL modes. Decomposing the modal field components into transverse and longitudinal field components yields:

$$\vec{E}\left(\vec{l},\tau\right) = \vec{E}_t e^{-\vec{\gamma}\cdot\vec{l}} e^{j\omega\tau} \tag{2.1a}$$

$$\vec{H}\left(\vec{l},\tau\right) = \vec{H}_t e^{-\vec{\gamma}\cdot\vec{l}} e^{j\omega\tau} \tag{2.1b}$$

in which the subscript t represents the transverse field components, and $\vec{l} = |l|\,\hat{l}$ represents the longitudinal coordinate vector in the direction of propagation of the mode $\hat{l}$. The vector $\vec{\gamma}$ is the mode's directional propagation constant, j the imaginary unit, ω is the excitation frequency, and τ is the time variable.

The assumed longitudinally-invariant cross-sectional profile also applies to the medium through which the electromagnetic wave propagates; that is, if a medium is described though its material tensors $[\sigma]$ (the conductivity tensor), $[\epsilon]$ (the permittivity tensor), and $[\mu]$ (the permeability tensor):

$$[\sigma]\left(\vec{l}\right) = [\sigma] \tag{2.2a}$$

$$[\epsilon]\left(\vec{l}\right) = [\epsilon] \tag{2.2b}$$

$$[\mu]\left(\vec{l}\right) = [\mu] \tag{2.2c}$$

2.1.3 The TEM Approximation

In their common, modern forms, Ampere's Law [288, 289] and Faraday's Law [290] may be expressed as:

$$\vec{\nabla}\times\vec{H} = [\sigma]\,\vec{E} + \frac{\partial}{\partial\tau}\left([\epsilon]\,\vec{E}\right) \tag{2.3a}$$

$$\vec{\nabla}\times\vec{E} = -\frac{\partial}{\partial\tau}\left([\mu]\,\vec{H}\right) \tag{2.3b}$$

with $\vec{E}$ and $\vec{H}$ being the electric and magnetic field components (respectively). The tensors may be decomposed into components relating the responses of the material to longitudinal and transverse fields, for example:

$$\begin{bmatrix}\left(\vec{\nabla}\times\vec{E}\right)_t\\ \left(\vec{\nabla}\times\vec{E}\right)_l\end{bmatrix} = -\frac{\partial}{\partial\tau}\left(\begin{bmatrix}[\mu_{tt}]\,[\mu_{tl}]\\ [\mu_{lt}]\,[\mu_{ll}]\end{bmatrix}\begin{bmatrix}\vec{H}_t\\ \vec{H}_l\end{bmatrix}\right) \tag{2.4}$$

where subscript l denotes the longitudinal components. Then, due to the assumption of propagation along a single direction, these may be re-expressed as (after the application of some mathematical and geometrical equalities):

$$\vec{\nabla}_t\times\vec{H}_t = \left([\sigma_{lt}]\,\vec{E}_t + \frac{\partial}{\partial\tau}\left([\epsilon_{lt}]\,\vec{E}_t\right)\right) + \left([\sigma_{ll}]\,\vec{E}_l + \frac{\partial}{\partial\tau}\left([\epsilon_{ll}]\,\vec{E}_l\right)\right) \tag{2.5a}$$

$$\left(\vec{\nabla}_l\times\vec{H}_t\right) + \left(\vec{\nabla}_t\times\vec{H}_l\right) = \left([\sigma_{tt}]\,\vec{E}_t + \frac{\partial}{\partial\tau}\left([\epsilon_{tt}]\,\vec{E}_t\right)\right) + \left([\sigma_{tl}]\,\vec{E}_l + \frac{\partial}{\partial\tau}\left([\epsilon_{tl}]\,\vec{E}_l\right)\right) \tag{2.5b}$$

$$\vec{\nabla}_t\times\vec{E}_t = -\frac{\partial}{\partial\tau}\left([\mu_{lt}]\,\vec{H}_t\right) - \frac{\partial}{\partial\tau}\left([\mu_{ll}]\,\vec{H}_l\right) \tag{2.5c}$$

$$\left(\vec{\nabla}_l\times\vec{E}_t\right) + \left(\vec{\nabla}_t\times\vec{E}_l\right) = -\frac{\partial}{\partial\tau}\left([\mu_{tt}]\,\vec{H}_t\right) - \frac{\partial}{\partial\tau}\left([\mu_{tl}]\,\vec{H}_l\right) \tag{2.5d}$$

Owing to the particular modal field distribution,

$$\vec{H}_l \approx \vec{0} \tag{2.6a}$$

$$\vec{E}_l \approx \vec{0} \tag{2.6b}$$

and subsequently, (2.5) reduce to:

$$\vec{\nabla}_t \times \vec{H}_t = [\sigma_{lt}]\,\vec{E}_t + \frac{\partial}{\partial \tau}\left([\epsilon_{lt}]\,\vec{E}_t\right) \tag{2.7a}$$

$$\vec{\nabla}_l \times \vec{H}_t = [\sigma_{tt}]\,\vec{E}_t + \frac{\partial}{\partial \tau}\left([\epsilon_{tt}]\,\vec{E}_t\right) \tag{2.7b}$$

$$\vec{\nabla}_t \times \vec{E}_t = -\frac{\partial}{\partial \tau}\left([\mu_{lt}]\,\vec{H}_t\right) \tag{2.7c}$$

$$\vec{\nabla}_l \times \vec{E}_t = -\frac{\partial}{\partial \tau}\left([\mu_{tt}]\,\vec{H}_t\right) \tag{2.7d}$$

Interestingly, it may be shown (see the derivations and discussion in Appendix A) that in order to support classical, decoupled wave equations as in (2.1), the media (generally, excluding the conductors which support TL modes) should be homogeneous, and isotropic.

In summary, various conditions are used to enforce the propagation of TEM (or, under approximation, quasi-TEM) modes in the presence of multiple conductors – that is, TL modes:

$\vec{H}_l \approx \vec{0}$ $\vec{E}_l \approx \vec{0}$	Negligible longitudinal fields
$[\sigma] \approx \sigma\,[I]$ $[\epsilon] \approx \epsilon\,[I]$ $[\mu] \approx \mu\,[I]$	Isotropic media
$\vec{\nabla}\sigma \approx \vec{0}$ $\vec{\nabla}\epsilon \approx \vec{0}$ $\vec{\nabla}\mu \approx \vec{0}$	Homogeneous media

Assumption Set 1: Requirements of TL Modes

In general in the remainder of this work, the TEM approximation will be assumed unless stated otherwise.

2.1.4 Consequences of non-TEM Modes

Since practical TLs do not support strictly TEM modes, there have arisen several debates within the community as to how to best compute the properties of the modes which actually exist in these TLs. Schelkunoff is generally considered as being one of the first to discuss various definitions of modal properties in terms of choosing various approximations, where the longitudinal components of the fields are neglected in order to define voltage and current (VI) from the non-TEM modes, or either power and

current (PI), or power and voltage (PV) [291–297], where:

$$V = -\int_{t_0}^{t_1} \vec{E}_t \cdot d\vec{r} \tag{2.8a}$$

$$I = \oint_D \vec{H}_t \cdot d\vec{r} \tag{2.8b}$$

$$P = \frac{1}{2} \iint_S \left(\vec{E}_t \times \vec{H}_t^* \right) \cdot d\vec{s} \tag{2.8c}$$

where in (2.8a) t_0 and t_1 are two points over which the mode extends, and $\vec{r}$ is tangential to the selected curve between these points. Equation (2.8b) details the integration of the tangential magnetic field around a conductor in any closed path D, to which $\vec{r}$ is tangential. Power of the mode is given by (2.8c), where ideally the transverse integration plane S encompasses all space, but is generally truncated for practical reasons. The complex conjugate of the magnetic field is taken to yield the steady-state power, which in general is still complex.

Characteristic impedance of these modes is a frequently discussed modal property, since its computation directly on various combinations of these properties [298–301]. The commonplace Microstrip (MS) TL is often discussed in the context of determining these properties [302–306], as it is a prevalent example of a quasi-TEM mode with substantial longitudinal field components, especially at higher frequencies.

The conclusion of these discussions appears to have been that indeed, modal properties may not be uniquely determined for non-TEM modes. However, due to the nature of the path-dependence in the computation of the modal voltage (2.8a), it appears that most opinions have settled on the notion that the use of PI quantities in determining modal properties results in the most accurate solutions. This is because that particular definition does not require the selection of an integration path in non-magnetic media (although care must still be taken in determining currents via integration around each conductor individually) [307–309].

2.1.5 The Telegrapher's Equations

The Telegrapher's equations, or equations which describe the propagation of voltages and currents in TL modes, are foundation to more advanced topics such as MTL theory. Critically, it is the link between the electric and magnetic fields, and the voltage and current of a given TL mode that make it such a powerful tool. A few core aspects of this process are the development of a geometric factor, which links the fields' interactions with their environment with parameters used in the TL circuit element, and the development of relations between the modes' propagation constants and characteristic impedances, which are not presented in the same way in other works. Because the understanding of these quantities are critical to the understanding of the constitutive medium parameters used to describe TL-MTMs, the relevant derivations are completed here in detail.

The derivations begin through the definition of potentials of the electric and magnetic fields which

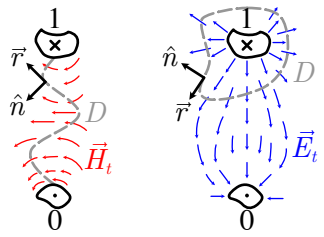

Figure 2.1: Example integration contours for D (represented with the dashed grey curve) for a) transverse magnetic fields $\vec{H}_t$ (represented with the red arrows) between conductors 0 and 1 (represented with the black curves), in which curve axis $\vec{r}$ represents the infinitesimal element of longitudinal length, and $\hat{n}$ represents the normal to the direction of the curve; and b) transverse electric fields $\vec{E}_t$ (represented with the blue arrows) around conductor 1, where curve axes $\vec{r}$, represents the infinitesimal element of longitudinal length, and $\hat{n}$ represents the surface normal. Unit vector $\hat{l}$ is taken to be positive directed into the page.

may be found inside of transmission-line environments. These potentials are defined as:

$$\phi_E = -\int_{t_0}^{t_1} \vec{E}_t \cdot d\vec{r} \tag{2.9a}$$

$$\phi_M = -\int_{t_0}^{t_1} \left(\left([\mu]\, \vec{H} \right)_t \times \hat{l} \right) \cdot d\vec{r} \tag{2.9b}$$

It may be noted that the potential quantities of (2.9) are equivalent to the more standard quantities of voltage (V) and magnetic flux (Φ). Then, fundamental electromagnetics links these potentials to the sources [16, 310]:

$$Q = CV \tag{2.10a}$$

$$I = L^{-1}\Phi \tag{2.10b}$$

where Q – the source of the electric potential – is the enclosed (free) electric charge (in the case of the two-dimensional transverse cross-section of the TL, per-unit-length). Due to the nature of the TL mode, it is assumed that the other conductor (conductor 0) possess the negative of this quantity, and that moreover, the voltage V between the conductors is related to this quantity by the capacitance C (also a per-unit-length quantity). Current I – the source of the magnetic potential – is the loop current (i.e., the magnitude of the current on either conductor), and L is in this case a per-unit-length inductance.

Applying the integral of (2.9) (that is, any contour D in the transverse plane from one conductor to the other as illustrated in Fig. 2.1a) to the TEM-reduced form of Ampere's Law (2.7b) yields the equation:

$$-\int_{t_0}^{t_1} \left(\vec{\nabla}_l \times \vec{H}_t \right) \cdot d\vec{r} = -\int_{t_0}^{t_1} \left([\sigma_{tt}]\, \vec{E}_t + \frac{\partial}{\partial \tau} \left([\epsilon_{tt}]\, \vec{E}_t \right) \right) \cdot d\vec{r} \tag{2.11}$$

Applying the various properties in Assumption Set 1 yields:

$$-\int_{t_0}^{t_1}\left(\vec{\nabla}_l \times \vec{H}_t\right)\cdot d\vec{r} = -\left(\sigma + \frac{\partial}{\partial\tau}\epsilon\right)\int_{t_0}^{t_1}\vec{E}_t \cdot d\vec{r} \tag{2.12}$$

where of course, the quantity on right is defined in (2.9) as the voltage:

$$-\int_{t_0}^{t_1}\left(\vec{\nabla}_l \times \vec{H}_t\right)\cdot d\vec{r} = \left(\sigma + \frac{\partial}{\partial\tau}\epsilon\right)V \tag{2.13}$$

Once again utilizing the specific form of the TL mode, inserting (2.1b) into the left-hand side gives:

$$-\int_{t_0}^{t_1}\left(\vec{\nabla}_l \times \vec{H}_t\right)\cdot d\vec{r} = -\frac{\partial}{\partial\vec{l}}\int_{t_0}^{t_1}\left(\hat{l} \times \vec{H}_t\right)\cdot d\vec{r} \tag{2.14}$$

The integrand on the right-hand side of (2.14) may be reduced by noting that it forms a *scalar triple product* [311], one relation of which is [312]:

$$\left(\vec{a}\times\vec{b}\right)\cdot\vec{c} = (\vec{c}\times\vec{a})\cdot\vec{b} \tag{2.15}$$

Then, noting that $d\vec{r} = \hat{r}dr$ and that $\hat{r}\times\hat{l} = \hat{n}$ (where $\hat{n}$ is the normal unit vector of the line integral in the transverse plane):

$$-\frac{\partial}{\partial\vec{l}}\int_{t_0}^{t_1}\left(\hat{l} \times \vec{H}_t\right)\cdot d\vec{r} = -\frac{\partial}{\partial\vec{l}}\int_{t_0}^{t_1}\left(\vec{H}_t\cdot\hat{n}\right)dr \tag{2.16}$$

Employing the definition of magnetic potential, or flux (B.10), where μ is again assumed to be homogeneous, and that the left-hand side then represents a magnetic flux through the integration curve (as depicted in Fig. 2.1a):

$$-\frac{\partial}{\partial\vec{l}}\mu^{-1}\Phi = \left(\sigma + \frac{\partial}{\partial\tau}\epsilon\right)V \tag{2.17}$$

Using (2.10b) in (2.17) yields:

$$\mu^{-1}L\frac{\partial}{\partial\vec{l}}I = -\left(\sigma + \frac{\partial}{\partial\tau}\epsilon\right)V \tag{2.18}$$

The quantity $\mu^{-1}L$ is known as the *geometric factor* of the TL and relates the TL mode's per-unit-length quantities to those of the medium in which it is embedded. Specifically,

$$g_L = \mu^{-1}L \tag{2.19}$$

such that (2.18) becomes:

$$\frac{\partial}{\partial\vec{l}}I = -g_L^{-1}\left(\sigma + \frac{\partial}{\partial\tau}\epsilon\right)V \tag{2.20}$$

Similarly, Faraday's law (2.7d) may be used to describe another relationship between currents and voltages. Integrating counter-clockwise around any closed contour D in the transverse plane which encompasses

only conductor 1 (as illustrated in Fig. 2.1b, and noting that a "positive" current is directed along $\hat{l}$):

$$\oint_D \left(\vec{\nabla}_l \times \vec{E}_t\right) \cdot d\vec{r} = -\oint_D \left(\frac{\partial}{\partial \tau}\mu\vec{H}_t\right) \cdot d\vec{r} \tag{2.21}$$

Once again, applying the notion that $[\mu]$ must be homogeneous, and assuming the integration loop is time-invariant:

$$\oint_D \left(\vec{\nabla}_l \times \vec{E}_t\right) \cdot d\vec{r} = \frac{\partial}{\partial \tau}\left(\mu I\right) \tag{2.22}$$

and applying the specific form of the propagating mode (2.1a):

$$\frac{\partial}{\partial \vec{l}}\oint_D \left(\hat{l} \times \vec{E}_t\right) \cdot d\vec{r} = \frac{\partial}{\partial \tau}\left(\mu I\right) \tag{2.23}$$

The application of a scalar triple product in this case requires noting that Fig. 2.1b details a different convention for $\hat{n}$ than the previous case (surface normal positive outwards), such that $\hat{r} \times \hat{l} = -\hat{n}$:

$$\frac{\partial}{\partial \vec{l}}\oint_D \left(\hat{l} \times \vec{E}_t\right) \cdot d\vec{r} = -\frac{\partial}{\partial \vec{l}}\oint_D \left(\vec{E}_t \cdot \hat{n}\right) dr \tag{2.24}$$

Gauss' Law [313, 314] may be invoked to solve the resulting integral:

$$\oint_S \epsilon\vec{E} \cdot d\vec{s} = Q \tag{2.25}$$

where S is any simple, closed surface and $d\vec{s}$ is the surface normal element (positive outwards), and Q is the enclosed (free) electric charge. Due to the nature of the TL mode, it is assumed that the other conductor (conductor 0) possess the negative of this quantity. Employing (2.25) and (2.10a) in (2.24) (using the curve D as the two-dimensional surface S) yields:

$$\epsilon^{-1}C\frac{\partial}{\partial \vec{l}}V = -\frac{\partial}{\partial \tau}\left(\mu I\right) \tag{2.26}$$

where the quantity $[\epsilon]^{-1}C$ is (the inverse of) a geometric factor, specifically:

$$g_C^{-1} = \epsilon^{-1}C \tag{2.27}$$

and therefore,

$$\frac{\partial}{\partial \vec{l}}V = -g_C^{-1}\frac{\partial}{\partial \tau}\left(\mu I\right) \tag{2.28}$$

It will then be assume that the materials are static (i.e., are time-invariant), and also linear:

$$\begin{gathered}\sigma\left(\tau\right) \approx \sigma \\ \epsilon\left(\tau\right) \approx \epsilon \\ \mu\left(\tau\right) \approx \mu \\ \sigma\left(V, I\right) \approx \sigma\end{gathered}$$

$$\epsilon\left(V,I\right)\approx\epsilon$$
$$\mu\left(V,I\right)\approx\mu$$

Assumption Set 2: Time-Invariant and Linear Media

Then, inserting the time-harmonic form of the mode gives:

$$\left(\frac{\partial}{\partial\tau}\epsilon V\right)=j\omega\epsilon V \tag{2.29a}$$

$$\left(\frac{\partial}{\partial\tau}\mu I\right)=j\omega\mu I \tag{2.29b}$$

Rearranging (2.20) and inserting it into (2.28) yields:

$$-\frac{\partial}{\partial\vec{l}}\left(\left(\sigma+j\omega\epsilon\right)^{-1}g_L\frac{\partial}{\partial\vec{l}}I\right)=-g_C^{-1}\left(j\omega\mu I\right) \tag{2.30}$$

Furthermore, invoking the longitudinal invariance of the materials (2.2),

$$\left(\frac{\sigma}{j\omega}+\epsilon\right)^{-1}g_L\frac{\partial^2}{\partial\vec{l}^2}I=g_C^{-1}\mu I \tag{2.31}$$

which may be reduced to the scalar wave equation (the Helmholtz form [315]):

$$\frac{\partial^2}{\partial\vec{l}^2}I=\left(\frac{\sigma}{j\omega}+\epsilon\right)g_L^{-1}g_C^{-1}\mu I \tag{2.32}$$

The same assumptions may applied to (2.7d) and (2.7b), to yield:

$$\frac{\partial}{\partial\vec{l}}\left(\hat{l}\times\vec{H}_t\right)=\left(\sigma+j\omega\epsilon\right)\vec{E}_t \tag{2.33a}$$

$$\frac{\partial}{\partial\vec{l}}\left(\hat{l}\times\vec{E}_t\right)=-\left(j\omega\mu\right)\vec{H}_t \tag{2.33b}$$

Re-arranging (2.33a) to solve for $\vec{E}_t$ and substituting it into (2.33b) yields:

$$-\frac{\partial^2}{\partial\vec{l}^2}\left(\left(\hat{l}\times\hat{l}\times\vec{H}_t\right)\left(\sigma+j\omega\epsilon\right)^{-1}\right)=-\left(j\omega\mu\right)\vec{H}_t \tag{2.34}$$

Since $\hat{l}\times\hat{l}\times\vec{H}_t=-\vec{H}_t$ [16], (2.34) may be re-arranged to the Helmholtz equation:

$$\frac{\partial^2}{\partial\vec{l}^2}\vec{H}_t=\left(\frac{\sigma}{j\omega}+\epsilon\right)\mu\vec{H}_t \tag{2.35}$$

The wave propagation constants of (2.32) and (2.35) are:

$$\left(\frac{\sigma}{j\omega}+\epsilon\right)g_L^{-1}g_C^{-1}\mu \tag{2.36a}$$

$$\left(\frac{\sigma}{j\omega}+\epsilon\right)\mu \tag{2.36b}$$

From (2.9a) and (2.9b), it becomes apparent that the fields $\vec{E}_t$ and $\vec{H}_t$ are linked with the quantities V and I (respectively) independent of phase. Physically speaking, it may be said that the voltages and currents of a TL mode must propagate at the same rate (and with the same rate of decay) as the fields which define the mode. Then, it becomes apparent that (2.36a) is equivalent to (2.36b), such that $g_L^{-1}g_C^{-1}=1$, and that therefore:

$$g_L = g_C^{-1} \equiv g \tag{2.37}$$

Then, using (2.37) in (2.20) and (2.28) yields:

$$\frac{\partial}{\partial\vec{l}}I = -g^{-1}\left(\sigma+j\omega\epsilon\right)V \tag{2.38a}$$

$$\frac{\partial}{\partial\vec{l}}V = -g\left(j\omega\mu I\right) \tag{2.38b}$$

Finally, (2.38) may be reduced, firstly by specifying a set propagation axis, typically taken to be the z-axis of cartesian coordinates, such that $\hat{l}=\hat{z}$ and $\hat{t}=\{\hat{x},\hat{y}\}$. Re-employing (2.19) and (2.27) as well yields the scalar equations:

$$\frac{\partial}{\partial z}I\left(z\right) = -\left(G+j\omega C\right)V\left(z\right) \tag{2.39a}$$

$$\frac{\partial}{\partial z}V\left(z\right) = -\left(j\omega L\right)I\left(z\right) \tag{2.39b}$$

where $G=g^{-1}\sigma$ is defined as the per-unit-length conductance of the TL mode. Typically, the complex μ is also expanded to accommodate losses by explicitly defining its imaginary components [16], which are related in this work to the source of resistivity in the TL's conductors:

$$\mu = \mu' - j\mu'' = \mu' - \frac{j}{\omega}r \tag{2.40}$$

Defining per-unit-length resistance $R=gr$, and recasting the definition of inductance L to refer to only the real component of μ, allows the insertion of (2.40) into (2.38b) to give:

$$\frac{\partial}{\partial z}V\left(z\right) = -\left(R+j\omega L\right)I\left(z\right) \tag{2.41}$$

The presence of a nonzero per-unit-length resistance R yields a longitudinal electric field [264], such that its existence violates the TEM approximation discussed in section 2.1.3. As such, R will generally considered to be zero in the remainder of this work, unless specified otherwise.

In general, the complex per-unit-length quantities are combined into per-unit-length admittance (Y) and impedance (Z) quantities:

$$Y = \left(G+j\omega C\right) \tag{2.42a}$$

$$Z = \left(R+j\omega L\right) \tag{2.42b}$$

Then, inserting (2.42) into (2.39) yields the compact form of the Telegrapher's equations:

$$\frac{\partial}{\partial z} I(z) = -YV(z) \tag{2.43a}$$

$$\frac{\partial}{\partial z} V(z) = -ZI(z) \tag{2.43b}$$

which describe the propagation of voltages and currents of a TL mode. Furthermore, combining the two equations of (2.43) yields the wave equations:

$$\frac{\partial^2}{\partial z^2} V(z) = ZYV(z) \tag{2.44a}$$

$$\frac{\partial^2}{\partial z^2} I(z) = YZI(z) \tag{2.44b}$$

where, since (2.44) represent wave equations, the quantities ZY and YZ are equal to the square of the modal propagation constants γ, such that

$$\gamma^2 = ZY \tag{2.45a}$$

$$\gamma^2 = YZ \tag{2.45b}$$

While (2.43) and (2.44) refer to total voltages and currents related to the two conductors, the system is capable of supporting two contra-directed modes simultaneously (e.g., one propagating in $\hat{z}$ and one propagating in -$\hat{z}$). The total voltages and currents are superpositions of the quantities of each of these directional waves, expressed as:

$$V(z) = V^+ e^{-\gamma z} + V^- e^{\gamma z} \tag{2.46a}$$

$$I(z) = I^+ e^{-\gamma z} + I^- e^{\gamma z} \tag{2.46b}$$

The quantities with the corresponding '+' symbol are those of the fields of a mode propagating along the $+z$ direction, while those with the '$-$' symbol are linked with those of the fields of a mode propagating along the $-z$ direction. It is critical to note that this work chooses to define the direction in which a mode is travelling with regards to phase (i.e., the exponent of the exponential function), rather than with regards to power – which is common in other works [181,182]. Considering next the case of a single mode, in which the magnitude of the contra-directed mode is zero. Inserting (2.46) into (2.43a) for the cases of $\{V^-, I^-\} = \vec{0}$ (representing the case of a forward-travelling wave), and $\{V^+, I^+\} = \vec{0}$ (representing the case of a backward-travelling wave) yields:

$$-\gamma I^+ e^{-\gamma z} = -YV^+ e^{-\gamma z} \tag{2.47a}$$

$$\gamma I^- e^{\gamma z} = -YV^- e^{\gamma z} \tag{2.47b}$$

Re-arranging (2.47) allows us to express the ratios:

$$\frac{V^+}{I^+} = Z_c = Y^{-1}\gamma \tag{2.48a}$$

$$\frac{V^-}{I^-} = -Z_c = -Y^{-1}\gamma \tag{2.48b}$$

where the quantity Z_c is known as the *characteristic impedance* of the mode. Inserting (2.46) into (2.43b) instead allows for the expression of the same characteristic impedances in a different form:

$$\frac{V^+}{I^+} = Z_c = \gamma^{-1}Z \tag{2.49a}$$

$$\frac{V^-}{I^-} = -Z_c = -\gamma^{-1}Z \tag{2.49b}$$

The Telegrapher's equations – inherently bound by the TEM approximation – possess frequency limits to which they are correct. In particular, as frequency increases conductor losses due to the skin and proximity effects become increasingly non-negligible, causing longitudinal fields which also tend to radiate [264]. Thus, these approximations are only considered valid below millimeter-wave or terahertz frequencies, and generally the TEM modes they describe may be ignored at optical frequencies or higher.

2.1.6 Backward Modes

Observing the wave equations of the fields (2.35) and circuit quantities (2.44b), it may be noticed that the propagation constant γ originates from these equations, where its value is squared. In order to extract γ, a square root operation must be used. In the absence of losses, γ will be entirely imaginary, and the two roots of γ^2 are $\pm\gamma$. Because the radicand evaluates to the same if both μ and ϵ have either a positive or negative sign, it must be the case that propagation occurs under either case. While typically only the case of both values positive are considered, Veselago was one of the first to point out the case of both quantities negative, and the myriad of interesting phenomena which could arise from such media [108]. Owing to the fact that γ is proportional to the effective index of refraction of the materials, those for which μ and ϵ possess negative entries (so-called *double-negative media*) have become known as *negative refractive index* media.

Due to Faraday's (2.5d) and Ampere's (2.5b) Laws' dependences on the constitutive material parameters, it may be observed that when these quantities are negative, an electric field generates a negative magnetic field, and vice-versa. This forms what is known as the left-handed triplet, where, for a given electric field, the power propagated in the opposite direction due to (2.8c). Note that although power may flow in the opposite direction, the propagation constant in the negative refractive index media still possesses the same sign as it does in the positive refractive index media. Because the propagation constant is proportional to the phase velocity of the mode, while the power flow is related to its group velocity, the direction of the phase and group velocities are oppositely directed for modes in double-negative media – hence the name *backward* modes (as opposed to the *forward* modes in double-positive media). These backward modes form a left-handed triplet with the electric field, magnetic field, and group velocity (as opposed to the right-handed triplet in double-positive media), such that double-negative media are sometimes known as *left-handed* media. In this work, it will always be assumed that the imaginary component of γ is positive, and that other properties such as the direction of power flow are taken relative to this direction.

Finally, an assumption is made in this work, which may be considered a trivial terminological definition, but nonetheless has important ramifications:

Geometric factors g are always positive.

Assumption Set 3: Positive Geometric Factors

Owing to the relations between the per-unit-length impedance (Z) and admittance (Y) of a mode, and the constitutive parameters in which the TL is embedded (2.19) and (2.27), Assumption Set 3 guarantees that for backward modes, Z and Y must be negative as well.

2.2 Coupled Mode Theory

2.2.1 History of Coupled-Mode Theory

Coupled-Mode Theory (CMT) involves the study of the uniform coupling of two modes. The study of a system involving only two modes appeared first in the works of Miller [316] and Pierce, [317], but the modern notations used are often attributed to Haus [318]. However, describing coupled transmission-line modes with CMT is generally credited to Schelkunoff, who derived equations describing the coupling of TL modes directly from Maxwell's equations [287].

2.2.2 Formulation

Considering the telegrapher's equations for two independent $\hat{z}$-directed modes:

$$\frac{\partial}{\partial z} V_1(z) = -Z_1 I_1(z) \tag{2.50a}$$

$$\frac{\partial}{\partial z} I_1(z) = -Y_1 V_1(z) \tag{2.50b}$$

$$\frac{\partial}{\partial z} V_2(z) = -Z_2 I_2(z) \tag{2.50c}$$

$$\frac{\partial}{\partial z} I_2(z) = -Y_2 V_2(z) \tag{2.50d}$$

in which the subscripts indicate which mode the various quantities refer to. These equations may be expressed in matrix form as:

$$\frac{\partial}{\partial z}\begin{bmatrix} V_1(z) \\ V_2(z) \\ I_1(z) \\ I_2(z) \end{bmatrix} = -\begin{bmatrix} 0 & 0 & Z_1 & 0 \\ 0 & 0 & 0 & Z_2 \\ Y_1 & 0 & 0 & 0 \\ 0 & Y_2 & 0 & 0 \end{bmatrix}\begin{bmatrix} V_1(z) \\ V_2(z) \\ I_1(z) \\ I_2(z) \end{bmatrix} \tag{2.51}$$

Coupling between the two modes is typically described in terms of a mutually-induced per-unit-length admittance or impedance (Y_m and Z_m, respectively). The total response of both the propagating modes and the coupled response is then given as:

$$\frac{\partial}{\partial z}V_1(z) = -Z_1 I_1(z) - Z_m I_2(z) \tag{2.52a}$$

$$\frac{\partial}{\partial z}I_1(z) = -Y_1 V_1(z) + Y_m V_2(z) \tag{2.52b}$$

$$\frac{\partial}{\partial z}V_2(z) = -Z_2 I_2(z) - Z_m I_1(z) \tag{2.52c}$$

$$\frac{\partial}{\partial z}I_2(z) = -Y_2 V_2(z) + Y_m V_1(z) \tag{2.52d}$$

Equations (2.52) may be expressed in matrix form as:

$$\frac{\partial}{\partial z}\begin{bmatrix} V_1(z) \\ V_2(z) \\ I_1(z) \\ I_2(z) \end{bmatrix} = -\begin{bmatrix} 0 & 0 & Z_1 & Z_m \\ 0 & 0 & Z_m & Z_2 \\ Y_1 & -Y_m & 0 & 0 \\ -Y_m & Y_2 & 0 & 0 \end{bmatrix}\begin{bmatrix} V_1(z) \\ V_2(z) \\ I_1(z) \\ I_2(z) \end{bmatrix} \tag{2.53}$$

or, in a condensed form:

$$\frac{\partial}{\partial z}\begin{bmatrix} \vec{V}(z) \\ \vec{I}(z) \end{bmatrix} = -\begin{bmatrix} [0] & [Z] \\ [Y] & [0] \end{bmatrix}\begin{bmatrix} \vec{V}(z) \\ \vec{I}(z) \end{bmatrix} \tag{2.54}$$

The underlying physics behind the next step is critical: while the matrices $[\gamma_V]$ and $[\gamma_I]$ describe how the voltages and currents propagate for each original mode 1 and 2, the quantities that are actually desired are the propagation constants of the *coupled* modes which exist in the coupled system. These new modes are similar to the isolated ones in the sense that they are defined by propagation of individual voltage and/or current waves; however, the voltages and currents involved belong to both isolated modes. These waves are expressed as:

$$\vec{V}(z) = \vec{V}e^{\gamma z} \tag{2.55a}$$

$$\vec{I}(z) = \vec{I}e^{\gamma z} \tag{2.55b}$$

inserting these relations into (2.54) yields:

$$\gamma\begin{bmatrix} \vec{V} \\ \vec{I} \end{bmatrix} = -\begin{bmatrix} [0] & [Z] \\ [Y] & [0] \end{bmatrix}\begin{bmatrix} \vec{V} \\ \vec{I} \end{bmatrix} \tag{2.56}$$

which is a standard eigenmode equation [319, 320]. Therefore, solving the eigenmodes of the matrix on the right-hand side of (2.56) gives the set of possible propagation constants γ, while the eigenvectors will contain information about the arbitrarily scaled voltages and currents of each of the coupled modes in terms of the original isolated modes.

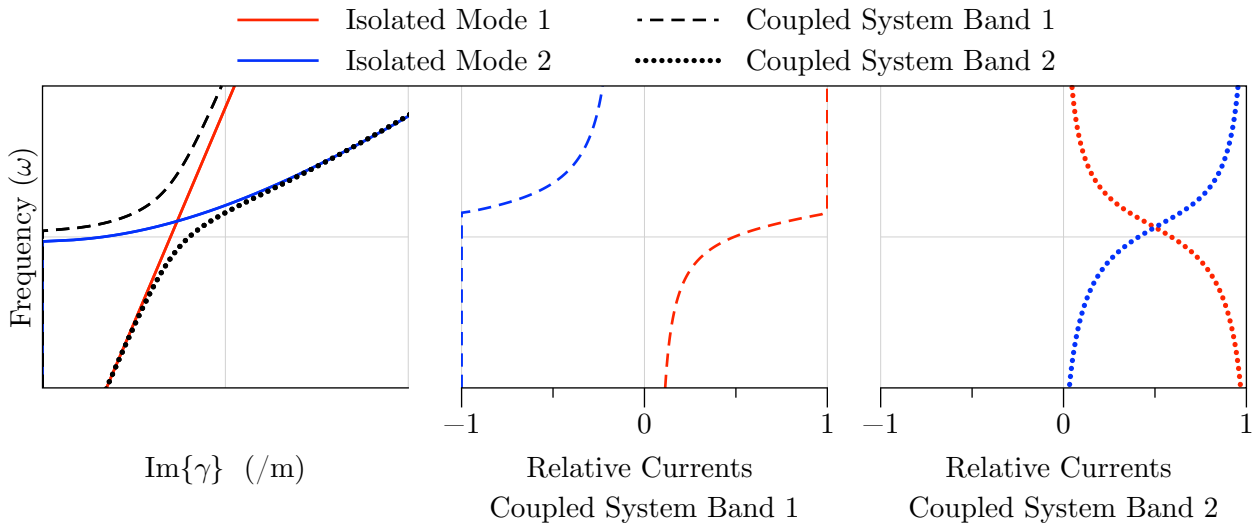

Figure 2.2: Example coupling diagrams of two forward modes. The middle and right-hand panels detail the current distributions for each band of the coupled system, in terms of those of the isolated modes. Currents on the reference conductor(s) of the modes not shown.

2.2.3 Modes and Bands

Oftentimes in the Literature of periodic structures, the terms "mode" and "band" are used interchangeably. In this work, the terms will be used with specific meanings:

- A mode is a given field distribution – or, in the TL domain, a set of currents and voltages. Modes generally have fairly stable properties with respect to frequency, although a given mode may not always be supported by a structure at any given frequency.
- A band is a continuous curve on a dispersion diagram. Bands may consist of one or more modes, and may represent a transition from a given mode at one frequency to another mode at another frequency. Therefore, it should not be expected that their properties are stable with respect to frequency.

In general, bands arise from the coupling of various modes. In systems which do not support coupling between modes, modes and bands become similar, although in general a mode may possess multiple bands.

2.2.4 Examples

Forward-Forward Coupling

Figure 2.2 depicts the coupling of modes when both are forward-directed – i.e., Z_1, Y_1, Z_2, Y_2, Z_m, and Y_m all possess positive imaginary values. The mode labelled "Isolated Mode 1" – represented with the red curve – is a typical non-dispersive mode; i.e., its properties are constant as a function of frequency. The mode labelled "Isolated Mode 2" – represented with the blue curve – is a forward mode, but which

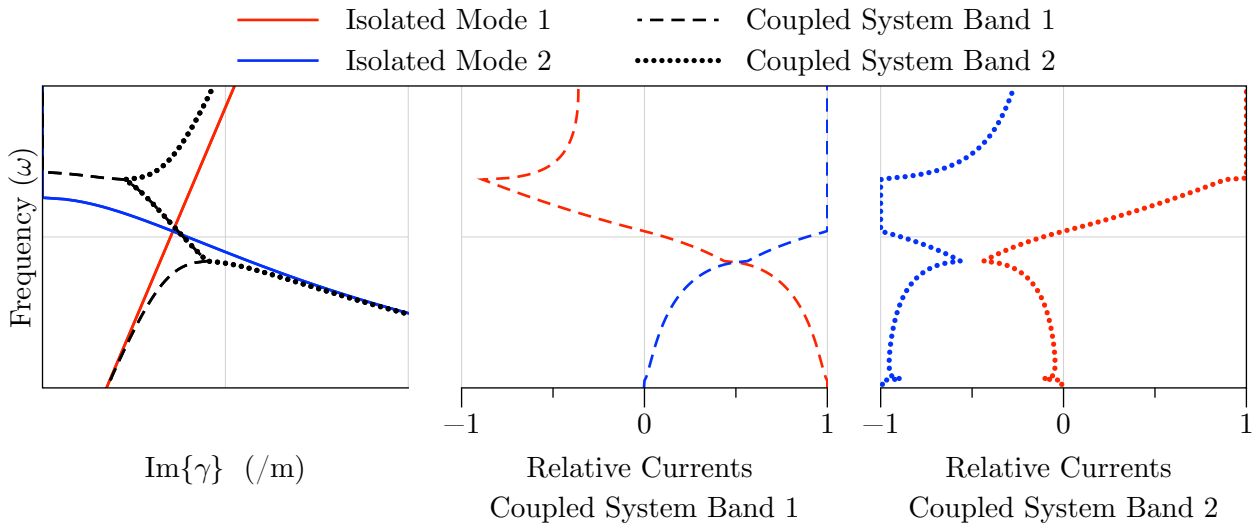

Figure 2.3: Example coupling diagrams of a forward mode with a backward mode. The middle and right-hand panels detail the current distributions for each band of the coupled system, in terms of those of the isolated modes. Currents on the reference conductor(s) of the modes not shown.

is cutoff below a certain frequency, where $\gamma \to 0$. The two modes couple in regions where they are phase-matched (overlap on the ω-γ plot) to yield the coupled system labelled "Coupled System", which has two bands that are indicated with the black dashed and dotted curves. It may be observed that in the coupling region, the propagation properties (and, by extension, other properties) of both the original modes have been distorted, such that neither mode is truly supported.

The distribution of currents belonging to the isolated modes (i.e., the current portions of the eigenvectors of (2.56)) are plotted in the center and right-hand panels for each of the coupled system's bands. These data detail how the properties of each band change with frequencies – in this case, how the currents of the bands change between being dominated by those of the isolated mode 1 and those of isolated mode 2 (and vice-versa for the other band). This is expected based on the dispersive properties of the bands shown in the left-hand panel, since clearly the bands transition from the dispersion properties of one isolated mode to the other as frequency increases.

Forward-Backward Coupling

Figure 2.3 depicts the coupling of modes when one is forward-directed and one is-backward-directed - i.e., Z_1, Y_1, Z_m, and Y_m possess positive imaginary values, while Z_2, Y_2 possess negative imaginary values. The mode labelled "Isolated Mode 1" – represented with the red curve – is the same non-dispersive mode as in the previous forward-forward coupling case. The mode labelled "Isolated Mode 2" – represented with the blue curve – is the backward mode, which only propagates over a certain frequency range. The two modes again couple in regions where they are phase-matched to yield the coupled system labelled "Coupled System", which similarly has two bands that are indicated with the black dashed and dotted curves. In the coupling region, however, both bands possess the same imaginary components of γ – these are complex modes which occur in complex-conjugate pairs [321–328].

These complex modes both have nearly identical properties: as indicated in the current distributions in the middle and right-hand panels, the relative currents have equal magnitudes but opposite signs over this frequency range. Band 1 of the coupled system is similar to isolated mode 1 at lower frequencies, and transitions to dominantly isolated mode 2 at higher frequencies, while band 2 of the coupled system exhibits the reverse. Interestingly, the relative currents are negative in the second coupled band at low frequencies, indicating that currents flow the opposite direction that they do at higher frequencies – as would be expected from a mode which incurs phase in the same direction in both bands in which it possesses backward properties, and bands in which it possesses forward properties.

The frequency region over which the complex modes exist is the *band gap*, a term borrowed from solid-state physics [329–331] since it describes a region in which the transfer of real power is impeded.

2.3 Multiconductor Transmission-Line Theory

2.3.1 History of Multiconductor Transmission Line Theory

The development of MTL theory naturally began alongside the development of TL theory, as it is a generalization of the latter. Similar figures as were involved with the development TL theory worked on the initial development of its extension of the multiconductor case. Lord Kelvin appears to have been the first to attempt to analyze the structures [332], although Heaviside repeated the analysis several years later with greater detail on solutions for both currents and potentials, and even briefly examined the properties of various TL modes supported by such structures [333].

In the early 20^{th} century, Pleijel [334], Levin [335], Carson [336] and others began analyzing shielded multi-stranded cables, as well as multiple parallel lines above a realistic earth model. Pipes formalized MTL theory using matrix notation [337–339], while Rice notably initiated the use of variables that are commonly used in the modern literature [340]. Classic and thorough texts encompassing many aspects of MTL theory have been authored more recently by Paul [264] and Faria [265].

2.3.2 Formulation

MTL theory generalizes the concepts of TL theory to the cases of more than two parallel conductors. As such, it naturally extends the concepts of voltages and currents to existing on many conductors simultaneously, with respect to an arbitrary – but established – reference conductor, such that there are $n-1$ currents and voltages described for a group of n conductors. Such a system may also be thought of as a generalized case of the previously introduced CMT, in which there exist more than two voltages and currents, and the mutual coupling parameters between each is strictly defined by the properties of the MTL system. As discussed in the establishing works [332, 333], it will be the case that the various voltages establish various currents, and vice-versa. The Telegrapher's equations (2.43) then become:

$$\frac{\partial}{\partial z}\vec{I}\,(z) = -\,[Y]\,\vec{V}\,(z) \tag{2.57a}$$

$$\frac{\partial}{\partial z}\vec{V}(z) = -[Z]\,\vec{I}(z) \tag{2.57b}$$

where the matrix quantities $[Y]$ and $[Z]$ are again the per-unit-length admittance and impedance quantities, expressed between each conductor and a pre-selected reference conductor. These matrices are required to be symmetric (i.e., $Y_{nm} = Y_{mn}$, etc.) due to reciprocity – a fact pointed out by Lord Kelvin in his original studies on the subject [332]. Due to the fact that the properties are expressed on the basis of the conductors – or, accessible *terminals*, the expression of the quantities in this basis has historically been referred to as the *terminal domain* (also to a lesser extent, the *natural domain*). The expression of quantities in the terminal domain in this work will be indicated with the subscript T, such that the previous expressions may be written as:

$$\frac{\partial}{\partial z}\vec{I}_T(z) = -[Y_T]\,\vec{V}_T(z) \tag{2.58a}$$

$$\frac{\partial}{\partial z}\vec{V}_T(z) = -[Z_T]\,\vec{I}_T(z) \tag{2.58b}$$

Similarly, the wave equations from TL theory (2.44) may be expressed as:

$$\frac{\partial^2}{\partial z^2}\vec{V}_T(z) = [Z_T]\,[Y_T]\,\vec{V}_T(z) \tag{2.59a}$$

$$\frac{\partial^2}{\partial z^2}\vec{I}_T(z) = [Y_T]\,[Z_T]\,\vec{I}_T(z) \tag{2.59b}$$

The total voltages and currents as expressed in terms of individual propagating waves (2.46) may also be written as

$$\vec{V}_T(z) = \vec{V}_T^{+}(z)\,e^{-\gamma z} + \vec{V}_T^{-}(z)\,e^{\gamma z} \tag{2.60a}$$

$$\vec{I}_T(z) = \vec{I}_T^{+}(z)\,e^{-\gamma z} + \vec{I}_T^{-}(z)\,e^{\gamma z} \tag{2.60b}$$

in which the particular meaning of γ in this context is akin to that used in section 2.2.2, but which will be specified shortly. From (2.59), this work defines the propagation constant matrices

$$[\gamma_V]^2 = [Z_T]\,[Y_T] \tag{2.61a}$$

$$[\gamma_I]^2 = [Y_T]\,[Z_T] \tag{2.61b}$$

where, by symmetry of $[Z_T]$ and $[Y_T]$, it may be observed that $[\gamma_V] = [\gamma_I]^T$. Then, analogous to the previously introduced characteristic impedances (2.48), defining:

$$\vec{V}_T^{+} = [Z_{cT}]\,\vec{I}_T^{+} \tag{2.62a}$$

$$\vec{V}_T^{-} = -[Z_{cT}]\,\vec{I}_T^{-} \tag{2.62b}$$

the characteristic impedances may then be expressed as:

$$[Z_{cT}] = [\gamma_V]\,[Y_T]^{-1} = [\gamma_V]^{-1}\,[Z_T] \tag{2.63a}$$

$$[Z_{cT}] = [Y_T]^{-1}\,[\gamma_I] = [Z_T]\,[\gamma_I]^{-1} \tag{2.63b}$$

2.3.3 MTL Modes

Owing to MTL theory's extension of TL theory to the case of more than two conductors, it is certain that MTLs will support multiple TL modes. However, it is not certain as to how these modes may be defined, or even how many of these modes exist. In order to shed light on these and other issues, some fundamentals of wave physics must first be employed.

Firstly, it is noted that the general form of a TL mode (2.1) is still valid, since this mode is defined by its electromagnetic field quantities, rather than any specific voltages or currents. Secondly, it may be noted that the field quantities refer to *all* of the fields in the mode's transverse plane, such that it must be the case that all of the fields everywhere in a transverse cross-section incur phase at the same rate γ. Finally, since by (2.9) and (2.10) the fields are directly related to the circuit quantities, it may be inferred that when a MTL mode is being considered, it must be the case that the mode exhibits *corporate propagation* – that is, all of the constituent voltages and currents incur phase at the same rate, γ. Essentially, this statement is written in terms of voltages and currents as (2.60). Combining this equation with the wave equations of (2.59) and using the notation of (2.61) yields:

$$\gamma^2 \vec{V}_T = [\gamma_V]^2\,\vec{V}_T \tag{2.64a}$$

$$\gamma^2 \vec{I}_T = [\gamma_I]^2\,\vec{I}_T \tag{2.64b}$$

which may be recognized as an eigenmode equation, in which γ^2 represents a given eigenvalue, and $\vec{V}_T$ and $\vec{I}_T$ represent the associated eigenvectors for each equation.

Even though the eigenvectors $\vec{V}_T$ and $\vec{I}_T$ possess in general arbitrary complex values, it may be demonstrated that in fact, their forms are limited due to the specific values of the propagation constants matrices in these eigenmode equations. The per-unit-length impedances and admittances may be separated into their real and imaginary components as:

$$[Z_T] = [R_T] + j\omega\,[L_T] \tag{2.65a}$$

$$[Y_T] = [G_T] + j\omega\,[C_T] \tag{2.65b}$$

where $[R_T]$, $[L_T]$, $[G_T]$, and $[C_T]$ are the per-unit-length terminal domain resistance, inductance, conductance, and capacitance matrices (respectively) of the TL. All of these matrices are positive-definite [341]. Substituting (2.65) into (2.61) and (2.64) yields

$$\left([R_T]\,[G_T] - \gamma^2\,[I] - \omega^2\,[L_T]\,[C_T] + j\omega\left([L_T]\,[G_T] - [R_T]\,[C_T]\right)\right)\vec{V}_T = \vec{0} \tag{2.66}$$

The requirement that $[R_T] \to 0$ for TEM modes [264] allows (2.66) to be expressed as:

$$\left(\gamma^2 \left[L_T\right]^{-1} + j\omega \left[G_T\right] - \omega^2 \left[C_T\right]\right) \vec{V}_T = \vec{0} \tag{2.67}$$

Equation (2.67) is a canonical form that has been investigated extensively in the literature of the modal analysis of mechanical systems [342–345]. In general for systems of symmetric matrices (i.e., exhibiting reciprocity), its modal solutions fall into two categories [345–347]:

- *Normal* modes, in which the eigenvectors $\vec{V}_T$ may possess any arbitrary amplitudes, but the phases of which are restricted to within integer multiples of π of each other.

- *Complex* modes, in which the eigenvectors $\vec{V}_T$ may possess any arbitrary phases, but are restricted to appearing in pairs, which are complex conjugates of one another.

Invoking another requirement of TEM modes – that they must be supported inside a homogenous medium – gives the requirement that $[G_T] = \frac{\sigma}{\epsilon} [C_T]$ [264] (which is similar in form to Lord Rayleigh's canonical *proportional damping* [342]). Defining a change of basis $\vec{V}_T = [T_V] \vec{W}$, in which $[T_V]$ is the set of eigenvectors $\vec{V}_T$ diagonalizes the eigenmode equations (2.64), and pre-multiplying by $[T_V]^T$ yields:

$$[T_V]^T \left(\gamma^2 \left[L_T\right]^{-1} + j\omega \frac{\sigma}{\epsilon} \left[C_T\right] - \omega^2 \left[C_T\right]\right) [T_V] \vec{W} = \vec{0} \tag{2.68}$$

In order for this system to support a complete set of modes, $[L_T]^{-1}$ and $[C_T]$ must be simultaneously diagonalizable via the congruence transform by $[T_V]$. This occurs if and only if the matrix product $[L_T][C_T]$ is diagonalizable [319]. However, given the previously enforced TEM conditions, this statement is equivalent to the existence of the propagation constants in (2.64). Since the existence of propagation constants is generally taken as a pre-supposition to conducting modal analysis, it is assumed to hold true henceforth.

It may then be demonstrated that the eigenmodes of such a system are real. The similarity transformation $[T_V]^{-1} [L_T] [C_T] [T_V]$ can be factored into the product of two individual similarity transformations:

$$[T_V]^{-1} [L_T] [C_T] [T_V] = \left([T_V]^{-1} [L_T]^{-1} [T_V]\right)^{-1} \left([T_V]^{-1} [C_T] [T_V]\right) \tag{2.69}$$

Since each of $[L_T]^{-1}$, $[C_T]$ is real and symmetric, it is guaranteed that each of these has eigenvalues. Since the eigenvalues of the matrix product are simply the product of these matrices' eigenvalues, it is the case that each of the eigenvalues of the left-hand side of (2.69) are real as well. Lastly, it is the case that if both the matrix product $[L_T][C_T]$ and its eigenvalues are real, then its eigenvectors (i.e., $[T_V]$) may be expressed as entirely real as well – which is necessarily true for normal modes. A similar derivation may be conducted using current eigenvectors rather than the voltage eigenvectors used in the previous derivations. Therefore, it may be concluded that modes under the TEM approximation (Assumption Set 1) are normal modes.

2.3.4 Domain Transformations

Since MTL systems may be described using either terminal or modal representations, naturally one may inquire as to the relationship between them. The notation of (2.64) may be expanded to include all possible eigensystem solutions:

$$[T_V]\,[\gamma_M]^2 = [\gamma_V]^2\,[T_V] \tag{2.70a}$$

$$[T_I]\,[\gamma_M]^2 = [\gamma_I]^2\,[T_I] \tag{2.70b}$$

where $[\gamma_M]$ is the diagonal matrix of modal propagation constants, $[T_V]$ the square matrix of voltage eigenvectors, and $[T_I]$ the square matrix of current eigenvectors. Equation (2.70) may then be re-arranged to the similarity transformation [319, 320]:

$$[T_V]\,[\gamma_M]^2\,[T_V]^{-1} = [\gamma_V]^2 \tag{2.71a}$$

$$[T_I]\,[\gamma_M]^2\,[T_I]^{-1} = [\gamma_I]^2 \tag{2.71b}$$

Inserting (2.71) back into the wave equations (2.59) and again using (2.61) yields:

$$\frac{\partial^2}{\partial z^2}\vec{V}_T(z) = [T_V]\,[\gamma_M]^2\,[T_V]^{-1}\,\vec{V}_T(z) \tag{2.72a}$$

$$\frac{\partial^2}{\partial z^2}\vec{I}_T(z) = [T_I]\,[\gamma_M]^2\,[T_I]^{-1}\,\vec{I}_T(z) \tag{2.72b}$$

which may be re-arranged to (noting the spatial invariance of the transformation matrices arises from the longitudinal invariance of the TL's geometric properties (2.2)):

$$\frac{\partial^2}{\partial z^2}[T_V]^{-1}\,\vec{V}_T(z) = [\gamma_M]^2\,[T_V]^{-1}\,\vec{V}_T(z) \tag{2.73a}$$

$$\frac{\partial^2}{\partial z^2}[T_I]^{-1}\,\vec{I}_T(z) = [\gamma_M]^2\,[T_I]^{-1}\,\vec{I}_T(z) \tag{2.73b}$$

It may be recognized that the quantities $[T_V]^{-1}\,\vec{V}_T(z)$ and $[T_I]^{-1}\,\vec{I}_T(z)$ represent change of bases to the respective quantities $\vec{V}_T(z)$ and $\vec{I}_T(z)$. In order to understand the new basis, it is observed that the matrix of propagation constants, $[\gamma_M]$ is diagonal, meaning that the set of equations (i.e., each of (2.73a) or (2.73b)) are decoupled. This of course describes the propagation of individual modes, where interestingly each mode may then be modelled as consisting of a single voltage and current, and described as an isolated two-conductor TL. Then, the quantities $\vec{V}_M(z) = [T_V]^{-1}\,\vec{V}_T(z)$ and $\vec{I}_M(z) = [T_I]^{-1}\,\vec{I}_T(z)$ may be defined – once again invoking the spatial independence of the transformation matrices:

$$\vec{V}_T = [T_V]\,\vec{V}_M \tag{2.74a}$$

$$\vec{I}_T = [T_I]\,\vec{I}_M \tag{2.74b}$$

The quantities $\vec{V}_M$ and $\vec{I}_M$ indicate the modal-domain voltages and currents, respectively, where along

similar veins to the subscript T, the subscript M will be used in general to indicate modal-domain quantities.

A power property of similar matrices is [320]:

$$[A]^k = [T]\,[D]^k\,[T]^{-1} \tag{2.75}$$

where $[D]$ is a diagonal matrix and $[T]$ represents a change of basis, or transformation matrix. Therefore, (2.71) may also be expressed as:

$$[\gamma_M] = [T_V]^{-1}\,[\gamma_V]\,[T_V] \tag{2.76a}$$

$$[\gamma_M] = [T_I]^{-1}\,[\gamma_I]\,[T_I] \tag{2.76b}$$

Using (2.74) in (2.58) yields:

$$\frac{\partial}{\partial z}\vec{I}_M(z) = -[T_I]^{-1}\,[Y_T]\,[T_V]\,\vec{V}_M(z) \tag{2.77a}$$

$$\frac{\partial}{\partial z}\vec{V}_M(z) = -[T_V]^{-1}\,[Z_T]\,[T_I]\,\vec{I}_M(z) \tag{2.77b}$$

Comparing (2.77) with the Telegrapher's equations (2.43) that are expected of each mode,

$$[Y_M] = [T_I]^{-1}\,[Y_T]\,[T_V] \tag{2.78a}$$

$$[Z_M] = [T_V]^{-1}\,[Z_T]\,[T_I] \tag{2.78b}$$

Similarly, it may be shown that terminal-domain characteristic impedances may be related with their modal-domain counterparts via:

$$[Z_{cM}] = [T_V]^{-1}\,[Z_{cT}]\,[T_I] \tag{2.79}$$

It must be noted that a suitable diagonalization to determine modal quantities may not always be possible [264, 265]. Although this only occurs in exceptionally rare, pathological cases, it has been shown [348, 349] that instead of a diagonalized matrix, the modal propagation constants form a matrix with the Jordan canonical form, in which case most of the proposed analysis does not hold. Therefore in general in this work, the following assumption is made:

The eigensystems of terminal-domain wave propagation of voltages and currents are diagonalizable.

Assumption Set 4: Diagonalizable Terminal-Domain Systems

2.3.5 Non-Uniqueness of MTL Properties

A notable property of eigenvectors is that they do not have unique values, as they may be scaled by any arbitrary constant [319,320]. Since the transformation matrices $[T_V]$ and $[T_I]$ are the eigenvectors of (2.59) and are determined independently, the columns of the matrices (i.e., the independent eigenvectors) may each be arbitrarily scaled. However, as described in section 2.3.4, these matrices are crucial in determining

many modal-domain properties of MTLs from their terminal-domain counterparts, which are explicitly defined.

Noting that the terminal-modal transformations of the propagation constants (2.76) use one of the transformation matrices and its inverse, it is the case that the scaling factors cancel out, such that they have no effect on the modal propagation constants. However, various other modal properties such as the per-unit-length admittances and impedances (2.78), or characteristic impedances, (2.79) use both transformation matrices. This means that the arbitrary scale factors do not cancel out, and therefore have a strong impact on these modal properties.

It has therefore been generally concluded that many of these modal properties, other than the ones for which the scale factors cancel, cannot be uniquely defined [264, 265, 279, 350]. Even still, a couple of attempts have been broadly used in a effort to constrain the possible values of the eigenvectors [350]:

- The normalization of the product $[T_I]^T [T_V]$, for which it was shown that the symmetric nature of $[\gamma_M]$, $[Z_T]$, $[Y_T]$ leads to the conclusion that, if $[D]$ is any diagonal matrix (typically chosen to be identity for convenience),
$$[T_I]^T [T_V] = [T_V]^T [T_I] = [D] \tag{2.80}$$
- A form of self-normalization of the matrix diagonals, such that
$$[T_I]^T [T_I] = [T_V]^T [T_V] = [I] \tag{2.81}$$
- Attempting to normalize via physical quantities such as voltage, current, and power [351, 352]; however, the processes in [351] are not examined in the context of producing modal values, while those in [352] do not produce unique results for a given geometry.

2.4 Periodic MTL Media

2.4.1 History of Periodic Transmission Line Media

The analysis of periodically loaded TL structures to effect a homogenous-like medium can be traced back to the work of Heaviside and other telegraph engineers as they realized the extent to which the commonplace coaxial telegraph cables were the limiting factors in their long-distance communication systems [280]. Heaviside in particular is noted for proposing to increase the effective inductance of undersea coaxial cables through regular insertion of "loading coils" (series inductors) along their lengths. Later developments were conducted – notably by Pupin [353,354] – starting at the end of the 19^{th} century, in which lumped reactive loading elements (shunt capacitors and series inductors) were used to emulate the phase effects of longer TLs [355–360].

Later on near the middle of the 20^{th} century, figures such as Kock [90, 91] and Brown [92–94] (among others [95,96,361]), developed artificial microwave lenses through employing periodic composites of metallic sheets and dielectric materials. These efforts gave rise to "artificial dielectrics", in which the bulk

properties of periodic, composite materials behave similar to dielectric materials, the constitutive parameters of which may be essentially arbitrarily specified [87–89, 362, 363]. Values of realizable permittivities included negative parameters, such that the behavior of plasmas could be studied at microwave frequencies [109, 111–114], notably by figures such as Rotman [110]. In the late 20$^{\text{th}}$ century, Yablonovitch [364–366] pioneered the development artificial lattices known as Photonic Bandgap Structures PBGs or Electromagnetic Bandgap Structures EBGs, in which the effective permittivity was negative over certain controlled frequency bands [367–373].

After the development of MTMs [108, 115, 116], their implementation was effected through the introduction of "left-handed" loading elements into TL sections – i.e., series capacitors and shunt inductors – in the Negative Refractive Index (NRI)-TL [254] and Composite Left-Right Handed TL (CLRH-TL) [374]; these came to be known as TL-MTMs [181,182]. The insertion of various reactive loading components into MTLs followed shortly thereafter in the development of MTL-MTMs [266–276], which support multiple, interacting TL modes, some of which form bandgaps. These phenomena complemented the study of EBGs and allowed for the development of TL-based bandgap structures, which have been used in a variety of applications – most notably, Surface Wave (SW)-mode suppression and filtering [268, 269, 271, 272, 375–381].

Just after the turn of the 21$^{\text{st}}$ century, 2D TL periodic lattices were developed to implement generalized MTMs [256–263].

2.4.2 Analysis

The analysis of generalized TL or MTL-based periodic media begins as it does with physical sold-state media: with Bloch's theorem [329]. This theorem states that the fields within one period in an infinite array (or, borrowing terms from crystallography, "unit cell" in a "lattice") are related to the structural parameters, as well as a given phase shift across the cell:

$$\vec{F}(\vec{r}) = \phi(\vec{r})\, e^{-\vec{\gamma}_B \cdot \vec{r}} \tag{2.82}$$

where $\vec{F}(\vec{r})$ is the field at a given position $\vec{r}$, ϕ details the effects of the unit-cell's structure on the fields, and $\vec{\gamma}_B$ is known as the *Bloch* propagation constant, which describes how the fields propagate through the lattice. Since the unit cell is assumed periodic, the function ϕ possesses this periodicity, such that

$$\phi\left(\vec{r} + \vec{d}\right) = \phi(\vec{r}) \tag{2.83}$$

where $\vec{d}$ describes the periods of the unit cell in the given coordinates. Then, (2.82) may be expressed at an offset $\vec{d}$ as:

$$\vec{F}\left(\vec{r} + \vec{d}\right) = \phi\left(\vec{r} + \vec{d}\right) e^{-\vec{\gamma}_B \cdot \vec{r}} e^{-\vec{\gamma}_B \cdot \vec{d}} \tag{2.84}$$

Inserting (2.83) into (2.84) yields:

$$\vec{F}\left(\vec{r} + \vec{d}\right) = \phi(\vec{r})\, e^{-\vec{\gamma}_B \cdot \vec{r}} e^{-\vec{\gamma}_B \cdot \vec{d}} \tag{2.85}$$

which, employing (2.82) reduces to

$$\vec{F}\left(\vec{r}+\vec{d}\right) = \vec{F}\left(\vec{r}\right) e^{-\vec{\gamma}_B \cdot \vec{d}} \tag{2.86}$$

In circuit-based networks where the properties of the supported TL modes are being sought, the vector $\vec{F}\left(\vec{r}\right)$ would correspond to the voltages and currents of the network at a grouping of terminals 1 and $\vec{F}\left(\vec{r}+\vec{d}\right)$ to another grouping of terminals 2 on the opposite sides of the unit cell. Then, the Bloch propagation constant may be related to wave propagation over the geometric distance that the wave travels through the unit cell d_{eff}, and (2.86) may be expressed as:

$$\begin{bmatrix} \vec{V}_2 \\ \vec{I}_2 \end{bmatrix} = \begin{bmatrix} \vec{V}_1 \\ \vec{I}_1 \end{bmatrix} e^{-\gamma_B d_{eff}} \tag{2.87}$$

It is pre-supposed that the unit cell may be expressed as some network description $[A]$, which relates various voltages and currents in the cell such that:

$$\begin{bmatrix} \vec{V}_1 \\ \vec{I}_1 \end{bmatrix} = [A] \begin{bmatrix} \vec{V}_2 \\ \vec{I}_2 \end{bmatrix} \tag{2.88}$$

Inserting (2.88) into (2.87) gives:

$$[A] \begin{bmatrix} \vec{V}_2 \\ \vec{I}_2 \end{bmatrix} = \begin{bmatrix} \vec{V}_2 \\ \vec{I}_2 \end{bmatrix} e^{\gamma_B d_{eff}} \tag{2.89}$$

The Bloch modes (that is, the modes which are solutions to Bloch's theorem, and including the various spatial harmonics that may satisfy the same phase conditions) may then be solved through noting that (2.89) is an eigenmode equation, where the Bloch propagation constants may be solved as

$$[\gamma_B] = \frac{ln\left(eig\left([A]\right)\right)}{d_{eff}} \tag{2.90}$$

Notably, since the eigenvectors represent the voltages and currents of waves travelling along both directions of the observed axis (2.62), the voltages and currents components of the vectors are related by the characteristic impedances, such that if (2.89) is expressed in the terminal domain:

$$\begin{bmatrix} [T_V] & [T_V] \\ \left([Z_{BT}]^{-1}[T_V]\right) & -\left([Z_{BT}]^{-1}[T_V]\right) \end{bmatrix}^{-1} [A] \begin{bmatrix} [T_V] & [T_V] \\ \left([Z_{BT}]^{-1}[T_V]\right) & -\left([Z_{BT}]^{-1}[T_V]\right) \end{bmatrix} = e^{[\gamma_B] d_{eff}} \tag{2.91}$$

The matrix of terminal-domain Bloch impedances $[Z_{BT}]$ (the periodic equivalent of the characteristic impedances of longitudinally invariant MTLs $[Z_{cT}]$) may then be extracted from the eigensystem (2.89). With information of both $[\gamma_B]$ and $[Z_{BT}]$, the eigensystem provides the necessary information to compute relevant other properties such as effective per-unit-length admittances and impedances (2.62), as well as the various properties in the modal domain (as given in section 2.3.4).

In the case of a single-dimensional system, the matrix $[A]$ has been used often in the literature as an $ABCD$ matrix [268–272, 375], although in the case of multi-dimensional systems, sets of homogenous

equations have been used as well [259, 260, 263]. Additionally, in these multidimensional systems, more complicated analyses than the simple eigensystem of (2.89) are often used due to the presence of various boundary conditions along various coordinates.

Not all periodic structures may be considered artificial media. Effective-medium theory enforces the requirements that the structures possess a physical period smaller than roughly one-tenth of a wavelength of the radiation under which the structures are excited ($d_{eff} \leq \lambda/10$). Additionally, only those modes which possess a relatively small phase shift across the unit-cell period may be considered as propagating through a homogenous medium ($\gamma_B d_{eff} \lesssim 90^\circ$).

2.4.3 Constitutive Medium Parameters

Oftentimes, TL modes are desired to be interfaced with free-space modes, particularly in the context of MTMs. In such situations, it convenient to describe the properties of the modes supported by a periodic medium in similar terms to those of the medium which support the free-space modes. In most cases, these parameters will be the constitutive medium parameters (permittivity and permeability of the media). There are no terminal-domain definitions of these parameters, such that they must be expressed on a per-mode basis. Since it is assumed the media are isotropic, the geometric factors of section 2.1.5 are expressed for each mode, and the diagonal matrix $[g]$ is used to indicate the set of all such geometric factors. Then,

$$[\epsilon] = \frac{1}{j\omega}\,[g]\,[Y_M] \tag{2.92a}$$

$$[\mu] = \frac{1}{j\omega}\,[g]^{-1}\,[Z_M] \tag{2.92b}$$

However, care must be taken in interpreting these equations. While the geometric factors for each mode link the modes' per-unit-length admittances and impedances with permittivities and permeabilities, respectively, MTL-MTMs may be embedded in non-homogenous media, in which case one may appreciate that the "effective" permittivity and permeability are dependent on the choice of field distributions – i.e., the choice of mode. However, it is generally assumed that when discussing constitutive medium parameters, a plane-wave mode is being assumed, and so that assumption will continue being used throughout this work. Then, it may also be noted that for the case of a plane wave incident on inhomogeneous media, the polarization of a given plane wave will also affect its observed constitutive parameters. Following the convention set out in previous work [257], it will be assumed that the incident plane waves exhibit a single polarization state which is implicit to the geometry at hand.
The wave impedances of the medium are then defined as:

$$\left([\mu]\,[\epsilon]^{-1}\right)^{\frac{1}{2}} = [g]^{-1}\left([Z_M]\,[Y_M]^{-1}\right)^{\frac{1}{2}} \tag{2.93}$$

which yields a formula for the calculation of $[g]$: comparing the wave impedance of a plane-wave in the medium in which the TL is embedded to the characteristic impedances of the various TL modes. The presence of non-TL components should not affect the values of $[g]$, such that (2.92) may be applied to determine the properties of various periodic networks, in particular MTMs.

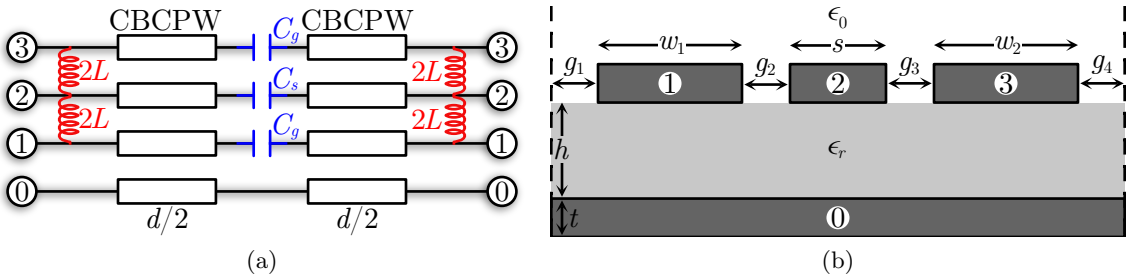

Figure 2.4: a) Example equivalent-circuit model of the MTM-EBG (without a shield conductor) used in this work, and b) transverse cross-sectional profile of an exemplary CBCPW TL.

2.5 The MTM-EBG

2.5.1 Development of the MTM-EBG

The Metamaterial Electromagnetic Bandgap Structure (MTM-EBG) [272,381,382] was developed after the introduction several prominent MTL-MTMs, such as the shielded Sievenpiper structure [266,268,269,271], NRI-TL coupler [267, 270], and others since the turn of the 21st century. The formulation of the MTM-EBG was inspired by the Uniplanar Compact Electromagnetic Bandgap Structure (UC-EBG) structure [383–387], in which it was observed that certain TL-like modes propagated along each outer section – which are comprised of multiple conductors – and which are also known to support one or more prominent bandgaps.

2.5.2 Analysis of the MTM-EBG

Unlike the previous MTMs based on MTLs, the host MTL of the MTM-EBG – a Conductor-Backed Coplanar Waveguide (CBCPW) – is known to support more than two TL modes, as well as a SW mode in some variations – all of which have no lower cutoff frequency. This has enabled its use in a number of diverse applications, including SW-mode suppression, parallel-plate-mode noise suppression, filtering [388–390], multi-band couplers [172–174, 176], feed networks [175], and antennas [143–145]. In the context of SW-mode suppression, it is useful to include a shield conductor in order to model the formed SW-mode bandgap; however, most applications have not considered interactions with this mode, and therefore an upper shield conductor is typically not included.

An exemplary unit cell, shown in Fig. 2.4a is examined in order to elucidate the structure's behaviors and properties. The structure contains two four-conductor MTL sections of equal length $d/2$, which are separated by a set of capacitors of values C_g and C_s, the former of which are placed in series in conductors 1 and 3, while the latter is placed in series with conductor 2. On either end of the unit cell, pairs of inductors are placed in shunt with conductors 1 and 2, and 2 and 3, all with values of $2L$. In the typical MTM-EBG, the host CBCPW has a transverse cross-sectional profile such as the one shown in Fig. 2.4b. This TL possesses a solid conductor (#0) backing on a dielectric with permittivity ϵ_r of thickness h. The upper three conductors (#1-#3) may generally possess differing properties, but are typically symmetric such that upper CPW ground conductors have widths $w_1 = w_2$, outer spacings of $g_1 = g_4$, CPW gap

widths $g_2 = g_3$, and CPW strip width s. All conductors are assumed to possess a thickness t. The dashed vertical lines indicate Perfect Magnetic Conductor (PMC) boundaries, employed here since often periodic transverse TLs are being used.

Rather than deriving the host TL's terminal-domain per-unit-length parameters from a particular geometry (obtained by specifying the various parameters of Fig. 2.4b), for simplicity they are determined from the modal domain via assumption of the supported modes (parameter synthesis). These modes are typically described with the (ideally, frequency-independent) definitions:

$$[T_I] = \begin{bmatrix} 0.33 & -1 & 0.4 \\ 0.34 & 0 & -1 \\ 0.33 & 1 & 0.4 \end{bmatrix} \tag{2.94}$$

The first mode (column) is specified with relative currents of $\{0.33, 0.34, 0.33\}$, which correspond to the relative weightings of currents on conductors 1, 2, and 3 (respectively), the values of which are strongly dependent on the relative sizes of the conductors (specifically, widths w_1, s, and w_3, also respective to the indices of the weighting vectors). This mode has been referred to as the Parallel Plate Waveguide (PPW)-like mode or Microstrip (MS)-like mode, depending on the application. Representative electric fields of this mode are shown in Fig. 2.5a. The second mode is referred to as the Coupled Slotline (CSL)-like mode; due to its contra-directional currents flanking both CPW gaps, it possesses no net current on the central CPW strip conductor (#2) when the upper conductors are symmetric. Representative electric fields of this mode are shown in Fig. 2.5b. The third mode is the CPW-like mode, in which most of the currents exist on the upper three conductors, but some currents are induced on the conductor backing as well. Representative electric fields of this mode are shown in Fig. 2.5c.

Typically, the propagation constants of these modes may appear in the form (at a frequency of $\omega = 2\pi \times 10^9$ Hz):

$$[\gamma_M] = \begin{bmatrix} j30 & 0 & 0 \\ 0 & j28 & 0 \\ 0 & 0 & j25 \end{bmatrix} /m \tag{2.95}$$

while the characteristic impedances typically possess values such as:

$$[Z_{cM}] = \begin{bmatrix} 50 & 0 & 0 \\ 0 & 150 & 0 \\ 0 & 0 & 100 \end{bmatrix} \Omega \tag{2.96}$$

The terminal-domain per-unit-length admittance and impedance matrices which define the TL may then be determined through the application of (2.76), (2.79), (2.63), and (2.78). Using these quantities, and further exemplary values of $d = 20$ mm, $L = 10$ nH, and $C_g = 1$ pF and C_s shorted ($C_s \to \infty$) allows the determination of the global $ABCD$ parameters with which to describe the unit cell. Then, application of (2.89) allows for the computation of the structure's dispersive properties, and of course scattering parameters may also be simply determined for a given number of unit cells [391].

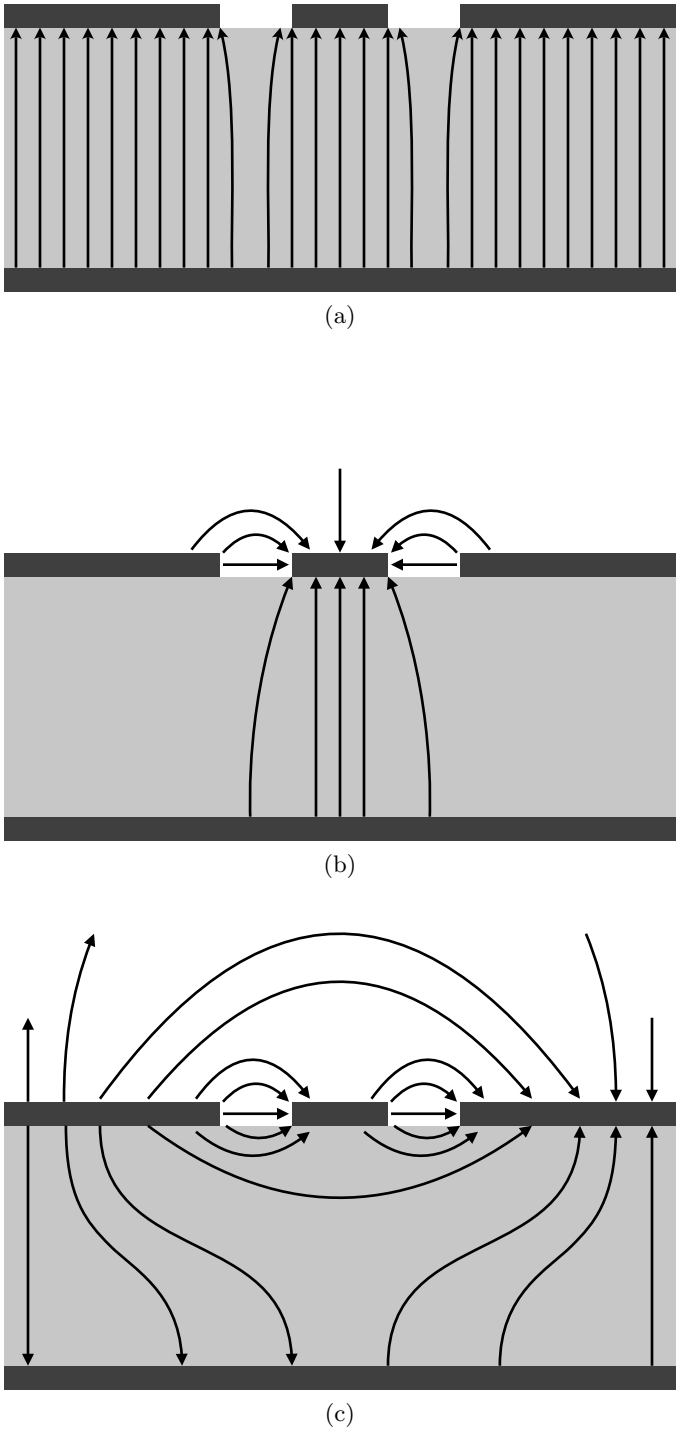

Figure 2.5: Representative electric-field distributions of a) the PPW-like mode, b) the CPW-like mode and, c) the CSL-like mode.

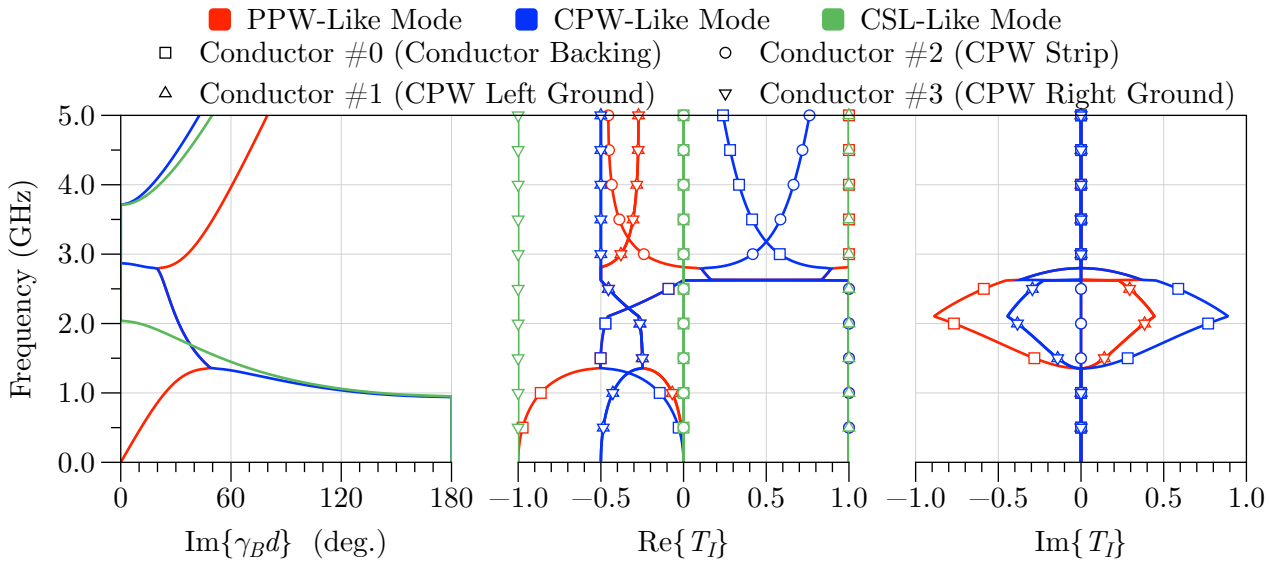

Figure 2.6: Dispersion properties of the example MTM-EBG. The Bloch propagation constants are given, along with the eigenvectors, which are the currents on each conductor for each Bloch mode. The colors of the band sections on the left correspond amongst all plots, while the various conductors are indicated with the various markers.

The structure's dispersive properties are shown in Fig. 2.6, where the imaginary components of the Bloch propagation constants are given on the left, and the real and imaginary components of the entries of the current transformation matrix (the system's eigenvectors) $[T_I]$ – each column of which will be referred to as a *mode definition* – are shown on the center and right panels, respectively. As expected due to field symmetry, the PPW-like and CPW-like modes couple, as described in section 2.2.4 and further in [381]. The CSL-like mode exhibits an odd-type field symmetry and therefore does not couple with the other two modes. Since the CPW-like mode exhibits negative per-unit-length admittances and impedances in its first band, it exhibits backward-wave behavior. This backward wave couples with the forward-wave PPW-like mode to form a bandgap and a set of complex modes between 1.36 GHz and 2.81 GHz, as described previously in section 2.2.4.

The mode definitions reveal additional information about the nature of the modes. It is unsurprising that outside of the complex-mode band, the mode definitions exhibit no imaginary components – since of course normal modes may be expressed as entirely real. The extent to which the PPW-like and CPW-like modes couple is a prominent feature of this data: at low frequencies, the modes are essentially unrelated, however, they readily start to converge to similar values as frequency increases. In the complex-mode region, the real components of the mode definitions of the two modes have the same values, as expected, while their imaginary components possess negative quantities of each other for each mode – expected since the eigenvectors of complex modes are complex conjugates. At higher frequencies the modes decouple and begin transitioning to values more akin to the natural host modes of the underlying MTL as defined in (2.94). The mode definitions of the CSL-like mode do not vary with frequency – as expected, since this mode does not couple with any other modes due to its field anti-symmetries – and are also expressed as

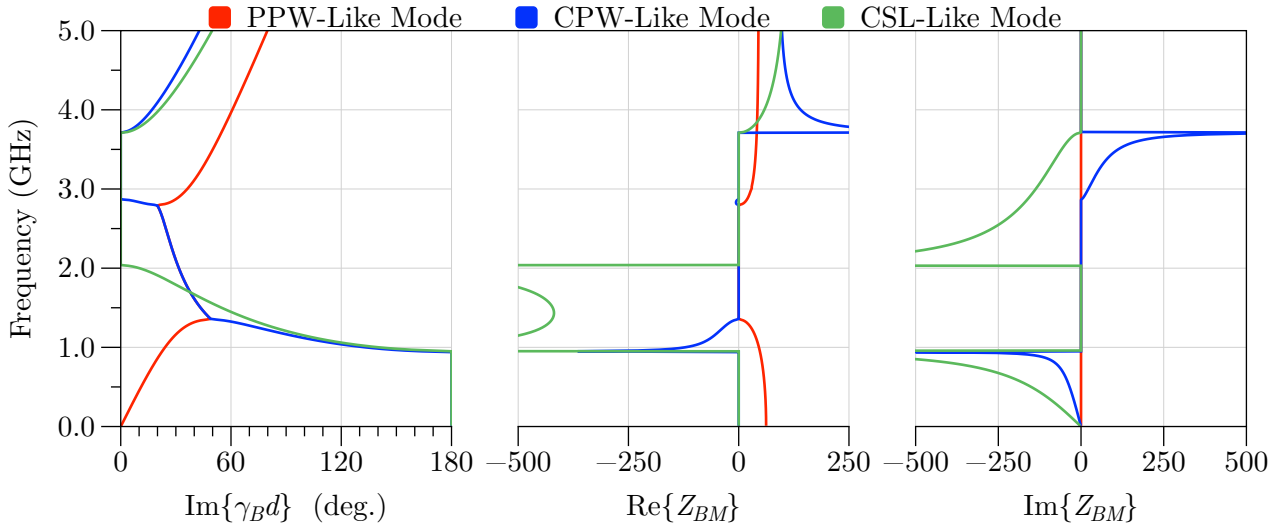

Figure 2.7: Bloch impedances $[Z_{BM}]$ of the example MTM-EBG, with the same dispersion data as in Fig. 2.6 shown on the left, and the real and imaginary components of Bloch impedance shown in the center and right panels, respectively.

entirely real.

The Bloch impedances $[Z_{BM}]$ of the MTM-EBG, computed using (2.91) and (2.79), are given in Fig. 2.7. The data indicate that the Bloch modes have positive real values in frequency ranges where they are forward modes, negative real values in frequency ranges where they are backward modes, and possess imaginary values in between propagating bands. The complex modes uniformly exhibit Bloch impedances of value zero; while such a result may be interesting, the analysis of complex MTL modes is currently an undefined process, which is considered to be outside of the scope of this thesis and will not be investigated further. At sufficiently high frequencies, the values appear to be approaching the values of the characteristic impedances of the host MTL modes, given in (2.96).

The constitutive medium parameters are also computed, using (2.92), (2.78), and (2.63). In order to compute these properties, the modal matrix of geometric factors $[g]$ must be determined. As described in section 2.4.3, this is simply accomplished by comparing the wave impedance of a plane-wave in the medium in which the host MTL is suspended (without the conductors, or course) to the characteristic impedance of each of the modes supported by the host MTL. Since the MTL's transverse cross-section – shown in Fig. 2.4b – already possesses boundary conditions on three of the four sides, it is reasonable to assume the plane wave of interest will be supported by these, and another electric boundary condition at a height satisfactory to make the domain square in shape. Since geometry is not specified in this example, a value of 350 Ω is assumed, which along with (2.96) yields a geometric factor matrix of:

$$[g] = \begin{bmatrix} 0.143 & 0 & 0 \\ 0 & 0.429 & 0 \\ 0 & 0 & 0.286 \end{bmatrix} \tag{2.97}$$

The resulting (relative) constitutive parameters, the real components of which are shown in Fig 2.8,

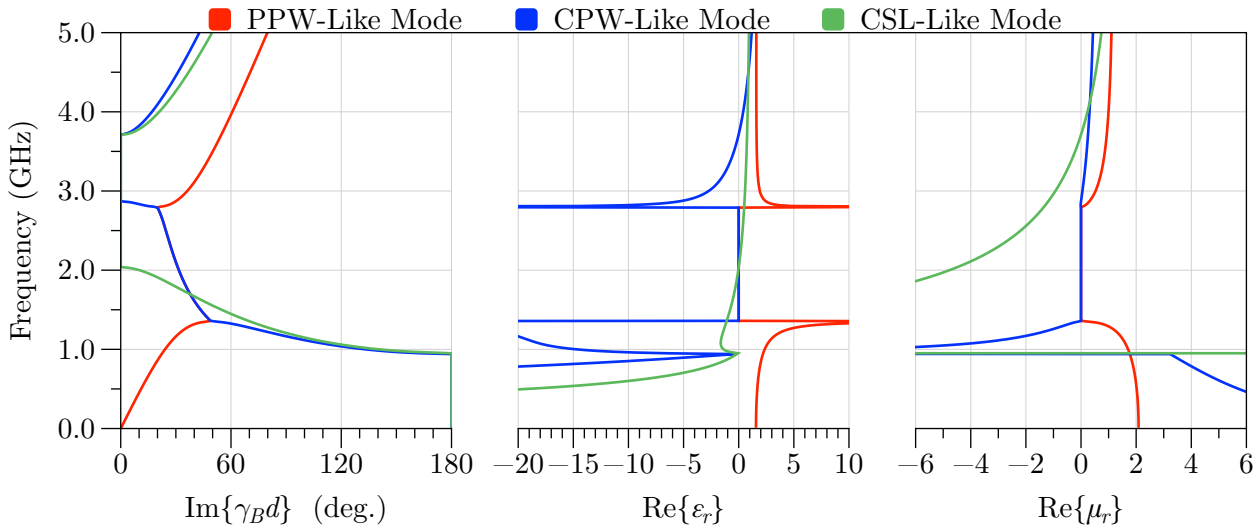

Figure 2.8: Effective relative constitutive parameters $[\epsilon_r]$ and $[\mu_r]$ of the Bloch modes of the example MTM-EBG, with the same dispersion data as in Fig. 2.6 shown on the left, with the real components of effective (relative) permittivity and permeability shown in the center and right panels, respectively. There is some ambiguity as to the correctness of the values of the CPW-like and CSL-like modes below the Bragg frequency (approximately 1 GHz), since the logarithm function used to determine the Bloch propagation constants possesses several branches.

are seen to possess simultaneously positive values for the forward-directed bands, simultaneously negative values in the backward-directed bands, and oppositely-signed values in between bands. Notably, once again the values are identically zero for the complex modes. There is some ambiguity as to the correctness of the values of the CPW-like and CSL-like modes below the Bragg frequency (approximately 1 GHz), since the logarithm function used to determine the Bloch propagation constants possesses several branches. Additionally, since the Bloch phase shifts are relatively large below this frequency, the structure may not be well-approximated as a homogenous medium with respect to these modes.

The scattering parameters of five MTM-EBG concatenated unit cells (computation of which is detailed in Appendix C), are shown in Fig. 2.9. It is necessary to note that these scattering parameters are given with respect to the modes of the host MTL, rather than the Bloch modes. This is done for the purpose of illustration only – as can be seen, the host modes generally well-approximate the Bloch modes, such that there is reasonable transmission over the propagating bands. Notably, the PPW-like and CPW-like modes exhibit rejection in the complex-mode region, confirming the lack of propagation – even with the propagation constants possessing substantial imaginary components. Although there are five unit cells – and so typically it is expected to see five Fabry-Perot resonances [392–394] at the frequencies corresponding to intervals of 36° – these resonances are not apparent for the PPW-like and CPW-like modes. This is due to the fact that the responses of the host MTL modes are being observed, rather than those of the Bloch modes directly. However, from Fig. 2.6 it may be observed that the host MTL CSL-like mode has the same definition as its frequency-independent Bloch mode, and therefore, these Fabry-Perot resonances may be readily observed. Of course, differences between this mode's characteristic impedance and Bloch impedances do result in a higher degree of reflection over both bands.

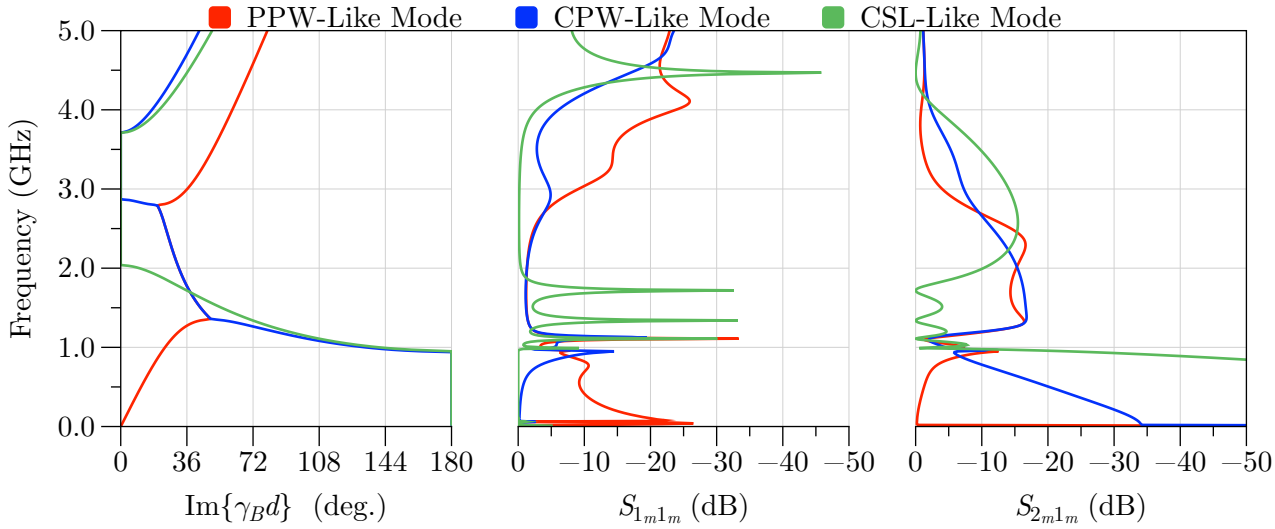

Figure 2.9: Scattering parameters of the various modes at ports 1 (1_m) and 2 (2_m) of five cascaded MTM-EBG unit cells (with respect to the host MTL modes), with the same dispersion data as in Fig. 2.6 shown on the left. The magnitudes of the reflection coefficients of each mode are shown in the center panel, while the transmission coefficient magnitudes are shown in the right panel.

Of course, the discussion of section 2.3.5 on the non-uniqueness of most MTL modal domain quantities applies to these Bloch modes as well. As such, the reader may inquire: *how can the meaning of these data be interpreted if their values are ambiguous*? This is indeed, a strongly valid question. The answer lies in the theory presented in Chapter 3, which lays out a process for uniquely determining these modal properties of normal modes under the TEM approximation, but it suffices to say that that process has been retroactively applied to these data, such that they may be considered correct.

Chapter 3

Theory

This chapter, unlike Chapter 2 on the background of the analyses of MTL-MTMs, derives new processes from basic physical principles.

3.1 Determination of MTL Modal Properties

In section 2.3.5, it was demonstrated that in the current state of understanding, many MTL modal properties may not be determined. This section builds upon previous derivations, demonstrating that modal properties are constrained to singular values under the correct assumptions. Specifically, since the system of eigenvectors (the mode definitions) may be arbitrarily scaled, they form an underdetermined system. Therefore, the prudent course of action is to introduce further constraints with which to reduce the ambiguity of the scaling factors, and produce a determinable system.

Some of the ideas, figures, and data presented in this section have been published [395]. In addition to this author, Dr. Ashwin Iyer (as a co-author of that work) contributed significantly to the ideas and explanations that will be presented.

3.1.1 Underdetermined Eigensystems

From relations such as (2.78), it becomes apparent that the use of both $[T_V]$ and $[T_I]$ introduces a number of ambiguities. Each column of each of matrix (that is, the mode definitions) is scaled by an arbitrary constant a_n, such that if the system possesses N modes, then there are $2N$ degrees of freedom available through scaling of the eigenvectors. That is, if the arbitrary scale factors represented by the diagonal matrices $\left[a^V\right]$ and $\left[a^I\right]$ scale the columns of transformation matrices $[T_V]$ and $[T_I]$, respectively:

$$[T_V]_{scaled} = \left[a^V\right][T_V] \tag{3.1a}$$

$$[T_I]_{scaled} = \left[a^I\right][T_I] \tag{3.1b}$$

where $[T_V]_{scaled}$ and $[T_I]_{scaled}$ are considered the correct solutions once proper scaling has been applied.

Then, if some terminal-modal domain relation such as (2.79) is combined with (3.1),

$$[Z_{cM}] = [T_V]^{-1}_{scaled} \left[a^V\right] [Z_{cT}] \left[a^I\right]^{-1} [T_I]_{scaled} \tag{3.2}$$

then it may be observed that the presence of the ambiguous scale factors give the quantities $[Z_{cM}]$ $2N$ degrees of freedom. In the modal analysis of MTLs, one common constraint is already typically employed: the equality of total power between the terminal and modal domains [264, 350], which may be expressed in terms of average real power as (using (2.74)):

$$P_{av} = \frac{1}{2}\Re\{\vec{I}^*_T \vec{V}_T\} = \frac{1}{2}\Re\{\vec{I}^*_M [T_I]^* [T_V] \vec{V}_M\} \tag{3.3}$$

where the $*$ operator indicates the conjugate transpose. Comparing the two sides of (3.3) yields the conclusion that:

$$[T_I]^* [T_V] = [I] \tag{3.4}$$

Then, inserting (3.1) into (3.4):

$$[T_I]^*_{scaled} \left[a^I\right]^{*^{-1}} \left[a^V\right]^{-1} [T_V]_{scaled} = [I] \tag{3.5}$$

which may be re-arranged to:

$$[T_V]^{-1}_{scaled} \left[a^V\right] = [T_I]^*_{scaled} \left[a^I\right]^{*^{-1}} \tag{3.6}$$

Inserting these relations into example modal properties, such as characteristic impedances (3.2) gives:

$$[Z_{cM}] = [T_I]^*_{scaled} \left[a^I\right]^{*^{-1}} [Z_{cT}] \left[a^I\right]^{-1} [T_I]_{scaled} \tag{3.7}$$

which, it may be noted, only possesses the one set of scaling factors $\left[a^I\right]$: therefore, the degrees of freedom of the system have been reduced from $2N$ to N though the application of the equality of total power between domains (3.3).

3.1.2 Postulating the Basis Invariance of Total Charges

Attention may then be turned to removing these remaining degrees of freedom, such that the modal quantities may be uniquely determined. While it may be possible that multiple relations may be found with which to reduce these degrees of freedom, only one such relation has been found to date. This relation is the equality of total power between domains, which stands as a postulate (although it has not been labelled as such, it cannot be proven). Since it involves the use of physical reasoning to drive the implementation of novel information, the same is done here – with the consideration of total charges instead of power. Specifically:

> The total charges of a given sign in the modal domain are equal to the total of those of the same sign in the terminal domain.

Postulate 1: Basis Invariance of Total Charges

In the frequency domain, the charges are directly proportional to currents, such that the above postulate and statements may be considered to hold for currents of a certain phase, rather than charges of a certain sign.

3.1.3 Implementation

To implement Postulate 1, it is firstly noted that since it was demonstrated in section 2.3.3 that MTL modes are normal modes, their currents will only exist in one of two phases. Expressed in real numbers, this means that the values they possess will only be positive, or negative, corresponding to the direction they are travelling along the TL axis z. Clearly, this is also the case for modal-domain currents, where (since each mode may be represented as an independent two-conductor TL) there are only two currents, which are oppositely directed. These statements may be expressed as:

$$\vec{I}_T = \vec{I}_T^{+z} - \vec{I}_T^{-z} \tag{3.8a}$$

$$\vec{I}_M = \vec{I}_M^{+z} - \vec{I}_M^{-z} \tag{3.8b}$$

such that the vector $\vec{I}_T^{+z}$ contains a zero entry wherever $\vec{I}_T^{-z}$ contains a nonzero entry, and vice-versa; similarly for the modal currents. All these vectors have the same lengths. It may be shown that for TL modes, the sum of all currents are zero [264] as a consequence of the conservation of charge (or currents), which holds in any basis. Therefore for a system with N non-reference terminals (or modes) n,

$$\sum_{n=0}^{n<N} I_{T_n} = 0 \qquad \Rightarrow \qquad \sum_{n=0}^{n<N} I_{T_n}^{+z} = \sum_{n=0}^{n<N} I_{T_n}^{-z} \tag{3.9a}$$

$$\sum_{n=0}^{n<N} I_{M_n} = 0 \qquad \Rightarrow \qquad \sum_{n=0}^{n<N} I_{M_n}^{+z} = \sum_{n=0}^{n<N} I_{M_n}^{-z} \tag{3.9b}$$

Then, with this formalism, Postulate 1 may be expressed as:

$$\sum_{n=0}^{n<N} I_{T_n}^{+z} = \sum_{n=0}^{n<N} I_{M_n}^{+z} \tag{3.10a}$$

$$\sum_{n=0}^{n<N} I_{T_n}^{-z} = \sum_{n=0}^{n<N} I_{M_n}^{-z} \tag{3.10b}$$

Next, the transformation matrix $[T_I]$ is similarly decomposed as the vectors in (3.8), into one matrix $\left[T_I^{+z}\right]$ for the positive components, and another $\left[T_I^{-z}\right]$ for the negative components, such that:

$$[T_I] = \left[T_I^{+z}\right] - \left[T_I^{-z}\right] \tag{3.11a}$$

$$\vec{I}_T^{+z} = \left[T_I^{+z}\right] \vec{I}_M \tag{3.11b}$$

$$\vec{I}_T^{-z} = \left[T_I^{-z}\right] \vec{I}_M \tag{3.11c}$$

Let $\vec{I}_T^{+z}\Big|_m$ and $\vec{I}_T^{-z}\Big|_m$ represent the positive- and negative-directed terminal currents (respectively) in the case that only a single mode m is excited, that is, combining (3.11b) and (3.11c):

$$\vec{I}_T^{+z}\Big|_m = \left[T_I^{+z}\right]\vec{\delta}_m I_{M_m}^{+z} \tag{3.12a}$$

$$\vec{I}_T^{-z}\Big|_m = \left[T_I^{-z}\right]\vec{\delta}_m I_{M_m}^{-z} \tag{3.12b}$$

where δ is the delta function, defined as:

$$\vec{\delta}_m = \begin{cases} 1, & \text{if } i = m \\ 0, & \text{otherwise} \end{cases} \quad \forall \text{ indices } i. \tag{3.13}$$

Also under the case of a single excited mode m, the expressions of (3.10) reduce to:

$$\sum_{n=0}^{n<N} \vec{I}_T^{+z}\Big|_m = I_{M_m}^{+z} \tag{3.14a}$$

$$\sum_{n=0}^{n<N} \vec{I}_T^{-z}\Big|_m = I_{M_m}^{-z} \tag{3.14b}$$

Inserting (3.11) into (3.14) yields:

$$\sum_{n=0}^{n<N} \left(\left[T_I^{+z}\right]\vec{\delta}_m I_{M_m}^{+z}\right) = I_{M_n}^{+z} \tag{3.15a}$$

$$\sum_{n=0}^{n<N} \left(\left[T_I^{-z}\right]\vec{\delta}_m I_{M_m}^{-z}\right) = I_{M_n}^{-z} \tag{3.15b}$$

The terms $I_{M_m}^{+z}$ and $I_{M_m}^{-z}$ cancel out of (3.15a) and (3.15b), respectively, leaving the equations:

$$\sum_{n=0}^{n<N} \left(\left[T_I^{+z}\right]\vec{\delta}_m\right) = 1 \tag{3.16a}$$

$$\sum_{n=0}^{n<N} \left(\left[T_I^{-z}\right]\vec{\delta}_m\right) = 1 \tag{3.16b}$$

which simply state that the sum of the entries in each column of the matrices $\left[T_I^{+z}\right]$ and $\left[T_I^{-z}\right]$ must be equal to one. Since all of the entries possess the same same phase, this means that the scale factors a_{mm}^I are each simply the sum of the entries in the m^{th} column of either $\left[T_I^{+z}\right]$ or $\left[T_I^{-z}\right]$ (which necessarily must be identical in order for the conservation of charge/currents to hold):

$$a_{mm}^I = \left(\sum_{n=0}^{n<N} \left(\left[T_I^{+z}\right]\vec{\delta}_m\right)\right)^{-1} = \left(\sum_{n=0}^{n<N} \left(\left[T_I^{-z}\right]\vec{\delta}_m\right)\right)^{-1} \tag{3.17}$$

Thus, since the eigenvector scale factors $\left[a^I\right]$ are no longer arbitrary, (3.7) is reduced in degrees of freedom from N to zero, and the modal properties possess a uniquely computable value. Of course, it is typically the case that the currents on the reference conductor are not included in the set of all currents $\vec{I}_T$. In this case, it is still possible to compute the value of a^I_{mm} through the use of either $\left[T_I^{+z}\right]$ *or* $\left[T_I^{-z}\right]$. This discussion, along with a proposed algorithm for performing the procedure of uniquely scaling $[T_V]$ and $[T_I]$, is given in Appendix D.

3.1.4 Validation

This section will examine two realistic examples of determining a MTL's modal properties. Ansys High Frequency Structural Simulator (HFSS) was used to extract the per-unit-length inductance and capacitance matrices in the terminal domain, as well as determine the propagation constants and characteristic impedances in the modal domain (chosen since these are the only available modal-domain properties), all computed at a frequency of 1 GHz. Since HFSS is understood to correctly compute the modal quantities from field data (using the built-in modal solver in the Driven Terminal simulation type), the results it produces may be considered physically accurate. The convergence criteria for the HFSS simulations were chosen to be extremely strict, in order to rigorously verify the proposed method. These criteria enforced a minimum of 20 converged passes with a convergence $\Delta\,|S|$ of 0.0001 and $\Delta\angle S$ of 0.1°. The validity and effectiveness of the proposed process is established by the corroboration of the HFSS modal values, given only the known terminal values.

Of course, modal quantities may be correctly analytically determined if the modal field profiles are known – for example, determining characteristic impedance from modal currents and total power, as described in Appendix E. HFSS follows a similar process numerically by solving the 2D fields of the supported modes on a wave port surface, and then computing the modal properties from these fields. The novelty of the proposed process is that it allows for the determination of modal properties given only the terminal-domain fields or properties, which are often much more simple to obtain.

Symmetric Three-Wire Line

This TL consists of three perfectly-conducting cylinders of diameter $d = 1.00$ mm suspended in a vacuum and spaced equally apart by a distance $s = 3.46$ mm, as shown in Fig. 3.1. Since the system is symmetric, the choice of reference conductor is arbitrary, and the lossless terminal-domain per-unit-length TL parameters matrices are 2×2 in size, with

$$\begin{aligned}[L_T] &= \begin{bmatrix} 0.7617 & 0.3808 \\ 0.3808 & 0.7617 \end{bmatrix} \mu H/m \\ [C_T] &= \begin{bmatrix} 19.5001 & -9.7500 \\ -9.7500 & 19.5001 \end{bmatrix} pF/m \end{aligned} \tag{3.18}$$

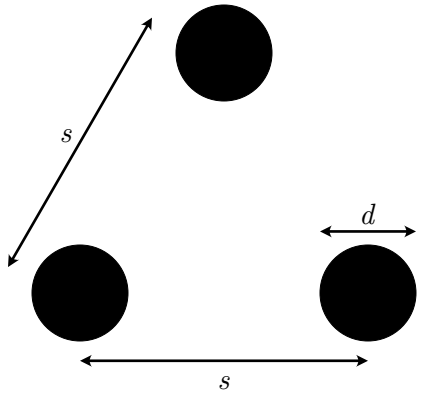

Figure 3.1: Setup of the three-wire TL. The conductors (black circles) or diameter d are similar and form an equilateral triangle with side length s.

which are used to compute the terminal-domain voltage propagation constants and characteristic impedances:

$$\begin{aligned}[\gamma_V] &= \begin{bmatrix} 20.9707 & 0.0000 \\ 0.0000 & 20.9707 \end{bmatrix} rad/m \\ [Z_{cT}] &= \begin{bmatrix} 228.2110 & 114.1050 \\ 114.1050 & 228.2110 \end{bmatrix} \Omega \end{aligned} \tag{3.19}$$

Note that the terminal-domain propagation constant matrix is already diagonal – this is a direct consequence of supporting TEM modes allowed by the homogeneous dielectric and lossless conductors. Using (2.61a) in (2.76a), as well as (2.79), yields the modal propagation constants and characteristic impedances:

$$\begin{aligned}[\gamma_M] &= diag \begin{bmatrix} 20.9707 \\ 20.9707 \end{bmatrix} rad/m \\ [Z_{cM}] &= diag \begin{bmatrix} 342.3160 \\ 114.1050 \end{bmatrix} \Omega \end{aligned} \tag{3.20}$$

along with the (unscaled) transformation matrices (where *diag* indicates the entries on the lead diagonal of a diagonal matrix, in which the off-diagonal entries are zero):

$$[T_V] = [T_I] = \frac{1}{\sqrt{2}} \begin{bmatrix} -1 & 1 \\ 1 & 1 \end{bmatrix} \tag{3.21}$$

which are the well-known mode definitions of the even and odd modes of the system [264, 350, 351, 396].

HFSS gives the modal propagation constants and characteristic impedances:

$$\begin{aligned}[\gamma_M]_{HFSS} &= diag\begin{bmatrix} 20.9707 \\ 20.9707 \end{bmatrix} rad/m \\ [Z_{cM}]_{HFSS} &= diag\begin{bmatrix} 228.2219 \\ 171.1665 \end{bmatrix} \Omega \end{aligned} \tag{3.22}$$

where it may be confirmed that the modal propagation constants are very similar (percent differences of less than 0.01% between HFSS direct eigenmode simulation and the data computed from the terminal-domain values). The characteristic impedances exhibit differences of 34.5% and 40.0%, respectively, between the calculated values and those reported by HFSS. This is expected, as the transformation matrices must be first corrected using the proposed processes.

Investigating the mode definitions in more detail, it can be noted that the unscaled matrices satisfy the equality of total power (3.4). However; the current transformation matrix $[T_I]$ does not satisfy the equality of total charges/currents (3.16), which is integral to the scaling process proposed in this work. Scaling the mode definitions through the application of this proposed constraint yields the matrices

$$\begin{aligned}\left[a^I\right] &= diag\begin{bmatrix} \sqrt{2} \\ \frac{\sqrt{2}}{2} \end{bmatrix} \\ [T_V]_{\text{scaled}} &= \begin{bmatrix} -0.5 & 1 \\ 0.5 & 1 \end{bmatrix} \\ [T_I]_{\text{scaled}} &= \begin{bmatrix} -1 & 0.5 \\ 1 & 0.5 \end{bmatrix} \end{aligned} \tag{3.23}$$

which have also been noted in the recent literature [352, 397]. Using these definitions in (2.79) gives:

$$[Z_{cM}] = diag\begin{bmatrix} 228.2110 \\ 171.1580 \end{bmatrix} \Omega \tag{3.24}$$

which are now in excellent agreement (a percent difference of less than 0.1% for both values on the diagonal) to the modal values given by HFSS (3.22) as compared with those in (3.20).

It should be noted that for this or similar geometries, which are commonly found in the analysis of power systems, the Fortescue [398] or Clarke [399] transformations are commonly used to transform the currents and voltages from the terminal domain into the desired basis of sequence components [400]. While these transformations are indeed a valid change of basis, the transformations do not generally diagonalize the terminal-domain propagation constants (2.64), and therefore do not constitute valid mode definitions.

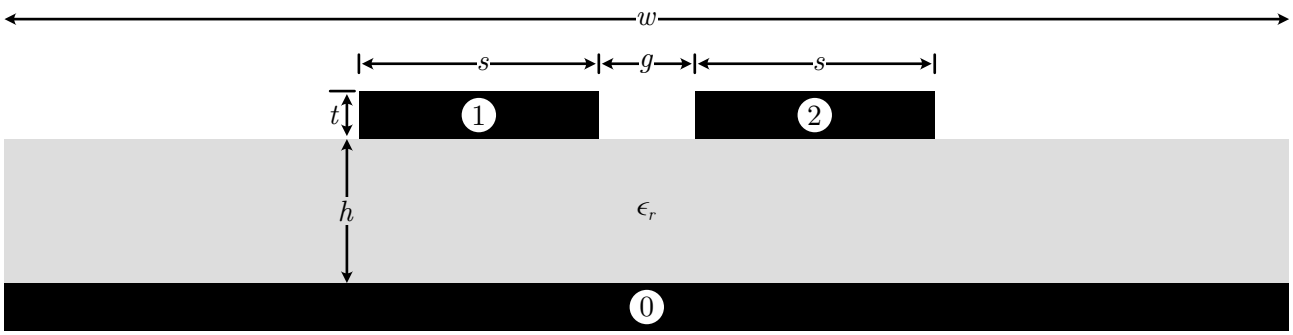

Figure 3.2: Physical arrangement and properties of the Conductor-Backed Coplanar Stripline (CBCPS). The simulation domain width w of 30 mm is not shown to scale. Image adapted from [395].

Conductor-Backed Coplanar Stripline

This Conductor-Backed Coplanar Stripline (CBCPS) MTL (which is equivalent to a symmetric pair of coupled MSs), detailed in Fig. 3.2, consists of three rectangular solid copper conductors of thickness $t = 35$ μm (bulk conductivity $\sigma = 58$ MS/m) on a Rogers RO-3003 substrate ($\epsilon_r = 3.0$, $\tan\delta = 0.0013$) with thickness $h = 1.524$ mm. The dielectric and conductor 0 (taken to be the reference conductor) have a total width of 30 mm, which is not shown to scale. The upper conductors 1 and 2 are symmetric with widths $s = 1.7$ mm and spacing $g = 0.4$ mm. The terminal-domain per-unit-length TL parameter matrices are 2×2 in size and extracted in HFSS as:

$$\begin{aligned}
[R_T] &= \begin{bmatrix} 5.6364 & 0.1963 \\ 0.1963 & 5.6364 \end{bmatrix} \Omega/m \\
[L_T] &= \begin{bmatrix} 0.3827 & 0.1452 \\ 0.1452 & 0.3827 \end{bmatrix} \mu H/m \\
[G_T] &= \begin{bmatrix} 4.7759 & -1.0613 \\ -1.0613 & 4.7759 \end{bmatrix} mS/m \\
[C_T] &= \begin{bmatrix} 73.1102 & -21.6745 \\ -21.6745 & 73.1102 \end{bmatrix} pF/m
\end{aligned} \tag{3.25}$$

which are used to solve the terminal-domain voltage propagation constants and characteristic impedances:

$$\begin{aligned}
[\gamma_V] &= \begin{bmatrix} 0.0582 + j31.2759 & -0.0107 + j1.4645 \\ -0.0107 + j1.4645 & 0.0582 + j31.2759 \end{bmatrix} rad/m \\
[Z_{cT}] &= \begin{bmatrix} 75.6818 - j0.0488 & 25.6249 + j0.0179 \\ 25.6249 + j0.0179 & 75.6818 - j0.0488 \end{bmatrix} \Omega
\end{aligned} \tag{3.26}$$

Using (2.61a) in (2.76a), as well as (2.79), yields the modal propagation constants and characteristic

impedances:

$$\begin{aligned}[\gamma_M] &= diag\left[\begin{array}{c} 0.0689 + j29.8114 \\ 0.0476 + j32.7403 \end{array}\right] rad/m \\ [Z_{cM}] &= diag\left[\begin{array}{c} 50.0570 - j0.0667 \\ 101.3070 - 0.0309 \end{array}\right] \Omega \end{aligned} \tag{3.27}$$

along with the (unscaled) transformation matrices:

$$[T_V] = [T_I] = \frac{1}{\sqrt{2}}\left[\begin{array}{cc} -1 & 1 \\ 1 & 1 \end{array}\right] \tag{3.28}$$

which again are the mode definitions of even and odd modes. HFSS gives the modal propagation constants and characteristic impedances:

$$\begin{aligned}[\gamma_M]_{HFSS} &= diag\left[\begin{array}{c} 0.0733 + j29.8120 \\ 0.0458 + j32.7410 \end{array}\right] rad/m \\ [Z_{cM}]_{HFSS} &= diag\left[\begin{array}{c} 100.2400 - j0.1369 \\ 50.3630 - j0.0124 \end{array}\right] \Omega \end{aligned} \tag{3.29}$$

where it may be confirmed that the modal propagation constants are very similar (percent differences of less than 0.01% between HFSS direct eigenmode simulation and the data computed from the terminal-domain values). The characteristic impedances appear to have values that are interchanged relative to those predicted by the typical mode definitions (3.28): a coincidence for this system that, nonetheless, illustrates that these mode definitions – based on unscaled transformation matrices – are expectedly in rather *strong disagreement* with HFSS.

Scaling the mode definitions through the application of the proposed constraint yields the matrices

$$\begin{aligned}\left[a^I\right] &= diag\left[\begin{array}{c} \sqrt{2} \\ \frac{\sqrt{2}}{2} \end{array}\right] \\ [T_V]_{\text{scaled}} &= \left[\begin{array}{cc} -0.5 & 1 \\ 0.5 & 1 \end{array}\right] \\ [T_I]_{\text{scaled}} &= \left[\begin{array}{cc} -1 & 0.5 \\ 1 & 0.5 \end{array}\right] \end{aligned} \tag{3.30}$$

Again using these definitions in (2.79) gives:

$$[Z_{cM}] = diag\left[\begin{array}{c} 100.1140 - j0.1334 \\ 50.6534 - j0.0154 \end{array}\right] \Omega \tag{3.31}$$

which are now in good agreement with percent differences of 0.13% and 0.57%, for the odd and even mode, respectively, to the modal values given by HFSS (3.29) as compared with those in (3.27). The dramatic improvement in accuracy seen in this case validates the proposed process, while the minor

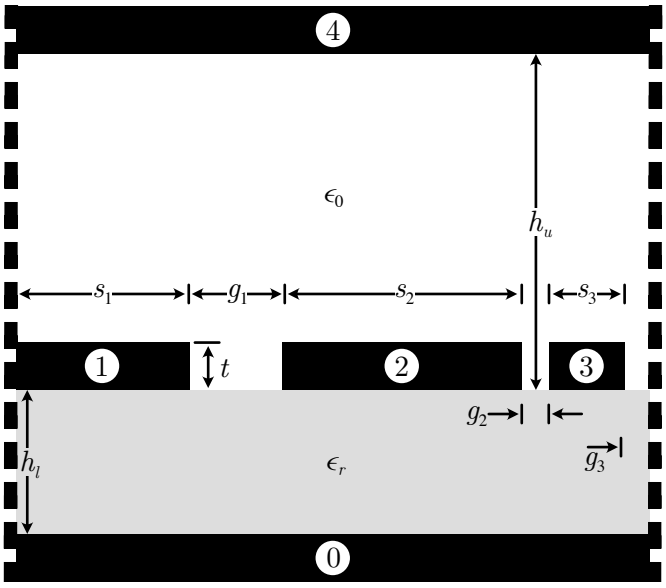

Figure 3.3: Physical arrangement and properties of the Shielded Conductor-Backed Coplanar Waveguide (SCBCPW). The vertical dashed lines on the sides indicate PMC boundary conditions. Image adapted from [395].

remaining discrepancies are limited to firstly the TEM approximation, and secondly errors introduced through numerical processing.

Asymmetric Shielded Conductor-Backed Coplanar Waveguide

This Shielded Conductor-Backed Coplanar Waveguide (SCBCPW) MTL, which exhibits physical asymmetry along both transverse axes, consists of five rectangular solid copper conductors of thickness $t = 35$ μm (bulk conductivity $\sigma = 58$ MS/m) on a Rogers RO-3010 substrate ($\epsilon_r = 11.2$, $\tan\delta = 0.0035$) with thickness $h_l = 1.270$ mm. The width of the simulation domain is 10 mm. The various other geometric parameters detailed in Fig. 3.3 are $s_1 = 1.8$ mm, $s_2 = 3.1$ mm, $s_3 = 0.8$ mm, $g_1 = 2.4$ mm, $g_2 = 1.3$ mm, $g_3 = 0.6$ mm, $h_u = 20$ mm. The domain is bounded on the sides with perfect magnetic conductors (PMCs). The terminal-domain per-unit-length TL parameter matrices are then 4×4 in size, with

$$
\begin{aligned}
[R_T] &= \begin{bmatrix} 5.7410 & 0.6158 & 0.4285 & 1.3669 \\ 0.6158 & 3.4829 & 0.7249 & 1.3292 \\ 0.4285 & 0.7249 & 9.7946 & 1.2298 \\ 1.3669 & 1.3292 & 1.2298 & 2.6073 \end{bmatrix} \Omega/m \\
[L_T] &= \begin{bmatrix} 0.4871 & 0.0589 & 0.0375 & 0.1613 \\ 0.0589 & 0.2844 & 0.0969 & 0.1613 \\ 0.0375 & 0.0969 & 0.5967 & 0.1612 \\ 0.1613 & 0.1613 & 0.1612 & 2.6769 \end{bmatrix} \mu H/m \\
[G_T] &= \begin{bmatrix} 4.1004 & -0.0920 & -0.0183 & -0.0004 \\ -0.0920 & 7.3164 & -0.2782 & -0.0005 \\ -0.0183 & -0.2782 & 3.0389 & -0.0016 \\ -0.0004 & -0.0005 & -0.0016 & 0.0001 \end{bmatrix} mS/m \\
[C_T] &= \begin{bmatrix} 192.9900 & -6.9559 & -0.7568 & -1.0823 \\ -6.9559 & 346.2750 & -17.4292 & -1.8796 \\ -0.7568 & -17.4292 & 145.6230 & -0.7419 \\ -1.0823 & -1.8796 & -0.7419 & 4.4208 \end{bmatrix} pF/m
\end{aligned}
\tag{3.32}
$$

which are used to solve the terminal-domain voltage propagation constants and characteristic impedances:

$$
\begin{aligned}
[\gamma_V] &= \begin{bmatrix} 0.1597 & 0.0139 & 0.0033 & 0.0002 \\ 0.0078 & 0.1646 & 0.0051 & 0.0001 \\ 0.0050 & 0.0110 & 0.1733 & 0.0002 \\ 0.0394 & 0.0680 & 0.0244 & 0.0012 \end{bmatrix} + j \begin{bmatrix} 60.5802 & 5.1182 & 1.1871 & 0.0215 \\ 2.9128 & 61.2832 & 2.9531 & 0.0191 \\ 1.7954 & 7.4158 & 57.7375 & 0.0214 \\ 12.1225 & 20.9886 & 8.3301 & 21.0419 \end{bmatrix} rad/m \\
[Z_{cT}] &= \begin{bmatrix} 50.1787 & 3.5449 & 2.0584 & 14.9098 \\ 3.5449 & 28.6587 & 6.7518 & 14.8751 \\ 2.0584 & 6.7518 & 63.9974 & 14.8850 \\ 14.9098 & 14.8751 & 14.8850 & 770.0090 \end{bmatrix} + j \begin{bmatrix} 0.0380 & 0.0041 & 0.0020 & 0.0169 \\ 0.0041 & 0.0204 & 0.0107 & 0.0177 \\ 0.0020 & 0.0107 & 0.0224 & 0.0224 \\ 0.0169 & 0.0177 & 0.0215 & 0.0229 \end{bmatrix} \Omega
\end{aligned}
\tag{3.33}
$$

Using (2.61a) in (2.76a), as well as (2.79), yields the modal propagation constants and characteristic impedances (in vector form):

$$[\gamma_M] = diag \begin{bmatrix} 0.0014 + j21.0236 \\ 0.1610 + j54.2975 \\ 0.1570 + j58.2701 \\ 0.1795 + j67.0516 \end{bmatrix} rad/m$$
$$[Z_{cM}] = diag \begin{bmatrix} 661.2290 - j0.1385 \\ 38.7598 + j0.0520 \\ 48.6598 - j0.0094 \\ 53.0236 + j0.0383 \end{bmatrix} \Omega \tag{3.34}$$

along with the (unscaled) transformation matrices:

$$[T_V] = \begin{bmatrix} -0.0005 & 0.2043 & 0.8007 & 0.5056 \\ -0.0004 & -0.4522 & -0.2335 & 0.5187 \\ -0.0005 & 0.8682 & -0.5516 & 0.5115 \\ 0.9999 & 0.0069 & 0.0056 & 0.4624 \end{bmatrix} + j \begin{bmatrix} 0.0000 & -0.0015 & 0.0005 & 0.0001 \\ 0.0000 & 0.006 & -0.0011 & 0.0000 \\ 0.0000 & 0.008 & 0.0012 & -0.0005 \\ 0.0000 & 0.0003 & -0.0002 & 0.0003 \end{bmatrix}$$
$$[T_I] = \begin{bmatrix} -0.2314 & 0.1880 & 0.8215 & 0.4624 \\ -0.3967 & -0.7764 & -0.4031 & 0.8263 \\ -0.1591 & 0.6015 & -0.4033 & 0.3216 \\ 0.8739 & 0.0000 & 0.0000 & 0.0007 \end{bmatrix} + j \begin{bmatrix} -0.0001 & -0.0011 & -0.0002 & 0.0001 \\ -0.0002 & 0.0006 & 0.0017 & 0.0000 \\ -0.0002 & 0.0011 & 0.0013 & -0.0004 \\ -0.0001 & 0.0000 & 0.0000 & 0.0000 \end{bmatrix} \tag{3.35}$$

It may be noted that although $[T_V]$ and $[T_I]$ are complex matrices, the relatively small imaginary components compared with the real components of the mode definitions still imply that the characteristic modes are *approximately* normal, as previously indicated should be the case. HFSS gives the modal propagation constants and characteristic impedances:

$$[\gamma_M]_{HFSS} = diag \begin{bmatrix} 0.0014 + j21.0240 \\ 0.1621 + j54.3010 \\ 0.1576 + j58.2720 \\ 0.1799 + j67.0550 \end{bmatrix} rad/m$$
$$[Z_{cM}]_{HFSS} = diag \begin{bmatrix} 756.1500 - j0.0521 \\ 57.6910 + j0.1264 \\ 71.6100 - j0.0361 \\ 16.8950 + j0.0133 \end{bmatrix} \Omega \tag{3.36}$$

where it may be confirmed that the modal propagation constants are very similar (percent differences of less than 0.01% in both cases), while the characteristic impedances differ greatly from those predicted in (3.34) through application of (2.79). Scaling the transformation matrices yields:

$$\left[a^I\right] = diag\begin{bmatrix} 1.1443 + j0.0001 \\ -1.2666 - j0.0009 \\ -1.2173 - j0.0003 \\ 0.6207 + j0.0001 \end{bmatrix}$$

$$[T_V]_{\text{scaled}} = \begin{bmatrix} -0.0005 & -0.1769 & -0.6751 & 0.9847 \\ -0.0004 & 0.3916 & 0.1969 & 1.0102 \\ -0.0005 & -0.7518 & 0.4651 & 0.9962 \\ 0.9996 & -0.0057 & -0.0048 & 0.9006 \end{bmatrix} \tag{3.37}$$

$$[T_I]_{\text{scaled}} = \begin{bmatrix} -0.2648 & -0.2381 & -1.0000 & 0.2871 \\ -0.4542 & 0.9834 & 0.4906 & 0.5129 \\ -0.1818 & -0.7619 & 0.4909 & 0.1996 \\ 1.0000 & 0.0000 & 0.0000 & 0.0004 \end{bmatrix}$$

Using these mode definitions to compute the modal impedances yields:

$$[Z_{cM}] = diag\begin{bmatrix} 756.9000 - j0.0452 \\ 56.6762 + j0.0177 \\ 70.2499 + j0.0474 \\ 16.8991 - j0.0130 \end{bmatrix} \Omega \tag{3.38}$$

which are now in good agreement (percent differences of 0.01%, 1.77%, 1.92%, 0.02% to the modal values given by HFSS (3.36) as compared with those in (3.34). It may be noted that the two modes with a roughly even distribution of fields in both dielectrics are those two that exhibit the highest error. This is unsurprising, since the contrast between relative permittivities of 1.0 and 11.2 is very high, and these modes are stretching the limitations of the TEM approximation, thereby incurring the most error when using processes derived for strictly TEM modes. This example illustrates, however, the robustness of the proposed process even in such extreme cases.

Summary

The results given in these examples demonstrate that the proposed process achieves agreement with computed field quantities. Moreover, the invocation of physical arguments such as the equality of total currents implies that this process is uniquely required to achieve that agreement – and that therefore, other methods should result in inherent contradictions.

Self-normalization of the current or voltage eigenvectors as described in (2.81) [264, 350] is typically used by most eigenmode solvers; indeed, this can be seen to be the case in the unscaled mode definitions of (3.21), (3.28), and (3.35). Since it was demonstrated that these do not produce results in agreement with at least the field solutions studied previously, this scaling process may be discounted as invalid. Quantitative results of these conclusions are provided in Table 3.1, which details comparisons of modal characteristic impedance values computed via self-normalization of eigenvectors with the values computed

Table 3.1: Comparison of Percent Differences in Modal Characteristic Impedances Produced by Traditional Self-Normalization and the Proposed Process with Respect to Data Produced by HFSS

Example	Self-Normalization	Proposed Method
Three-Wire Line	34.50%, 40.00%	$< 0.01\%$ both cases
CBCPS	66.78%, 67.18%	$< 0.01\%$ both cases
Asymmetric SCBCPW	13.39%, 39.26%, 38.16%, 103.34%	0.01%, 1.77%, 1.92%, 0.02%

from HFSS.

3.1.5 Experimental Validation

The predicted modal characteristic impedance values may also be confirmed via experiment. Modal characteristic impedances of two different CBCPS MTLs are confirmed though the excitation of each of their two propagation modes. Specifically, the proposed setup consists of a length of CBCPS, connected on either end to a feeding two-conductor TL. The equivalent-circuit models of two such designs are shown in Figs. 3.4 and 3.5. The validation of the modal characteristic impedance values occurs in observing the scattering of the total system: since the characteristic impedances of the two-conductor feeding TLs are well known as well as determinable, and if the feed lines excite predominantly a single mode of the MTL, then the observed scattering parameters should correspond with particular modal characteristic impedances values. For example, the return losses should be low (at least 20 dB over a wide bandwidth) for a matched modal impedance, and high for an unmatched case, both with a predictable frequency response corresponding to the MTL lengths.

In order to excite each mode of the CBCPS MTLs, two different feed TLs are designed. Since the characteristic modes are simply the odd and even modes (described by the mode definitions in (3.30)), a CPS TL may be used to excite the odd mode, and a MS TL may be used to excite the even mode. The impedances of these lines are chosen to be 100 Ω and 50 Ω, respectively, such that the design in section 3.1.4 should represent the matched case for both even and odd modes. Designed on the same RO-3003 substrate, the MS has a width of 3.8 mm, and the CPS has a strip width $s = 1.4$ mm and spacing $g = 0.2$ mm. The second CBCPS, representing the mismatched case, is designed on an identical substrate with geometrical parameters $s = 0.23$ mm and $g = 0.55$ mm, for which the proposed analytical process predicts impedances of roughly 200 Ω and 100 Ω for the odd and even modes, respectively.

The connections between the two-conductor feed lines and the MTLs are also detailed in Figs. 3.4 and 3.5. The even mode is excited in the MTLs through shorting the MS to both upper-layer conductors, such that they possess the same voltage and the currents are equally divided between them. The conductor backing of both the feed and CBCPS are connected directly together. The odd-mode feed connects each conductor of the CPS directly to each of the upper-layer conductors of the CBCPS, while the conductor backing of the CBCPS is left floating with no connection. This ensures that the currents and voltages are equal and opposite on the upper-layer conductors.

Both feed line types are connected to a Vector Network Analyzer (VNA) via Sub-Miniature 'A' (SMA) connectors and coaxial phase-stable measurement cables. The MS TL is directly connected to one SMA

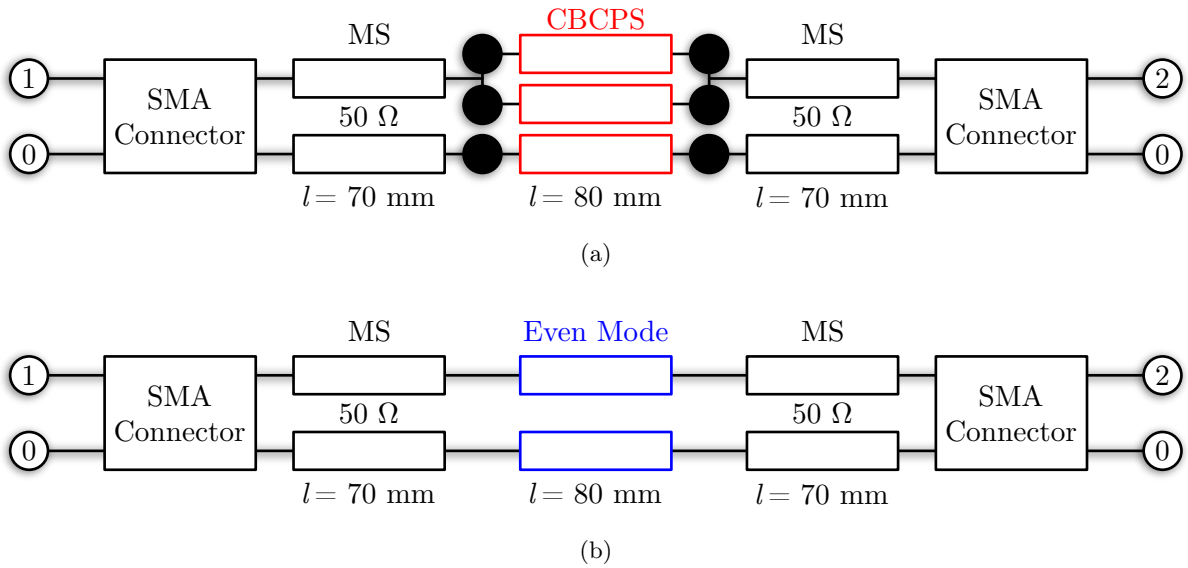

Figure 3.4: Equivalent-circuit models of the experimental even-mode structures: a) the terminal domain layout, and b) the equivalent modal-domain circuit. Images adapted from [395].

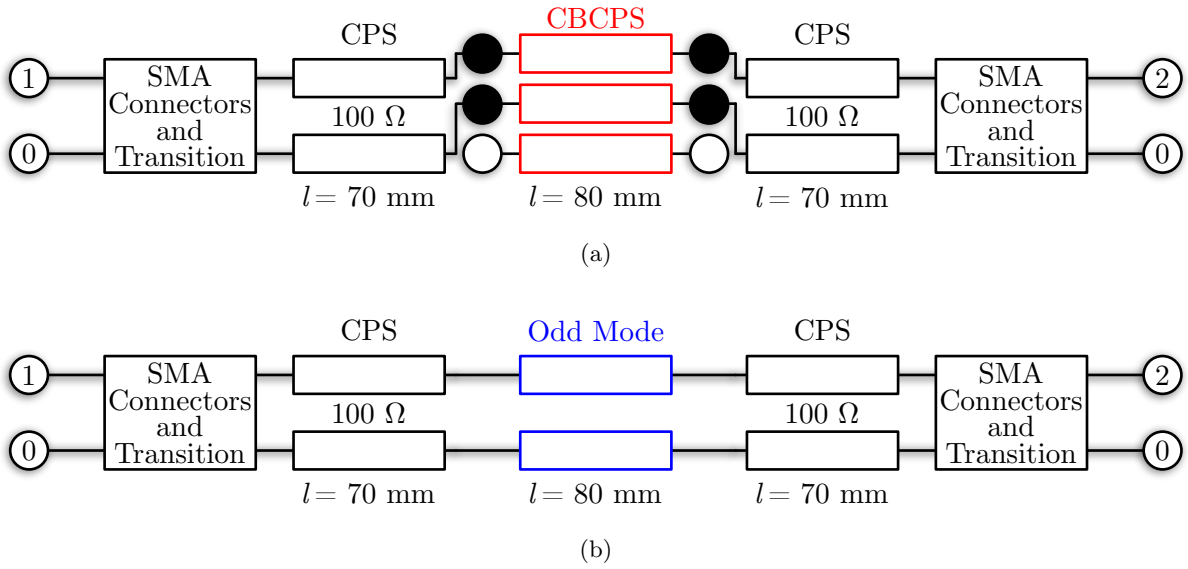

Figure 3.5: Equivalent-circuit models of the experimental odd-mode structures: a) the terminal domain layout, and b) the equivalent modal-domain circuit. Images adapted from [395].

connector, while the two conductors of the CPS are split and individually connected each to a SMA connector (the details of this transition are given below), such that the odd mode must be differentially excited – these transition sections are included in the equivalent-circuit models of Figs. 3.4b and 3.5b

The scattering parameters of the two terminal-domain circuit models are given in Fig. 3.6 for each of the two CBCPSs (matched and mismatched), where the dotted curves indicate the data computed from these circuit models. As expected, the data exhibit low reflection and high transmission when the feed lines are matched to the CBCPS, and vice-versa when they are not.

The entire system of connectors, transition sections, feed lines, and CBCPS sections are then simulated in HFSS – the layouts of which are shown in Figs. 3.7 and 3.8 – and the results are given in Fig. 3.6, via the dashed curves, where they are seen to be in good agreement with the circuit-models' data.

The devices are then fabricated using a LPKF U3 laser-based milling machine, which is calibrated to achieve a positional accuracy of at least 10 μm across each PCB. Shown in Figs. 3.9, the fabrications are visually inspected and the positional inaccuracies are estimated to be at most 2 μm in the regions of interest; particularly, the 50 μm gaps in the CPS feed transitions sections.

The devices are connected to a four-port VNA, as shown in Fig. 3.10, where a styrofoam base has been used to support the structures and mitigate parasitic coupling with any metallic features in the table below. The measured scattering parameters are given in Fig. 3.6 via the solid curves, where the odd-mode scattering parameters are obtained via modal transformation from the four-port terminal-domain data as described in Appendix C.

Layout of the Odd-Mode Transition

Since the VNA interfaces with its test devices via coaxial modes, an inherent unbalance of currents will always develop whenever a transition to planar TLs is used. In order to excite a purely balanced mode for the odd-mode feedline, two connections are used to excite a single mode in a differential fashion [295]. While electrically small, this transition section still needs to be precisely designed in order to achieve the low levels of reflection required for this work. This design consists of two individual 61 Ω slotlines (SLs) which merge into one 100 Ω line. 61 Ω was chosen as the Slotline (SL) impedance instead of the ideal 50 Ω, due to the fact that, on the chosen substrate, the required SL gap would be smaller than 50 μm, which was deemed the smallest that could be reliably fabricated via the LPKF ProtoLaser U3 laser milling machine. Even still, a return loss of greater than 29 dB was achieved for the transition. The geometric parameters of the feed section are given in Fig. 3.11, where $c = 0.05$ mm, $w = 5.00$ mm, $f = 4.00$ mm, $l = 1.05$ mm, $d = 2.50$ mm, $g = 0.20$ mm, $s = 1.40$ mm. The simulated magnitudes of the scattering parameters of these feed-line transitions are shown in Fig. 3.12, where the SMA connectors are at port 2 and the waveport-excited TLs at port 1. It may be observed that excellent matching is achieved; the scattering parameters of the even-mode MS transition (SMA to MS) is also shown for comparison purposes, showing comparable matching levels.

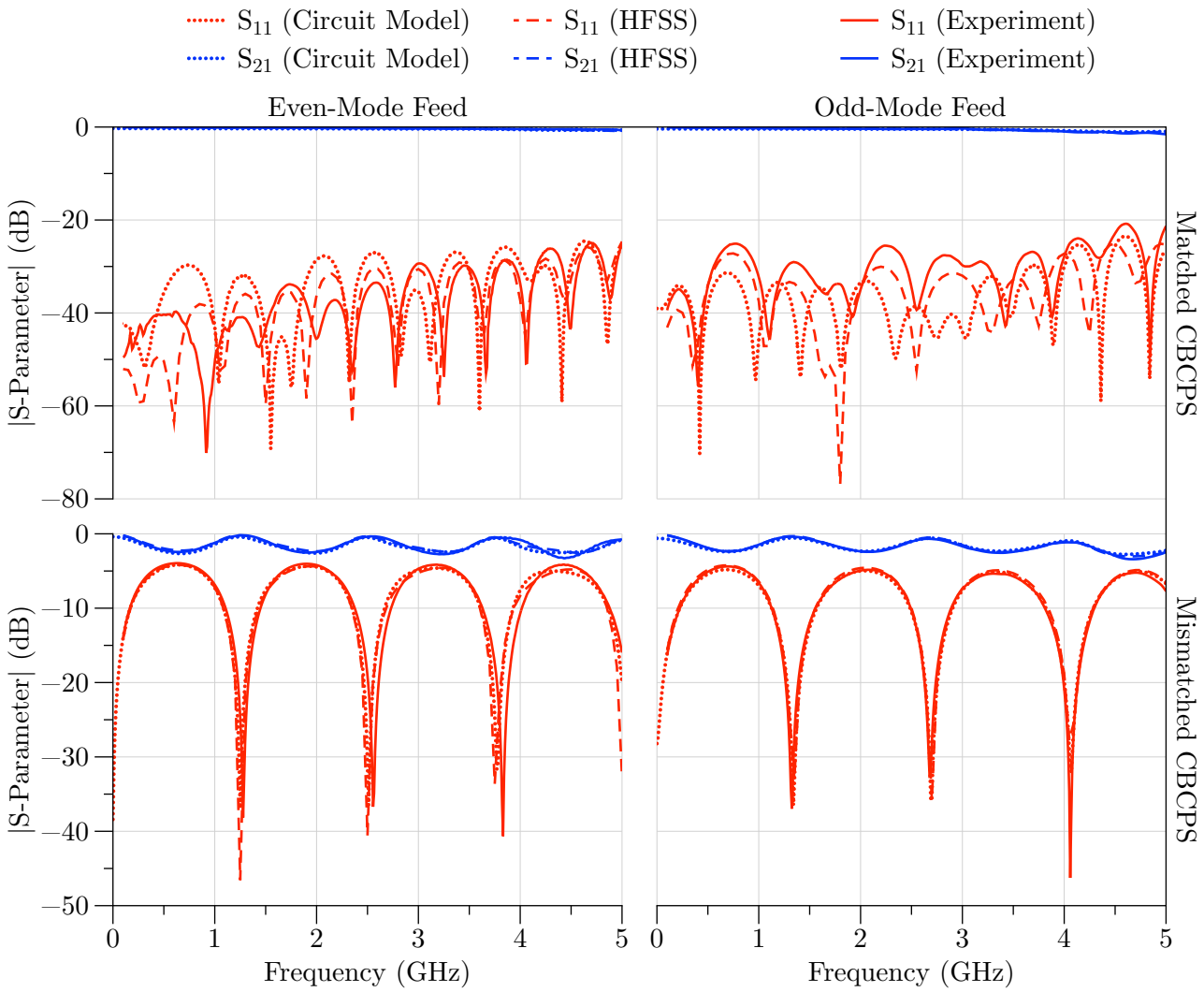

Figure 3.6: Scattering parameters of the four circuits investigate in this section: dotted curves represent the data from the equivalent-circuit models, the dashed curves indicate data obtained from full-wave solver HFSS, and the solid curves indicate experimentally-obtained data. The fact that all data sets from varying sources exhibit good agreement is validation of the theory, and in particular, Postulate 1. Image adapted from [395].

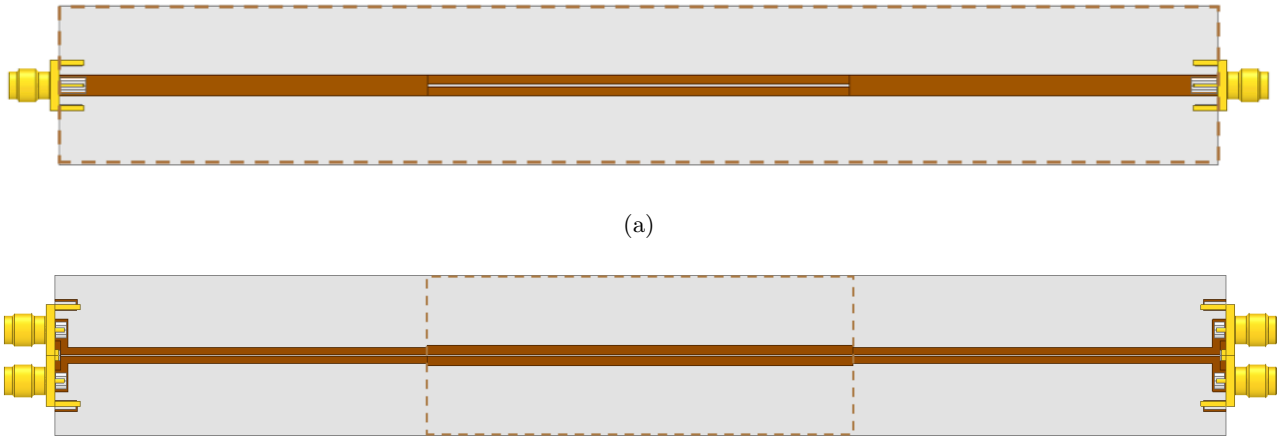

(a)

(b)

Figure 3.7: Simulation models of the matched CBCPS structures: a) even-mode MS feed, b) odd-mode CPS feed, where the dashed lines indicate the location of the conductor backing. Images from [395].

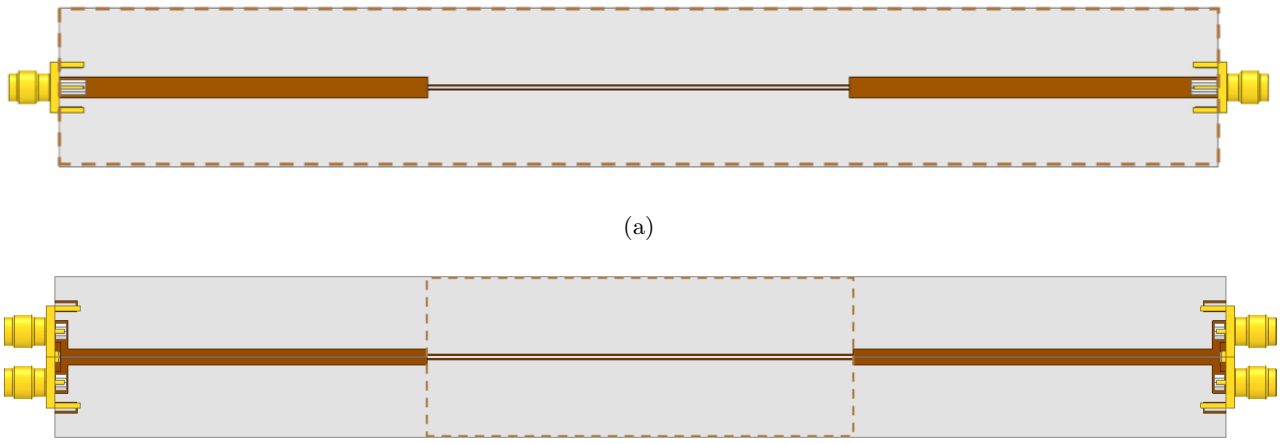

(a)

(b)

Figure 3.8: Simulation models of the mismatched CBCPS structures: a) even-mode MS feed, b) odd-mode CPS feed, where the dashed lines indicate the location of the conductor backing. Images from [395].

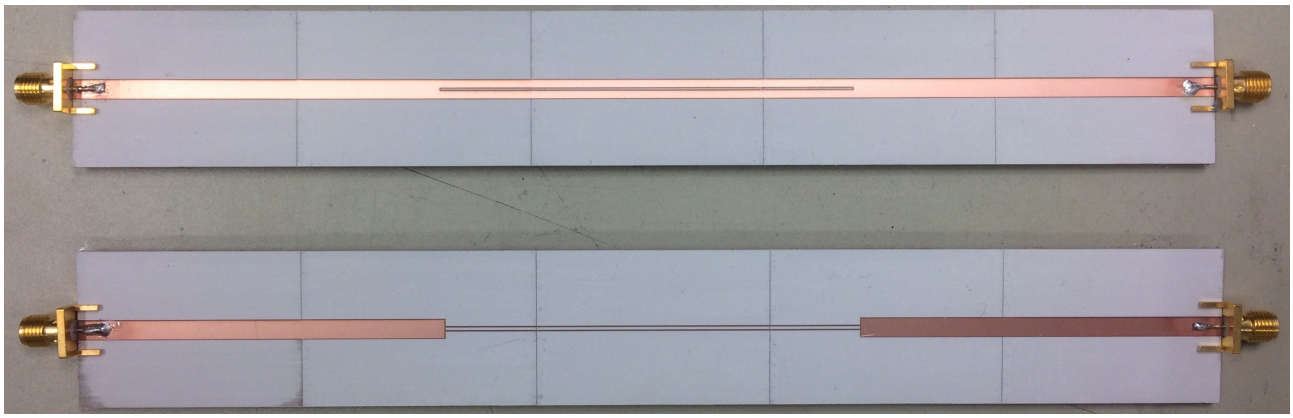

(a)

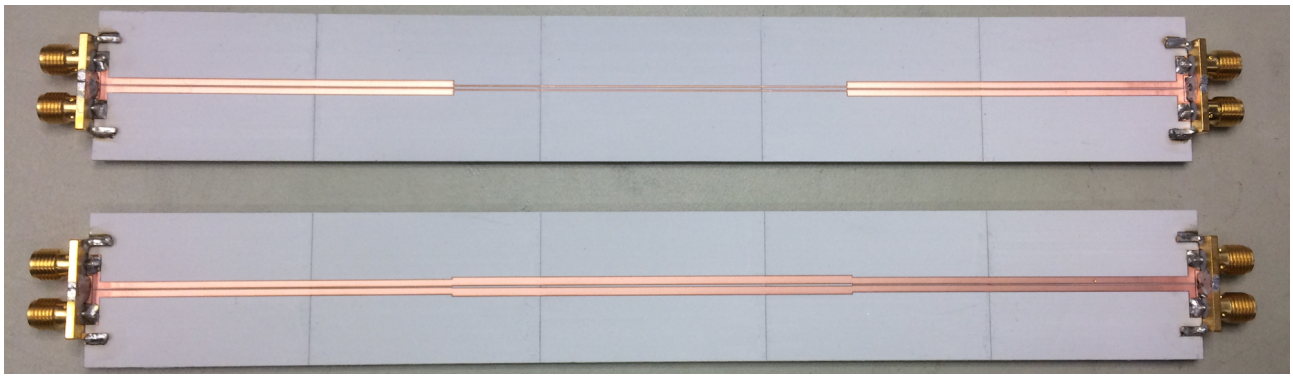

(b)

Figure 3.9: Fabricated CBCPS structures: a) even-mode MS feed, b) odd-mode CPS feed. Images from [395].

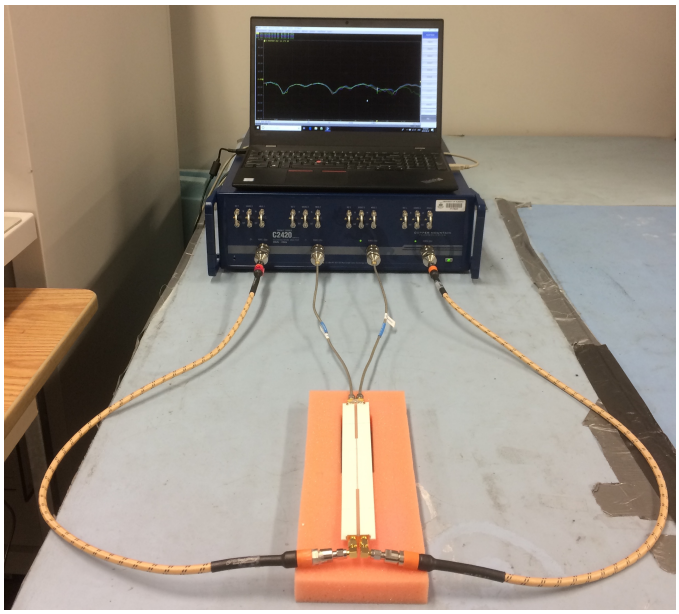

Figure 3.10: Experimental setup of the odd-mode-excited CBCPS test structure connected to a four-port VNA. Image from [395].

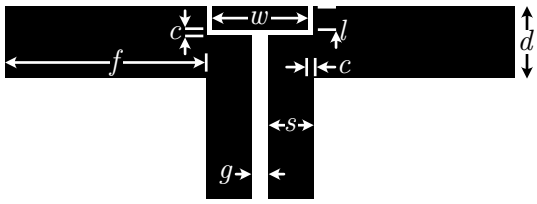

Figure 3.11: Geometric parameters of the CPS feed to SMA connectors transition. The SMAs excite the outer strips from the top with a common conductor between them, which ensures a series excitation. Image adapted from [395].

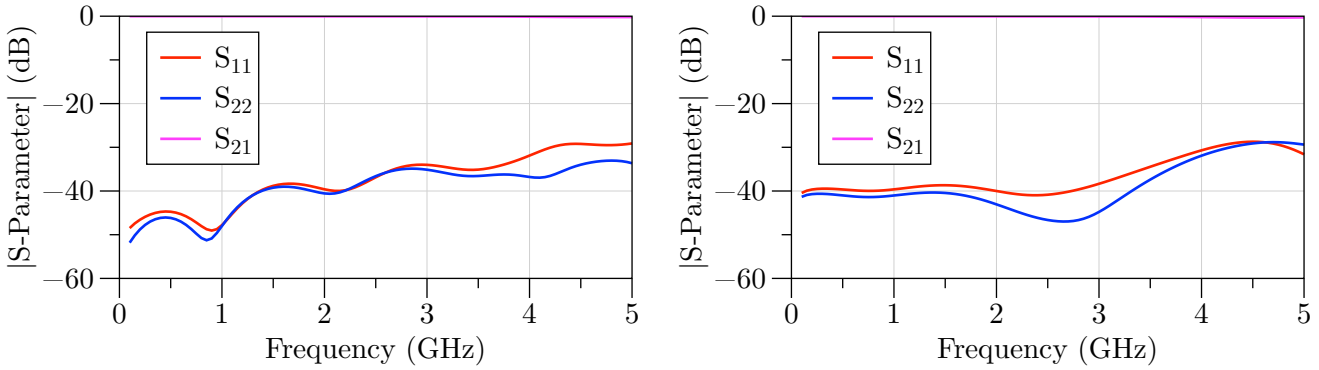

Figure 3.12: Simulated scattering parameters of the SMA connectors and transition regions for: a) even-mode excitation, b) odd-mode excitation. Images adapted from [395].

Discussion on Results

The high level of agreement among the various data sets in Fig. 3.6 indicated that the modal-domain circuit models of Figs. 3.4b and 3.5b are valid, high-fidelity representations of the corresponding terminal-domain circuit models of Figs. 3.4a and 3.5a, repectively. With the return loss of the matched cases better than 20 dB over the very large bandwidth of 0.1 to 5.0 GHz, it may be concluded that, indeed, the MTL is well matched to 50 and 100 Ω for the even and odd modes, respectively, which must then be its modal impedance values, as predicted by the proposed process. It is critical to note that this stands in stark contrast to the modal impedances computed with the commonplace (self-normalized) mode definitions (3.28), which predict that these MTL sections would always be mismatched – lending further credibility to the proposed process. Additionally, the scattering parameters of the mismatched cases align readily with the those predicted by the equivalent-circuit model, indicating that these predicted values are indeed those observed in experiment.

The finite – but small – S_{11} ripples observed in the matched cases below -20 dB are attributed to impedance mismatches between the MTL and the feed lines. These minor mismatches arise from the fact that the modal impedances of the MTL sections (with values given in (3.29) are not identical to those of the feed lines. The MTL modal impedance are not exactly 50 and 100 Ω due to the consideration of a minimum geometrical step size of 0.01 mm in simulation, which is also likely close to the actual fabrication error of the laser milling system.

Since both modes are validated, both in the matched and mismatched cases, it has been experimentally established that a) the modal characteristic impedances of the MTLs are not arbitrary; their values do affect matching with standard two-conductor TLs, and furthermore, b) these modal values may be successfully predicted by scaling of the mode definitions using the proposed process.

3.2 M-Parameters

In extending the two-port formalism of the previous work into multiple ports – distributed over multiple dimensions, in which various ports may possess differing numbers of terminals – it becomes necessary to provide a rigorous, flexible framework with which to describe these generalized networks. Historically, various parameters such as scattering parameters are used to describe such networks; however, each type of network parameter has its own advantages and drawbacks. M-Parameters are introduced in this work as a highly convenient parameter form with which to conduct the following analyses. These parameters represent sets of homogenous, linear equations, which express the voltages and current relations amongst all terminals in a sourceless environment. While the use of such sets of equations for dispersion analysis is not novel – nor are they required for the analyses presented later in this work, or even more computationally efficient to use than other parameters – this section seeks to formalize such network descriptions, and provides some insight on how they may be implemented and manipulated in determining numerical solutions to typical dispersion problems.

3.2.1 Existing Parameters and Deficincies

Of course, various parameters already exist by which generalized networks may be described. Examples include the scattering S-Parameters, two-port $ABCD$-Parameters, admittance Y-Parameters, and impedance Z-Parameters [391]. While these parameters each have their own advantages, they also each have drawbacks which make them undesirable for the generalized analyses presented in this work. While it is possible that the presented M-Parameters possess similar deficiencies – such as the inability to model certain linear, sourceless, networks – none have been found as of the time of this writing.

S-Parameters

Voltage-based S-Parameters are defined as [391, 401]:

$$\vec{V}^- = [S]\,\vec{V}^+ \tag{3.39}$$

Although very convenient and widely used at microwave frequencies, the primary drawback to these parameters is that they are very non-intuitive for simple components: for example, it is not readily obvious what the S-Parameters of a series resistor are, or how one would express a series of ideal interconnections. Therefore, there is a relatively substantial overhead in converting these parameters to/from other more convenient, intuitive description forms. Historically, sub-components of a given network may all be described with a common reference impedance (commonly, 50 Ω), such that they may be easily combined and solved. However, in other situations where the sub-networks are described with differing reference impedances, generalized S-Parameters (i.e., power waves [402]) must be used, which add to the complexity of the formulation, as well as precluding simple basis transformations such as those discussed in Appendix C. The use of complex impedances in S-Parameters is a matter of some ambiguity, since a single, rigorous definition for determining S-Parameters in such cases does not appear to have been produced or accepted [403].

$ABCD$-Parameters

$ABCD$-Parameters are defined as (noting that the currents at port 2 are defined propagating *outwards*, a fact reflected here by using a negative sign) [391]:

$$\begin{bmatrix} \vec{V}_1 \\ \vec{I}_1 \end{bmatrix} = \begin{bmatrix} [A]\,[B] \\ [C]\,[D] \end{bmatrix} \begin{bmatrix} \vec{V}_2 \\ -\vec{I}_2 \end{bmatrix} \tag{3.40}$$

By definition, $ABCD$-Parameters are meant to model networks with two distinct observation points: an input, and an output. This inherently means that they are clumsy for the determination of parameters of multidimensional networks, although they have been used for the purpose [277, 278]. Unfortunately, these parameters do not work well in describing systems which have a differing number of conductors on the output than the input (as the non-square matrices may not be inverted), and they may not be used to model simple networks which contain nodes, such as that shown in Fig. 3.13a.

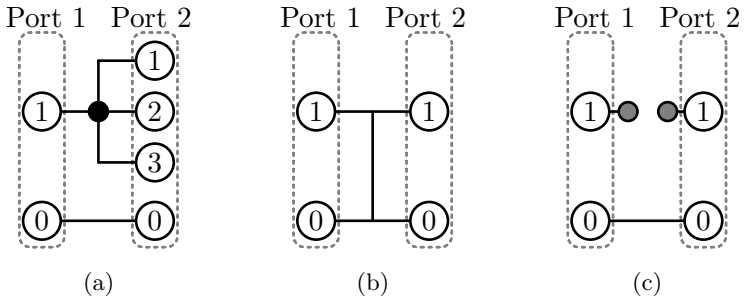

Figure 3.13: Examples of circuits which may not be well-described with standard parameters: a) a tee-junction may not be well-described with $ABCD$-Parameters, b) a shunt short-circuit may not be well-described with Y-Parameters and c) a series open-circuit may not be well-described with Z-Parameters.

Y-Parameters

Y-Parameters are defined as [391]:

$$\vec{I} = [Y]\,\vec{V} \tag{3.41}$$

Y-Parameters, which express the currents at various terminals as a function of the voltages on the same terminals, are quite versatile and may be used in many situations – except in the case where there exists a short circuit (as shown in Fig. 3.13b) and the current may not be determined as a function of voltages.

Z-Parameters

Similarly, Z-Parameters are defined as the inverse of Y-Parameters [391]:

$$\vec{V} = [Z]\,\vec{I} \tag{3.42}$$

The Z-Parameters express the voltages at various terminals as a function of the currents on the same terminals. However, they cannot be used to describe the case where there exists an open circuit (as shown in Fig. 3.13c), from which the voltage may not be determined as a function of currents.

3.2.2 Terminology

Before M-Parameters are defined, some terminology must be clarified. In particular, the Literature typically interchanges the definition of the terms *terminal* and *port*, or defines a port as two terminals. While useful for simple systems, these terms are not particularly useful for discrete clusters of multiple terminals. Therefore, in this work, the following terminology will be used:

- A *terminal* represents the ending of a single conductor, on which a current and a potential may be defined.
- A *port* represents a grouping of an arbitrary number of terminals. Typically, one of the terminals is selected to serve as the reference, such that the voltages on the remaining terminals are gauged

with respect to the reference conductor's potential. Additionally, it will be assumed that the port servers as the ending of a MTL, such that the currents are assumed to be balanced (sum to zero) at each port.

The currents on the terminals are always defined as proceeding inwards into a port (with the exception of the reference terminal – if present – for which it is assumed positive current is proceeding outwards).

3.2.3 Matrix Layout

Considering a general network with N ports, and $M(n)$ terminals m on port n, the voltages and currents of all the terminals are expressed in sequence, for each port in sequence. The voltages of the terminals are grouped together, as are the currents of each terminal, as:

$$[M] \cdot \left[\vec{V}_1 \, \vec{I}_1 \, \vec{V}_2 \, \vec{I}_2 \ldots \vec{V}_n \, \vec{I}_n \right]^T = \vec{0} \tag{3.43}$$

where $[M]$ is the matrix of M-Parameters, and the subscripts of the voltage and current vectors (of which the various entries correspond to the terminals at each port) indicate the port numbers they correspond to. The matrix is equal to $\vec{0}$ – i.e., the set of equations it represents is homogeneous – because it represents a sourceless network. Moreover, since the network does not include any boundary conditions, the matrix will always be of size $p \times 2p$, where p is the number of non-reference terminals in the system. With this formalism, the various example networks of Fig. 3.13 may be expressed.

The tee-network of Fig. 3.13a (re-indexing the terminals to follow the convention set in section 3.2.2) may be described with four equations: three which detail that the voltages at the non-reference terminals are equal (various sets of equations are possible), and one detailing that the sum of currents over the non-reference terminals is zero. A resulting matrix $[M]$ is detailed in (3.44a). The shunt short-circuit shown in Fig. 3.13b may be described with two equations: one stating that the voltage at terminal 1 is zero, and one stating that the voltage at terminal 2 is also zero. Similarly, the series open-circuit shown in Fig. 3.13c may also be described with two equations: one stating that the current on terminal 1 is zero, and one stating that the current on terminal 2 is also zero.

$$\begin{array}{c} V_1^1 - V_1^2 = 0 \\ V_2^1 - V_2^2 = 0 \\ V_2^2 - V_3^2 = 0 \\ I_1^1 + I_2^1 + I_2^2 + I_2^3 = 0 \end{array} \quad \Rightarrow \quad [M_{Tee}] = \begin{array}{c} \begin{array}{cccccccc} V_1^1 & I_1^1 & V_2^1 & V_2^2 & V_2^3 & I_2^1 & I_2^2 & I_2^3 \end{array} \\ \left[\begin{array}{cccccccc} 1 & 0 & -1 & 0 & 0 & 0 & 0 & 0 \\ 0 & 0 & 1 & -1 & 0 & 0 & 0 & 0 \\ 0 & 0 & 0 & 1 & -1 & 0 & 0 & 0 \\ 0 & 1 & 0 & 0 & 0 & 1 & 1 & 1 \end{array} \right] \end{array} \tag{3.44a}$$

$$\begin{array}{c} V_1^1 = 0 \\ V_2^1 = 0 \end{array} \quad \Rightarrow \quad [M_{Short}] = \begin{array}{c} \begin{array}{cccc} V_1^1 & I_1^1 & V_2^1 & I_2^1 \end{array} \\ \left[\begin{array}{cccc} 1 & 0 & 0 & 0 \\ 0 & 0 & 1 & 0 \end{array} \right] \end{array} \tag{3.44b}$$

$$\begin{matrix} I_1^1 = 0 \\ I_2^1 = 0 \end{matrix} \quad \Rightarrow \quad [M_{Open}] = \begin{matrix} \\ \end{matrix} \begin{matrix} V_1^1 & I_1^1 & V_2^1 & I_2^1 \end{matrix} \begin{bmatrix} 0 & 1 & 0 & 0 \\ 0 & 0 & 0 & 1 \end{bmatrix} \tag{3.44c}$$

3.2.4 Diagonalization

Oftentimes (as will be demonstrated in later in this chapter), it will become necessary to invert part of the matrix $[M]$. One particular challenge associated with this process is deciding which rows are to be included in the inversion: since the set of equations is homogeneous, the rows of the matrix may be sorted without consequence. In this work, inversion is best guaranteed by diagonalizing the matrix, and inverting the uppermost rows. This diagonalization may be accomplished using the ability to freely sort rows.

The particular process to perform diagonalization in this work is the QR diagonalization, which accepts an input matrix $[M]$ and produces an orthonormal matrix $[Q]$ and an upper triangular matrix $[R]$, as [319, 404, 405]:

$$[M] = [Q]\,[R] \tag{3.45}$$

While $[Q]$ will typically be a square matrix, $[R]$ will of course have the same dimensions as $[M]$. Moreover, due to the homogeneity of $[M]$, it may be pre-multiplied by any matrix (of the appropriate dimensions) without affecting its meaning. In this sense, $[R]$ is just another form of $[M]$ – both describe the same network. The matrix $[Q]$ then describes the row manipulations taking place in the diagonalization, which can include the sorting of rows.

3.3 Generalized Dispersion Analysis

This section builds upon the analysis of periodic structures to effect an analytical eigensystem in the form of Bloch's theorem (2.91). This extends the concepts of individual waves travelling though one-dimensional networks, to individual waves travelling through multidimensional networks. Using the M-Parameters introduced in section 3.2, a rigorous, analytical process is developed that allows for the determination of the properties of Bloch modes supported by generalized, multidimensional, multimodal MTL networks.

3.3.1 Unit-Cell Conditions

As dispersion analysis concerns the study of periodic media, and the media under investigation interfaces with its environment via discrete sets of voltages and currents, a number of restrictions must be met in order for a generalized network to be analyzed as a periodic structure. These conditions are:

1. The physical dimensions of the unit cell must form a Bravais lattice, which are the shapes necessary for a periodic pattern to fill a given space [406, 407].

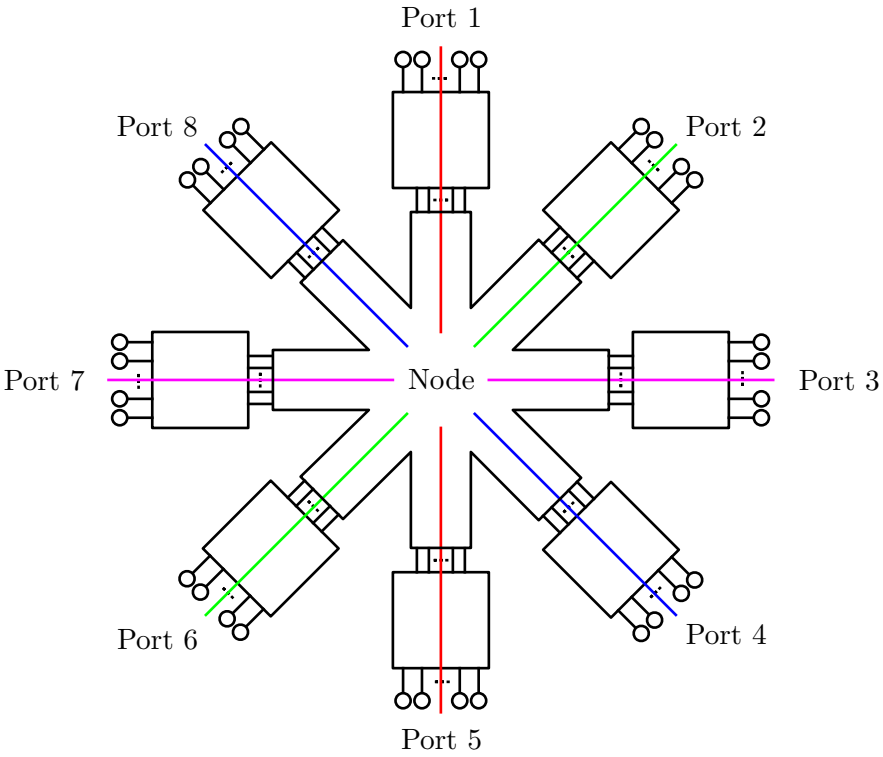

Figure 3.14: Layout of an example generalized unit cell, in this particular case with 4 axis and 8 ports. The colored lines indicate the various axes, and the ports are indexed starting at 1 at the vertical and incrementing clockwise.

2. The unit cell must have discrete, definable axes, each of which geometrically passes through the center of the unit cell and connectors to the ports on opposing side of the cell, in order to apply Bloch's theorem (2.87).

3. Each port must possess the same number of terminals as the port on the opposing side of the unit cell, in order to apply Bloch's theorem (2.87).

3.3.2 Unit-Cell Conventions

In addition to the requirements imposed by the physics, a number of conventions are also employed in this work. One such convention is the layout of the unit cells: it is assumed that each unit cell consists of a central "node" region on which all of the conductors converge (without necessarily being connected), while the remainder of the cell consists of "branch" sections which connect the node to the adjacent cells. The branches are laid out along the cell's axes, such that each axis possesses two branch networks (the networks may be open-circuits). An example of this configuration is shown in Fig. 3.14, in which the colored lines indicate the various axes.

The ports are all indexed starting from 1 (which could be any arbitrarily selected port), and the index increments by one for each port, transversing either clockwise or counterclockwise around the unit cell. Thus, for a network with N ports, each axis will be coincident with one port n, and another port

$n + (N/2)$. N will always be an even number.

Lastly, it is taken that each port represents an MTL termination, such that the currents are balanced (i.e., sum to zero) at each port. This statement is another use of the TEM approximation, where it allows the disregard of the coupling of higher-order evanescent non-TEM modes that realistically exist at physical junctions. While each port may have a designated reference conductor, there is no requirement for the reference conductors at differing ports to be related.

In summary, the assumptions made as to the properties of the unit cells investigated in this work are given in Assumption Set 5:

- Unit cells investigated in this work possess a central node to which all branches are attached.
- There are two branches per unit-cell axis.
- There is one port attached to each branch at the outer edge of the unit cell.
- The currents at each port sum to zero.
- There are N ports per unit cell, where N is an even number.
- Port n is coincident with port $n + (N/2)$ of the adjacent unit cell.

Assumption Set 5: Assumed Unit-Cell Properties

3.3.3 Formulation

Given these conditions and conventions, the generalized unit cell may be analyzed and its dispersive properties determined. It is important to note that while the following derivations may seem elaborate, the general idea behind the math is simply vector substitution of known quantities, to solve for the remaining unknowns. For a network such as that given in Fig. 3.14 with N ports n, the matrix $[M]$ is expressed as (illustrated using the color coding of the axes from the figure):

$$\begin{bmatrix} [M_{11}] & [M_{12}] & \cdots & [M_{1(N/2)}] & [M_{1(1+(N/2))}] & \cdots & [M_{1N}] \\ [M_{21}] & [M_{22}] & \cdots & [M_{2(N/2)}] & [M_{2(2+(N/2))}] & \cdots & [M_{2N}] \\ \vdots & \vdots & \ddots & \vdots & \vdots & \ddots & \vdots \\ [M_{(N/2)1}] & [M_{(N/2)2}] & \cdots & [M_{(N/2)(N/2)}] & [M_{(N/2)(2+(N/2))}] & \cdots & [M_{(N/2)N}] \end{bmatrix} \cdot \begin{bmatrix} \vec{V}_1 & \vec{I}_1 & \vec{V}_2 & \vec{I}_2 & \cdots & \vec{V}_{(N/2)} & \vec{I}_{(N/2)} & \vec{V}_{(1+(N/2))} & \vec{I}_{(1+(N/2))} & \cdots & \vec{V}_N & \vec{I}_N \end{bmatrix}^T = \vec{0} \tag{3.46}$$

Bloch's theorem (2.87) may be applied between each port n and $n + (N/2)$ as:

$$\begin{bmatrix} \vec{V}_n \\ \vec{I}_n \end{bmatrix} = \begin{bmatrix} \vec{V}_{(n+(N/2))} \\ -\vec{I}_{(n+(N/2))} \end{bmatrix} e^{-\gamma_n d_n} \tag{3.47}$$

in which γ_n is the phase shift observed between the two points in the unit cell, and d_n is the distance

between the points along the axis n, such that (3.46) may be expressed as:

$$\begin{bmatrix} [M_{11}] & [M_{12}] & \dots & [M_{1(N/2)}] & [M_{1(1+(N/2))}] & \dots & [M_{1N}] \\ [M_{21}] & [M_{22}] & \dots & [M_{2(N/2)}] & [M_{2(2+(N/2))}] & \dots & [M_{2N}] \\ \vdots & \vdots & \ddots & \vdots & \vdots & \ddots & \vdots \\ [M_{(N/2)1}] & [M_{(N/2)2}] & \dots & [M_{(N/2)(N/2)}] & [M_{(N/2)(2+(N/2))}] & \dots & [M_{(N/2)N}] \end{bmatrix} \cdot \begin{bmatrix} \vec{V}_1 & \vec{I}_1 & \vec{V}_2 & \vec{I}_2 & \dots & \vec{V}_{(N/2)} & \vec{I}_{(N/2)} & \vec{V}_1 e^{\gamma_1 d_1} & -\vec{I}_1 e^{\gamma_1 d_1} & \dots & \vec{V}_{(N/2)} e^{\gamma_{(N/2)} d_{(N/2)}} & -\vec{I}_{(N/2)} e^{\gamma_{(N/2)} d_{(N/2)}} \end{bmatrix}^T = \vec{0} \tag{3.48}$$

Generally, it is the case that a few of the phase shifts are specified while the remaining are to be solved. As such, the columns of $[M]$ are sorted so that the ports for which the phase shifts are specified are on the left-hand side, while the ports the phase shifts of which are to be solved are on the right-hand side (this sorted matrix is distinguished from the original as $[M_{sorted}]$). For example, taking the structure of Fig. 3.14, if the phase shifts along the first, second and fourth principle axis (corresponding to indices $n = 1$, $n = 2$, and $n = 4$) are to be solved while the remaining ($n = 3$) are specified, then sorting the columns of $[M]$ yields:

$$[M_{sorted}] \cdot \{\vec{V}, \vec{I}\}_{sorted} = \begin{bmatrix} [M_{13}] & [M_{17}] & [M_{11}] & [M_{12}] & [M_{14}] & [M_{15}] & [M_{16}] & [M_{18}] \\ [M_{23}] & [M_{27}] & [M_{21}] & [M_{22}] & [M_{24}] & [M_{25}] & [M_{26}] & [M_{28}] \\ [M_{33}] & [M_{37}] & [M_{31}] & [M_{32}] & [M_{34}] & [M_{35}] & [M_{36}] & [M_{38}] \\ [M_{43}] & [M_{47}] & [M_{41}] & [M_{42}] & [M_{44}] & [M_{45}] & [M_{46}] & [M_{48}] \\ [M_{53}] & [M_{57}] & [M_{51}] & [M_{52}] & [M_{54}] & [M_{55}] & [M_{56}] & [M_{58}] \\ [M_{63}] & [M_{67}] & [M_{61}] & [M_{62}] & [M_{64}] & [M_{65}] & [M_{66}] & [M_{68}] \\ [M_{73}] & [M_{77}] & [M_{71}] & [M_{72}] & [M_{74}] & [M_{75}] & [M_{76}] & [M_{78}] \\ [M_{83}] & [M_{87}] & [M_{81}] & [M_{82}] & [M_{84}] & [M_{85}] & [M_{86}] & [M_{88}] \end{bmatrix} \cdot \begin{bmatrix} \vec{V}_3 & \vec{I}_3 & \vec{V}_3 e^{\gamma_3 d_3} & -\vec{I}_3 e^{\gamma_3 d_3} & \vec{V}_1 & \vec{I}_1 & \vec{V}_2 & \vec{I}_2 & \vec{V}_4 & \vec{I}_4 & \vec{V}_1 e^{\gamma_1 d_1} & -\vec{I}_1 e^{\gamma_1 d_1} & \vec{V}_2 e^{\gamma_2 d_2} & -\vec{I}_2 e^{\gamma_2 d_2} & \vec{V}_4 e^{\gamma_4 d_4} & -\vec{I}_4 e^{\gamma_4 d_4} \end{bmatrix}^T = \vec{0} \tag{3.49}$$

Moreover, since some of the phase shifts are known ($\gamma_3 d_3$, in this example), the known exponential quantities may be integrated into each appropriate column of $[M_{sorted}]$, along with the negative signs on the current vectors. Then, leaving columns with two similar vectors, the columns corresponding to the

axes of the known phase shifts may simply be summed, such that:

$$
\begin{aligned}
&[M_{sorted,2}] \cdot \{\vec{V}, \vec{I}\}_{sorted,2} = \\
&\begin{bmatrix}
[M_{13}] + [M_{17}]\,[N]\,e^{\gamma_3 d_3} & [M_{11}] & [M_{12}] & [M_{14}] & [M_{15}] & [M_{16}] & [M_{18}] \\
[M_{23}] + [M_{27}]\,[N]\,e^{\gamma_3 d_3} & [M_{21}] & [M_{22}] & [M_{24}] & [M_{25}] & [M_{26}] & [M_{28}] \\
[M_{33}] + [M_{37}]\,[N]\,e^{\gamma_3 d_3} & [M_{31}] & [M_{32}] & [M_{34}] & [M_{35}] & [M_{36}] & [M_{38}] \\
[M_{43}] + [M_{17}]\,[N]\,e^{\gamma_3 d_3} & [M_{41}] & [M_{42}] & [M_{44}] & [M_{45}] & [M_{46}] & [M_{48}] \\
[M_{53}] + [M_{57}]\,[N]\,e^{\gamma_3 d_3} & [M_{51}] & [M_{52}] & [M_{54}] & [M_{55}] & [M_{56}] & [M_{58}] \\
[M_{63}] + [M_{67}]\,[N]\,e^{\gamma_3 d_3} & [M_{61}] & [M_{62}] & [M_{64}] & [M_{65}] & [M_{66}] & [M_{68}] \\
[M_{73}] + [M_{77}]\,[N]\,e^{\gamma_3 d_3} & [M_{71}] & [M_{72}] & [M_{74}] & [M_{75}] & [M_{76}] & [M_{78}] \\
[M_{83}] + [M_{87}]\,[N]\,e^{\gamma_3 d_3} & [M_{81}] & [M_{82}] & [M_{84}] & [M_{85}] & [M_{86}] & [M_{88}]
\end{bmatrix} \\
&\cdot \begin{bmatrix}
\vec{V}_3 & \vec{I}_3 & \vec{V}_1 & \vec{I}_1 & \vec{V}_2 & \vec{I}_2 & \vec{V}_4 & \vec{I}_4 & \vec{V}_1 e^{\gamma_1 d_1} & -\vec{I}_1 e^{\gamma_1 d_1} & \vec{V}_2 e^{\gamma_2 d_2} & -\vec{I}_2 e^{\gamma_2 d_2} & \vec{V}_4 e^{\gamma_4 d_4} & -\vec{I}_4 e^{\gamma_4 d_4}
\end{bmatrix}^T \\
&= \vec{0}
\end{aligned}
\tag{3.50}
$$

where $[N]$ is defined as a square matrix of arbitrary dimension (determined by its use), equal to identity but with the lower half of the matrix negated:

$$
[N] = \begin{bmatrix} [I] & [0] \\ [0] & -[I] \end{bmatrix} \tag{3.51}
$$

The matrix $[N]$ is used to accommodate the negative sign of the current vectors. The matrix $[M_{sorted,2}]$ of (3.50) may be expressed in a generalized, partitioned form as:

$$
\begin{bmatrix} [M_{spec1}] & [M_{solve1}] \\ [M_{spec2}] & [M_{solve2}] \end{bmatrix} \begin{bmatrix} \{\vec{V}, \vec{I}\}_{spec} \\ \{\vec{V}, \vec{I}\}_{solve} \end{bmatrix} = \vec{0} \tag{3.52}
$$

where $\vec{V}_{spec}$ and $\vec{I}_{spec}$ are the voltages and currents of the ports on which the phase shifts have been specified, and $\vec{V}_{solve}$ and $\vec{I}_{solve}$ are the voltages and currents of the ports that the phase shifts are being solved on:

$$
\{\vec{V}, \vec{I}\}_{spec} = \begin{bmatrix} \vec{V}_3 & \vec{I}_3 \end{bmatrix}^T \tag{3.53a}
$$

$$
\{\vec{V}, \vec{I}\}_{solve} = \begin{bmatrix} \vec{V}_1 & \vec{I}_1 & \vec{V}_2 & \vec{I}_2 & \vec{V}_4 & \vec{I}_4 & \vec{V}_1 e^{\gamma_1 d_1} & -\vec{I}_1 e^{\gamma_1 d_1} & \vec{V}_2 e^{\gamma_2 d_2} & -\vec{I}_2 e^{\gamma_2 d_2} & \vec{V}_4 e^{\gamma_4 d_4} & -\vec{I}_4 e^{\gamma_4 d_4} \end{bmatrix}^T \tag{3.53b}
$$

In order to properly partition the matrix $[M_{sorted,2}]$, it must first be diagonalized (as described in section 3.2.4) to ensure the invertibility of the partition $[M_{spec1}]$, which will be employed shortly. Of course, there is no guarantee that any arbitrary matrix is diagonalizable, however, since the matrix represents a network in which the various ports may be related to each other, it is assumed in this work that the networks investigated are not defective (i.e., contain no terminals independent of the rest), such that the matrices $[M]$ that represent their behavior are therefore diagonalizable:

The terminals of the networks investigated in this work are dependent on all the others, such that the matrices $[M]$ which describe the networks are always diagonalizable.

Assumption Set 6: Diagonalizable M-Parameters

Invoking Assumption Set 6, the diagonalization is accomplished through pre-multiplication by the inverse of some diagonalization matrix $[Q]$ to yield a diagonalized 1×2 aspect-ratio matrix $[R]$. Then,

$$[R] = [Q]^{-1}\,[M_{sorted,2}] = \begin{bmatrix} [R_{11}] & [R_{12}] & [R_{13}] & [R_{14}] & [R_{15}] & [R_{16}] & [R_{17}] \\ [R_{21}] & [R_{22}] & [R_{23}] & [R_{24}] & [R_{25}] & [R_{26}] & [R_{27}] \\ [R_{31}] & [R_{32}] & [R_{33}] & [R_{34}] & [R_{35}] & [R_{36}] & [R_{37}] \\ [R_{41}] & [R_{42}] & [R_{43}] & [R_{44}] & [R_{45}] & [R_{46}] & [R_{47}] \\ [R_{51}] & [R_{52}] & [R_{53}] & [R_{54}] & [R_{55}] & [R_{56}] & [R_{57}] \\ [R_{61}] & [R_{62}] & [R_{63}] & [R_{64}] & [R_{65}] & [R_{66}] & [R_{67}] \\ [R_{71}] & [R_{72}] & [R_{73}] & [R_{74}] & [R_{75}] & [R_{76}] & [R_{77}] \\ [R_{81}] & [R_{82}] & [R_{83}] & [R_{84}] & [R_{85}] & [R_{86}] & [R_{87}] \end{bmatrix} \tag{3.54}$$

several entries of which will be equal to [0] due to diagonalization. Partitioning $[R]$ horizontally and vertically into four sets, such that the square sub-matrix $[M_{spec1}]$ has dimensions of the size of $\vec{V}_{spec}+\vec{I}_{spec}$ gives:

$$[M_{spec1}] = \begin{bmatrix} [R_{11}] \end{bmatrix} \tag{3.55a}$$

$$[M_{solve1}] = \begin{bmatrix} [R_{12}] & [R_{13}] & [R_{14}] & [R_{15}] & [R_{16}] & [R_{17}] \end{bmatrix} \tag{3.55b}$$

$$[M_{spec2}] = \begin{bmatrix} [R_{21}] \\ [R_{31}] \\ [R_{41}] \\ [R_{51}] \\ [R_{61}] \\ [R_{71}] \\ [R_{81}] \end{bmatrix} \tag{3.55c}$$

$$[M_{solve2}] = \begin{bmatrix} [R_{22}] & [R_{23}] & [R_{24}] & [R_{25}] & [R_{26}] & [R_{27}] \\ [R_{32}] & [R_{33}] & [R_{34}] & [R_{35}] & [R_{36}] & [R_{37}] \\ [R_{42}] & [R_{43}] & [R_{44}] & [R_{45}] & [R_{46}] & [R_{47}] \\ [R_{52}] & [R_{53}] & [R_{54}] & [R_{55}] & [R_{56}] & [R_{57}] \\ [R_{62}] & [R_{63}] & [R_{64}] & [R_{65}] & [R_{66}] & [R_{67}] \\ [R_{72}] & [R_{73}] & [R_{74}] & [R_{75}] & [R_{76}] & [R_{77}] \\ [R_{82}] & [R_{83}] & [R_{84}] & [R_{85}] & [R_{86}] & [R_{87}] \end{bmatrix} \tag{3.55d}$$

Inserting the lower set (subscript 2) of equations in (3.52) into the upper (subscript 1) yields the Schur

complement [408, 409]:

$$\Big([M_{solve2}] - [M_{spec2}]\,[M_{spec1}]^{-1}\,[M_{solve1}]\Big)\,\{\vec{V},\vec{I}\}_{solve} = [M_{reduced}]\,\{\vec{V},\vec{I}\}_{solve} = \vec{0} \tag{3.56}$$

Re-arranging the columns of $[M_{reduced}]$ such that each of the voltages and currents of $\{\vec{V},\vec{I}\}_{solve}$ are grouped into two sets – with and without the phase shifts – gives:

$$\begin{bmatrix} [M_{reduced1}] & | & [M_{reduced2}] \end{bmatrix} \cdot \begin{bmatrix} \vec{V}_1 & \vec{V}_2 & \vec{V}_4 & \vec{I}_1 & \vec{I}_2 & \vec{I}_4 & \vec{V}_1 e^{\gamma_1 d_1} & \vec{V}_2 e^{\gamma_2 d_2} & \vec{V}_4 e^{\gamma_4 d_4} & -\vec{I}_1 e^{\gamma_1 d_1} & -\vec{I}_2 e^{\gamma_2 d_2} & -\vec{I}_4 e^{\gamma_4 d_4} \end{bmatrix}^T = \vec{0} \tag{3.57}$$

And re-arranged to:

$$[M_{reduced1}] \begin{bmatrix} \vec{V}_1 \\ \vec{V}_2 \\ \vec{V}_4 \\ \vec{I}_1 \\ \vec{I}_2 \\ \vec{I}_4 \end{bmatrix} = -\,[M_{reduced2}]\,[N] \begin{bmatrix} \vec{V}_1 e^{\gamma_1 d_1} \\ \vec{V}_2 e^{\gamma_2 d_2} \\ \vec{V}_4 e^{\gamma_4 d_4} \\ \vec{I}_1 e^{\gamma_1 d_1} \\ \vec{I}_2 e^{\gamma_2 d_2} \\ \vec{I}_4 e^{\gamma_4 d_4} \end{bmatrix} \tag{3.58}$$

At this point, the unknown phases on the various branches are related to the voltages and currents across the axis of the unit cell. In the case of Brillouin zone contours traversing multiple axes, it is typically the case that:

$$\gamma_1 d_1 = \gamma_2 d_2 = \gamma_4 d_4 = \gamma_B d_{eff} \tag{3.59}$$

where γ_B is the propagation constant of the Bloch wave, and d_{eff} is the effective period of the Bloch wave – which will depend on a combination of the unit-cell's geometry, as well as its direction of travel through the cell. In this case, (3.58) reduces to:

$$[M_{reduced1}] \begin{bmatrix} \vec{V}_1 \\ \vec{V}_2 \\ \vec{V}_4 \\ \vec{I}_1 \\ \vec{I}_2 \\ \vec{I}_4 \end{bmatrix} = -\,[M_{reduced2}]\,[N] \begin{bmatrix} \vec{V}_1 \\ \vec{V}_2 \\ \vec{V}_4 \\ \vec{I}_1 \\ \vec{I}_2 \\ \vec{I}_4 \end{bmatrix} e^{\gamma_B d_{eff}} \tag{3.60}$$

which may be solved using a generalized eigensystem decomposition process.

3.4 Generalized Network Concatenation

While the previous section 3.3 assumes that the unit-cell's network is given as some matrix $[M]$, it is often the case that the equations describing the network are unknown – since the network is itself composed of various combinations of smaller, more simple elements and interconnections. While traditional methods exist for compiling descriptions of networks into a single, large matrix, these methods are often computa-

tionally inefficient due to the fact that the matrices are often eigendecomposed – a very expensive process. This section proposes a method of concatenating the matrices representing the internal components of a unit-cell network, such that the resulting matrix $[M]$ is only a function of the voltage and current variables on the outer ports of the network – thereby allowing for a much more rapid eigendecomposition. A "trivial" matrix assembly process based on solving determinants of a global network matrix is examined, and then the proposed process is introduced, and derived. Both processes are then quantified via the same example network – from which the comparable gains in computational efficiency may be readily obtained.

3.4.1 Example Unit Cell

The network shown in Fig. 3.15 is used in this section to illustrate a comparison between the trivial dispersion analysis process and the proposed process of this work. The network is composed of various simple components, and contains a nodal region indicated with the dashed curves. It is an anisotropic network with two axes (and hence, four ports) along the horizontal and vertical directions. The ports along the vertical axis contain three non-reference conductors, while the ports along the horizontal axis have two non-reference conductors – all ports are assumed to share a common reference conductor (not shown in the figure). The interconnection in the central node may be described with the 10×20 M-Parameter matrix:

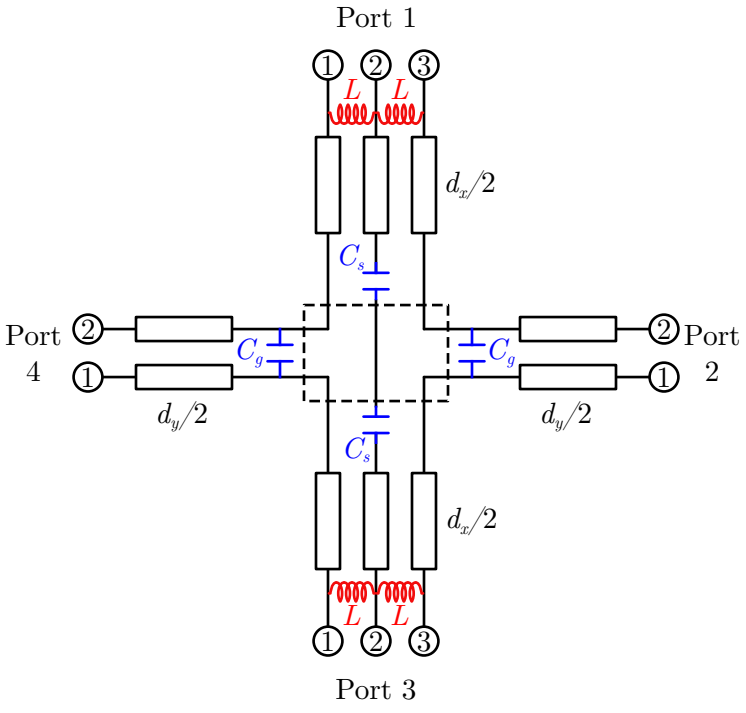

Figure 3.15: Example circuit model used in section 3.4. The unit-cell is composed of various components, interconnected by the nodal region indicated with the dashed curves. The ports all share a common reference (not shown).

$$[M_{Node}] =$$

$$\begin{array}{c} \begin{matrix} V_1^1 & V_1^2 & V_1^3 & I_1^1 & I_1^2 & I_1^3 & V_2^1 & V_2^2 & I_2^1 & I_2^2 & V_3^1 & V_3^2 & V_3^3 & I_3^1 & I_3^2 & I_3^3 & V_4^1 & V_4^2 & I_4^1 & I_4^2 \end{matrix} \\ \left[\begin{array}{cccccccccccccccccccc} 1 & 0 & 0 & 0 & 0 & 0 & 0 & 0 & 0 & 0 & 0 & 0 & 0 & 0 & 0 & 0 & 0 & -1 & 0 & 0 \\ 0 & 0 & 0 & 1 & 0 & 0 & 0 & 0 & 0 & 0 & 0 & 0 & 0 & 0 & 0 & 0 & 0 & 0 & 0 & 1 \\ 0 & 1 & 0 & 0 & 0 & 0 & 0 & 0 & 0 & 0 & 0 & -1 & 0 & 0 & 0 & 0 & 0 & 0 & 0 & 0 \\ 0 & 0 & 0 & 0 & 1 & 0 & 0 & 0 & 0 & 0 & 0 & 0 & 0 & 0 & 1 & 0 & 0 & 0 & 0 & 0 \\ 0 & 0 & 1 & 0 & 0 & 0 & 0 & -1 & 0 & 0 & 0 & 0 & 0 & 0 & 0 & 0 & 0 & 0 & 0 & 0 \\ 0 & 0 & 0 & 0 & 0 & 1 & 0 & 0 & 0 & 1 & 0 & 0 & 0 & 0 & 0 & 0 & 0 & 0 & 0 & 0 \\ 0 & 0 & 0 & 0 & 0 & 0 & 1 & 0 & 0 & 0 & 0 & 0 & -1 & 0 & 0 & 0 & 0 & 0 & 0 & 0 \\ 0 & 0 & 0 & 0 & 0 & 0 & 0 & 0 & 1 & 0 & 0 & 0 & 0 & 0 & 0 & 1 & 0 & 0 & 0 & 0 \\ 0 & 0 & 0 & 0 & 0 & 0 & 0 & 0 & 0 & 0 & 1 & 0 & 0 & 0 & 0 & 0 & -1 & 0 & 0 & 0 \\ 0 & 0 & 0 & 0 & 0 & 0 & 0 & 0 & 0 & 0 & 0 & 0 & 0 & 1 & 0 & 0 & 0 & 0 & 1 & 0 \end{array}\right] \end{array} \tag{3.61}$$

which is derived by equating the voltages and currents on the either end of each conductor. The remaining components may be trivially derived, being simple two-port networks of inductors, capacitors, or TLs.

3.4.2 Trivial Network Solution Process

Although the investigation of multidimensional, multimodal, periodic TL networks is historically lacking, there exists an intuitive solution process which will be referred to in this work as the *trivial* process. The process determines the dispersion properties of a network of interconnected components by forgoing the derivation given in section 3.3. Rather than forming the problem into that of a typical eigensystem, a global matrix describing the behavior of each component – as well as the behavior of each interconnection and boundary condition – is assembled, and its determinant solved. Valid solutions at which the networks operates are then given by a determinant of zero. In practical implementation, frequency is swept and the zero-crossing points are returned as solutions at which the network satisfies the boundary conditions.

The example network of Fig. 3.15 is investigated in a component-by-component manner, and the resulting matrix $[M]$ for each component is inserted in a global $[M]$ matrix. The connections between each network are then input, and then finally the boundary conditions in terms of Bloch's theorem are input, for certain selected phase angles. The matrix is assembled at an assumed frequency, having final dimensions (and necessarily being square, in order to possess a unique solution) of 204×204. In block form, the global matrix then has the layout given in (3.62).

The determinant of $[M_{Global}]$ is then taken. Since the matrix represents a set of homogenous linear equations, at frequencies at which the determinant is zero, a non-trivial solution exists [319, 320] – indicating that the input Bloch phase shifts support a mode at the given frequency. Each Bloch phase shift may then be swept over the desired range(s) to produce a solution space.

However, this method possesses several considerable drawbacks. The solution via this method does not yield a set of voltages or currents, so no information is gained other than the existence of some unknown

$$[M_{Global}] =$$

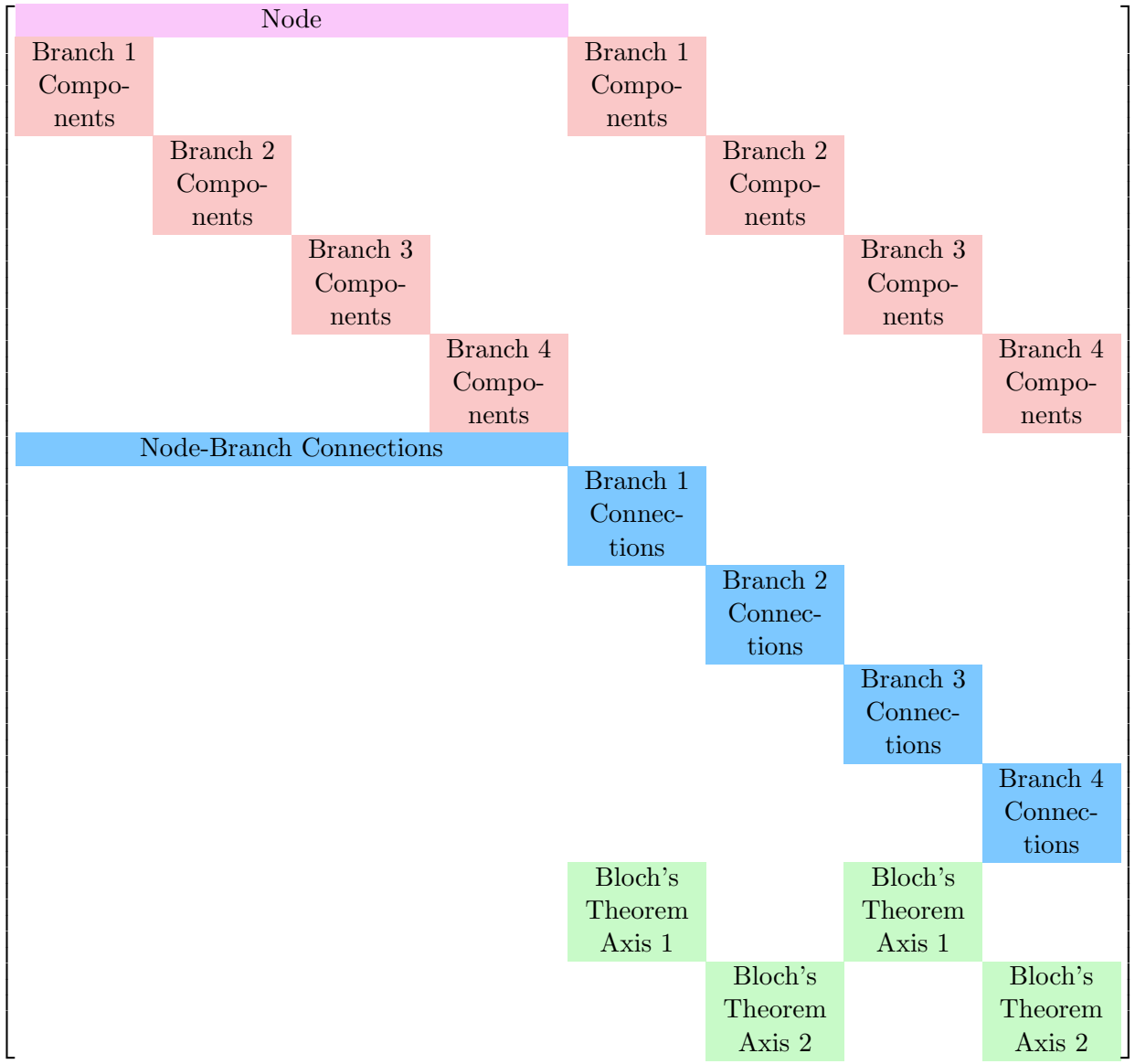
Node
Branch 1 Components
Branch 1 Components
Branch 2 Components
Branch 2 Components
Branch 3 Components
Branch 3 Components
Branch 4 Components
Branch 4 Components
Node-Branch Connections
Branch 1 Connections
Branch 2 Connections
Branch 3 Connections
Branch 4 Connections
Bloch's Theorem Axis 1
Bloch's Theorem Axis 1
Bloch's Theorem Axis 2
Bloch's Theorem Axis 2

(3.62)

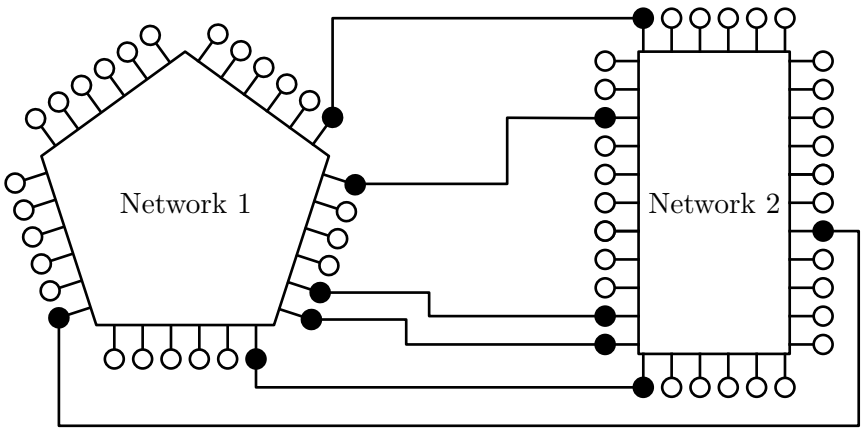

Figure 3.16: Figurative circuit used to illustrate generalized network concatenation. The two networks have various terminals interconnected as illustrated. The process determines the matrix $[M]$ corresponding to the the voltage and current quantities of the resulting unconnected terminals, knowing only the M-Parameters of the two individual networks, and the interconnections between them.

mode given the input conditions. No other information may be determined from the system, e.g., the properties of these supported modes. The computation of the determinants of such large matrices is very time-consuming, since the number of computations scales exponentially with the size of the matrix ($O\left(n^3\right)$ for Gaussian elimination and $O\left(n!\right)$ for cofactor expansion [410–412]). In comparison, the computational time for matrix multiplication is at most $O\left(n^3\right)$ and possibly as low as $O\left(n^{2.38}\right)$ – for a larger number of much smaller matrices [413–415].

3.4.3 Formulation

In order to overcome these many challenges, it is instructive to look back to existing solutions. The solution process with which to determine modal properties of two-port networks – as described in chapter 2 – directly solves the propagation constants from a given network, from which other modal properties may also be derived. The matrix representations of these networks are assembled from their sub-networks' matrix representations; when $ABCD$-Parameters are used this process is known as *concatenation*, in which two matrices representing connected networks are combined to form a new, third matrix or roughly the same size, but with a loss of information as to the voltages and currents on the connected terminals [391]. A similar process is desired in order to effect the dispersion analysis of section 3.3, but generalized to the multiport, multidimensional case: generalized network concatenation.

Referring to the figurative depiction of such a scenario shown in Fig. 3.16, it may be observed that there are two networks which have various terminals connected to each other. It is the goal of generalized network concatenation to determine the resulting matrix $[M]$ corresponding to the voltage and current quantities of the total remaining unconnected terminals of both networks, given the M-Parameters of each network – specified as $[M_1]$ and $[M_2]$ – as well as the details of the interconnections between the two

networks. That is, the networks are specified as:

$$[M_1] \cdot \left[\vec{V}_1(N_1) \;\; \vec{I}_1(N_1) \;\; \vec{V}_2(N_1) \;\; \vec{I}_2(N_1) \;\; \ldots \;\; \vec{V}_n(N_1) \;\; \vec{I}_n(N_1) \right]^T = \vec{0} \tag{3.63a}$$

$$[M_2] \cdot \left[\vec{V}_1(N_2) \;\; \vec{I}_1(N_2) \;\; \vec{V}_2(N_2) \;\; \vec{I}_2(N_2) \;\; \ldots \;\; \vec{V}_n(N_2) \;\; \vec{I}_n(N_2) \right]^T = \vec{0} \tag{3.63b}$$

where (N_1) and (N_2) indicate the voltage and current quantities of Network 1 and Network 2, respectively. Next, the matrices and vectors are sorted and partitioned into two groups: those corresponding to the voltages and currents at the connected terminals, and those at the unconnected terminals. These will be indicated with the subscripts c and u, respectively.

$$\begin{aligned} &[M_1] \cdot \left[\vec{V}_1(N_1) \;\; \vec{I}_1(N_1) \;\; \vec{V}_2(N_1) \;\; \vec{I}_2(N_1) \;\; \ldots \;\; \vec{V}_n(N_1) \;\; \vec{I}_n(N_1) \right]^T = \\ &\quad [M_{1c}] \cdot \left[\vec{V}_{1c}(N_1) \;\; \vec{I}_{1c}(N_1) \;\; \ldots \;\; \vec{V}_{nc}(N_1) \;\; \vec{I}_{nc}(N_1) \;\; \vec{0} \;\; \ldots \;\; \vec{0} \right]^T + \\ &\quad [M_{1u}] \cdot \left[\vec{0} \;\; \ldots \;\; \vec{0} \;\; \vec{V}_{1u}(N_1) \;\; \vec{I}_{1u}(N_1) \;\; \ldots \;\; \vec{V}_{nu}(N_1) \;\; \vec{I}_{nu}(N_1) \right]^T = \vec{0} \end{aligned} \tag{3.64a}$$

$$\begin{aligned} &[M_2] \cdot \left[\vec{V}_1(N_2) \;\; \vec{I}_1(N_2) \;\; \vec{V}_2(N_2) \;\; \vec{I}_2(N_2) \;\; \ldots \;\; \vec{V}_n(N_2) \;\; \vec{I}_n(N_2) \right]^T = \\ &\quad [M_{2c}] \cdot \left[\vec{V}_{1c}(N_2) \;\; \vec{I}_{1c}(N_2) \;\; \ldots \;\; \vec{V}_{nc}(N_2) \;\; \vec{I}_{nc}(N_2) \;\; \vec{0} \;\; \ldots \;\; \vec{0} \right]^T + \\ &\quad [M_{2u}] \cdot \left[\vec{0} \;\; \ldots \;\; \vec{0} \;\; \vec{V}_{1u}(N_2) \;\; \vec{I}_{1u}(N_2) \;\; \ldots \;\; \vec{V}_{nu}(N_2) \;\; \vec{I}_{nu}(N_2) \right]^T = \vec{0} \end{aligned} \tag{3.64b}$$

Representing the sorted vectors as:

$$\left[\vec{V}_c^1 \;\; \vec{I}_c^1 \right]^T = \left[\vec{V}_{1c}(N_1) \;\; \vec{I}_{1c}(N_1) \;\; \ldots \;\; \vec{V}_{nc}(N_1) \;\; \vec{I}_{nc}(N_1) \;\; \vec{0} \;\; \ldots \;\; \vec{0} \right]^T \tag{3.65a}$$

$$\left[\vec{V}_u^1 \;\; \vec{I}_u^1 \right]^T = \left[\vec{0} \;\; \ldots \;\; \vec{0} \;\; \vec{V}_{1u}(N_1) \;\; \vec{I}_{1u}(N_1) \;\; \ldots \;\; \vec{V}_{nu}(N_1) \;\; \vec{I}_{nu}(N_1) \right]^T \tag{3.65b}$$

$$\left[\vec{V}_c^2 \;\; \vec{I}_c^2 \right]^T = \left[\vec{V}_{1c}(N_2) \;\; \vec{I}_{1c}(N_2) \;\; \ldots \;\; \vec{V}_{nc}(N_2) \;\; \vec{I}_{nc}(N_2) \;\; \vec{0} \;\; \ldots \;\; \vec{0} \right]^T \tag{3.65c}$$

$$\left[\vec{V}_u^2 \;\; \vec{I}_u^2 \right]^T = \left[\vec{0} \;\; \ldots \;\; \vec{0} \;\; \vec{V}_{1u}(N_2) \;\; \vec{I}_{1u}(N_2) \;\; \ldots \;\; \vec{V}_{nu}(N_2) \;\; \vec{I}_{nu}(N_2) \right]^T \tag{3.65d}$$

Then, (3.64) becomes:

$$[M_{1c}] \cdot \left[\vec{V}_c^1 \;\; \vec{I}_c^1 \right]^T + [M_{1u}] \cdot \left[\vec{V}_u^1 \;\; \vec{I}_u^1 \right]^T = \vec{0} \tag{3.66a}$$

$$[M_{2c}] \cdot \left[\vec{V}_c^2 \;\; \vec{I}_c^2 \right]^T + [M_{2u}] \cdot \left[\vec{V}_u^2 \;\; \vec{I}_u^2 \right]^T = \vec{0} \tag{3.66b}$$

It may be noted that due to the connections, $\left[\vec{V}_c^1 \vec{I}_c^1\right]^T = \left[\vec{V}_c^2 \;\; -\vec{I}_c^2\right]^T \equiv \left[\vec{V}_c \vec{I}_c\right]^T$. At this point, the two matrices are be combined into one supermatrix, such that:

$$\begin{bmatrix} [M_{1c}] & [M_{1u}] & [0] \\ [N]\,[M_{2c}] & [0] & [M_{2u}] \end{bmatrix} \cdot \left[\vec{V}_c \;\; \vec{I}_c \;\; \vec{V}_u^1 \;\; \vec{I}_u^1 \;\; \vec{V}_u^2 \;\; \vec{I}_u^2 \right]^T = \vec{0} \tag{3.67}$$

Then, the matrix is partitioned such that:

$$\begin{bmatrix} [M_A] & [M_B] \\ [M_C] & [M_D] \end{bmatrix} \cdot \begin{bmatrix} \vec{V}_c & \vec{I}_c & \vec{V}_u^1 & \vec{I}_u^1 & \vec{V}_u^2 & \vec{I}_u^2 \end{bmatrix}^T = \vec{0} \tag{3.68}$$

The partition $[M_A]$ is not necessarily $[M_{1c}]$, being a square matrix of size $dim\left(\vec{V}_c\right) + dim\left(\vec{I}_c\right)$. The rest of the partitions are sized appropriately based on this value. Then, the matrix should be diagonalized (as discussed in section 3.2.4), to yield:

$$\begin{bmatrix} [R_A] & [R_B] \\ [R_C] & [R_D] \end{bmatrix} \cdot \begin{bmatrix} \vec{V}_c & \vec{I}_c & \vec{V}_u^1 & \vec{I}_u^1 & \vec{V}_u^2 & \vec{I}_u^2 \end{bmatrix}^T = \vec{0} \tag{3.69}$$

Taking the Schur complement yields the solution:

$$\Big([R_D] - [R_C]\,[R_A]^{-1}\,[R_B]\Big) \cdot \begin{bmatrix} \vec{V}_u^1 \\ \vec{I}_u^1 \\ \vec{V}_u^2 \\ \vec{I}_u^2 \end{bmatrix} = \vec{0} \tag{3.70}$$

where $\Big([R_D] - [R_C]\,[R_A]^{-1}\,[R_B]\Big)$ is the resulting matrix $[M]$ of the concatenated system.

3.4.4 Quantitative Comparison

Having examined two processes with which to compute the dispersive properties of general MTL-based unit cells (the "trivial" process and the proposed process), they may now be compared. Comparison will be achieved by running the proposed methods on the same machine, and comparing the *CPU time* (that is, the time the machine spends executing the process) that the computation of a dispersion digram requires. The following data presented in this section were obtained by performing matrix multiplication using the open-source C++ linear algebra library *Eigen* [416], which was used for its ability to perform generalized eigendecomposition on complex matrices using 128-bit floating point precision (such precision may alleviate some errors when working with complex eigensystems, see [417], also discussion and associated references in [418]).

The example network of Fig. 3.15 is solved with the following parameters: $d_x = 20$ mm, $d_y = 30$ mm, $L = 10$ nH, $C_s = 1.0$ GF, $C_g = 1.0$ pF. The MTL segments have their properties synthesized via the mode definitions:

$$[T_I]_x = \begin{bmatrix} 0.33 & -1 & 0.45 \\ 0.34 & 0 & -1 \\ 0.33 & 1 & 0.45 \end{bmatrix} \tag{3.71a}$$

$$[T_I]_y = \begin{bmatrix} 0.5 & 1 \\ 0.5 & -1 \end{bmatrix} \tag{3.71b}$$

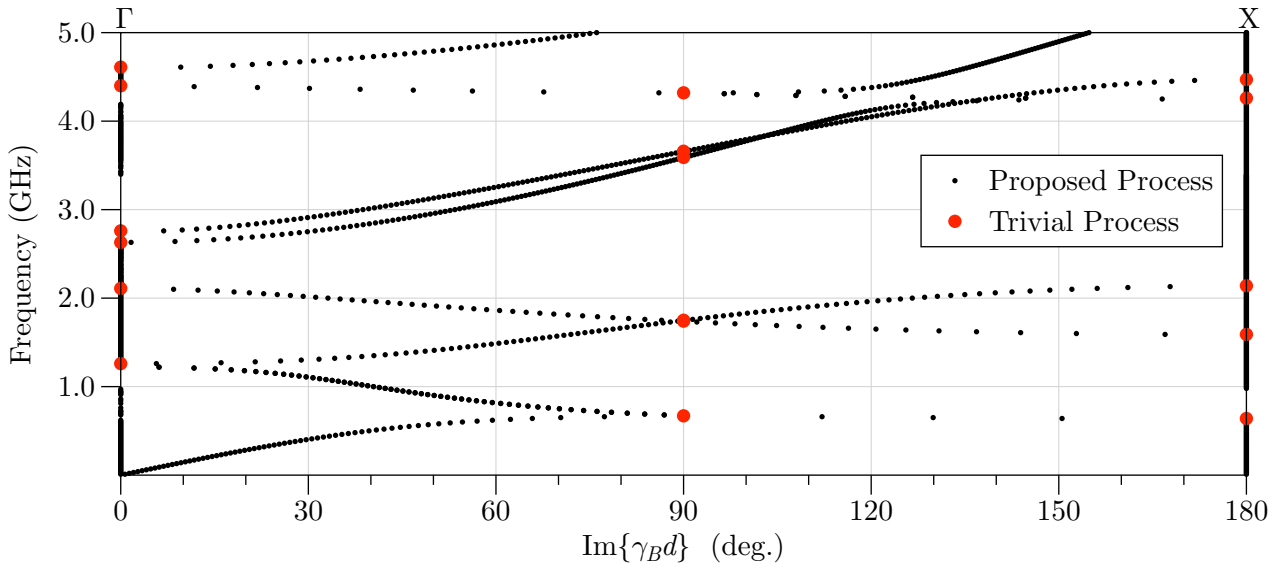

Figure 3.17: Results of computing the Γ-X portion of the dispersion diagram of the network shown in Fig. 3.15. The small black dots are the results of using the proposed process, while the larger red dots indicate the results of the trivial process. Both are in good agreement, but the results of the trivial process took much longer to compute in total than all of the results of the proposed process (see Table 3.2).

and modal properties:

$$[\gamma_M]_x = j \begin{bmatrix} 32.73 & 0 & 0 \\ 0 & 30.425 & 0 \\ 0 & 0 & 29.651 \end{bmatrix} rad/m \tag{3.72a}$$

$$[\gamma_M]_y = j \begin{bmatrix} 32.101 & 0 \\ 0 & 29.902 \end{bmatrix} rad/m \tag{3.72b}$$

$$[Z_{cM}]_x = \begin{bmatrix} 45.081 & 0 & 0 \\ 0 & 187.86 & 0 \\ 0 & 0 & 104.91 \end{bmatrix} \Omega \tag{3.72c}$$

$$[Z_{cM}]_y = \begin{bmatrix} 61.768 & 0 \\ 0 & 158.17 \end{bmatrix} \Omega \tag{3.72d}$$

The Γ-X portion of the dispersion diagram is computed using the trivial and proposed methods and shown in Fig. 3.17, where both methods have been solved using a frequency step of 10 MHz, minimum frequency of 10 MHz, and maximum frequency of 5 GHz. The results of the proposed process are given with the black dots, and the results of the trivial process (computed only at the dispersion points of 0°, 90°, and 180°) are given by the red dots. Using the "profiler" tool in Xcode Version 11.3.1 (build 11C504) [419] using a macOS 10.14.6 operating system on a 3.2 GHz Quad-Core Intel Xeon processor, the CPU time of the given processes are captured and reported over their lifetimes.

The resulting data are in excellent agreement, where only three different phase angles have been obtained for the trivial process due to the lengthy simulation times involved. Of course, the trivial process

Table 3.2: Comparisons of Computational Aspects of the Trivial Process Versus the Proposed Process

	Trivial Process	**Proposed Process**
Total CPU Time for 500 Frequency Points	49.18 s	9.20 s
Estimated Time to Solve Dispersion Plot (1° Resolution)	8852.40 s	9.20 s
Total Memory Used for 500 Frequency Points	18.06 MiB	27.48 MiB

requires examination of both frequency and phase points to produce results, whereas the proposed process yields the phase angles while requiring an input frequency only: this is a major advantage of the proposed process. Additionally, the trivial process would become exponential more lengthy if the real part of the Bloch propagation constants were being determined as well – whereas the proposed process returns it along with the imaginary part – as well as others previously mentioned.

The CPU times for computation of all the frequency points in the specified range (i.e., 500 points) are given in Table 3.2, which for the trivial process only solves a few frequency points at one phase angle, while in the case of proposed process, the complex Bloch propagation constants for all three modes are solved. Multiplying the time result of the trivial process for one phase angle by 180 to estimate the time it would take to compute the entire Γ-X Brillouin zone over this frequency range (as done in the Table's second row) allows comparing the two processes more directly, since the entire dispersion diagram is solved in both cases (although the trivial process does not find the real components of the Bloch propagation constants). Finally, the total memory used to solve 500 frequency points are given in the bottom row; the proposed process does use roughly 50% more memory than the trivial method (as it is constantly creating and releasing smaller matrices throughout the concatenation process, rather than populating one larger matrix as the trivial method does), but again, this is for all phase angles for the proposed process, and only one phase angle for the trivial process.

In summary, this process demonstrates that the proposed dispersion analysis process of section 3.3 in combination with the generalized network concatenation process proposed in this section is quantitatively numerically more efficient at solving the dispersive properties of generalized network-based unit cells than the baseline, zeroth-order "trivial" process – by nearly a factor of one thousand.

Chapter 4

Applications

Having developed an understanding and rigorous analytical framework for analyzing the Bloch modes supported by multidimensional MTL-MTMs, attention may be turned to various applications of this work. To begin, section 4.1 investigates the use of one-dimensional bandgap structures in developing novel devices with enhanced functionalities. Section 4.2 investigates modelling a canonical 2D EBG with an intersection of 1D MTM-EBG unit cells.

4.1 Novel One-Dimensional MTM-EBG-Based Devices

Some of the ideas, figures, and data presented in this section have been published [173, 176, 420]. In addition to this author, Dr. Ashwin Iyer, Mr. Braden Smyth, and Mr. Jacob Brown (as co-authors of some of these works) contributed to the ideas and explanations that will be presented.

4.1.1 Modulating Bandgap Size with Capacitor Placement

Early on in the study of the MTM-EBG, its use as a system with multiple series capacitors in its CPW ground and strip conductors was investigated [381]. Further investigations has revealed that in the common configuration with series loading capacitors in the CPW ground conductors only (C_g, as shown

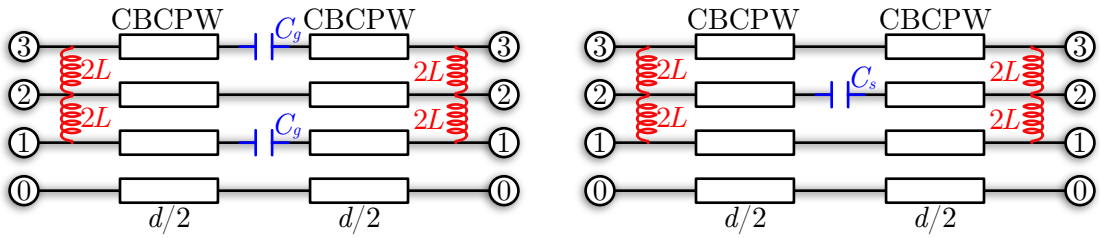

Figure 4.1: a) Example circuit model of the MTM-EBG, with series loading capacitor C_g in the CPW ground conductors, and b) Example circuit model of the MTM-EBG, with series loading capacitor C_s in the CPW strip conductor. Figures adapted from [176].

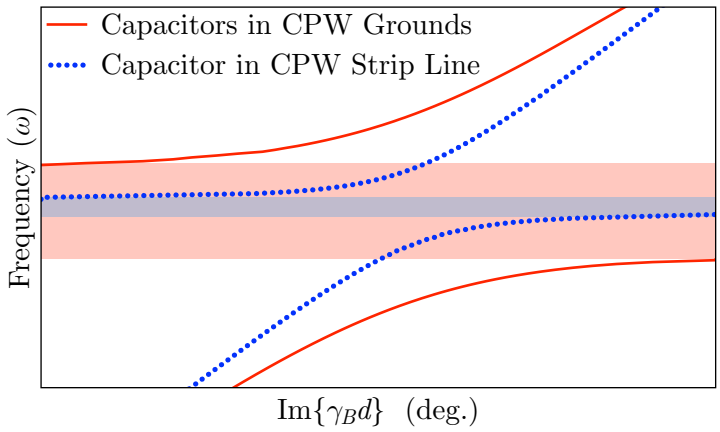

Figure 4.2: Example dispersion diagram, where the curves result from placing the MTM-EBG's loading capacitors in the CPW ground conductors (red solid curves) and the same value of parallel capacitance in the CPW strip conductor instead (blue dotted curves). Figure adapted from [176].

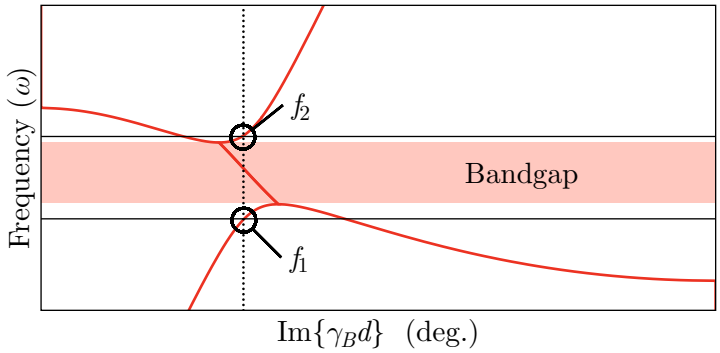

Figure 4.3: Example dispersion diagram, exhibiting a bandgap (highlighted) caused by the coupling of two contra-directed modes. Figure adapted from [176].

in Fig. 4.1a) does not – contrary to oversimplified intuition – possess the same dispersive properties as loading the CPW strip conductor with a series capacitance (C_s, as shown in Fig. 4.1b) with a value of $2C_g$. Rather, as shown in the exemplary dispersion diagram of Fig. 4.2, the case with the series loading capacitance in the CPW strip exhibits a much smaller bandgap than the case with the series loading capacitance in the CPW grounds.

This behavior may be used to select between a relatively wide or small bandgap with otherwise minimal changes to the EBG, as used in the following subsections.

4.1.2 Effecting Dual-Band Responses with Bandgap Phenomena

Consider the dispersion diagram shown in Fig. 4.3, in which a bandgap is highlighted. The bandgap in this case is caused by the phase-matching and mutual coupling of two contra-directed modes, as studied in section 2.2. Due to the specific shape of the dispersion curves on both sides of the bandgap, the curves pass through the same phase angle at two different frequencies, as indicated in the figure by f_1 and f_2.

Table 4.1: Geometrical parameters of the two MTM-EBGs used in the dual-band quadrature hybrid coupler (reference Fig. 4.4).

Parameter	**50 Ω Design**	**35 Ω Design**
Length d	18.8 mm	18.6 mm
Width w	1.3 mm	2.1 mm
CPW strip width s	0.4 mm	0.4 mm
CPW gap width g	0.2 mm	0.6 mm
Strip inductor width l	0.1 mm	0.1 mm
Interdigitated capacitor length c	11.6 mm	9.8 mm
Number of interdigitated capacitor fingers N_f	3	3
Interdigitated capacitor finger width/spacing f	0.1 mm	0.1 mm

By using this particular phenomenon of EBGs, devices which rely on set phase shifts for their operation (e.g., various couplers [391]) may be augmented with dual-band functionality, simply by replacing the traditional TL section which provides this phase shift, with a purposefully designed EBG.

Of course, by nature of the modes in the vicinity of the bandgap, one or both of the operating bands will generally be dispersive – i.e., possessing a substantial change in phase velocity and/or Bloch impedance with frequency, and therefore, a more narrow-band performance than the canonical, low-dispersion TL sections. This appears to be a design tradeoff of the proposed technique.

4.1.3 A Dual-Band Quadrature Hybrid Coupler for GPS Applications

Using the previously introduced concepts, a dual-band quadrature hybrid coupler is introduced, designed to operate at the relatively closely-spaced frequencies of Global Positioning System (GPS) L1 and L2 (1.575 GHz and 1.228 GHz, respectively [421,422]). Unlike other proposed dual-band quadrature hybrids [423–432] the dual-band response of this coupler is effected by simply removing portions of the copper out of the canonical coupler's existing MS lines, meaning that the overall footprint of the device is left nearly untouched while giving the coupler additional performance.

Both branches of the canonical coupler (which possesses 50 Ω and 35 Ω MS-mode impedances) are implemented using similar topologies, shown in Fig. 4.4, in which the series loading capacitance is placed in the CPW strip conductor, and implemented as an interdigitated capacitor. The two MTM-EBG variants are designed to provide their respective Bloch impedance values, while both presenting a phase shift of 90° at the two operating frequencies. These design dimensions – using a 1.254 mm Rogers RO-3010 substrate [433] with 35 μm copper cladding – are given in Table 4.1. A layout of the coupler, fed with 50 Ω MSs, is shown in Fig. 4.5, where one of the 35 Ω MTM-EBGs is detailed. The various geometric details of the coupler are: coupler width $W = 23.56$ mm, coupler length $D = 19.60$ mm, feed line spacing $S = 20.50$ mm, and feed line width $M = 1.40$ mm.

The two operating bands are selected as follows: the lower band is set by the length of the MTM-EBG,

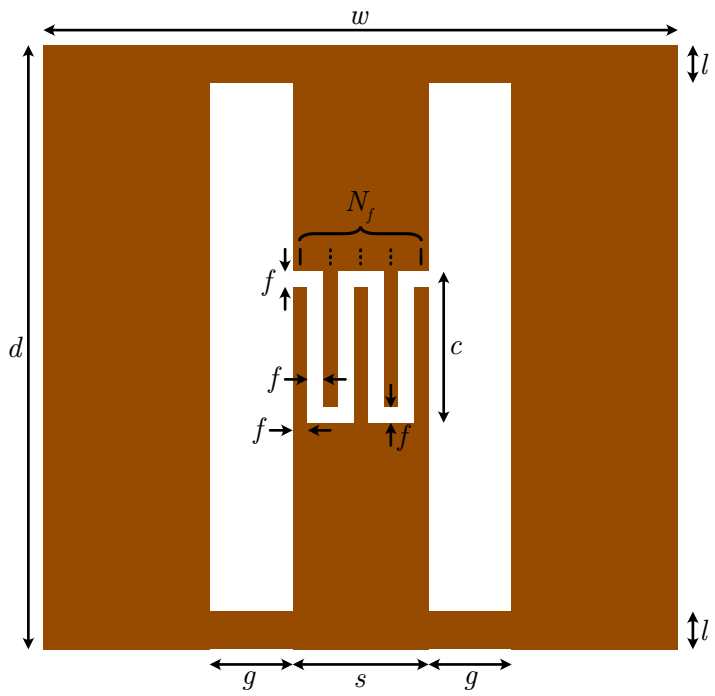

Figure 4.4: Layout of the upper-layer conductors of an MTM-EBG (conductor backing not shown), in which the loading capacitance is placed in series with the CPW strip conductor, and implemented as an interdigitated capacitor.

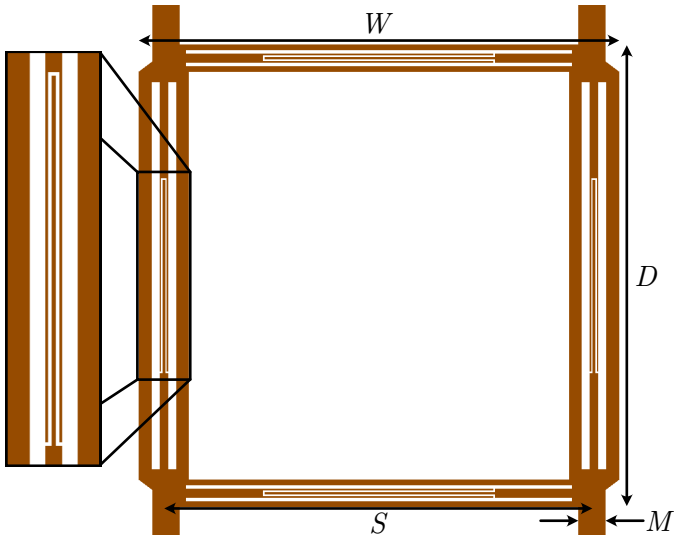

Figure 4.5: Layout of the upper-layer conductors of the proposed dual-band coupler (conductor backing not shown), in which MTM-EBG unit cells have been inserted into the traditional MS lines of the canonical coupler. Figure adapted from [176].

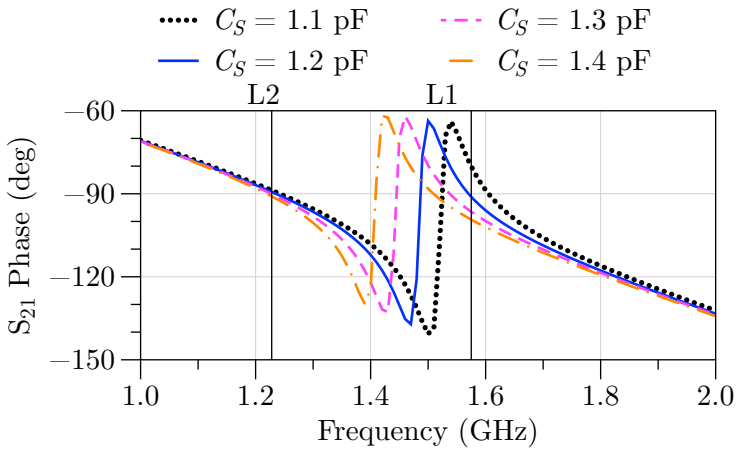

Figure 4.6: Simulated phase of S_{21} of the 50-Ω MTM-EBG with multiple values of loading capacitance C_s. Figure adapted from [176].

for which the MS-like mode is nearly non-dispersive. Then, the capacitance value is swept until the upper frequency's phase shift over the length of the cell is the same as the lower frequency's. The phase shift varies relatively linearly with capacitance, as indicated in Fig. 4.6. The Bloch impedance of the MS-like mode is controlled primarily by the total width of the CPW w. The final tuned scattering parameters of the two MTM-EBGs (referenced, of course, to differing impedances) are shown in Fig. 4.7 (as determined using HFSS), where it is observed that the MTM-EBGs produce 90° of phase with minimal losses at both frequencies.

The coupler was fabricated using an LPKF Laser & Electronics AG Protolaser U3 laser milling machine [434]; the resulting device is shown in Fig. 4.9 with the SMA connectors attached. The scattering parameters of the device were obtained with an Agilent PNA-X N5244A [435], and compared with those obtained by HFSS in Fig. 4.8 (in which simulation data is given by the red solid curves, and experimentally obtained data is given by the blue dotted curves). Generally, the agreement is good, although there is slightly higher reflection and lower transmission at the L1 band than at the L2 band. The operating bandwidths, given by the -10 dB return loss points, of 300 MHz and 170 MHz at the GPS L2 and L1 bands, respectively are relatively narrow, but adequate for the narrowband GPS application – where 20.46 MHz of bandwidth is necessary for the higher-accuracy p-code reception.

The dark hatching lines prevalent in the inset of Fig. 4.9 give the processed dielectric its grey color, it is hypothesized that these lines are a result of the U3's laser strongly interacting with the dielectric during the milling process, causing the resulting regions to possess increased loss. As a result, the substrate simulated in HFSS was given an anisotropic loss tangent of 0.05 in the plane of the copper, and the manufacturer-specified 0.035 into the dielectric. These parameters, along with the bulk-value relative permittivity of 11.2, yielded the simulation data that agrees moderately well with experiment. The important scattering values are detailed in Table 4.2, the data of which indicate that the coupler operates sufficiently well for the purpose at both bands.

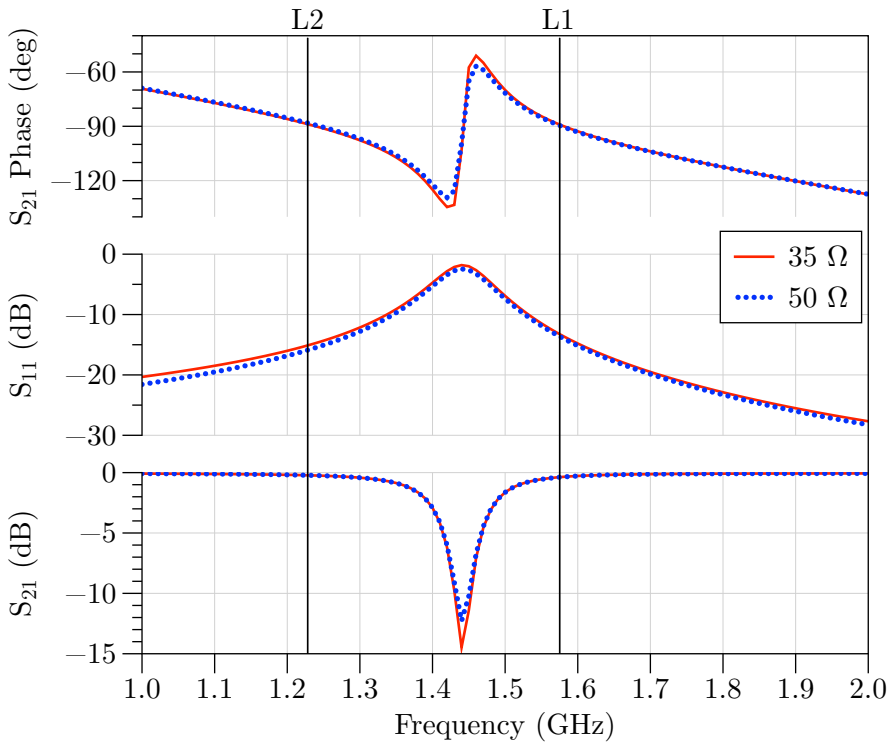

Figure 4.7: Simulated scattering parameters of the designed MTM-EBGs as determined with HFSS. The vertical solid bars indicated the operating frequencies of GPS L1 and L2, at which the MTM-EBGs are seen to produce 90° of phase with minimal losses. Figure adapted from [176].

Table 4.2: Simulated and Measured S-Parameters of the Dual-Band Coupler at its Operating Frequencies of GPS L2 (1.228 GHz) and L1 (1.575 GHz)

	Simulated		Measured	
Parameter	L2	L1	L2	L1
S_{11} (dB)	-21.04	-15.20	-26.21	-14.05
S_{21} (dB)	-3.61	-4.39	-3.56	-5.50
S_{31} (dB)	-3.67	-4.49	-3.56	-5.30
S_{41} (dB)	-18.58	-27.38	-18.40	-18.38
$\angle S_{21} - \angle S_{21}$ (deg)	89.44	84.76	89.25	92.65

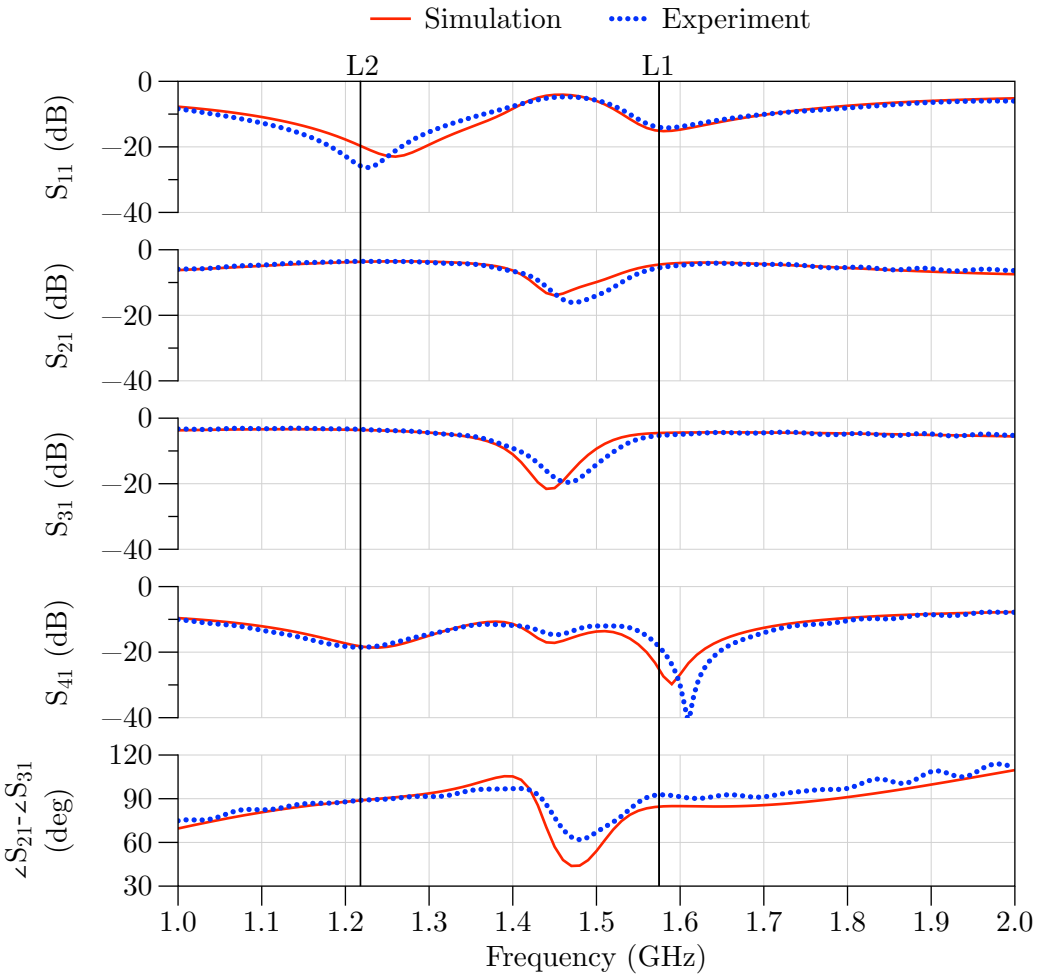

Figure 4.8: Simulated versus measured scattering parameters of the designed MTM-EBGs as determined with HFSS. The vertical solid bars indicated the operating frequencies of GPS L1 and L2, at which the MTM-EBGs are seen to produce 90° of phase with minimal losses. Figure adapted from [176].

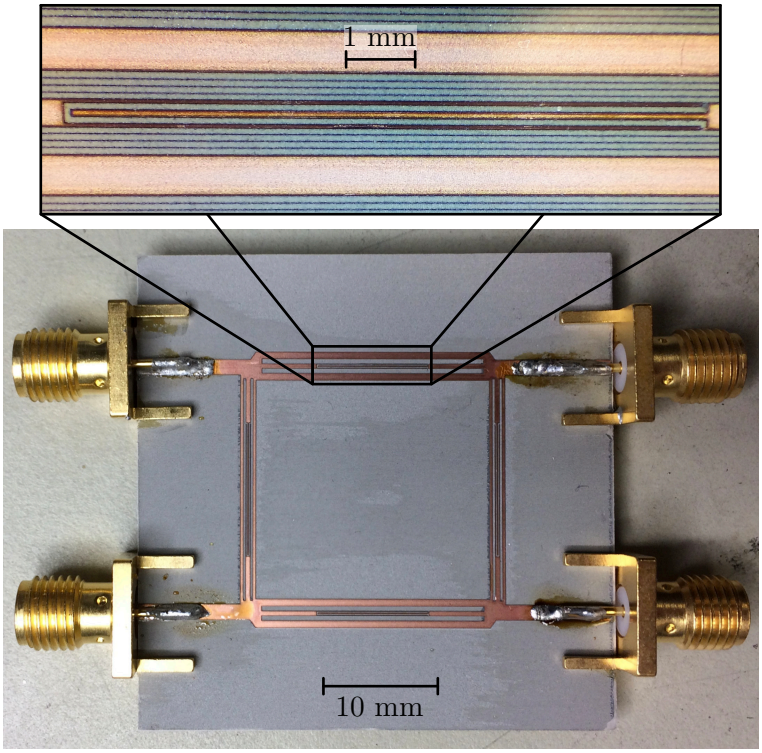

Figure 4.9: Fabricated dual-band MTM-EBG-enabled quadrature hybrid coupler. The inset shows the interdigitated capacitor with 100 μm feature sizes. Figure adapted from [176].

4.1.4 A Common-Mode Filter Without a Defected Ground Plane

One observation of typical MTM-EBG unit-cell responses is that the CSL-like mode typically possesses a backward-wave band in the vicinity of the MS-like/CPW-like bandgap. This dispersion phenomenon was exploited in [420] to develop a common-mode filter, which passes a differentially-driven mode while suppressing the common mode between its two input conductors and conductor backing [436] – where the differential mode is mediated by the MTM-EBG's CSL mode, and the common mode is mediated primarily by the MTM-EBG's MS-like mode. Due to the MTM-EBG's inherent advantage as a uniplanar structure, the filter may be completely printed without disturbing the conductor backing, as is common with many proposed common-mode filters based on defected ground structures [437–440]. Defecting the solid conductor backing can lead to signal coupling between layers, and even excitable radiation modes at certain frequencies – therefore, this solution is not desired in multilayer PCB environments.

The necessary features of such an EBG-based common-mode filter are that: a) there exists a common-mode bandgap in the same frequency range over which the differential mode propagates, and b) the device is impedance-matched to the desired differential-mode impedance. The circuit model of such an EBG unit cell is the topology with the loading capacitors in the CPW ground conductors given in Fig. 4.1a, where, owing to the desire to have the differential mode impedance-matched over as wide a band as possible, the "stop-band closure" condition is used [254], which sets the conditions for the ratio of the loading inductance L to loading capacitance C_g. The values of these components decides the operating band,

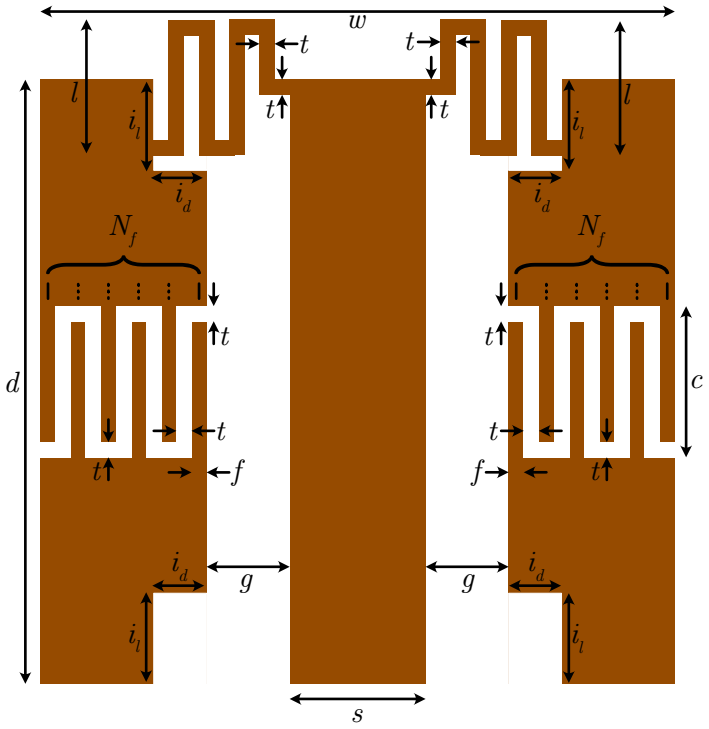

Figure 4.10: Layout of the upper-layer conductors of an MTM-EBG (conductor backing not shown), in which the loading capacitance is placed in series with the CPW ground conductors, and implemented as interdigitated capacitors, while the loading inductors are implemented as meandered inductors which span portions of adjacent unit cells.

which was chosen to be in the sub-10 GHz range.

The filter is designed to be constructed on a Rogers RO-3003 substrate (with a relative permittivity $\epsilon_r = 3.0$ and loss tangent $\tan\delta = 0.001$) [441] with 35 μm copper cladding, where due to the pre-selected modal impedances of $Z_{common} = 25\ \Omega$ and $Z_{differential} = 100\ \Omega$, the host CBCPS possesses strip widths of 3.0 mm and spacing of 1.5 mm. The layout of the filter's MTM-EBG unit cells is described by the parameters given in Fig. 4.10, where the meandered inductors extend slightly out of each unit cell, and the outer most inductors in the cascade of the four cells are physically larger to accommodate the double inductance values required for proper input/Bloch impedances. The various parameters specified in the figure are given in Table 4.3, which result in effective values for the printed reactive loading components of $C_g = 0.4$ pF and $L = 4.0$ nH.

The unit cell possesses dispersive properties shown in Fig. 4.11, which gives both the results of the equivalent-circuit model, as well as HFSS data, which are in reasonable agreement – with the exceptions of an unexpected transverse resonance of the cell near 9.0 GHz that is not captured in the circuit model, and minor interactions with the TM_{10} SW-mode near 5.0 GHz. There is minor detuning of the bands near the X-point around 2.0 GHz, where most likely the physical size of the loading components are not accounted for in the circuit model, as observed in [381]. This effect is most likely also responsible for the small opening of the CSL-like mode's bands near 5.0 GHz, which causes relatively sizeable divergence of

Table 4.3: Geometrical parameters of the proposed common-mode filter, and its embedded MTM-EBGs (reference Fig. 4.10).

Parameter	Value
Unit Cell Length d	5.0 mm
Unit Cell Width w	7.5 mm
CPW Strip Width s	0.2 mm
CPW Gap Width g	0.7 mm
Interdigitated Capacitor Length c	2.1 mm
Meandered Inductor Length l	1.1 mm
Number of Interdigitated Capacitor Fingers N_f	14
Width of Interdigitated Capacitor Fingers f	0.1 mm
Gaps Between of Interdigitated Capacitor Fingers t	0.1 mm
Width of Inductor Meanders t	0.1 mm
Spacing Between Inductor Meanders t	0.1 mm
Inductor Inset Depth i_d	0.4 mm
Inductor Inset Length i_l	0.8 mm
Lengths of Outer Two Meandered Inductors l	2.1 mm
Substrate Width H	30 mm
Substrate Length W	60 mm

the Bloch impedance of this mode between the circuit and HFSS models. However, the dominant desired features of the bandgap in the MS mode between roughly 1.8 GHz and 4.4 GHz, and the roughly 100 Ω CSL-mode impedance over a broad bandwidth are present, indicating that the EBG should work for the intended purpose.

The filter was laid out and simulated in HFSS as shown in Fig. 4.12, and was once again fabricated on a Protolaser U3, where the RO-3003 material is much less sensitive to the laser than the RO-3010 substrate used in section 4.1.3, and therefore does not incur nearly the same amount of losses, or deviation from its simulated isotropic permittivity. The resulting fabrication is shown in Fig. 4.13, where the inset details the level of fabrication accuracy used to construct the fine 100 μm features of the interdigitated capacitors and meandered inductors. The substrate length W is 60 mm and the width H is 30 mm.

The resulting scattering parameters, expressed on a basis of common and differential modes (the process of which is described in general in Appendix C), are given in Fig. 4.14, where it may be seen that the data resulting from the HFSS simulation (dotted curves) and those obtained through measurement of the fabricated device (solid curves) are in good agreement. The simulation data show suppression of the common mode (S_{21cc} < -10 dB) over the 1.6 to 4.2 GHz band, while the fabricated device was found to possess a slightly wider suppression band of 1.6 to 4.4 GHz. Good matching of the differential mode (S_{11dd} < -10 dB) is observed in simulation above 2.4 GHz up until it interacts with a transverse resonance of the MTM-EBG unit cell near 8.5 GHz – similar performance was observed in experiment, with a very slightly higher lower cutoff frequency near 2.4 GHz, yet a high-frequency transverse resonance starting

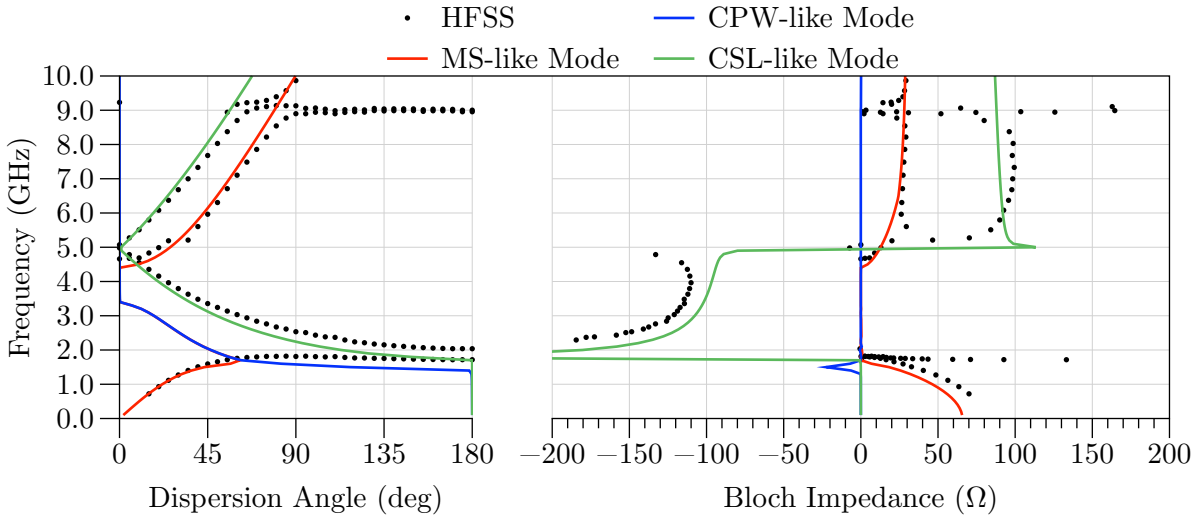

Figure 4.11: Bloch dispersion angles and impedances of the proposed coupler, as determined though the equivalent-circuit mode (colored solid curves) and HFSS model (black dots). Generally, the two are in good agreement, with the obvious exception of a resonant mode near 9.0 GHz, which is not predicted by the circuit model. Figure adapted from [420].

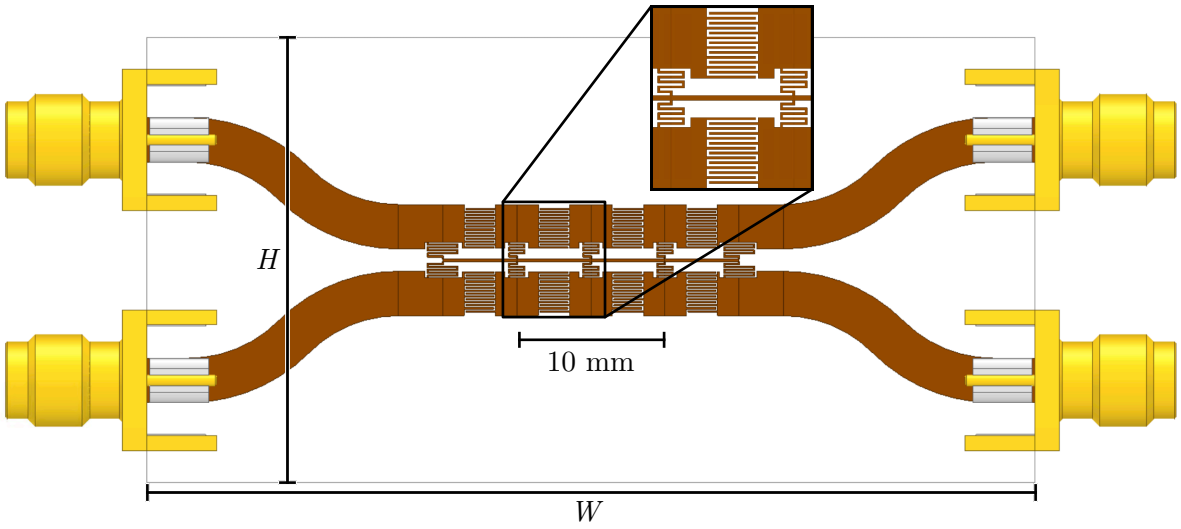

Figure 4.12: HFSS model layout of the upper-layer conductors of the proposed filter (conductor backing not shown). The series loading capacitors are implemented as interdigitated capacitors, while the shunt loading inductors are implemented as meandered inductors which span portions of adjacent unit cells. The entire PCB has dimensions of length W and width H. The SMA connectors have been modelled for additional accuracy. The inset shows the 100 μm interdigitated capacitors and meandered inductors in detail.

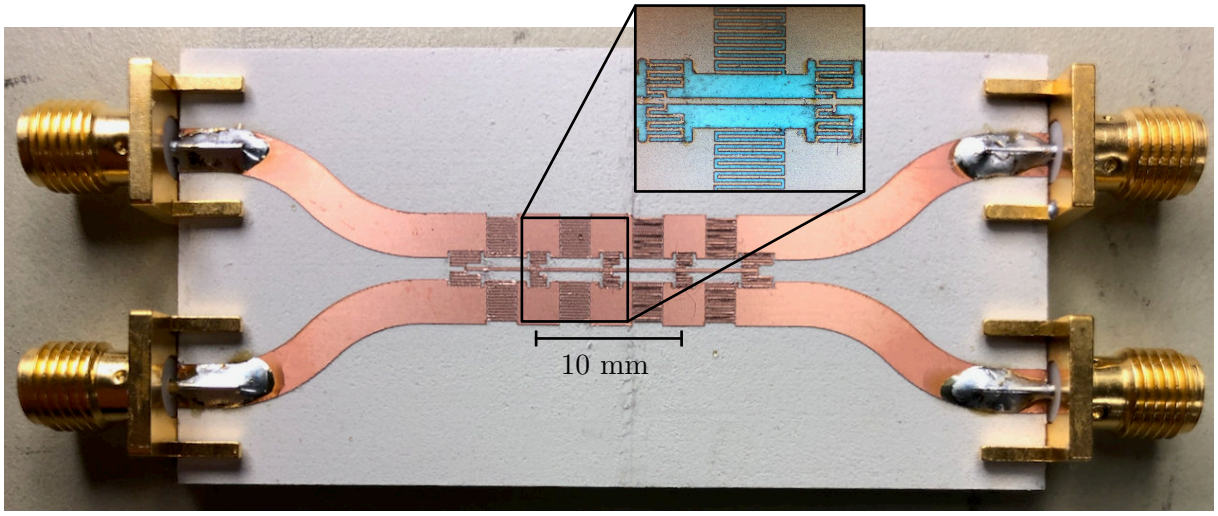

Figure 4.13: Layout of the upper-layer conductors of the fabricated filter (conductor backing not shown). The inset shows the relatively high fabrication quality of the 100 μm features. Figure adapted from [420].

to interfere with transmission above roughly 9.0 GHz. The small reflection coefficient of the differential mode over this band indicates that the device is reasonably well impedance-matched to the expected 100 Ω.

Of course, it should be noted that prediction of the the Bloch impedance directly from dispersive quantities is only possible through the analysis of section 3.1 – and, to this author's knowledge, has not been obtained before for a MTL-MTM.

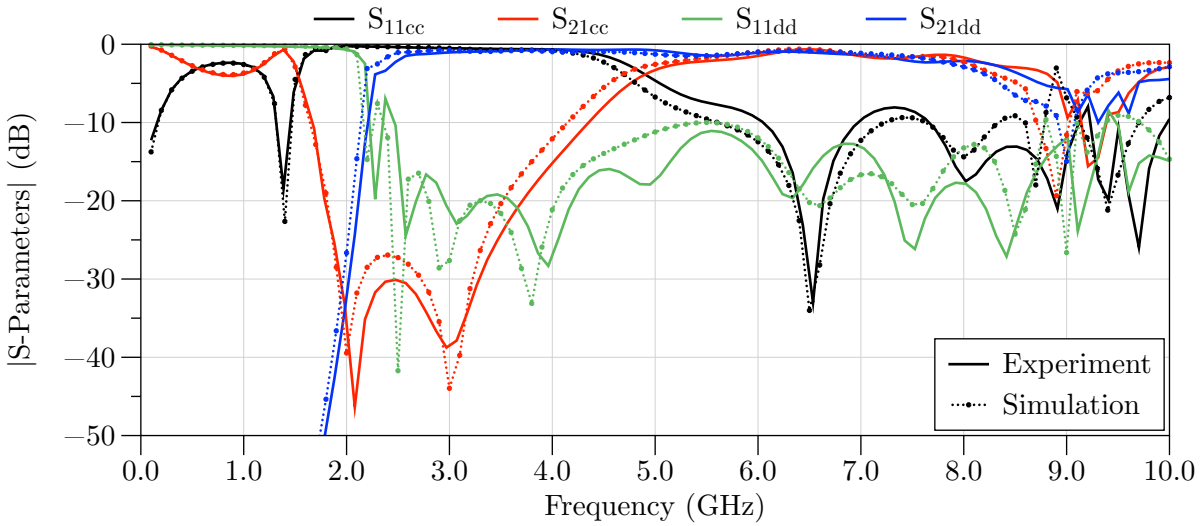

Figure 4.14: Layout of the upper-layer conductors of an MTM-EBG (conductor backing not shown), in which the loading capacitance is placed in series with the CPW ground conductors, and implemented as interdigitated capacitors, while the loading inductors are implemented as meandered inductors which span portions of adjacent unit cells. Figure adapted from [420].

4.2 Modelling the UC-EBG

Various specific figures and portions of this section have been submitted for publication in the *IEEE Trans. Antennas Propag.* as "The MTM-EBG as a Rigorous Multiconductor Model of the UC-EBG and Approaches for Miniaturization" by S. Barth and A. K. Iyer. The ideas presented in the work were generally a collaborative effort by the authors.

4.2.1 The UC-EBG and Simple Circuit Models

The Uniplanar Compact Electromagnetic Bandgap Structure (UC-EBG) [368,383–387] is a canonical EBG structure highly used due to its uniplanar nature, which allows it to be fabricated without vias using only simple mechanical-milling- or chemical-etching-based PCB fabrication processes. It has found use in a variety of microwave applications, such as TL-mode suppression [383], SW-mode-suppressing antenna ground planes [385, 386], artificial magnetic conductors [387], and waveguide miniaturization [384] among others. The UC-EBG unit cell consists of metallic patches, which are indicated by the dark regions of Fig. 4.15. The currently ubiquitous equivalent-circuit model of the UC-EBG's bandgap consists of an L-C resonant tank [442], identified as originating with a resonance of the equivalent series inductance (L) of the thin strip sections and series loading capacitors (C) of the gaps between adjacent unit cells, as indicated in Fig. 4.15.

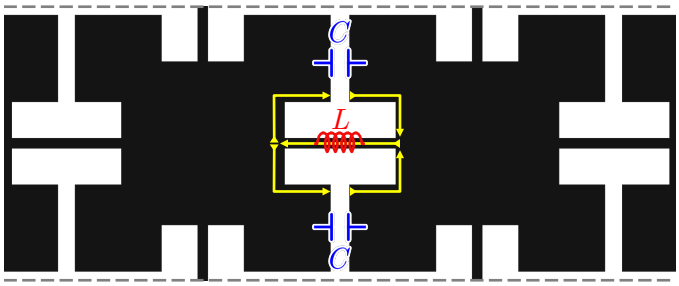

Figure 4.15: A portion of a 2D infinite array of UC-EBG unit cells, which is periodic along both the horizontal and vertical axes (where the dashed lines indicate the vertical periodic boundaries). The canonical model identifies the primary bandgap mechanism as a resonance (with current paths indicated by the (yellow) solid arrow current paths) created by the equivalent series inductance L and effective series loading capacitance C.

However, as a first-order approximation, this resonator model possesses a few serious deficiencies. Modeling only a single resonance of a given TL mode (i.e., arrangement of voltages and currents on the structure) does not capture the mode's dispersive or complex mode properties, nor does it provide any insight as to the nature of the other modes supported by the structure. The model cannot provide any information on the nature of the interaction between the resonant mode and any other supported modes; including the nature of the prominent bandgap it supports. Neither can the model provide insight on how to control the bandgap's size other than through adjusting the effective L or C of this resonance, which only roughly approximate the location of the bandgap. The conductor backing/ground plane is often overlooked by this model; while it is known that its presence affects the nature of the bandgap [443], the exact nature

of coupling or why this affects the bandgap to such a large degree is poorly understood. Additionally, although some effort can be made to miniaturize the structure through meandering the inductive strip and interdigitating the capacitive gaps [443–446], the resonance generally exists at frequencies where the unit-cell periods are a significant fraction of a guided wavelength in size (e.g. a quarter-wavelength). These electrically appreciable unit cell periods imply very coarse sampling of the fields – prohibiting the EBGs from acting as a homogenous medium – which is especially disadvantageous in radiating applications where the cells are placed close to radiating elements, and diminishes any advantages gained from effective-medium approaches. The unit cell size also impedes device miniaturization; for example, antennas with UC-EBG-based ground planes must be relatively large to accommodate multiple unit cells, or similarly a substantial amount of PCB space must be used to accommodate multiple unit cells for filter or noise-suppression applications. Thus, the miniaturization of the individual unit cells, and thus an array of unit cells, would allow the UC-EBG to present a more attractive alternative to current solutions.

4.2.2 A First-Order Proposed 2D MTL Circuit Model of the UC-EBG

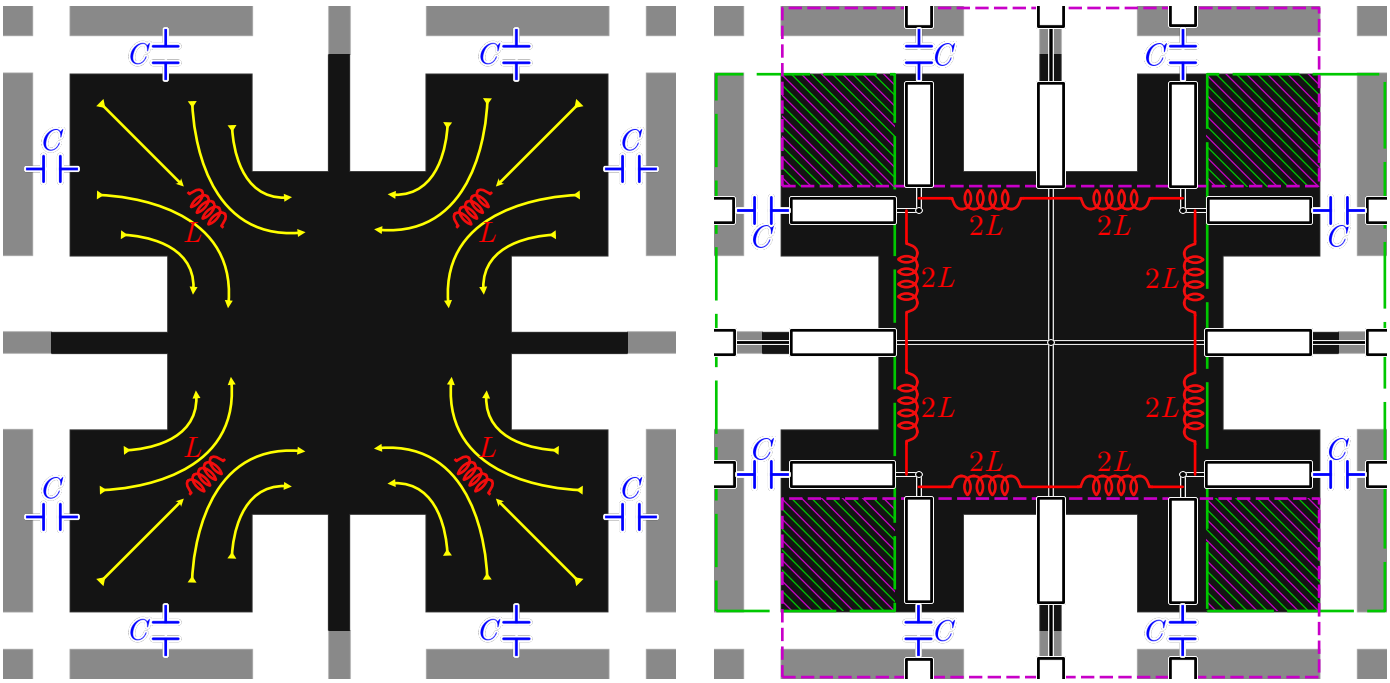

Figure 4.16: One (conductor-backed) UC-EBG unit cell (highlighted) of an infinite array, detailing: a) the fields and equivalent loading circuit components observed in the vicinity of the structure's bandgap, specifically the equivalent loading capacitances (the gaps between adjacent unit cells) and inductances (the constraining of the currents, indicated by the yellow curves), and b) the proposed first-order circuit model resulting from this field distribution. The green (long-dashed) rectangles correspond to the CBCPW sections on the horizontal axis, while the purple (short-dashed) rectangles represent the CBCPW sections on the vertical axis. The diagonally shaded regions where the green and purple rectangles overlap are the corner sections not accounted for in the model.

Table 4.4: Geometrical parameters of the UC-EBG and 2D-MTM-EBG structures shown in Fig. 4.19.

Parameter	**Value**
Period d	20.0 mm
Corner Length l	4.5 mm
Node Length a	10.0 mm
Strip Width s	1.0 mm
Gap Width g	1.0 mm
CPW Ground Conductors Width w	3.5 mm

Figure 4.16a presents a more intricate view of the fields observed on the UC-EBG structure in two dimensions (conductor backing not shown). In the figure, the dominant capacitance is still attributed to the gaps between adjacent unit cells; however, the primary inductance mechanism is described as originating with the constraining of currents as they pass from the outer sections of the EBG into its central nodal region. This mechanism, only available in a 2D description of the unit cell, represents a distinctly differing mechanism for the operation of the unit cell, since the size of the CPW strip conductor does not necessarily play a major role in the behavior of the unit cell. Such an arrangement of fields gives rise to the first-order circuit model, shown in Fig. 4.16b, where the regions bounded by the green (long-dashed) rectangles represent proposed CBCPW sections on the horizontal axis, while the purple (short-dashed) rectangles represent proposed CBCPW sections on the vertical axis. This model cannot capture the diagonally shaded corner sections where the green and purple rectangles overlap, but these are suspected to possess a relatively small effect on the quality of the structure's dominant bandgaps.

The equivalent-circuit model is shown for clarity on its own in Fig. 4.17, where it becomes readily apparent that each branch of the unit cell is half of the MTM-EBG unit-cell shown in Fig. 4.18, where the cell has been bisected by the vertical dashed line, and the resulting parallel shunt inductors split in two – each possessing double the value of the original inductance. Thus, it may be claimed that the UC-EBG is well-modelled as a 2D intersection of MTM-EBG sections. Since the MTM-EBG's band structure may be rigorously modelled, it would be expected that the UC-EBG may also be rigorously modelled using this equivalent circuit.

4.2.3 Full-Wave Simulations

The dispersive properties of the UC-EBG are simulated in HFSS using its eigenmode solver. Constructed on a 1.524 mm-thick RO-3003 substrate (with relative permittivity $\epsilon_r = 3.0$ and loss tangent $\tan\delta = 0.001$) with 35 μm copper cladding, the geometric properties of the upper layer are given in Fig. 4.19a (solid conductor backing not shown) and Table 4.4. To make a fair comparison with the proposed circuit model, a second structure is also simulated as shown in Fig. 4.19b, which differs only from the first in that the unmodelled outer corner sections of the cell have been removed, and series loading capacitances (represented with the solid blue surfaces) each with capacitance values of 0.1 pF – to accommodate the missing capacitance of the corner sections – have been placed in the gaps between adjacent cells.

The results of these simulations are given in Fig. 4.20, in which the canonical UC-EBG model's results

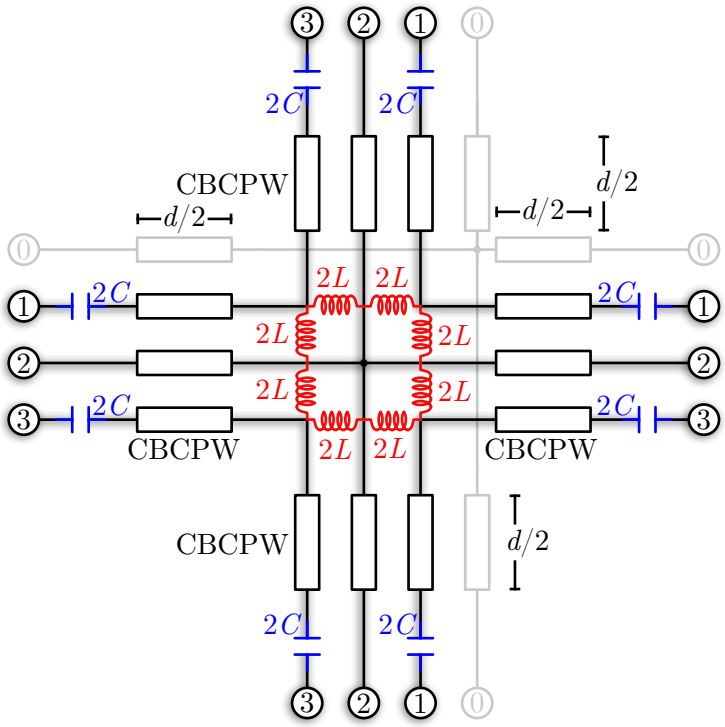

Figure 4.17: Proposed first-order 2D circuit model of the UC-EBG. The nodal region, for which currents are constrained when travelling in or out of, is represented with a set of shunt inductors, each with a value of $2L$, while the outer branches are modelled as CBCPW sections loaded with series capacitors in the CPW ground conductors, with values of $2C$. The conductor backing is represented by the washed-out conductor #0, which is connected in a shunt configuration along both axes. It may be observed that each branch then corresponds with one-half of one MTM-EBG unit-cell, as indicated in Fig. 4.18.

are given by the solid curves, and modified structure of Fig. 4.19b (hereon referred to as the 2D-MTM-EBG) simulation's data are given with the dashed curves. The various colors – as opposed to schemes used in other, similar works – are not used to identify the individual bands, but rather indicate what type of mode definitions the band possesses along the axis of the Brillouin zone contour. The mode definitions generally inherent the properties of the host TLs, such that in the investigated cases these may be classified as (similar to the MTM-EBG) MS-like (red), CPW-like (blue), CSL-like (green), and SW-like (black). There exist numerous higher-frequency bands above those shown in the following figures which exhibit many interesting phenomena, but these have been removed for clarity so that focus can be placed on the lower-frequency common bands of interest.

The structures both contain two dominant bandgaps: the MS-like bandgap that extends from the X/Y-point of the MS-like (red) band – to a frequency above the displayed 6.0 GHz – and the smaller SW-mode bandgap near 3.9 GHz for the UC-EBG (or 4.2 GHz for the 2D-MTM-EBG) in the Γ-X Brillouin Zone, and near both 3.8 GHz and 4.6 GHz in the Γ-M Brillouin zone for both structures. The UC-EBG possesses two bands, one based on the CPW-like mode (blue curves) and one based on the CSL-like mode (green curves), which exist in very similar frequency bands between 3.7 GHz and 3.9 GHz. The CPW-like

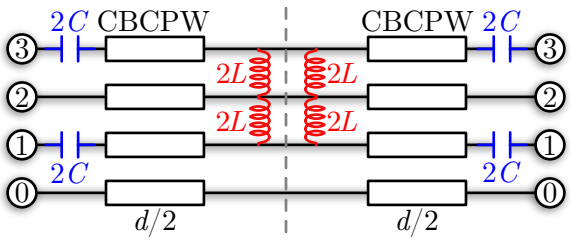

Figure 4.18: A 1D MTM-EBG unit cell, with series loading capacitors in the CPW ground conductors and with a line of symmetry down the middle, dividing the shunt loading inductors into two parallel inductors with double their initial values. Each half of the unit cell may be observed to be one of the branches in the 2D model of Fig. 4.17.

mode interacts with the SW-like mode, whereas the CSL-like mode does not; otherwise the modes possess nearly identical dispersive properties. The 2D-MTM-EBG, in contrast, possesses two bands with similar properties, but these bands are not similar to each other: the CSL-like mode decreases in frequency from the Γ-point to the X/Y-point, while the CPW-like mode increases with frequency over the same range. Interestingly, it may be observed that the CPW-like and CSL-like modes switch between each other between various Brillouin zones. This is due to the fact that CPW-like fields propagating along one axis tend to occur alongside CSL-like fields existing on the other axis, although other combinations exist.

Another large discrepancy between the two structures is the location of the M-point of the upper CSL-like band, which is near 4.8 GHz for the UC-EBG, while closer to 5.8 GHz for the 2D-MTM-EBG – yielding a much larger operation bandwidth for the upper CSL-like band in the 2D-MTM-EBG structure.

Identification of Propagating Modes

In order to establish similarities with the MTM-EBG, the modes in various bands of the Γ-X Brillouin zone are investigated. The observed band structure is then hypothesized to result from the coupling of a number of these modes, indicated with various representative dispersion curves. The electric-field vectors ($\vec{E}$) and surface current-density vectors ($\vec{J}$) shown in Fig. 4.21 are obtained at a dispersion angle of 30° – chosen since the angle is relatively far from any coupling regions of the various modes.

The fields of the MS-like mode (red curves of Fig. 4.20) at 0.43 GHz are shown in Figs. 4.21a ($\vec{J}$) and 4.21b ($\vec{E}$). The electric field is primarily vertical and strongest inside the substrate, as expected of the MS-like mode. The currents are predominantly driven through the CPW strip, as expected at low frequencies due to the high impedance presented by the series capacitors.

The SW-like mode (black curves of Fig. 4.20) at 1.24 GHz are shown in Figs. 4.21c ($\vec{J}$) and 4.21d ($\vec{E}$). The electric fields are essentially vertical everywhere, with the strongest fields in the air above the upper layer, as expected of the TM_{10} SW mode. Notably, the currents for the most part ignore pathing through the conductors, and exist primarily in the direction of propagation of the wave, regardless of the shape of the conductors on which they are supported. This is a sure indication that the mode is non-TEM, and cannot be simply modelled with a TL network – as such, it has not even been attempted in this work.

The upper band of the CPW-like mode (blue curves of Fig. 4.20) at 3.95 GHz are shown in Figs. 4.21e ($\vec{J}$) and 4.21f ($\vec{E}$). The electric field is primarily vertical and strongest inside the substrate, as expected of

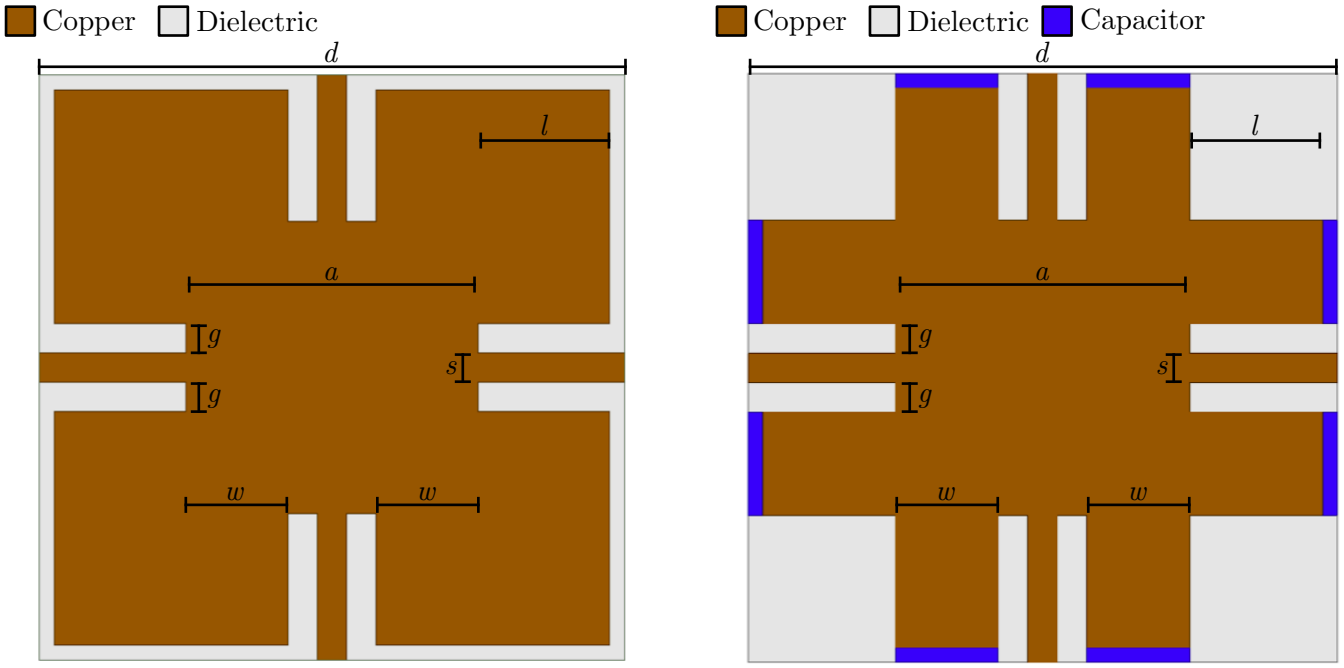

Figure 4.19: HFSS simulation layouts of a) a canonical UC-EBG structure, and b) a proposed equivalent structure (the 2D-MTM-EBG) in which the outer corner sections of (a) have been removed, and series loading capacitors inserted into the gap in the CPW ground conductors between adjacent unit cells. The unit cells are symmetric about both axis. Conductor backings not shown.

the MS-like mode. The fields are seen to be roughly similar to those of the MS-like mode in most aspects, except for the transverse axis on which the fields appear to possess a more CSL-like configuration.

Since it is known that the band(gaps)s of the MTM-EBG arise due to the coupling of its various even modes, it is hypothesized that the same phenomenon occurs in the UC-EBG. A figurative depiction of the origin of the UC-EBG's band structure is given in Fig. 4.22a. In the case of this structure, with respect to the MS-like mode (indicated by the red curves), the structure appears as a regular grid. From the perspective of the CPW-like mode (indicated by the blue curves), however, the UC-EBG may appear as a grid containing series capacitors, with a small shunt inductance presented by the central node. This type of network has been identified and analyzed in [259], where it demonstrated that the mode is backward. A representative coupled system due to the coupling of these modes is given by the dashed green curves, which possesses new properties such as the large prominent bandgap that is manifested as a 2D universal bandgap across all Brillouin zone contours rather than just along one axis. Such coupled modes are found in the various bands of the UC-EBG structure as the MS-like mode (red curves), CPW-like mode (blue curves), and SW-like mode (black curves) in Fig. 4.20.

The UC-EBG is observed to also support various bands of two different CSL-based modes: one which possesses CPW-like fields on its transverse axis, and another which possesses CSL-like fields on its transverse axis, as indicated in Figs. 4.23. The former, fields of which are shown in Figs. 4.23a ($\vec{J}$) and

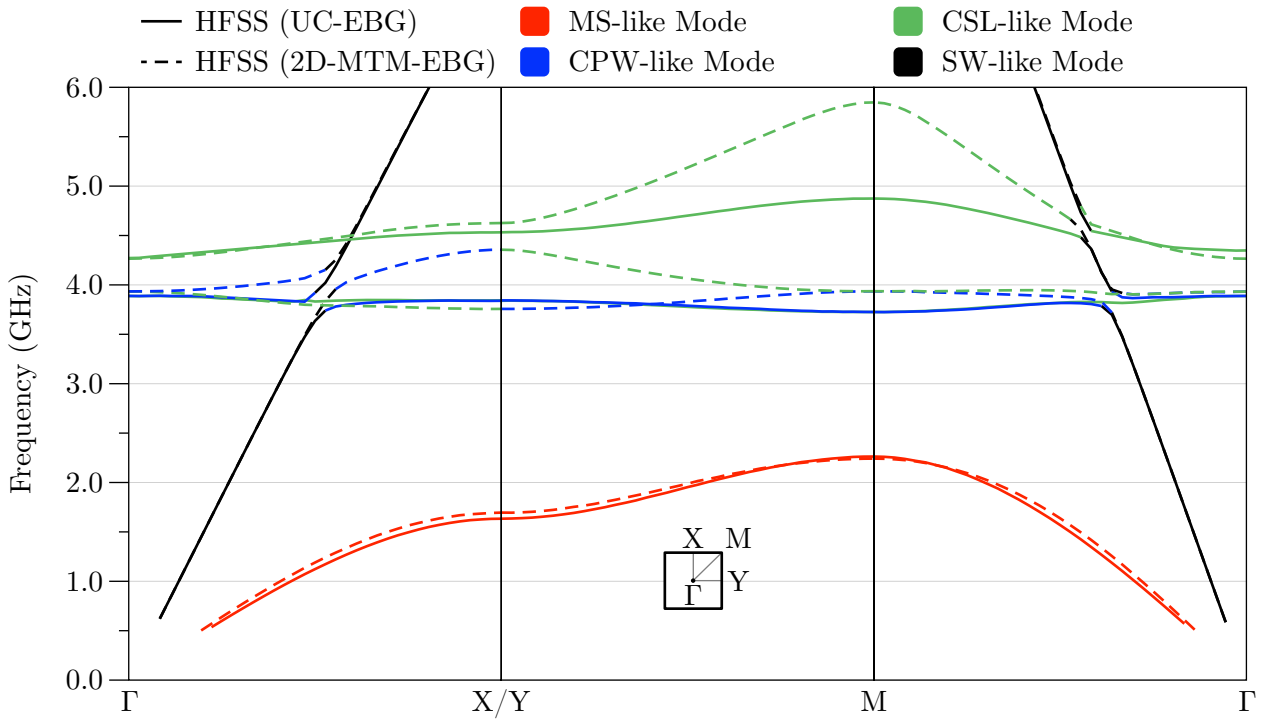

Figure 4.20: Simulated dispersive properties (imaginary components only) of the two unit cells investigated using HFSS, corresponding to the structures shown in Figs. 4.19. Various modes are specified by color as indicated, where the modes are categorized based on mode definitions determined along the dominant axis of propagation, such that there are often color discontinuities in each band along the Brillouin zone contours.

4.23b ($\vec{E}$), is a backward mode which generally exhibits a relatively flat dispersion band, indicating it is highly resonant. Inspection of the fields suggest that this resonance is primarily along the the transverse axis, where the CPW-like fields tend to dominate. The latter mode is a forward mode which exhibits regular CSL-like fields along both axes, as observed in Figs. 4.23c ($\vec{J}$) and 4.23d ($\vec{E}$). Since these modes are both odd-type modes (being based on the CSL-like field distribution) in the Γ-X Brillouin zone, neither couples with any of the even modes in the same zone.

Comparison With First-Order Circuit Model

The results of determining the dispersive properties of the first-order circuit mode of Fig. 4.17 are compared with those of the 2D-MTM-EBG model in Fig. 4.24, where the inductance values $2L$ were given a value of 1.5 nH – selected by matching the Γ-points of the CPW-like modes near 3.9 GHz. Values of $d = 10$ mm and $2C = 0.4$ pF were used to model the TL sections of the unit cell and corresponding gap capacitances, where the MTL model properties were extracted from an HFSS simulation as given in (4.1).

$$[G_M] = \begin{bmatrix} 0.0479 + j34.4332 & 0 & 0 \\ 0 & 0.0460 + j31.6339 & 0 \\ 0 & 0 & 0.0616 + j29.8321 \end{bmatrix} /m \tag{4.1a}$$

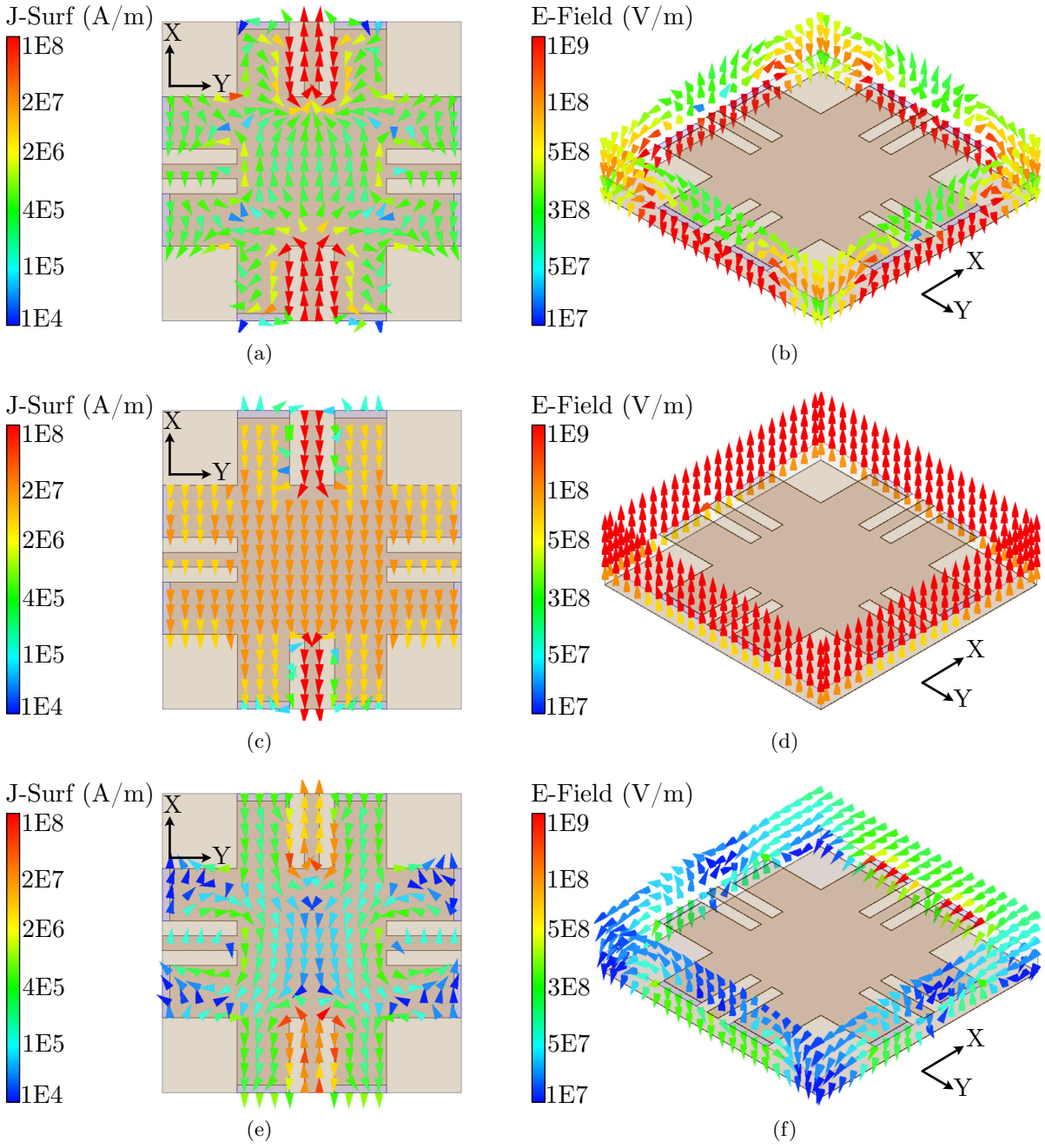

Figure 4.21: Surface-current vectors (on the top face of the unit cell) (a, c, e) and electric-field vectors (on the transverse planes to the unit-cell axes) (b, d, f) from the even modes of an HFSS simulation model at a dispersion angle of 30° (from Fig. 4.19b): MS-like (red curves) (a, b), at 0.43 GHz; SW-like (black curves) (c, d), at 1.24 GHz; CPW-like (blue curves) (e, f), at 3.95 GHz. Propagation is X-directed in all cases. The fields are shown at phases specifically chosen to highlight various relevant aspects of the modes.

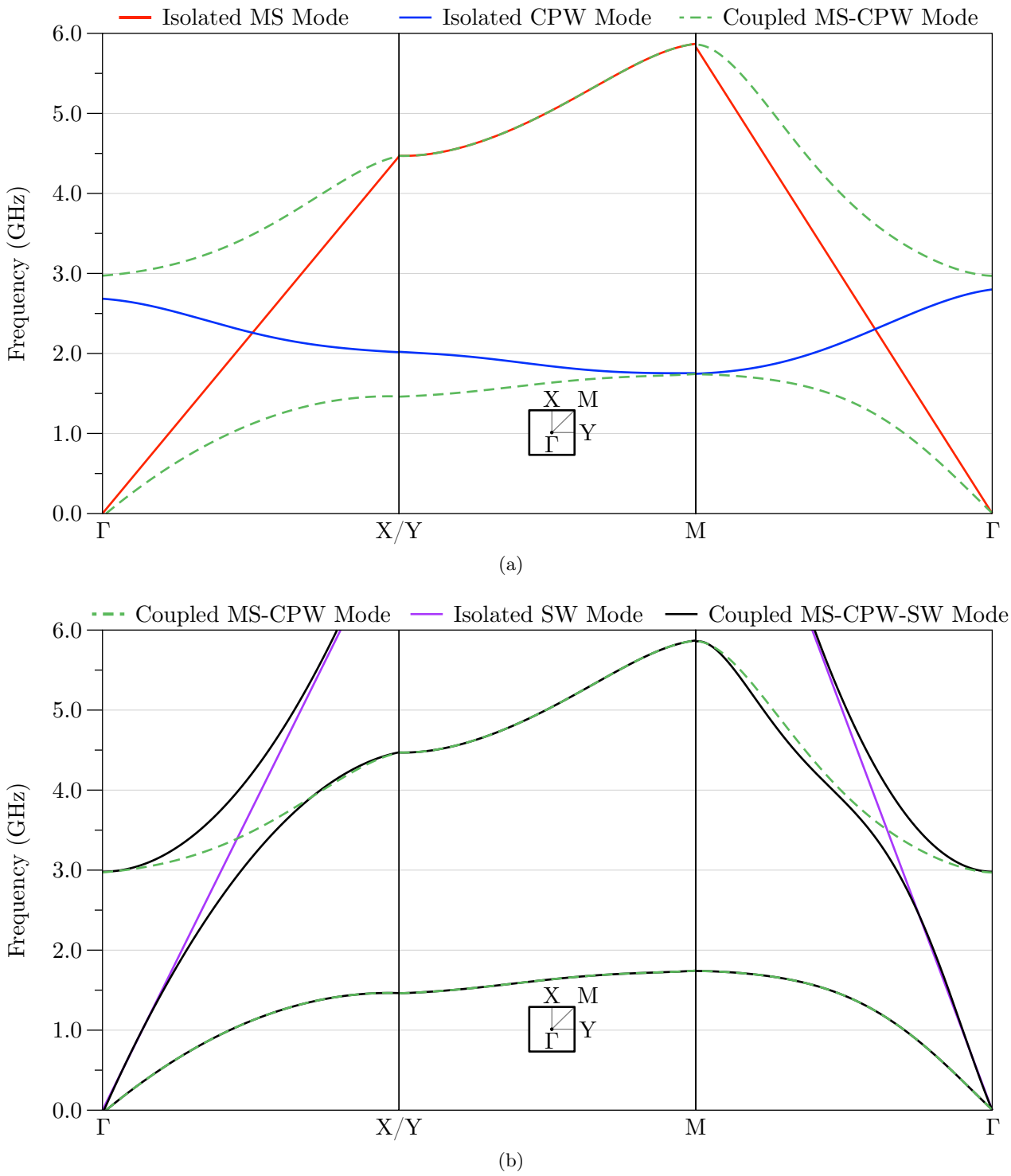

Figure 4.22: Figurative depictions of the couplings of various modes to form the observed even-mode bands of the UC-EBG: a) the isolated MS-like (red curves) and CPW-like modes (blue curves) couple to form the band structure given by the dashed green curves, and b) the coupled MS-CPW system (dashed green curves) and SW-like mode (purple curves) couple to form the band structure given by the black curves (coupling exaggerated for clarity).

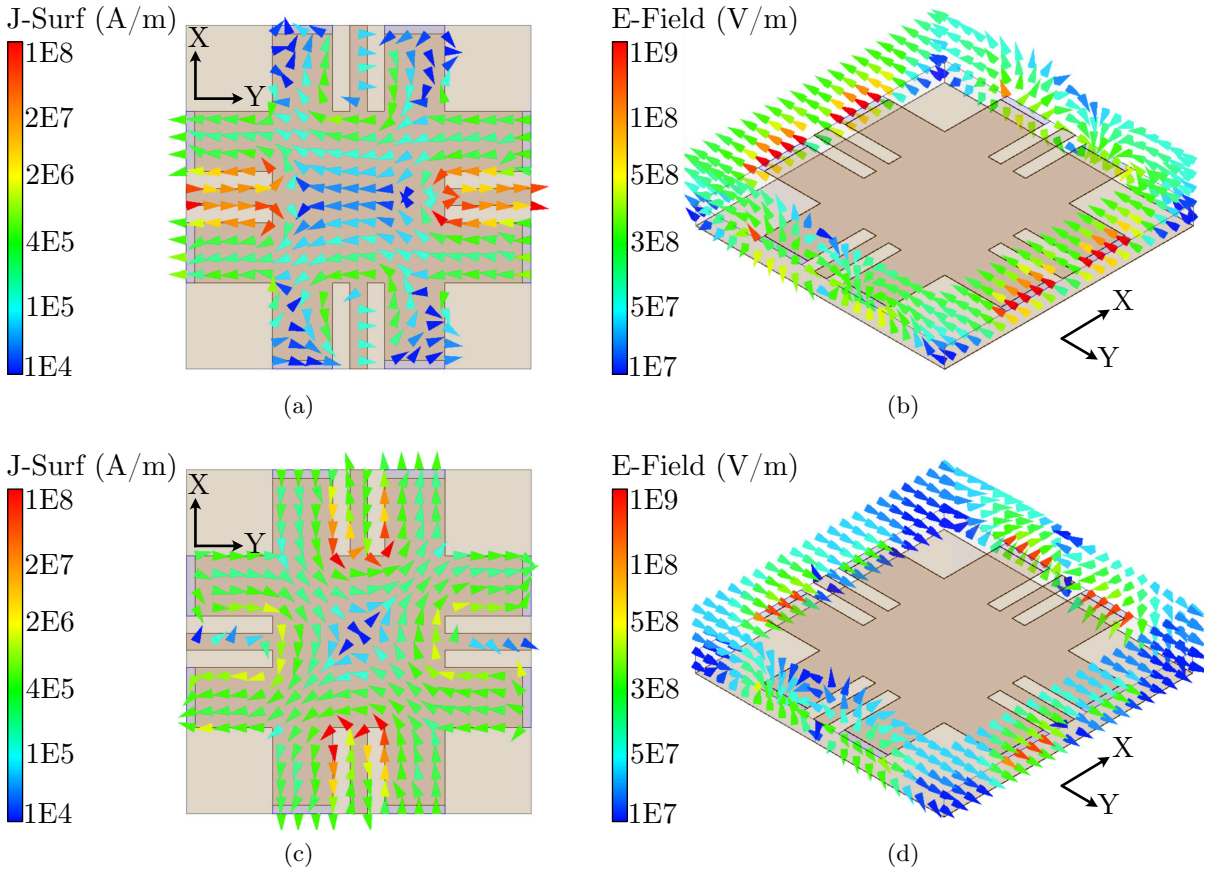

Figure 4.23: Surface-current vectors (on the top face of the unit cell) (a, c) and electric-field vectors (on the transverse planes to the unit-cell axes) (b, d) from the modes exhibiting CSL-like fields along the dominant axis of propagation of an HFSS simulation model at a dispersion angle of 30° (from Fig. 4.19b) (green curves): CPW-like on the transverse (Y) axis (a, b), at 3.91 GHz; CSL-like on the transverse (Y) axis (c, d), at 4.30 GHz. Propagation is X-directed in all cases. The fields are shown at phases specifically chosen to highlight various relevant aspects of the modes.

$$[Z_{cM}] = \begin{bmatrix} 26.7704 - j0.0044 & 0 & 0 \\ 0 & 97.4225 - j0.0355 & 0 \\ 0 & 0 & 85.8982 - j0.0928 \end{bmatrix} \Omega \tag{4.1b}$$

$$[T_I] = \begin{bmatrix} 0.4139 & 1.0000 & 0.5000 \\ 0.1720 & 0.0000 & -0.9412 \\ 0.4139 & -1.0000 & 0.5000 \end{bmatrix} \tag{4.1c}$$

While the first-order circuit model appears to capture some of the main dispersive properties of the cell, it may be observed that in general, the agreement with HFSS data is poor. As might be expected many of the bands are resonant-type exhibiting a nearly flat dispersion curve – most likely due to the relatively small value of inductance used in the model. Many of the bands are displaced from those of the HFSS data, indicating that the model does not capture the correct modal behavior of the structure, especially at higher frequencies above the lowest MS-like band. Notably, there are two complex modes in the Γ-M dispersion region, formed as a result of coupling between the MS-like and CPW-like modes. While HFSS does not solve for complex modes, it does not predict the various bands in the vicinity of these complex modes, indicating that these modes may not exist in the HFSS structures.

For these many reasons, it becomes apparent that this model is insufficient to adequately describe the complexities of the unit cell. One of the least-well modelled regions is the central node, which, being modelled with shunt inductors does not even capture phase information related to propagation through this region – which encompasses half of the area of the unit cell. Therefore, a more sophisticated model is sought in order to improve the accuracy of this model.

4.2.4 A Second-Order Circuit Model of the UC-EBG

Of course, it should be expected that a few inductors will not reasonably model the central node of the unit cell, especially for some designs of the UC-EBG in which the node occupies a substantial fraction of the unit-cell's area. As such, a more sophisticated modes is desired, one which takes into account some of the geometrical and electrical properties of the nodal region. Such a model may be found in works on artificial dielectrics (as discussed in section 1.2.2; see works such as [363] on the Transmission-Line Matrix solutions to Maxwell's equations), which employ grids of TL elements to model wave propagation in multiple dimensions. Using such a modelling approach yields the equivalent-circuit of Fig. 4.25a, in which the shunt loading inductors have been replaced with a grid of smaller TL elements, with lengths of either $a/3$ or $a/6$ with effective permittivity $\epsilon/2$, as indicated in Fig. 4.25b. The permittivity ϵ, and other properties of the TL sections used to model the node are determined through extracting the properties of a PPW of width a on a 1.524 mm-thick RO-3003 substrate (with relative permittivity $\epsilon_r = 3.0$ and loss tangent $\tan\delta = 0.001$) with 35 μm copper cladding. It should be noted that there is some flexibility in choosing these values, since there exists no known rigorously "correct" solution.

The resulting data are given in Fig. 4.26, where it may be noted that there is much better agreement between the circuit and HFSS data than the previous first-order circuit model of Fig. 4.24. The upper bands near 4-5 GHz are much more accurately represented, with their dispersive properties mostly

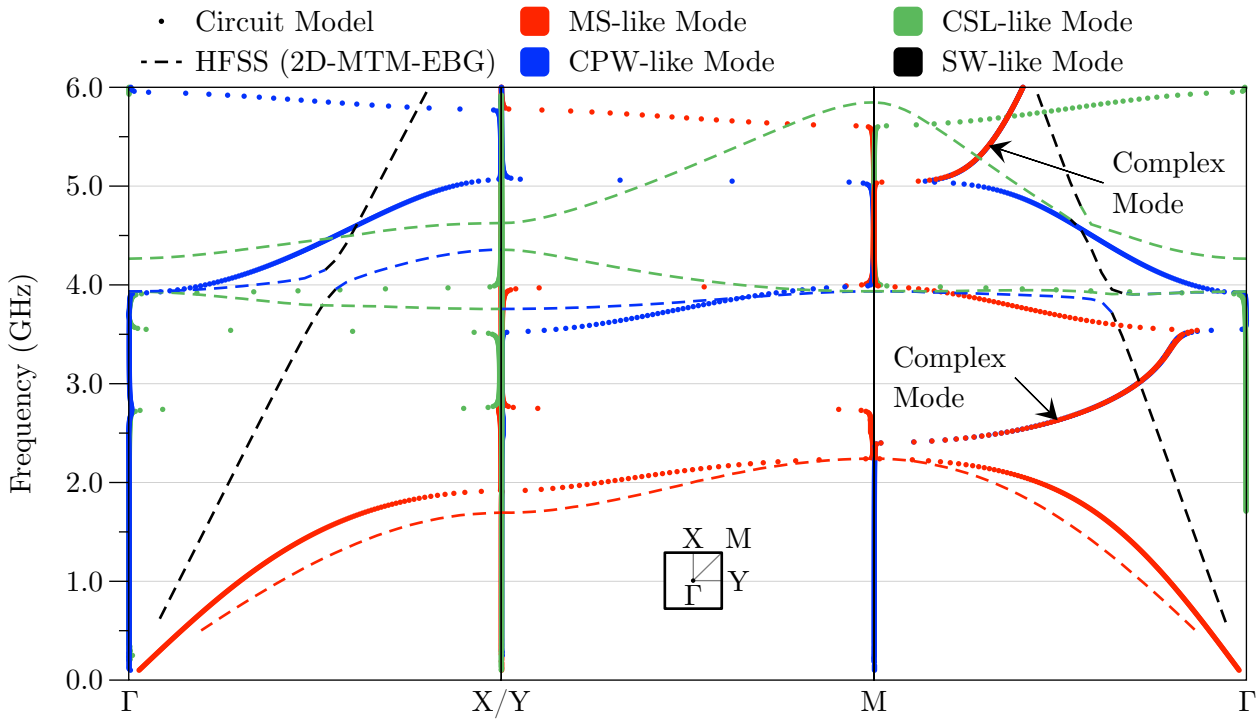

Figure 4.24: Simulated dispersive properties (imaginary components only) of the 2D-MTM-EBG simulated in HFSS, corresponding to the structure shown in Figs. 4.19b (indicated with the dashed curves), and the dispersive properties of the first-order equivalent-circuit model shown in Fig. 4.17 (indicated with the solid points). Although the circuit-model reproduces some key dispersive properties of the unit cell, the data are generally in poor agreement.

reproduced qualitatively by the circuit model. Interestingly, the complex modes which exist in the MS-CPW-mode bandgaps in all Brillouin zones are not coincident at the X/Y-point near 2.6 GHz. Further investigation yields that at this frequency the modes possess the same complex propagation constants in both zones, with real components of roughly 230 nepers. The meaning of such an arrangement – while interesting – is uncertain, and not investigated further in this work.

4.2.5 Miniaturizing the UC-EBG

To further illustrate the value of the proposed model, this section investigates the agreement between the data produced by the second-order circuit model and the HFSS simulation model in the case of much more extreme miniaturization. To produce such miniaturization, the loading capacitances $2C$ are increased to values of 5.0 pF from 0.4 pF. The resulting data are shown in Fig. 4.27, where it may be observed that two data sets are in much closer agreement. This indicates that the circuit model may be used to rapidly and accurately predict the behaviors of highly miniaturized UC-EBG structures, which has not been previously modelled to such a high degree of accuracy.

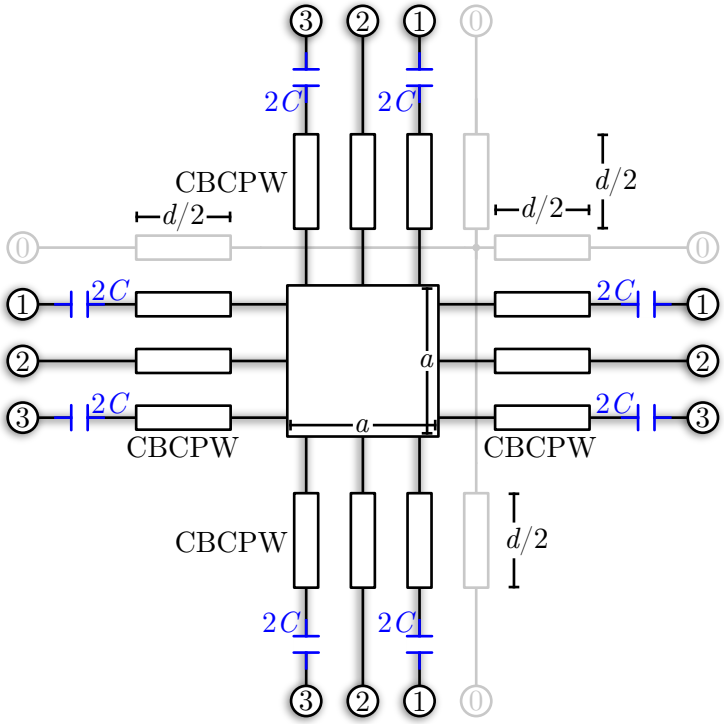

(a)

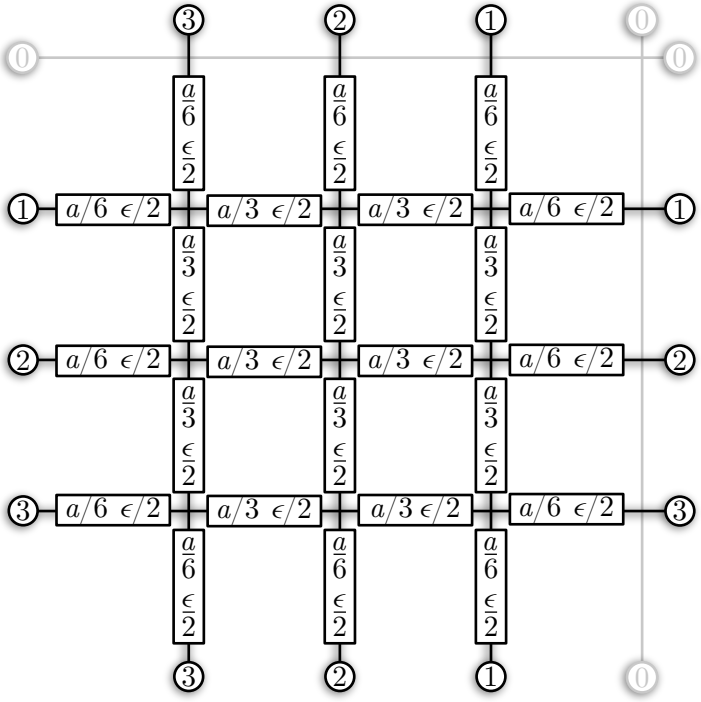

(b)

Figure 4.25: a) Proposed second-order 2D circuit model of the UC-EBG. The nodal region's inductors of the first order-model shown in Fig. 4.17 are replaced with the square network shown in Fig. 4.25b of dimension a. b) Proposed grid network of TLs, each with a length $a/6$ and effective permittivity $\epsilon/2$.

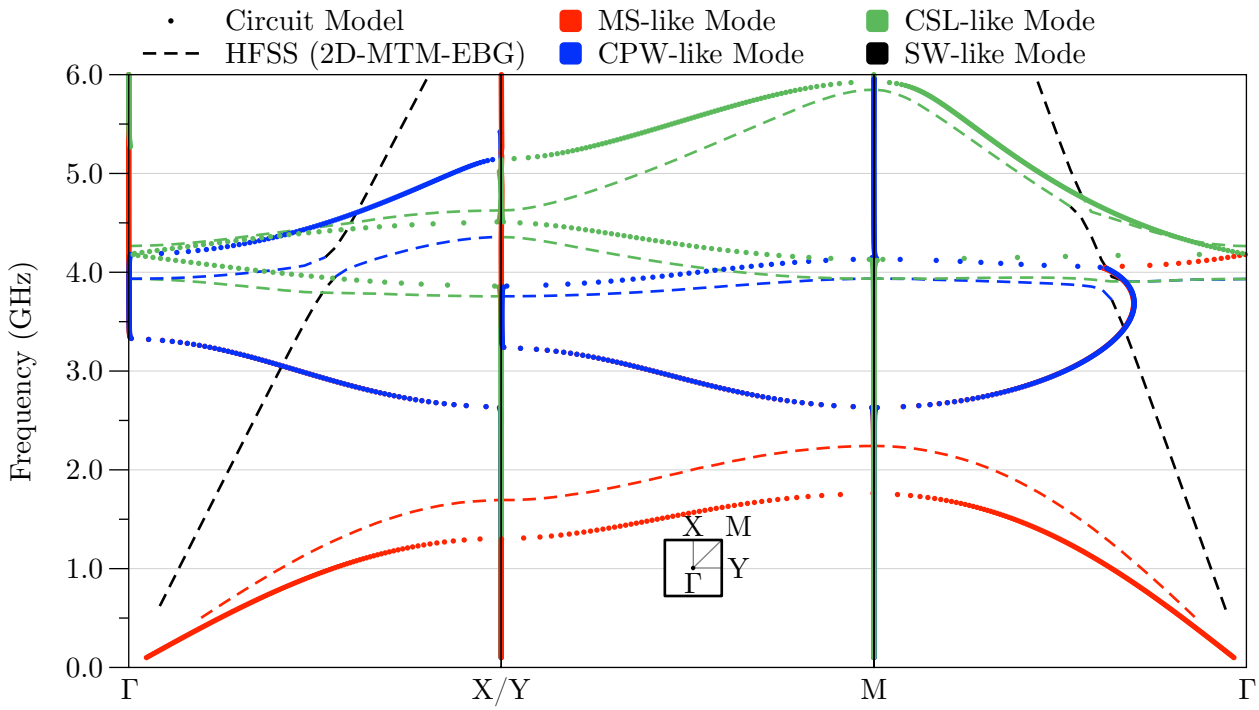

Figure 4.26: Simulated dispersive properties (imaginary components only) of the 2D-MTM-EBG simulated in HFSS, corresponding to the structure shown in Figs. 4.19b (indicated with the dashed curves), and the dispersive properties of the second-order equivalent-circuit model shown in Fig. 4.25a (indicated with the solid points). The circuit-model data are in much better agreement with the HFSS data than those of the first-order model of Fig. 4.24.

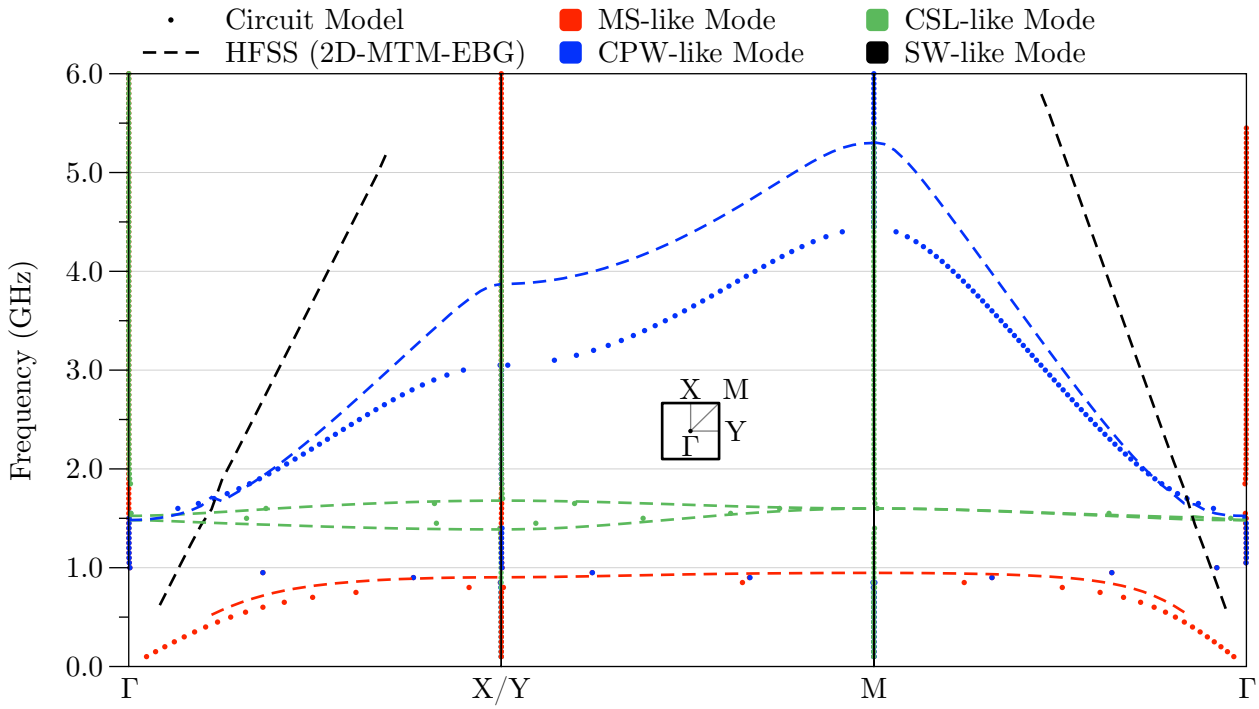

Figure 4.27: Simulated dispersive properties (imaginary components only) of the HFSS (dashed curves) and equivalent-circuit (solid points) models, miniaturized with loading capacitance values of $2C = 5.0$ pF. The data are generally in good agreement, demonstrating the utility of the model towards predicting the behavior of miniaturized structures such as the UC-EBG.

4.3 Examples

While the previous sections have focused primarily dispersive properties (i.e., Bloch propagation constants) of various networks, this section utilizes the full extent of the theory developed in Chapter 3 to determine various model properties of proposed complex MTL-MTM networks. These properties are confirmed via their extraction from full-wave HFSS simulations, and comparison with those data predicted by the circuit models – where it is found that in general, the two data sets are in good agreement. Three examples are studied to illustrate the diversity of models which may be solved via the generalized proposed processes: a 2D, two-axis, anisotropic model of the MTM-EBG, a 2D, three-axis, effectively isotropic hexagonal structure based on a planar arrangement of CBCPS lines, and finally a 3D, three-axis, effectively isotropic primitive cubic lattice structure based on the series intersection of four co-linear wires.

These examples show that the modal properties of the structures may be rapidly and accurately determined from equivalent-circuit models, even in frequency ranges where no between a mode's propagation bands where full-wave solvers generally do not determine any modal properties at all (although of course technically possible, these modes are often considered undesired and not available to the end user in HFSS).

Regrettably, there are a few notable minor unavoidable issues with the process process and/or data. Solving the generalized eigensystems of dense, complex, matrices to a high degree of precision is not a trivial task. The numerical solver used was not always able to find solutions of the eigenmodes and/or eigenvectors at all frequency points, especially in the Γ-M and Γ-R Brillouin zones. At the frequency points where the solver did not function as desired, the solver output a warning that the matrices were ill-conditioned, and proceeded to fill in the values with essentially random data. For the purposes of clarity, these points have been manually removed from the data, such that there are a few notable gaps in the circuit model data. Additionally, the HFSS solver unfortunately solves for not only the TL modes predicted the circuit analysis, but also many non-TL modes which may exist in a given structure as well (such as the TM_0 SW mode). Once again – for the purposes of clarity – these modes have been manually edited out from the data, but there are regrettably a handful of data points resulting from the coupling of the TL and non-TL modes which exist as deviations from these ideal case of only TL modes. The presence of the non-TL modes was determined by investigating the balance of currents in the modes: since the calculated currents of non-TEM modes should not balance, they are readily identifiable.

Currents are extracted from HFSS as complex quantities using (2.8b), where their values have been essentially arbitrarily scaled by the HFSS eigensolver. As such, these values are scaled before they are presented, using the same process presented in section 3.1.3 as the current eigenvectors determined from the equivalent-circuit models. However, the Bloch impedance quantities extracted from HFSS are not scaled and are presented exactly as computed by HFSS, since the scaling factors of the powers and (the squares of) currents are related and directly cancel through the application of E.2.

Applications of the MTM structures described in this section extend to the large range of possible and useful devices discussed in section 1.1, among others.

4.3.1 A 2D Model of a MTM-EBG

A 2D equivalent-circuit model of the MTM-EBG structure is proposed and analyzed in this section. The unit cell is again designed on a conductor-backed 60-mil-thick RO-3003 dielectric possessing 35 μm copper thickness. Unlike the original 1D MTM-EBG model (presented in section 2.5) – which simply models the capacitive gaps as presenting an effective series capacitance to the host CBCPW – this model seeks to model the transversely-propagating TL modes supported across this gap. To emphasize the importance of these region, the MTM-EBG is designed with smaller CPW ground regions, as shown in Fig. 4.28a, where the MTL nature of the lines long both axes become apparent. A proposed circuit model – while already introduced in Fig. 3.15 – is given for convenience as Fig. 4.28b, where the conductors around the transverse capacitive gap have been modelled as a CBCPS. The various properties of the unit cell are given in Table 4.5. As a result of these modifications, the unit cell is analyzed on a rectangular Bravais lattice, which will exhibit strong anisotropy.

The specified geometric properties give the host CBCPW along the x-axis the properties (at a frequency $\omega = 2\pi \times 1.0$ GHz):

$$[\gamma_M]_x = diag \begin{bmatrix} 0.0566 + j33.0190 \\ 0.0683 + j30.4700 \\ 0.0749 + j29.6390 \end{bmatrix} \tag{4.2a}$$

$$[Z_{cM}]_x = diag \begin{bmatrix} 45.7780 - j0.0043 \\ 189.4700 - j0.0670 \\ 106.5600 - j0.1433 \end{bmatrix} \tag{4.2b}$$

$$[T_I]_x = \begin{bmatrix} 0.3488 & 1.000 & 0.5000 \\ 0.3024 & 0.000 & -0.9010 \\ 0.3488 & -1.000 & 0.5000 \end{bmatrix} \tag{4.2c}$$

and the specified geometric properties along the y-axis gives the host CBCPS the properties (at a frequency $\omega = 2\pi \times 1.0$ GHz):

$$[\gamma_M]_y = diag \begin{bmatrix} 0.0600 + j32.5640 \\ 0.0750 + j29.9600 \end{bmatrix} \tag{4.3a}$$

$$[Z_{cM}]_y = diag \begin{bmatrix} 63.4680 - j0.0135 \\ 159.7100 - j0.0923 \end{bmatrix} \tag{4.3b}$$

$$[T_I]_y = \begin{bmatrix} 0.5000 & 1.0000 \\ 0.5000 & -1.0000 \end{bmatrix} \tag{4.3c}$$

With the node equations given in (3.61), the dispersive properties of the unit cell may be computed via the proposed processes, and compared with the data obtained for an equivalent structure solved in HFSS. The resulting dispersion diagram is given in Fig. 4.29, where the phase shifts produced by the circuit model are given with the black dots, and the similar data produced by HFSS are given by the solid

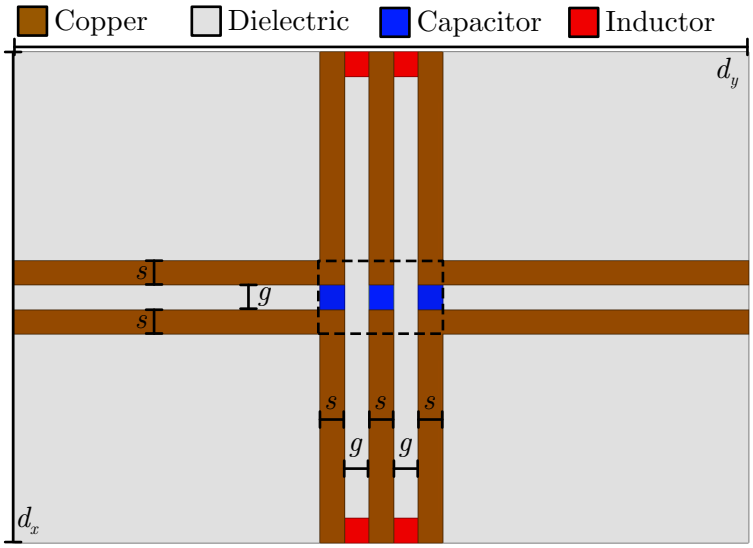

(a)

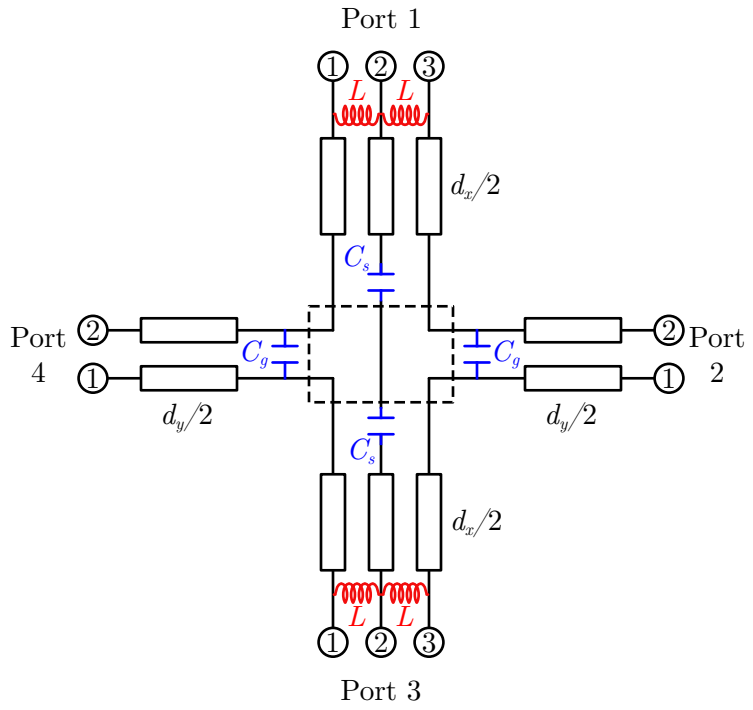

(b)

Figure 4.28: The MTM-EBG unit cell studied in this example: a) HFSS layout with indicated dimensions given in Table 4.5, designed on a conductor-backed 60-mil-thick RO-3003 dielectric with 35 μm copper thickness, and b) proposed 2D equivalent-circuit model of the MTM-EBG. The unit-cell's capacitive gaps are modelled as supporting a CBCPS MTL on the axis transverse to the typical direction of propagation. The rectangular unit cell is anisotropic, and consists of two axes interconnected by the nodal region indicated with the dashed curves. The ports all share a common reference (not shown).

Table 4.5: Parameters of the MTM-EBG structure and circuit model shown in Fig. 4.28.

Parameter	**Value**
X-Axis period d_x	20.0 mm
Y-Axis period d_y	30.0 mm
Strip Width s	1.0 mm
Gap Width g	1.0 mm
Loading Inductance L	10.0 nH
Grounds Loading Capacitance C_g	1.0 pF
Strip Loading Capacitance C_s	1.0 F ($\to \infty$)

colored curves. The dispersion data are generally in good agreement between the two models. The largest discrepancies may be attributed the physical size of the node, which has dimensions of 3 mm × 2 mm, but which is not taken into account by the circuit model.

Additionally, for each Brillouin zone, the Bloch phase shifts, Bloch impedances, and current mode definitions are given for each mode in Fig. 4.30. The Bloch properties of the modes are computed as discussed in Appendix E. One again, it may be observed that there is good agreement between the properties predicted by the circuit model and HFSS. It is a critical point to this work that if the proper scaling of the mode definitions (as discussed in section 3.1) are not completed, there is no reason for the current mode definitions, modal Bloch impedances, and other modal properties to agree between the extracted HFSS data and circuit mode data at all – other than of course by coincidence. The fact that the values agree well is corporate validation of the many theories and analyses presented in this work.

4.3.2 A 2D Loaded Hexagonal Unit-Cell

This section investigates a 2D hexagonal unit cell, comprised of a solid conductor backing and CPS lines along each fundamental lattice vector. The lines are loaded with inductors and capacitors, to yield some interesting dispersion behaviors. The unit cell – which is symmetric about all three axes – is again designed on a conductor-backed 60-mil-thick RO-3003 dielectric possessing 35 μm copper thickness. The layout of the unit cell's simulation model in HFSS is shown in Fig. 4.31a – with various properties detailed in Table 4.6 – and the proposed equivalent-circuit model is shown in Fig. 4.31b.

The specified geometric properties give the host CBCPS (at a frequency $\omega = 2\pi \times 1.0$ GHz):

$$[\gamma_M] = diag \begin{bmatrix} 0.0484 + j32.9110 \\ 0.0953 + j29.3470 \end{bmatrix} \tag{4.4a}$$

$$[Z_{cM}] = diag \begin{bmatrix} 98.969 - j0.0000 \\ 159.39 - j0.0000 \end{bmatrix} \tag{4.4b}$$

$$[T_I] = \begin{bmatrix} 0.5000 & 1.000 \\ 0.5000 & -1.000 \end{bmatrix} \tag{4.4c}$$

In the center nodal region of the unit cell (indicated by the dashed lines in the circuit model of

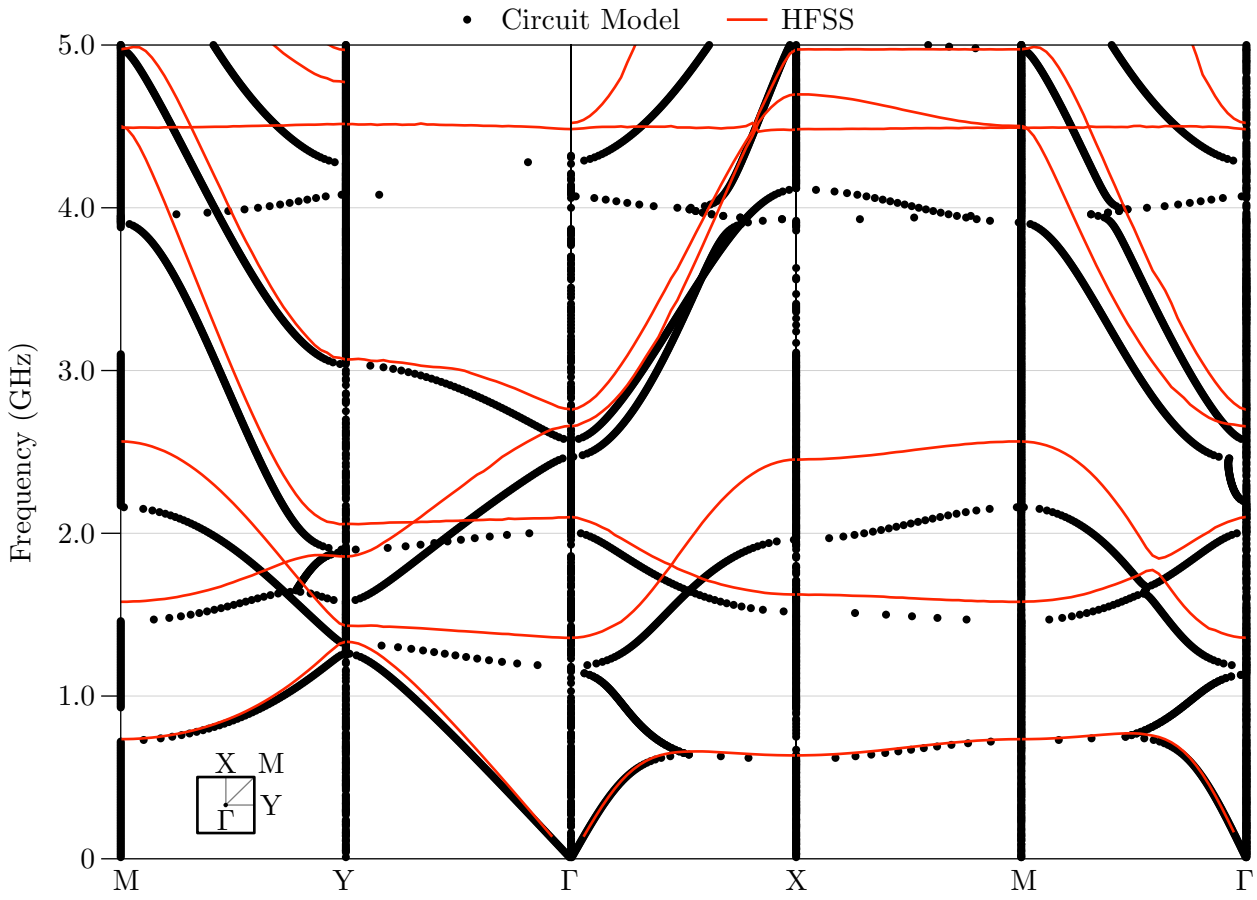

Figure 4.29: Dispersion diagram of the example MTM-EBG. The circuit model's data (back dots) and HFSS data (red solid curves), are generally in good agreement, although the agreement diverges as frequency increases, most likely due to the cell's unmodelled nodal region. Qualitatively, the data are very similar, indicating that the model is predicting – in general – the correct modal behaviors.

Table 4.6: Parameters of the hexagonal unit cell and circuit model shown in Fig. 4.31a.

Parameter	**Value**
Sides Spacing d	$\sqrt{3} \times 10.0$ mm
Strip Width s	0.5 mm
Gap Width g	0.5 mm
Inductor Width w_L	0.5 mm
Capacitor Width w_C	0.5 mm
Loading Inductance L	5.0 nH
Loading Capacitance C	1.0 pF

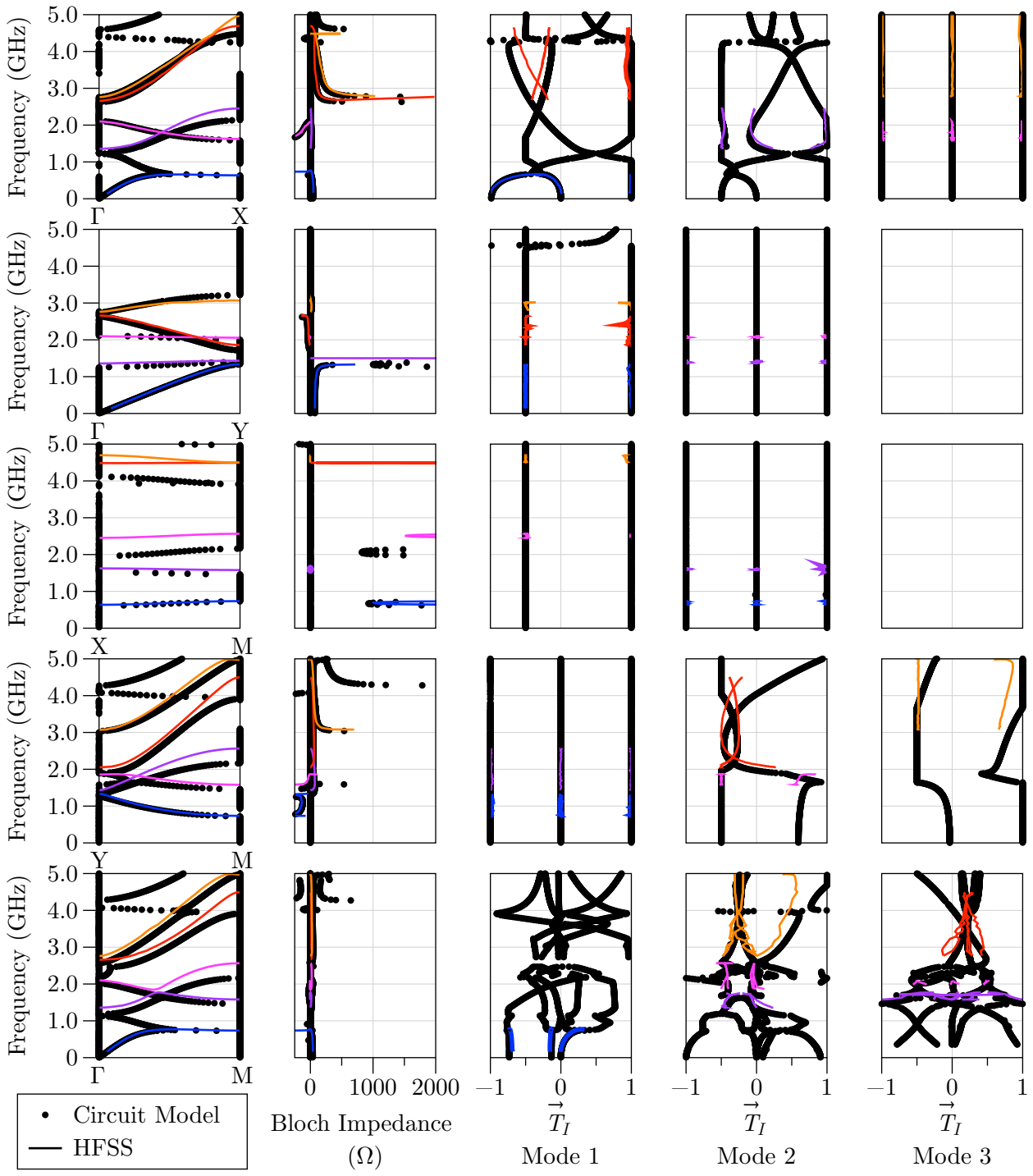

Figure 4.30: Dispersion properties of the example MTM-EBG between 0 and 5 GHz. The circuit model's data (back dots) and HFSS data (colored solid curves), are good qualitative agreement, although the agreement diverges as frequency increases, most likely due to the cell's unmodelled nodal region. Columns from left to right give imaginary components of Bloch phase shifts, real components of Bloch impedances, and real components of the current mode definitions for each mode. Rows from top to bottom detail the Γ-X, Γ-Y, X-M, X-M, and Γ-M Brillouin zone contours, respectively.

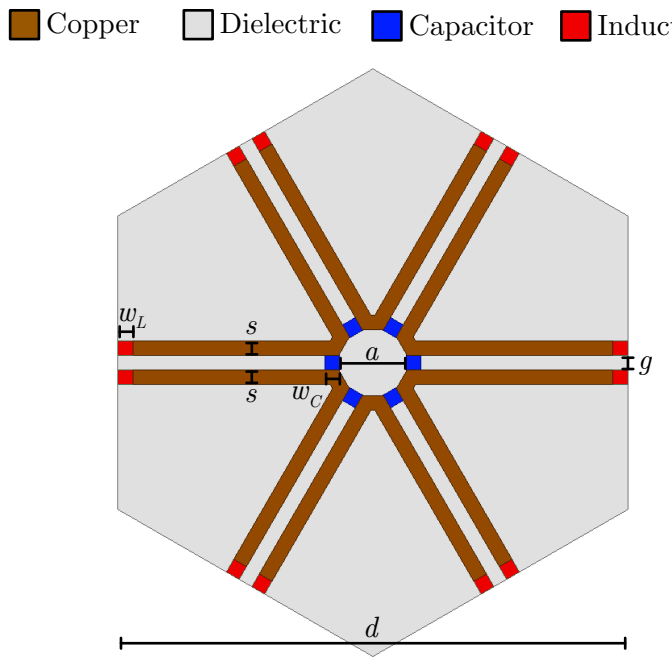

(a)

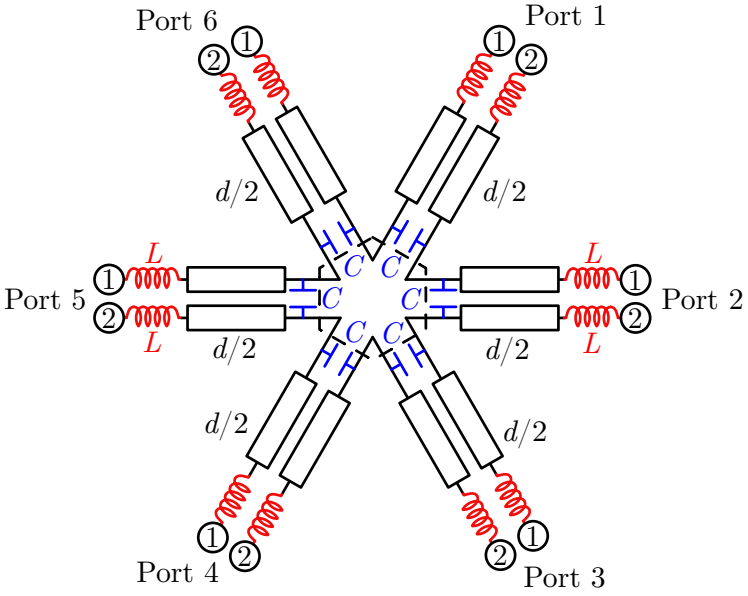

(b)

Figure 4.31: The hexagonal unit cell studied in this example: a) HFSS layout with indicated dimensions given in Table 4.6, designed on a conductor-backed 60-mil-thick RO-3003 dielectric with 35 μm copper thickness, and b) proposed 2D equivalent-circuit model of the structure. The ports all share a common reference due to the solid conductor backing (not shown).

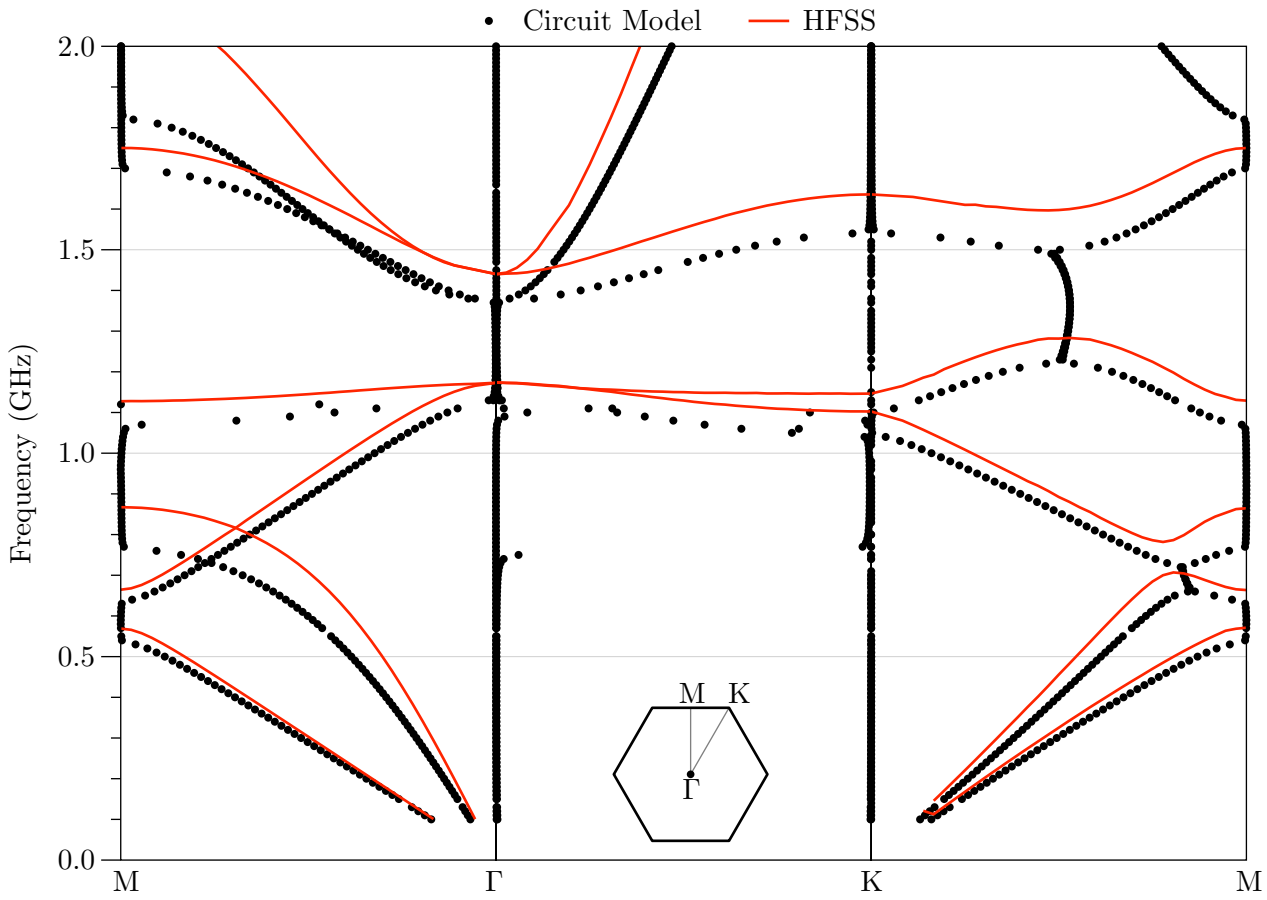

Figure 4.32: Dispersion diagram of the example hexagonal unit cell. The circuit model's data (back dots) and HFSS data (red solid curves), are generally in good agreement, although the agreement diverges as frequency increases, most likely due to the cell's unmodelled nodal region. Qualitatively, the data are very similar, indicating that the model is predicting – in general – the correct modal behaviors.

Fig. 4.31b), the strips are connected to their nearest neighbor from the adjacent axis, and the resulting M-parameters indicates that conductors possess equal currents and voltages. The data produced by the HFSS simulation and equivalent circuit models are shown in the Fig. Fig. 4.32, where it is observed that the circuit model once again faithfully reproduces the qualities of the band diagram predicted by the HFSS model. The various frequency shifts and other discrepancies are once again attributed to the lack of modelling of the nodal region, which was not accounted for in the circuit model.

Additionally, for each Brillouin zone, the Bloch phase shifts, Bloch impedances, and current mode definitions are given for each mode in Fig. 4.33. One again, it may be observed that there is good agreement between the properties predicted by the circuit model and HFSS – with the exception of some of the Bloch impedance values in the M-K zone. In-depth investigation yields that curiously, both the circuit model and the currents extracted from HFSS indicate that many of the bands are in fact mildly complex – despite the fact that the bands do not appear in conjugate pairs, and that HFSS has no issues finding these bands.

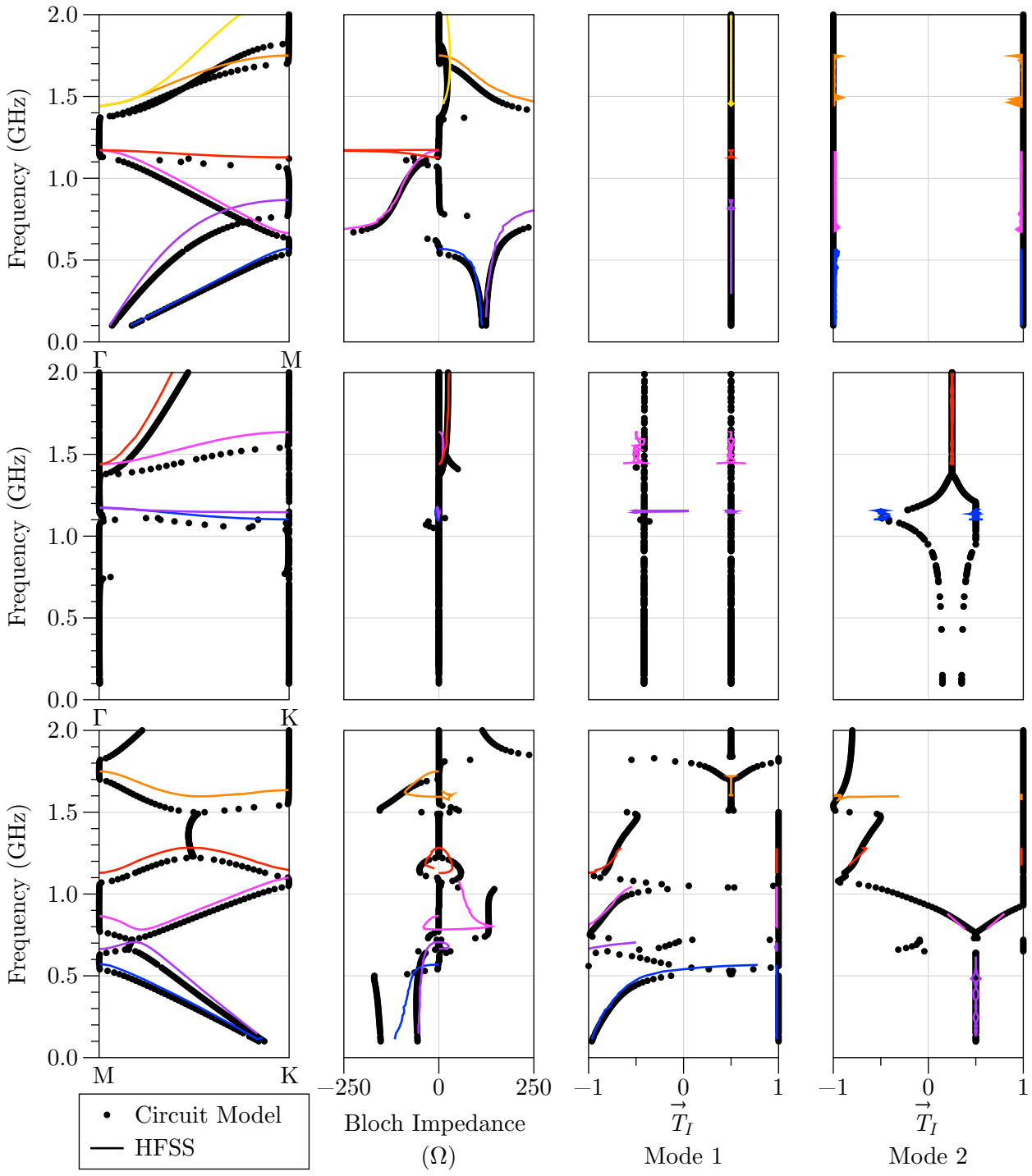

Figure 4.33: Dispersion properties of the example hexagonal unit cell between 0 and 2 GHz. The circuit model's data (back dots) and HFSS data (colored solid curves), are good qualitative agreement, although the agreement diverges as frequency increases, most likely due to the cell's unmodelled nodal region. Columns from left to right give imaginary components of Bloch phase shifts, real components of Bloch impedances, and real components of the current mode definitions for each mode. Rows from top to bottom detail the Γ-M, Γ-K, and K-M Brillouin zone contours, respectively.

Table 4.7: Parameters of the primitive cubic unit cell and circuit model shown in Fig. 4.37.

Parameter	**Value**
Cubic Period (Side Length) d	25.0 mm
Node Size a	6.0 mm
Wire Conductor Radius r	0.5 mm
Wire Conductor Spacing (center-to-center) s	2.8 mm
FR-4 Slab Width w	1.5 mm
FR-4 Slab Thickness t	10.0 mils
Inductor Length l_L	1.0 mm
Capacitor Length l_C	1.0 mm
Loading Inductance L	10.0 nH
Loading Capacitance C	1.0 pF

4.3.3 A 3D Loaded Primitive Cubic Unit-Cell

Finally, this section investigates a 3D primitive cubic unit cell, comprised of the intersection of four parallel cylindrical wire conductors along each fundamental lattice vector. The lines are loaded with series inductors and shunt capacitors at the node, which models the symmetrical condensed nodal topology of Johns [447]. The unit cell – which is symmetric about all three axes – is ideally suspended in a vacuum. However, the embedding of the unit cell in a homogenous medium allows for the eigensystem to be solved by any arbitrary set of degenerate modes, which in turns means that any arbitrary Bloch impedance may be produced (the modes still each have a single, determinable, impedance value). In order to mitigate this result, a small asymmetric strip of lossy FR-4 material is inserted between the conductors on each axis, which breaks the modal degeneracy of the system and forces both HFSS and the circuit model to produce consistent sets of modes. The layout of the unit cell's simulation model in HFSS is shown in Figs. 4.34a and 4.34b – with various properties detailed in Table 4.7 – and the proposed equivalent-circuit model is shown in Fig. 4.34c.

The specified geometric properties give the host four-wire MTL (at a frequency $\omega = 2\pi \times 1.0$ GHz):

$$[\gamma_M] = diag \begin{bmatrix} 0.0462 + j22.3030 \\ 0.0282 + j20.9544 \\ 0.0213 + j20.9601 \end{bmatrix} \tag{4.5a}$$

$$[Z_{cM}] = diag \begin{bmatrix} 187.4100 - j0.0444 \\ 59.9930 - j0.0571 \\ 196.8400 - j0.1606 \end{bmatrix} \tag{4.5b}$$

$$[T_I] = \begin{bmatrix} -1.0000 & -0.5000 & 0.0000 \\ 0.0000 & 0.5000 & 1.0000 \\ 1.0000 & -0.5000 & 0.0000 \end{bmatrix} \tag{4.5c}$$

The conductors are connected in the center nodal region (which is not included in the circuit model) as

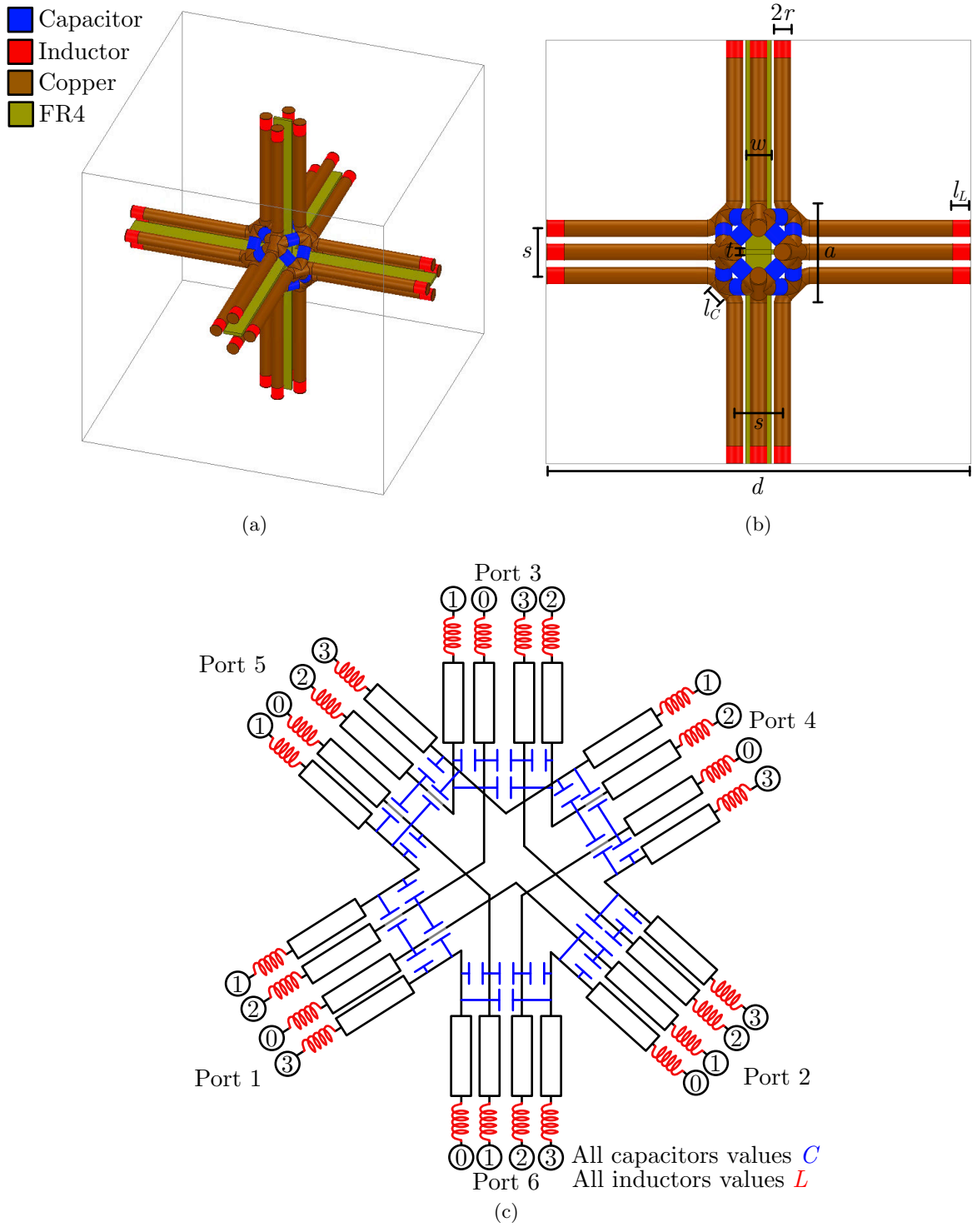

Figure 4.34: The primitive cubic unit cell studied in this example: a) HFSS layout (trimetric view) and b) HFSS layout (face-centered view) with indicated dimensions given in Table 4.7, in which the FR4 slabs exists for the sole purpose of breaking degenerate modes, and c) proposed equivalent-circuit model of the structure, in which all loading capacitors (near the center nodal region) have value C, and loading inductors (on the outer edges of the unit cell) possess value L.

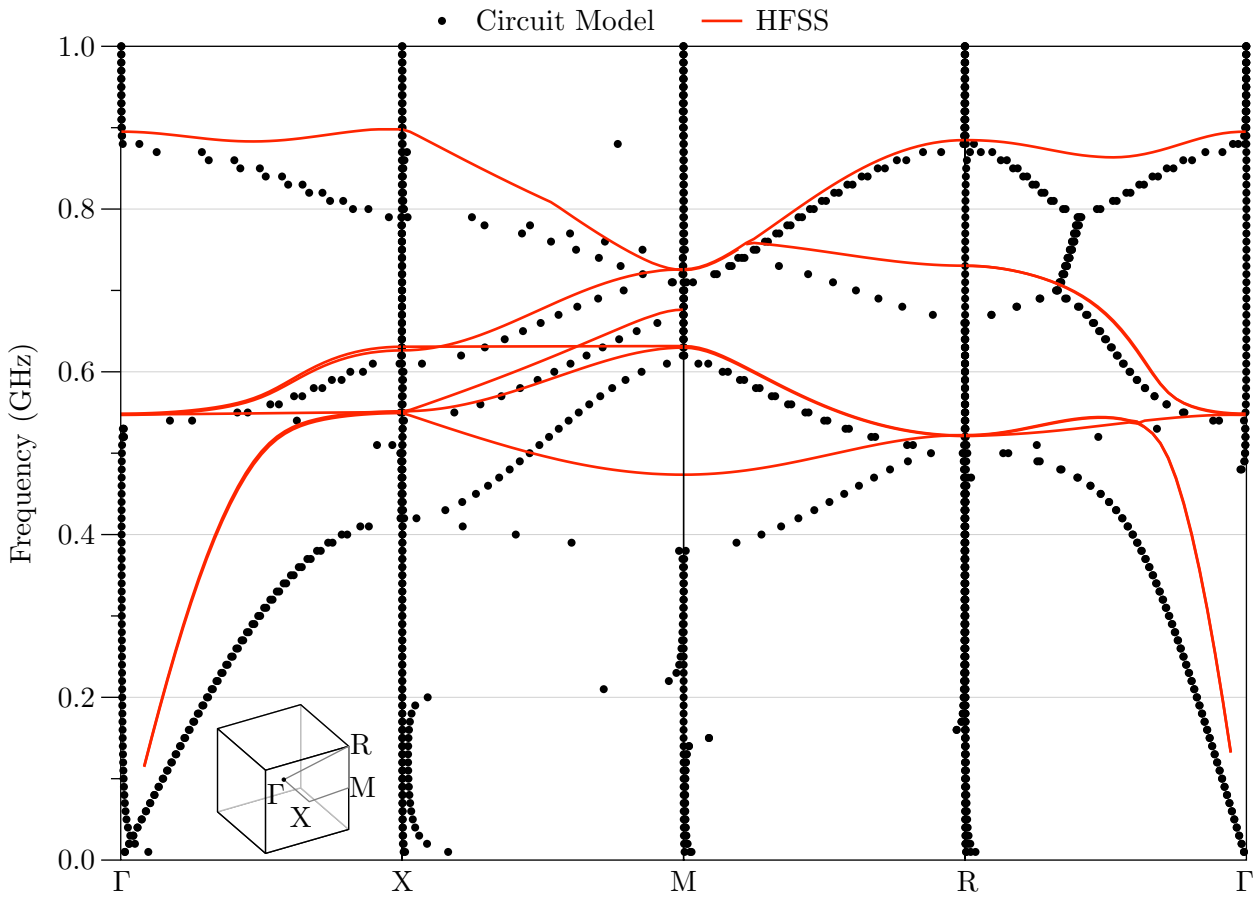

Figure 4.35: Dispersion diagram of the example primitive cubic unit cell. The circuit model's data (back dots) and HFSS data (red solid curves), are in reasonable (though not good) agreement. In particular, the lowest-frequency bands are significantly different, indicating underlying issues with the model.

specified in the series condensed node model. The data produced by the HFSS simulation and equivalent circuit models are shown in the figures below, with the Bloch phase shifts over the full Brillouin zone contours given in Fig. 4.35 – where it is observed that the circuit model reproduces the band diagram predicted by the HFSS model to a reasonable degree both qualitatively and qualitatively. However, the agreement between the two data sets is not nearly as good as the previous examples, especially in the low-frequency bands. The unmodelled nodal region once again likely contributes to various frequency shifts and other small variations among the data, however, this should not impact the low-frequency bands in the Γ-X and Γ-R regions as much as it appears to. Therefore, it is expected that there is some new phenomena occurring in this unit cell that is not present in the previous cells – as will be elaborated on shortly.

Again, for each Brillouin zone, the Bloch phase shifts, Bloch impedances, and current mode definitions are given for each mode in Fig. 4.36. Various discrepancies in each zone are discussed.

The topmost row details the Bloch modal properties in the Γ-X Brillouin zone contour. While the mode definitions appear to all be in agreement, both the Bloch impedances and Bloch phase shifts do not

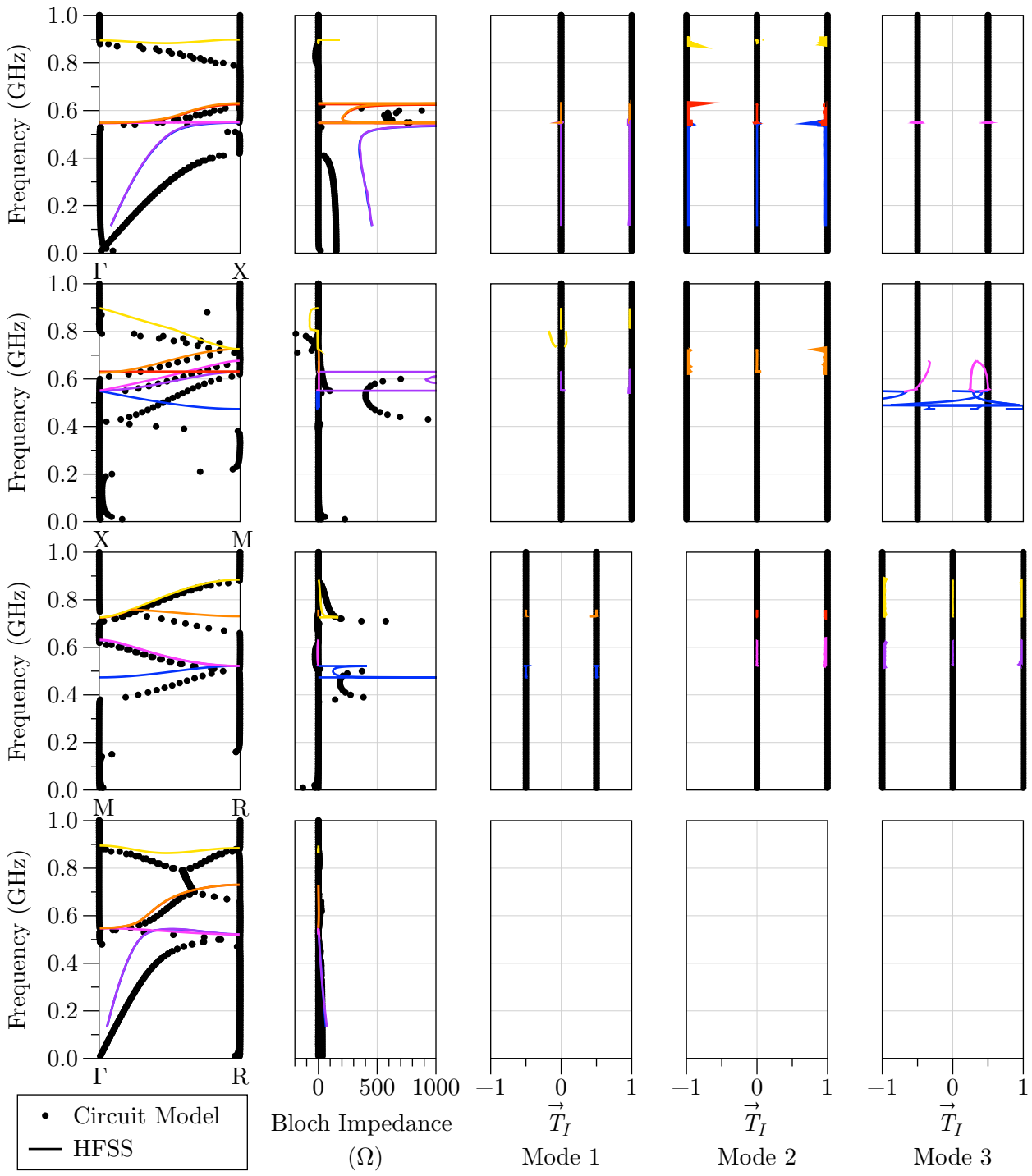

Figure 4.36: Dispersion properties of the example primitive cubic unit cell between 0 and 1 GHz. The circuit model's data (back dots) and HFSS data (colored solid curves), agree qualitatively as well as quantitatively to some extent. Columns from left to right give imaginary components of Bloch phase shifts, real components of Bloch impedances, and real components of the current mode definitions for each mode. Rows from top to bottom detail the Γ-X, X-M, M-R, and Γ-R Brillouin zone contours, respectively. While the mode definitions appear to all be in agreement, both the Bloch impedances and Bloch phase shifts do not agree, including at sufficiently low frequencies.

agree, including at sufficiently low frequencies where the effects of parasitics are diminished.

Curiously, the Bloch impedances of the lowest bands possess a relatively large slope at their lowest frequencies, which is not seen in other non-dispersive bands of previous models. Considering these discrepancies, a possible reason is that the TL modes defined in (4.5) – while correct for an isolated system of four conductors – actually interact with other modes. This is not to say other bands of other modes, but rather modes which yield the same voltage and current mode definitions for the observed conductors, yet which couple with adjacent unit cells (for example) – yielding drastically different impedance and propagation constants, as observed in the data. This hypothesis is supported through observation of the electric fields of one of the lowest-frequency modes on one $y-z$ face of the unit cell, shown in Fig. 4.37a, where indeed the fields extend strongly to the edges of the unit cell, similar to those of a plane wave.

Proceeding on the assumption that the inclusion of the modelling of periodic boundaries on the host MTL should assist with resolving this discrepancy, the host MTL is modified with PEC boundaries on the vertical boundaries of the cross-section, and PMC boundaries on the horizontal boundaries, to emulate a polarization-dependent set of periodic boundary conditions. The electric-field distributions of the first two modes of this new MTL which are similar to the field distribution of Fig. 4.37a are shown in Figs. 4.37b and 4.37c. Note that while the fields of Fig. 4.37b relatively strong inside the region of MTL conductors (similar to the fields of Fig. 4.37a), the fields inside the region of MTL conductors in Fig. 4.37c possess a relatively low magnitude – and vice-versa for the fields outside the region of MTL conductors for the two modes. Therefore, combining them with even weighting should produce fields more like those observed in the unit-cell of Fig. 4.37a – which is demonstrated in Fig. 4.37d, and which appears to be in good agreement with the unit-cell fields. Unfortunately, a method for producing a "second-order" equivalent-circuit model based on these information could not be validated, and is considered an effort outside of the scope of this work.

The Bloch modal properties in the X-M Brillouin zone contour indicate that the Bloch phase shifts and impedances are in relatively reasonable agreement, given the differences in band structure predicted by the circuit and HFSS models. However, it may be seen that some of the bands given by HFSS possess frequency-dependent mode definitions – observable in the right-most panel – which do not agree with the frequency-independent modes predicted by the circuit model. The existence of these curious modal properties appear to be further evidence that there exist other effects in the MTL environment past what is being predicted by the circuit model.

While the data shown for the M-R Brillouin zone contour are in good agreement with each other, the Γ-R Brillouin zone data possess several deficiencies. Firstly, the modal currents could not be successfully extracted from HFSS (the mode definitions varied at nearly every point, reminiscent of the data produced by multiple degenerate modes). Secondly, the lower bands of the HFSS data possess properties not predicted by the circuit model at low frequencies, indicating once again issues with the host MTL. The higher-frequency bands predicted by HFSS are much more dispersive than those predicted by the circuit model, resulting in sharp decreases in the Bloch impedance values.

It is noted that these various issues with this particular primitive cubic structure may be overcome through the development of a more rigorous circuit model (in particular, a more elaborate model for

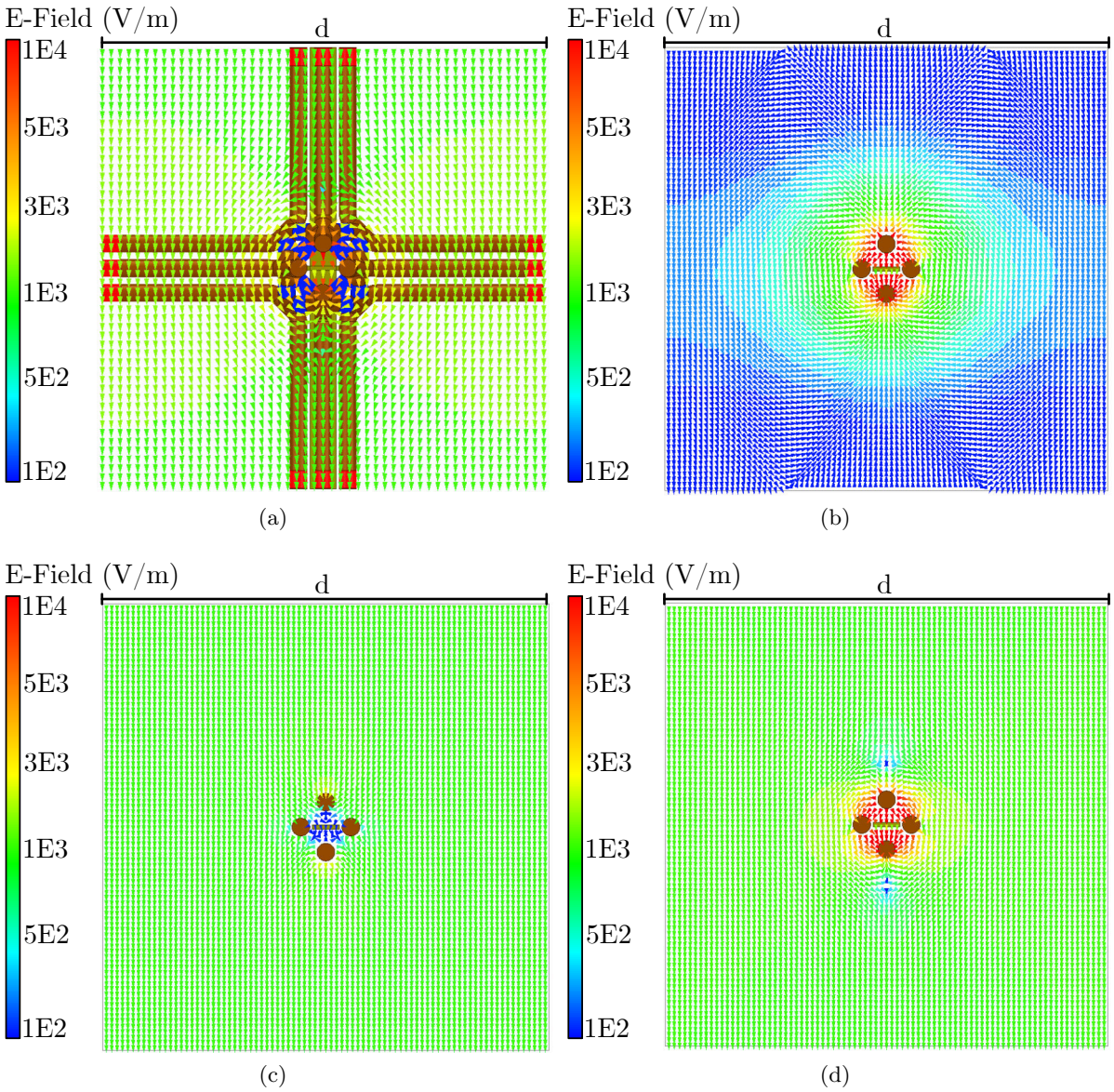

Figure 4.37: Electric-field distributions a) the transverse cross section of the primitive cubic unit cell in the $y-z$ plane; b) the associated TL mode of the host MTL best fitting the observed field distribution in Fig. 4.37a; c) the mode most similar to that of Fig. 4.37a, which is supported by PECs on the vertical unit-cell boundaries; and d) a weighted combination of the modes of Fig. 4.37b and Fig. 4.37c, which possesses may qualities similar to that of the unit cell shown in Fig. 4.37a.

the nodal region of the structure and a more sophisticated host MTL model). However, these have not been completed as they are considered to be outside of the scope of this work – which is primarily to demonstrate that such analyses may, in general, be successfully performed given a valid circuit model.

Chapter 5

Conclusion

5.1 Summary

This thesis has examined many facets of TEM wave propagation: starting with fundamental electromagnetic fields propagating in homogenous media, to TL modes in common multiconductor waveguides and TL-based periodic media, to multidimensional MTM networks comprised of various conductor and loading configurations. By using the commonalities among propagation modes in all cases, it has been shown that the properties of the modes supported by these complex networks may be readily determined – a process which greatly simplifies the design process of modern MTL-based MTMs. While there exist several disagreements between full-wave HFSS and circuit-model data for the most sophisticated structures that were not conclusively resolved, the core work of this thesis – the rapid computation of the Bloch modal properties of multidimensional, MTL-based MTMs – appears to have been successfully validated.

It was demonstrated that a key property of TL modes is that they are normal – i.e., all of the components of the mode possess phases within an integer multiple of π of each other. It was postulated that total charges (or currents) between the modal and terminal representations of the modes were equivalent; with this information, it was demonstrated that the mode definition matrices $[T_I]$ may be scaled to a unique set of values within a sign. Knowledge of the mode definitions allows for the computation of unique modal properties – such as characteristic impedance – which was validated experimentally.

In order to work with sophisticated networks, a new set of parameters – M-Parameters – were formally introduced and rigorously defined to overcome some of the shortfalls of other network representations such as $ABCD$-Parameters, Z-Parameters, or Y-Parameters. Using these parameters, a novel dispersion analysis for the computation of Bloch modal properties of a given network was derived, along with a method for concatenating general networks into one larger network described by a single set of M-Parameters. It was shown that the proposed process is more numerically efficient than the baseline "trivial process" by nearly a factor of one thousand.

Using the knowledge of advanced dispersion phenomena and modal properties, new devices were designed and analyzed. It was demonstrated that bandgap size could be modulated in a capacitively-loaded CBCPW unit cell through selection of which conductors the capacitor(s) were placed in. It was also shown that both bands on either side of bandgap could be used to produce similar phase shifts at

two different frequencies, allowing a host of novel dual-band devices to be designed and experimentally validated (such as the dual-band quadrature hybrid coupler investigated in this work) while using minimal additional resources such as PCB area. Using knowledge of MTL modal properties, a novel, fully-printed common-mode filter was designed and experimentally validated, which offers a wide suppression band without the need for vias or defected ground planes. One of the most prominent examples of the dispersion analysis is the modelling of the UC-EBG structure, which was investigated in detail, and found to be reasonably well-modelled as an intersection of MTM-EBG structures. It was further shown that, by replacing the nodal region with a model of the PPW as a grid of intersecting conductors, a higher level of accuracy could be achieved.

Lastly, a number of sophisticated unit cells – a 2D model of the MTM-EBG structure, a 2D hexagonal structure, and a 3D primitive cubic structure – were investigated. The dispersive properties of the unit cells, along with impedance and modal currents were extracted from full-wave solver HFSS. These data were compared with those obtained from proposed circuit models, and – aside from some obscure results obtained for the 3D structure, requiring future research – were found to be in reasonable agreement with each other.

5.2 Future Work

Undoubtedly, the large breadth of materials studied in this work leaves many loose ends. From a theoretical perspective, a large, gaping, hole left in this work is the inability to compute modal properties of complex modes. Since these modes are not normal, there does not exist any suitable method by which the mode definitions may be scaled – so these are ambiguous as well when observing complex modes. The failure in obtaining excellent quantitative agreement between HFSS simulations and the circuit-model-based simulations of Section 4.3 is most generally due to the lack of node models for the various structures. Modelling of these regions with more sophisticated parasitic components should allow for the rapid, accurate, modelling of these unit cells – and of course, solving the various modal issues plaguing the 3D cubic structures is of interest to parts of the electromagnetics community focused on achieving an isotropic, volumetric, miniaturized MTM element.

Applications of volumetric MTMs were not studied in this work. However, now that the analytical foundations have been determined, the ideas presented in Section 1.2.3 may be implemented with a rigorous methodology for analyzing, designing, and miniaturizing the associated devices. Of particular interest in 3D printing of such volumetric structures – with recent advances in the technology, it may soon be possible to fully print 3D lattice-based devices based on metallic elements. Such a process, free of present-day constraints such as cost and manufacturing complexity, could dramatically increase adoption of MTMs in modern technology.

Bibliography

[1] T. S. Rappaport, Y. Xing, O. Kanhere, S. Ju, A. Madanayake, S. Mandal, A. Alkhateeb, and G. C. Trichopoulos, "Wireless communications and applications above 100 GHz: Opportunities and challenges for 6G and beyond," *IEEE Access*, vol. 7, pp. 78 729–78 757, 2019.

[2] D. Chandramouli, R. Liebhart, and J. Pirskanen, *5G for the Connected World*, 1st ed. Hoboken, New Jersey, USA: John Wiley & Sons, Inc., 2019.

[3] "WRC-15: Radio regulations articles, article 2, section 1: Frequency and wavelength bands," International Telecommunication Union, Tech. Rep., Jan. 2016.

[4] "IEEE 521-2019: IEEE standard letter designations for radar-frequency bands," Institute of Electrical and Electronics Engineers, Tech. Rep., Jan. 2019.

[5] C. Blackman and S. Forge, "PE 631.060: 5G deployment: State of play in europe, USA and asia," European Parliament's Committee on Industry, Research and Energy, Tech. Rep., Apr. 2019.

[6] F. Boccardi, R. W. Heath, A. Lozano, T. L. Marzetta, and P. Popovski, "Five disruptive technology directions for 5G," *IEEE Commun. Mag.*, vol. 52, no. 2, pp. 74–80, 2014.

[7] C.-X. Wang, F. Haider, X. Gao, X.-H. You, Y. Yang, D. Yuan, H. M. Aggoune, H. Haas, S. Fletcher, and E. Hepsaydir, "Cellular architecture and key technologies for 5G wireless communication networks," *IEEE Commun. Mag.*, vol. 52, no. 2, pp. 122–130, 2014.

[8] M. Shafi, A. F. Molisch, P. J. Smith, T. Haustein, P. Zhu, P. D. Silva, F. Tufvesson, A. Benjebbour, and G. Wunder, "5G: A tutorial overview of standards, trials, challenges, deployment, and practice," *IEEE J. Sel. Areas Commun.*, vol. 35, no. 6, pp. 1201–1221, 2017.

[9] D. Muirhead, M. A. Imran, and K. Arshad, "A survey of the challenges, opportunities and use of multiple antennas in current and future 5G small cell base stations," *IEEE Access*, vol. 4, pp. 2952–2964, 2016.

[10] M. N. Patwary, S. J. Nawaz, M. A. Rahman, S. K. Sharma, and M. M. Rashid, "The potential short- and long-term disruptions and transformative impacts of 5G and beyond wireless networks: Lessons learnt from the development of a 5G testbed environment," *IEEE Access*, vol. 8, pp. 11 352–11 379, 2020.

[11] R. Mittra, "Some challenges in millimeter wave antenna designs for 5G," in *International Symposium on Antennas and Propagation*, Busan, Korea, Jan. 2019.

[12] B. Javidi, E. Tajahuerce, and P. Andres, *Multi-dimensional Imaging*. Hoboken, NJ, USA: John Wiley & Sons, Inc., 2014.

[13] R. Zekavat and R. M. Buehrer, *Handbook of Position Location: Theory, Practice, and Advances*. Hoboken, NJ, USA: John Wiley & Sons, Inc., 2019.

[14] J. W. Strutt, "Investigations in optics, with special reference to the spectroscope," *The London, Edinburgh and Dublin Philosophical Magazine and Journal of Science, 5th series*, vol. 8, no. 49, pp. 261–274, 1879.

[15] E. Abbe, "Beitrage zur theorie des mikroskops und der mikroskopischen wahrnehmung," *Archiv fur Mikroskopische Anatomie*, vol. 9, pp. 413–418, 1873.

[16] C. A. Balanis, *Advanced Engineering Electromagnetics*, 1st ed. Hoboken, New Jersey, USA: John Wiley & Sons, Inc., 1989.

[17] W. B. Weir, "Automatic measurement of complex dielectric constant and permeability at microwave frequencies," *Proc. IEEE*, vol. 62, no. 1, pp. 33–36, 1974.

[18] S. Coyle, K. Lau, N. Moyna, D. O'Gorman, D. Diamond, F. Di Francesco, D. Costanzo, P. Salvo, M. G. Trivella, D. E. De Rossi, N. Taccini, R. Paradiso, J. Porchet, A. Ridolfi, J. Luprano, C. Chuzel, T. Lanier, F. Revol-Cavalier, S. Schoumacker, V. Mourier, I. Chartier, R. Convert, H. De-Moncuit, and C. Bini, "BIOTEXbiosensing textiles for personalised healthcare management," *IEEE Trans. Inf. Technol. Biomed.*, vol. 14, no. 2, pp. 364–370, 2010.

[19] O. Kucera and M. Cifra, "Radiofrequency and microwave interactions between biomolecular systems," *Journal of Biological Physics*, vol. 42, no. 1, pp. 1–8, 2016.

[20] D. Fels, M. Cifra, and F. Scholkmanns, *Fields of the Cell*. Kerala, India: Research Signpost, 2015.

[21] K. Soga and J. Schooling, "Infrastructure sensing," *Interface Focus*, vol. 6, no. 4, 2016.

[22] M. Wang, J. Lynch, and H. Sohn, *Sensor Technologies for Civil Infrastructures, Volume 1*. Cambridge, UK: Woodhead Publishing, 2014.

[23] S. Vern, *Advances in Remote Sensing for Infrastructure Monitoring*. Berlin, DE: Springer, 2020.

[24] "ETSI EN 302 217-4: Fixed radio systems; characteristics and requirements for point-to-point equipment and antennas," European Telecommunications Standards Institute, Tech. Rep., Jan. 2009.

[25] "ITU-R F.699-6: Reference radiation patterns for fixed wireless system antennas for use in coordination studies and interference assessment in the frequency range from 100 MHz to about 70 GHz," International Telecommunication Union, Tech. Rep., Jan. 2004.

[26] M. Morgan, *Reflectionless Filters*. Boston, MA, USA: Artech House, 2017.

[27] J.-M. M.-F. Roberto Gomez-Garcia, Dimitra Psychogiou and L. Yang, "Avoiding RF isolators," *IEEE Microw. Mag.*, vol. 21, no. 12, pp. 68–86, 2020.

[28] M. OHanlon, "Forecasting change in military technology, 2020-2040," The Brookings Institution, Tech. Rep., Jan. 2019.

[29] D. Parker, "Microwave industry outlook - defense applications," *IEEE Trans. Microw. Theory Tech.*, vol. 50, no. 3, pp. 1039–1041, 2002.

[30] J. I. Agbinya, *Wireless Power Transfer*, 2nd ed. Gistrup, Denmark: River Publishers, 2016.

[31] N. Shinohara, *Recent Wireless Power Transfer Technologies via Radio Waves*, 1st ed. Gistrup, Denmark: River Publishers, 2017.

[32] C. T. Rim and C. Mi, *Wireless Power Transfer for Electric Vehicles and Mobile Devices*, 1st ed. Hoboken, New Jersey, USA: Wiley-IEEE Press, 2017.

[33] R. S. Elliott, *Electromagnetics: History, Theory, and Applications*, 1st ed. Hoboken, New Jersey, USA: Wiley-IEEE Press, 1993.

[34] B. Banerjee, *An Introduction to Metamaterials and Waves in Composites*, 1st ed. Oxfordshire, United Kingdom: Taylor & Francis, 2011.

[35] A. Kamal, J. Clarke, and M. H. Devoret, "Noiseless non-reciprocity in a parametric active device," *Nature Physics*, vol. 7, pp. 311–315, 2011.

[36] T. Kodera, D. L. Sounas, and C. Caloz, "Artificial faraday rotation using a ring metamaterial structure without static magnetic field," *Applied Physics Letters*, vol. 99, p. 031114, 2011.

[37] C. Caloz, A. Alu, S. Tretyakov, D. Sounas, K. Achouri, and Z.-L. Deck-Leger, "Electromagnetic nonreciprocity," *Physical Review Applied*, vol. 10, no. 4, p. 047001, 2018.

[38] A. Kord, D. L. Sounas, and A. Alu, "Microwave nonreciprocity," *Proc. IEEE*, vol. 108, no. 10, pp. 1728–1758, 2020.

[39] X. Wang, A. Daz-Rubio, H. Li, S. A. Tretyakov, and A. Alu, "Theory and design of multifunctional space-time metasurfaces," *Physical Review Applied*, vol. 13, no. 4, p. 044040, 2020.

[40] D. L. Sounas, C. Caloz, and A. Alu, "Giant non-reciprocity at the subwavelength scale using angular momentum-biased metamaterials," *Nature Communications*, vol. 4, p. 2407, 2013.

[41] N. A. Estep, D. L. Sounas, J. Soric, and A. Alu, "Magnetic-free non-reciprocity and isolation based on parametrically modulated coupled-resonator loops," *Nature Physics*, vol. 10, p. 923927, 2014.

[42] D. L. Sounas and A. Alu, "Nonreciprocity based on nonlinear resonances," *IEEE Antennas Wireless Propag. Lett.*, vol. 17, no. 11, pp. 1958–1962, 2018.

[43] Z. Xiao, D. L. Sounas, A. Nagulu, M. Tymchenko, T. Dinc, H. Krishnaswamy, and A. Alu, "Role of synchronization in magnetless nonreciprocal devices based on commutated transmission lines," *Physical Review Applied*, vol. 13, p. 064033, 2020.

[44] Y. Hadad, J. C. Soric, and A. Alu, "Breaking temporal symmetries for emission and absorption," *Proceedings of the National Academy of Sciences of the United States of America*, vol. 27, p. 8424, 2016.

[45] ——, "Temporal switching to extend the bandwidth of thin absorbers," *Optica*, vol. 8, no. 1, pp. 24–29, 2021.

[46] A. Krasnok, D. G. Baranov, A. Generalov, S. Li, and A. Alu, "Coherently enhanced wireless power transfer," *Physical Review Letters*, vol. 120, no. 143901, 2018.

[47] B. Clerckx and E. Bayguzina, "Waveform design for wireless power transfer," *IEEE Trans. Signal Process.*, vol. 64, no. 23, pp. 6313–6328, 2016.

[48] F. Yand and Y. Rahmat-Samii, *Surface Electromagnetics with Applications in Antenna, Microwave, and Optical Engineering*, 1st ed. Cambridge, UK: Cambridge University Press, 2019.

[49] D. Ramaccia, D. L. Sounas, A. Alu, F. Bilotti, and A. Toscano, "Nonreciprocity in antenna radiation induced by space-time varying metamaterial cloaks," *IEEE Antennas Wireless Propag. Lett.*, vol. 17, no. 11, pp. 1968–1972, 2018.

[50] C. M. Bender and S. Boettcher, "Real spectra in non-hermitian hamiltonians having PT symmetry," *Physical Review Letters*, vol. 80, no. 24, p. 5243, 1998.

[51] S. Ma and S. M. Anlage, "Gain-driven discrete breathers in PT-symmetric nonlinear metamaterials," *Physical Review Letters*, vol. 110, no. 5, p. 053901, 2013.

[52] M. A. K. Othman, V. Galdi, and F. Capolino, "Exceptional points of degeneracy and PT symmetry in photonic coupled chains of scatterers," *Physical Review B*, vol. 95, no. 10, p. 104305, 2017.

[53] C. A. Valagiannopoulos, F. Monticone, and A. Alu, "PT-symmetric planar devices for field transformation and imaging," *Journal of Optics*, vol. 18, no. 4, p. 044028, 2016.

[54] P.-Y. Chen, M. Sakhdari, M. Hajizadegan, Q. Cui, M. M.-C. Cheng, R. El-Ganainy, and A. Alu, "Generalized paritytime symmetry condition for enhanced sensor telemetry," *Nature Electronics*, vol. 1, pp. 297–304, 2018.

[55] Y. J. Zhang, H. Kwon, M.-A. Miri, E. Kallos, H. Cano-Garcia, M. S. Tong, and A. Alu, "Noninvasive glucose sensor based on parity-time symmetry," *Physical Review Applied*, vol. 11, no. 4, p. 044049, 2019.

[56] A. Kord, D. L. Sounas, and A. Alu, "Active microwave cloaking using parity-time-symmetric satellites," *Physical Review Applied*, vol. 10, no. 5, p. 054040, 2018.

[57] M. V. Berry, "Physics of nonhermitian degeneracies," *Czechoslovak Journal of Physics*, vol. 54, p. 10391047, 2004.

[58] M. Y. Nada, M. A. K. Othman, F. Yazdi, D. Oshmarin, A. F. Abdelshafv, and C. Filippo, "Unique charactersitics and applications of systems with exceptional points of degeneracy," in *Proceedings of the IEEE International Symposium on Antennas and Propagation & USNC/URSI National Radio Science Meeting*, Boston, MA, USA, Jul. 2018.

[59] M. Y. Nada, T. Mealy, F. Yazdi, A. F. Abdelshafy, A. Figotin, and F. Capolino, "General conditions to realize exceptional points of degeneracy and applications," in *Proceedings of the 12th International Congress on Artificial Materials for Novel Wave Phenomena (Metamaterials)*, Espoo, Finland, Aug. 2018.

[60] J. L. Miller, "Exceptional points make for exceptional sensors," *Physics Today*, vol. 70, no. 10, p. 23, 2017.

[61] J. Wiersig, "Review of exceptional point-based sensors," *Photonics Research*, vol. 8, no. 9, pp. 1457–1467, 2020.

[62] M. S. Rider, S. J. Palmer, S. R. Pocock, X. Xiao, P. A. Huidobro, and V. Giannini), "A perspective on topological nanophotonics: Current status and future challenges," *Journal of Applied Physics*, vol. 125, no. 12, p. 120901, 2020.

[63] S. Ma and S. M. Anlage, "Microwave applications of photonic topological insulators," *Nano Letters*, vol. 116, no. 25, p. 250502, 2020.

[64] D. J. Bisharat and D. F. Sievenpiper, "Electromagnetic-dual metasurfaces for topological states along a 1D interface," *Laser & Photonics Reviews*, vol. 3, no. 10, p. 1900126, 2019.

[65] G. Hu, Q. Ou, G. Si, Y. Wu, J. Wu, Z. Dai, A. Krasnok, Y. Mazor, Q. Zhang, Q. Bao, C.-W. Qiu, and A. Alu, "Wireless power transfer through asymmetric topological edge states in diatomic chains of coupled meta-atoms," *Applied Physics Letters*, vol. 117, no. 13, pp. 134 106–134 111, 2020.

[66] O. Kafri and I. Glatt, *The Physics of Moire Metrology*, 1st ed. New York, USA: John Wiley & Sons, 1990.

[67] J. W. Strutt, "On copying diffraction-gratings, and on some phenomena connected therewith," *The London, Edinburgh, and Dublin Philosophical Magazine and Journal of Science*, vol. 11, no. 67, pp. 196–205, 1881.

[68] G. J. M. Indebetouw and R. Czarnek, *Selected Papers on Optical Moire and Applications*, 1st ed. Bellingham, Washington, USA: SPIE Press, 1992.

[69] S. Carr, D. Massatt, S. Fang, P. Cazeaux, M. Luskin, and E. Kaxiras, "Twistronics: Manipulating the electronic properties of two-dimensional layered structures through their twist angle," *Physical Review B*, vol. 95, no. 7, p. 075420, 2017.

[70] Y. Deng, M. Oudich, N. J. Gerard, J. Ji, M. Lu, and Y. Jing, "Magic-angle bilayer phononic graphene," *Physical Review B*, vol. 102, no. 18, p. 180304, 2020.

[71] G. Hu, Q. Ou, G. Si, Y. Wu, J. Wu, Z. Dai, A. Krasnok, Y. Mazor, Q. Zhang, Q. Bao, C.-W. Qiu, and A. Alu, "Topological polaritons and photonic magic angles in twisted a-MoO3 bilayers," *Nature*, vol. 582, pp. 209–213, 2020.

[72] G. Hu, A. Krasnok, Y. Mazor, C.-W. Qiu, and A. Alu, "Moire hyperbolic metasurfaces," *Nano Letters*, vol. 20, no. 5, pp. 3217–3224, 2020.

[73] P. J. Crepeau and P. R. McIsaac, "Consequences of symmetry in periodic structures," *Proc. IEEE*, vol. 52, no. 1, pp. 33–43, 1964.

[74] G. L. Trigg, "Higher symmetries," *Physical Review Letters*, vol. 14, no. 13, p. 479, 1965.

[75] O. Quevedo-Teruel, G. Valerio, Z. Sipus, and E. Rajo-Iglesias, "Periodic structures with higher symmetries: Their applications in electromagnetic devices," *IEEE Microw. Mag.*, vol. 21, no. 11, pp. 36–49, 2020.

[76] R. Kieburtz and J. Impagliazzo, "Multimode propagation on radiating traveling-wave structures with glide-symmetric excitation," *IEEE Trans. Antennas Propag.*, vol. 18, no. 1, pp. 3–7, 1970.

[77] A. Hessel, M. H. Chen, R. C. M. Li, and A. A. Oliner, "Propagation in periodically loaded waveguides with higher symmetries," *Proc. IEEE*, vol. 61, no. 2, pp. 183–195, 1973.

[78] O. Dahlberg, R. C. Mitchell-Thomas, and O. Quevedo-Teruel, "Reducing the dispersion of periodic structures with twist and polar glide symmetries," *Scientific Reports*, vol. 7, p. 10136, 2017.

[79] F. Ghasemifard, M. Norgren, and O. Quevedo-Teruel, "Twist and polar glide symmetries: an additional degree of freedom to control the propagation characteristics of periodic structures," *Scientific Reports*, vol. 8, p. 11266, 2018.

[80] O. Dahlberg, F. Ghasemifard, G. Valerio, and O. Quevedo-Teruel, "Propagation characteristics of periodic structures possessing twist and polar glide symmetries," *EPJ Applied Metamaterials*, vol. 6, p. 14, 2019.

[81] O. Quevedo-Teruel, "Glide symmetries and their application for electromagnetic periodic structures," in *Proceedings of the 2019 International Symposium on Antennas and Propagation (ISAP)*, Xi'an, China, Oct. 2019.

[82] A. G. V. Melsen, *From atomos to atom: The history of the concept atom*, 1st ed. Manhattan, New York, United States: Harper and Brothers, 1960.

[83] J. Munday, "A new twist on the quantum vacuum," *Physics Today*, vol. 74, no. 10, p. 74, 2019.

[84] H. B. G. Casimir and D. Polder, "The influence of retardation on the london-van der waals forces," *Physical Review*, vol. 73, no. 4, pp. 360–372, 1948.

[85] T. C. Choy, *Effective Medium Theory: Principles and Applications*. Oxford, United Kingdom: Oxford University Press, 2016.

[86] O. Vanbesien, *Artificial Materials*. Hoboken, NJ, USA: John Wiley & Sons, Inc., 2012.

[87] C. Ssskind, "Obstacle-type artificial dielectrics for microwaves," *Journal of the British Institution of Radio Engineers*, vol. 12, no. 1, pp. 49–60, 1952.

[88] R. W. Corkum, "Isotropic artificial dielectric," *Proceedings of the IRE*, vol. 40, no. 5, pp. 574–587, 1952.

[89] L. Lewin, "The electrical constants of a material loaded with spherical particles," *Journal of the Institution of Electrical Engineers - Part III: Radio and Communication Engineering*, vol. 94, no. 27, pp. 65–68, 1947.

[90] W. E. Kock, "Metal-lens antennas," *Proceedings of the I.R.E.*, vol. 34, no. 11, pp. 828–836, 1946.

[91] ——, "Metallic delay lenses," *The Bell System Technical Journal*, vol. 27, no. 1, pp. 58–82, 1948.

[92] J. Brown, "The design of metallic delay dielectrics," *Proceedings of the IEE - Part III: Radio and Communication Engineering*, vol. 97, no. 45, pp. 45–48, 1950.

[93] J. Brown and S. S. D. Jones, "Microwave lenses," *Electronic Engineering*, vol. 22, pp. 127–131, 1950.

[94] J. Brown, "Artificial dielectrics having refractive indices less than unity," *Proceedings of the IEE - Part IV: Institution Monographs*, vol. 100, no. 5, pp. 51–62, 1953.

[95] S. B. Cohn, "Microwave measurements on metallic delay media," *Proceedings of the IRE*, vol. 41, no. 9, pp. 1177–1183, 1953.

[96] E. Jones and S. Cohn, "Surface matching of dielectric lenses," *1958 IRE International Convention Record*, vol. 2, pp. 46–53, 1954.

[97] N. Engheta and R. W. Ziolkowski, *Metamaterials: Physics and Engineering Explorations*. Hoboken, NJ, USA: John Wiley & Sons, Inc., 2006.

[98] F. Capolino, *Theory and Phenomena of Metamaterials*. Oxfordshire, United Kingdom: Taylor and Francis Group, LLC, 2009.

[99] T. J. Cui, D. Smith, and R. Liu, *Metamaterials: Theory, Design, and Applications*. New York, New York, USA: Springer Science+Business Media, LLC, 2010.

[100] R. W. Ziolkowski and A. D. Kipple, "Causality and double-negative metamaterials," *Physical Review E*, vol. 68, no. 2, pp. 1–9, 2013.

[101] S. Gupta and C. Caloz, "Perfect dispersive medium for real-time signal processing," *IEEE Trans. Antennas Propag.*, vol. 64, no. 12, pp. 5299–5308, 2016.

[102] Z. Szab, G.-H. Park, R. Hedge, and E.-P. Li, "A unique extraction of metamaterial parameters based on Kramers-Kronig relationship," *IEEE Trans. Microw. Theory Tech.*, vol. 58, no. 10, pp. 2646–2653, 2010.

[103] Z. Szab, "Closed form Kramers-Kronig relations to extract the refractive index of metamaterials," *IEEE Trans. Microw. Theory Tech.*, vol. 65, no. 4, pp. 1150–1159, 2017.

[104] D. R. Smith and N. Kroll, "Negative refractive index in left-handed materials," *Physical Review Letters*, vol. 85, no. 14, pp. 2933–2936, 2000.

[105] J. B. Pendry, "Positively negative," *Nature 'News and Views'*, vol. 423, pp. 22–23, 2003.

[106] ——, "Negative refraction," *Contemporary Physics*, vol. 45, no. 3, pp. 191–202, 2004.

[107] A. K. Iyer, A. Alu, and A. Epstein, "Metamaterials and metasurfaceshistorical context, recent advances, and future directions," *IEEE Trans. Antennas Propag.*, vol. 68, no. 3, pp. 1223–1231, 2020.

[108] V. G. Veselago, "The electrodynamics of substances with simultaneously negative values of ϵ and μ," *Soviet Physics Uspekhi*, vol. 10, no. 4, pp. 509–514, 1968.

[109] R. N. Bracewell, "Analogues of an ionized medium: Applications to the iono-sphere," *Wireless Engineering*, vol. 31, pp. 320–326, 1954.

[110] W. Rotman, "Plasma simulation by artificial dielectrics and parallel-plate media," *IRE Transactions on Antennas and Propagation*, vol. 10, no. 1, pp. 82–95, 1962.

[111] J. B. Pendry, A. J. Holden, W. J. Stewart, and I. Youngs, "Extremely low frequency plasmons in metallic mesostructures," *Physical Review Letters*, vol. 76, pp. 4773–4776, 1996.

[112] D. F. Sievenpiper, M. E. Sickmiller, and E. Yablonovitch, "3D wire mesh photonic crystals," *Physical Review Letters*, vol. 76, pp. 2480–2483, 1996.

[113] D. F. Sievenpiper, E. Yablonovitch, J. N. Winn, S. Fan, P. R. Villeneuve, and J. D. Joannopoulos, "3D metallo-dielectric photonic crystals with strong capacitive coupling between metallic islands," *Physical Review Letters*, vol. 80, pp. 2829–2832, 1998.

[114] J. B. Pendry, A. J. Holden, D. J. Robbins, and W. J. Stewart, "Low frequency plasmons in thin wire structures," *Journal of Physics: Condensed Matter*, vol. 10, pp. 4785–4809, 1998.

[115] ——, "Magnetism from conductors and enhanced nonlinear phenomena," *IEEE Trans. Microw. Theory Tech.*, vol. 47, no. 11, pp. 2075–2084, 1999.

[116] D. R. Smith, W. J. Padilla, D. C. Vier, S. C. Nemat-Nasser, and S. Schultz, "Composite medium with simultaneously negative permeability and permittivity," *Physical Review Letters*, vol. 84, no. 18, pp. 4184–4187, 2000.

[117] J. B. Pendry, "Negative refraction makes a perfect lens," *Physical Review Letters*, vol. 85, p. 3966, 2000.

[118] A. M. H. Wong and G. V. Eleftheriades, "Advances in imaging beyond the diffraction limit," *IEEE Photon. J.*, vol. 4, no. 2, pp. 586–589, 2012.

[119] S. Mandal, "Superlens-based nanoscale imaging," *IEEE Potentials*, vol. 33, no. 2, pp. 17–20, 2014.

[120] A. Moreira, P. Prats-Iraola, M. Y. G. Krieger, I. Hajnsek, and K. P. Papathanassiou, "A tutorial on synthetic aperture radar," *IEEE Geosci. Remote Sens. Mag.*, vol. 1, no. 1, pp. 6–43, 2013.

[121] M. Soumekh, "Bistatic synthetic aperture radar inversion with application in dynamic object imaging," *IEEE Trans. Signal Process.*, vol. 39, no. 9, pp. 2044–2055, 1991.

[122] D. Nion and N. D. Sidiropoulos, "Tensor algebra and multidimensional harmonic retrieval in signal processing for MIMO radar," *IEEE Trans. Signal Process.*, vol. 58, no. 11, pp. 5693–5705, 2010.

[123] A. J. Devaney, "Time reversal imaging of obscured targets from multistatic data," *IEEE Trans. Antennas Propag.*, vol. 53, no. 5, pp. 1600–1610, 2005.

[124] S. S. Ahmed, A. Schiessl, and L.-P. Schmidt, "A novel fully electronic active real-time imager based on a planar multistatic sparse array," *IEEE Trans. Microw. Theory Tech.*, vol. 59, no. 12, pp. 3567–3576, 2011.

[125] K. Chetty, G. E. Smith, and K. Woodbridge, "Through-the-wall sensing of personnel using passive bistatic WiFi radar at standoff distances," *IEEE Trans. Geosci. Remote Sens.*, vol. 50, no. 4, pp. 1218–1226, 2012.

[126] M. E. Yavuz and F. L. Teixeira, "Spacefrequency ultrawideband time-reversal imaging," *IEEE Trans. Geosci. Remote Sens.*, vol. 46, no. 4, pp. 1115–1124, 2008.

[127] A. K. Iyer and G. V. Eleftheriades, "A multilayer negative-refractive-index transmission-line (NRI-TL) metamaterial free-space lens at x-band," *IEEE Trans. Antennas Propag.*, vol. 55, no. 10, pp. 2746–2753, 2007.

[128] S. M. Rudolph and A. Grbic, "Super-resolution focusing using volumetric, broadband NRI media," *IEEE Trans. Antennas Propag.*, vol. 56, no. 9, pp. 2963–2969, 2008.

[129] A. K. Iyer and G. V. Eleftheriades, "Free-space imaging beyond the diffraction limit using a veselago-pendry transmission-line metamaterial superlens," *IEEE Trans. Antennas Propag.*, vol. 57, no. 6, pp. 1720–1727, 2009.

[130] S. M. Rudolph and A. Grbic, "A broadband three-dimensionally isotropic negative-refractive-index medium," *IEEE Trans. Antennas Propag.*, vol. 60, no. 8, pp. 3661–3669, 2012.

[131] S. Das, H. Nguyen, G. N. Babu, and A. K. Iyer, "Free-space focusing at C-band using a flat fully printed multilayer metamaterial lens," *IEEE Trans. Antennas Propag.*, vol. 63, no. 11, pp. 4702–4714, 2015.

[132] A. Erentok and R. W. Ziolkowski, "Metamaterial-inspired efficient electrically small antennas," *IEEE Trans. Antennas Propag.*, vol. 56, no. 3, pp. 691–707, 2008.

[133] A. Erentok, P. L. Luljak, and R. W. Ziolkowski, "Characterization of a volumetric metamaterial realization of an artificial magnetic conductor for antenna applications," *IEEE Trans. Antennas Propag.*, vol. 53, no. 1, pp. 160–172, 2005.

[134] C. Caloz, T. Itoh, and A. Rennings, "CRLH metamaterial leaky-wave and resonant antennas," *IEEE Antennas Propag. Mag.*, vol. 50, no. 5, pp. 25–39, 2008.

[135] R. W. Ziolkowski and A. Erentok, "Metamaterial-based efficient electrically small antennas," *IEEE Trans. Antennas Propag.*, vol. 54, no. 7, pp. 2113–2130, 2006.

[136] A. Alu, F. Bilotti, N. Engheta, and L. Vegni, "Subwavelength, compact, resonant patch antennas loaded with metamaterials," *IEEE Trans. Antennas Propag.*, vol. 55, no. 1, pp. 13–25, 2007.

[137] S. Lim, C. Caloz, and T. Itoh, "Metamaterial-based electronically controlled transmission-line structure as a novel leaky-wave antenna with tunable radiation angle and beamwidth," *IEEE Trans. Microw. Theory Tech.*, vol. 53, no. 1, pp. 161–173, 2005.

[138] R. W. Ziolkowski, P. Jin, and C.-C. Lin, "Metamaterial-inspired engineering of antennas," *Proc. IEEE*, vol. 99, no. 10, pp. 1720–1731, 2011.

[139] F. Bilotti, A. Alu, and L. Vegni, "Design of miniaturized metamaterial patch antennas with μ-negative loading," *IEEE Trans. Antennas Propag.*, vol. 56, no. 6, pp. 1640–1647, 2008.

[140] K. Li, C. Zhu, L. Li, Y. M. Cai, and C. H. Liang, "Design of electrically small metamaterial antenna with ELC and EBG loading," *IEEE Antennas Wireless Propag. Lett.*, vol. 12, pp. 678–681, 2013.

[141] J. Park, Y. Ryu, and J. Lee, "Mu-zero resonance antenna," *IEEE Trans. Antennas Propag.*, vol. 58, no. 6, pp. 1865–1875, 2010.

[142] Z. Liu and Y. Guo, "Compact low-profile dual band metamaterial antenna for body centric communications," *IEEE Antennas Wireless Propag. Lett.*, vol. 14, pp. 863–866, 2015.

[143] B. P. Smyth, S. Barth, and A. K. Iyer, "Dual-band microstrip patch antenna using integrated uniplanar metamaterial-based EBGs," *IEEE Trans. Antennas Propag.*, vol. 64, no. 12, pp. 5046–5053, 2016.

[144] S. Barth and A. K. Iyer, "A low-profile dual-band circular patch antenna for GPS using metamaterial-based EBGs," in *Proceedings of the IEEE International Symposium on Antennas and Propagation*, San Diego, CA, USA, Jul. 2017, pp. 1727 – 1728.

[145] S. Barth, B. P. Smyth, and A. K. Iyer, "Embedded MTM-EBGs for antenna applications," in *Proceedings of the USNC-URSI National Radio Science Meeting*, Boulder, CO, USA, Jan. 2019.

[146] P. Jin and R. W. Ziolkowski, "Multi-frequency, linear and circular polarized, metamaterial-inspired, near-field resonant parasitic antennas," *IEEE Trans. Antennas Propag.*, vol. 59, no. 5, pp. 1446–1459, 2011.

[147] M. A. Antoniades and G. V. Eleftheriades, "Multiband compact printed dipole antennas using nri-tl metamaterial loading," *IEEE Trans. Antennas Propag.*, vol. 60, no. 12, pp. 5613–5626, 2012.

[148] C.-C. Lin, P. Jin, and R. W. Ziolkowski, "Multi-functional, magnetically-coupled, electrically small, near-field resonant parasitic wire antennas," *IEEE Trans. Antennas Propag.*, vol. 59, no. 3, pp. 714–724, 2011.

[149] M. R. Booket, A. Jafargholi, M. Kamyab, H. Eskandari, M. Veysi, and S. Mousavi, "Compact multiband printed dipole antenna loaded with single-cell metamaterial," *IET Microwaves, Antennas & Propagation*, vol. 6, no. 1, pp. 17–23, 2012.

[150] S. Ferdous, A. Hossain, S. M. H. Chowdhury, M. R. C. Mahdy, and M. Abdul, "Reduced and conventional size multi-band circular patch antennas loaded with metamaterials," *IET Microwaves, Antennas & Propagation*, vol. 7, no. 9, p. 768776, 2013.

[151] J. C. Soric, N. Engheta, S. Maci, and A. Alu, "Omnidirectional metamaterial antennas based on ϵ-near-zero channel matching," *IEEE Trans. Antennas Propag.*, vol. 61, no. 1, p. 3344, 2013.

[152] J. L. Volakis and K. Sertel, "Narrowband and wideband metamaterial antennas based on degenerate band edge and magnetic photonic crystals," *Proc. IEEE*, vol. 99, no. 10, pp. 1732–1745, 2011.

[153] C. G. Ryan and G. V. Eleftheriades, "Two compact, wideband, and decoupled meander-line antennas based on metamaterial concepts," *IEEE Antennas Wireless Propag. Lett.*, vol. 11, pp. 1277–1280, 2012.

[154] D. Ramaccia, F. Scattone, F. Bilotti, and A. Toscano, "Broadband compact horn antennas by using EPS-ENZ metamaterial lens," *IEEE Trans. Antennas Propag.*, vol. 61, no. 6, pp. 2929–2937, 2013.

[155] J. M. M. Bait-Suwailam, M. S. Boybay, and O. M. Ramahi, "Electromagnetic coupling reduction in high-profile monopole antennas using single-negative magnetic metamaterials for MIMO applications," *IEEE Trans. Antennas Propag.*, vol. 58, no. 9, pp. 2894–2902, 2010.

[156] S. Thummaluru and R. Chaudhary, "Mu-negative metamaterial filter-based isolation technique for MIMO antennas," *Electronics Letters*, vol. 53, no. 10, pp. 644–646, 2017.

[157] J. M. M. Bait-Suwailam, M. S. Boybay, and O. M. Ramahi, "Mutual coupling reduction for high-performance densely packed patch antenna arrays on finite substrate," *IEEE Trans. Antennas Propag.*, vol. 64, no. 5, pp. 1653–1660, 2016.

[158] L. Zhang, S. Zhang, Z. Song, Y. Liu, L. Ye, and Q. H. Liu, "Adaptive decoupling using tunable metamaterials," *IEEE Trans. Microw. Theory Tech.*, vol. 64, no. 9, pp. 2730–2739, 2016.

[159] R. W. Ziolkowski, "Propagation in and scattering from a matched metamaterial having a zero index of refraction," *Physical Review E*, vol. 70, no. 4, pp. 1–12, 2004.

[160] A. Alu, M. G. Silveirinha, A. Salandrino, and N. Engheta, "Epsilon-near- zero metamaterials and electromagnetic sources: Tailoring the radiation phase pattern," *Physical Review B*, vol. 75, no. 15, pp. 1–13, 2007.

[161] F. P. Casares-Miranda, C. Camacho-Penalosa, and C. Caloz, "High-gain active composite right/left-handed leaky-wave antenna," *IEEE Trans. Antennas Propag.*, vol. 54, no. 8, pp. 2292–2300, 2006.

[162] Y. He, N. Ding, L. Zhang, W. Zhang, and B. Du, "Short-length and high-aperture-efficiency horn antenna using low-loss bulk anisotropic metamaterial," *IEEE Antennas Wireless Propag. Lett.*, vol. 14, pp. 1642–1645, 2006.

[163] J. P. Turpin, Q. Wu, D. H. Werner, B. Martin, M. Bray, and E. Lier, "Low cost and broadband dual-polarization metamaterial lens for directivity enhancement," *IEEE Trans. Antennas Propag.*, vol. 60, no. 12, pp. 5717–5726, 2012.

[164] E. Forati, G. W. Hanson, and D. F. Sievenpiper, "An epsilon-near-zero total-internal-reflection metamaterial antenna," *IEEE Trans. Antennas Propag.*, vol. 63, no. 5, pp. 1909–1916, 2015.

[165] C. Caloz, "Metamaterial dispersion engineering concepts and applications," *Proc. IEEE*, vol. 99, no. 10, pp. 1711–1719, 2011.

[166] R. Islam and G. V. Eleftheriades, "Phase-agile branch-line couplers using metamaterial lines," *IEEE Microw. Wireless Compon. Lett.*, vol. 14, no. 7, pp. 340–342, 2004.

[167] P.-L. Chi and T. Itoh, "Miniaturized dual-band directional couplers using composite right/left-handed transmission structures and their applications in beam pattern diversity systems," *IEEE Trans. Microw. Theory Tech.*, vol. 57, no. 7, pp. 1207–1215, 2009.

[168] R. Islam and G. V. Eleftheriades, "Compact corporate power divider using metamaterial NRI-TL coupled-line couplers," *IEEE Microw. Wireless Compon. Lett.*, vol. 18, no. 7, pp. 440–442, 2008.

[169] H. V. Nguyen and C. Caloz, "Generalized coupled-mode approach of metamaterial coupled-line couplers: Coupling theory, phenomenological explanation, and experimental demonstration," *IEEE Trans. Microw. Theory Tech.*, vol. 55, no. 5, pp. 1029–1039, 2007.

[170] M. Bemani and S. Nikmehr, "Dual-band n-way series power divider using CRLH-TL metamaterials with application in feeding dual-band linear broadside array antenna with reduced beam squinting," *IEEE Trans. Circuits Syst. I*, vol. 60, no. 12, pp. 3239–3246, 2013.

[171] C. Ryan and G. Eleftheriades, "Design of a printed dual-band coupled-line coupler with generalised negative-refractive index transmission lines," *IET Microwaves, Antennas & Propagation*, vol. 6, no. 6, pp. 705–712, 2012.

[172] B. P. Smyth and A. K. Iyer, "Dual-band Wilkinson power divider using uniplanar metamaterial-based EBGs," in *IEEE AP-S Symposium on Antennas and Propagation and USNC/URSI National Radio Science Meeting*, San Diego, CA, Jul. 2017, pp. 457–458.

[173] S. Barth and A. K. Iyer, "A dual-band quadrature hybrid coupler using embedded MTM-EBGs," in *Proceedings of the IEEE International Symposium on Antennas and Propagation and USNC/URSI Radio Science Meeting*, Boston, MA, Jul. 2018, pp. 199–200.

[174] J. A. Brown and A. K. Iyer, "Design and characterization of a dual-band impedance transformer based on an embedded MTM-EBG," in *IEEE International Symposium on Antennas and Propagation and USNC/URSI Radio Science Meeting*, Atlanta, GA, Jul. 2019.

[175] J. A. Brown, S. Barth, B. P. Smyth, and A. K. Iyer, "Dual-band microstrip corporate feed network using an embedded metamaterial-based EBG)," *IEEE Trans. Antennas Propag.*, vol. 67, no. 11, pp. 7031–7039, 2019.

[176] S. Barth, B. P. Smyth, J. A. Brown, and A. K. Iyer, "Theory and design of dual-band microstrip networks using embedded metamaterial-based electromagnetic bandgap structures (MTM-EBGs)," *IEEE Trans. Antennas Propag.*, vol. 68, no. 3, pp. 1761–1772, 2020.

[177] G. V. Eleftheriades, "A generalized negative-refractive-index transmission-line (NRI-TL) metamaterial for dual-band and quad-band applications," *IEEE Microw. Wireless Compon. Lett.*, vol. 17, no. 6, pp. 415–417, 2007.

[178] F. Martin, *Artificial Transmission Lines for RF and Microwave Applications.* Hoboken, NJ, USA: John Wiley & Sons, Inc., 2015.

[179] J. C. Soric and A. Alu, "Longitudinally independent matching and arbitrary wave patterning using ϵ-near-zero channels," *IEEE Trans. Microw. Theory Tech.*, vol. 63, no. 11, pp. 3558–3567, 2015.

[180] S. S. M. Khaleghi, G. Moradi, R. S. Shirazi, and A. Jafargholi, "Microstrip line impedance matching using ENZ metamaterials, design, and application," *IEEE Trans. Microw. Theory Tech.*, vol. 67, no. 4, pp. 2243–2251, 2019.

[181] C. Caloz and T. Itoh, *Electromagnetic Metamaterials: Transmission Line Theory and Microwave Applications.* Hoboken, NJ: Wiley-IEEE Press, 2005.

[182] G. V. Eleftheriades and K. G. Balmain, *Negative-Refraction Metamaterials: Fundamental Principles and Applications*. Hoboken, NJ: Wiley-IEEE Press, 2005.

[183] C. H. Ahn, J.-W. Choi, G. Beaucage, J. H. Nevin, J.-B. Lee, A. Puntambekar, and J. Y. Lee, "Disposable smart lab on a chip for point-of-care clinical diagnostics," *Proc. IEEE*, vol. 92, no. 1, pp. 154–173, 2004.

[184] N. Manaresi, A. Romani, G. Medoro, L. Altomare, A. Leonardi, M. Tartagni, and R. Guerrieri, "A CMOS chip for individual cell manipulation and detection," *IEEE J. Solid-State Circuits*, vol. 38, no. 12, pp. 2297–2305, 2003.

[185] D. P. Rose, M. E. Ratterman, D. K. Griffin, L. Hou, N. Kelley-Loughnane, R. R. Naik, J. A. Hagen, I. Papautsky, and J. C. Heikenfeld, "Adhesive RFID sensor patch for monitoring of sweat electrolytes," *IEEE Trans. Biomed. Eng.*, vol. 62, no. 6, pp. 1457–1465, 2015.

[186] T. Chretiennot, D. Dubuc, and K. Grenier, "A microwave and microfluidic planar resonator for efficient and accurate complex permittivity characterization of aqueous solutions," *IEEE Trans. Microw. Theory Tech.*, vol. 61, no. 2, pp. 972–978, 2013.

[187] E. Yoon and K. D. Wise, "An integrated mass flow sensor with on-chip cmos interface circuitry," *IEEE Trans. Electron Devices*, vol. 39, no. 6, pp. 1376–1386, 1992.

[188] M. S. A. Abouelwafa and E. J. M. Kendall, "The use of capacitance sensors for phase percentage determination in multiphase pipelines," *IEEE Trans. Instrum. Meas.*, vol. 29, no. 1, pp. 24–27, 1980.

[189] P. Cong, W. H. Ko, and D. J. Young, "Wireless batteryless implantable blood pressure monitoring microsystem for small laboratory animals," *IEEE Sensors J.*, vol. 10, no. 2, pp. 243–254, 2010.

[190] P. Salvo, F. D. Francesco, D. Costanzo, C. Ferrari, M. G. Trivella, and D. D. Rossi, "A wearable sensor for measuring sweat rate," *IEEE Sensors J.*, vol. 10, no. 10, pp. 1557–1558, 2010.

[191] M. H. Zarifi, H. Sadabadi, S. H. Hejazi, M. Daneshmand, and A. Sanati-Nezhad, "Noncontact and nonintrusive microwave-microfluidic flow sensor for energy and biomedical engineering," *Scientific Reports*, vol. 8, no. 1, p. 139, 2018.

[192] C. Liu, J.-B. Huang, Z. Zhu, F. Jiang, S. Tung, Y.-C. Tai, and C.-M. Ho, "A micromachined flow shear-stress sensor based on thermal transfer principles," *J. Microelectromech. Syst.*, vol. 8, no. 1, pp. 90–99, 1999.

[193] B. Jakoby, R. Beigelbeck, F. Keplinger, F. Lucklum, A. Niedermayer, E. K. Reichel, C. Riesch, T. Voglhuber-Brunnmaier, and B. Weiss, "Miniaturized sensors for the viscosity and density of liquids-performance and issues," *IEEE Trans. Ultrason., Ferroelectr., Freq. Control*, vol. 57, no. 1, pp. 111–120, 2010.

[194] G. Liang, Y. Wang, D. Mei, K. Xi, and Z. Chen, "Flexible capacitive tactile sensor array with truncated pyramids as dielectric layer for three-axis force measurement," *J. Microelectromech. Syst.*, vol. 24, no. 5, pp. 1510–1519, 2015.

[195] J.-B. Chossat, Y.-L. Park, R. J. Wood, and V. Duchaine, "A soft strain sensor based on ionic and metal liquids," *IEEE Sensors J.*, vol. 13, no. 9, pp. 3405–3414, 2013.

[196] G. C. M. Meijer, G. Wang, and F. Fruett, "Temperature sensors and voltage references implemented in cmos technology," *IEEE Sensors J.*, vol. 1, no. 3, pp. 225–234, 2001.

[197] B. Zhang and M. Kahrizi, "High-temperature resistance fiber bragg grating temperature sensor fabrication," *IEEE Sensors J.*, vol. 7, no. 4, pp. 586–591, 2007.

[198] A. Ukil, H. Braendle, and P. Krippner, "Distributed temperature sensing: Review of technology and applications," *IEEE Sensors J.*, vol. 12, no. 5, pp. 885–892, 2012.

[199] D. Girbau, A. Ramos, A. Lazaro, S. Rima, and R. Villarino, "Passive wireless temperature sensor based on time-coded uwb chipless rfid tags," *IEEE Trans. Microw. Theory Tech.*, vol. 60, no. 11, pp. 3623–3632, 2012.

[200] M. Schueler, C. Mandel, M. Puentes, and R. Jakoby, "Metamaterial inspired microwave sensors," *IEEE Microw. Mag.*, vol. 13, no. 2, pp. 57–68, 2012.

[201] A. Ebrahimi, W. Withayachumnankul, S. Al-Sarawi, and D. Abbott, "High-sensitivity metamaterial-inspired sensor for microfluidic dielectric characterization," *IEEE Sensors J.*, vol. 14, no. 5, pp. 1345–1351, 2014.

[202] A. K. Horestani, C. Fumeaux, S. F. Al-Sarawi, and D. Abbott, "Displacement sensor based on diamond-shaped tapered split ring resonator," *IEEE Sensors J.*, vol. 13, no. 4, pp. 1153–1160, 2013.

[203] F.-Y. Meng, Q. Wu, D. Erni, K. Wu, and J.-C. Lee, "Polarization-independent metamaterial analog of electromagnetically induced transparency for a refractive-index-based sensor," *IEEE Trans. Microw. Theory Tech.*, vol. 60, no. 10, pp. 3013–3022, 2012.

[204] A. K. Horestani, D. Abbott, and C. Fumeaux, "Rotation sensor based on horn-shaped split ring resonator," *IEEE Sensors J.*, vol. 13, no. 8, pp. 3014–3015, 2013.

[205] A. Ebrahimi, W. Withayachumnankul, S. F. Al-Sarawi, and D. Abbott, "Metamaterial-inspired rotation sensor with wide dynamic range," *IEEE Sensors J.*, vol. 14, no. 8, pp. 2609–2614, 2014.

[206] W. Withayachumnankul, K. Jaruwongrungsee, C. Fumeaux, and D. Abbott, "Metamaterial-inspired multichannel thin-film sensor," *IEEE Sensors J.*, vol. 12, no. 5, pp. 1455–1458, 2012.

[207] R. Melik, E. Unal, N. K. Perkgoz, B. Santoni, D. Kamstock, C. Puttlitz, and H. V. Demir, "Nested metamaterials for wireless strain sensing," *IEEE J. Sel. Topics Quantum Electron.*, vol. 16, no. 2, pp. 450–458, 2010.

[208] A. Ebrahimi, J. Scott, and K. Ghorbani, "Differential sensors using microstrip lines loaded with two split-ring resonators," *IEEE Sensors J.*, vol. 18, no. 14, pp. 5786–5793, 2018.

[209] M. Abdolrazzaghi, M. Daneshmand, and A. K. Iyer, "Strongly enhanced sensitivity in planar microwave sensors based on metamaterial coupling," *IEEE Trans. Microw. Theory Tech.*, vol. 66, no. 4, pp. 1843–1855, 2018.

[210] R. Panwar, S. Puthucheri, D. Singh, and V. Agarwala, "Design of ferritegraphene-based thin broadband radar wave absorber for stealth application," *IEEE Trans. Magn.*, vol. 51, no. 11, p. 2802804, 2015.

[211] J. Lee, Y. Hong, S. Bae, J. Jalli, G. S. Abo, W. Seonug, W. Ahn, S. Park, C. Choi, and J. Lee, "Broadband ni $_{x}$zn $_{0.8-x}$cu $_{0.2}$fe $_{2}$o $_{4}$ electromagnetic absorber for 1 ghz application," *IEEE Trans. Magn.*, vol. 45, no. 10, pp. 4230–4233, 2009.

[212] Q. Zhang, L. Bai, X. Liu, C. Liu, and X. Cui, "Simplified transparent conductive oxides-based ultrabroadband absorber design," *J. Lightw. Technol.*, vol. 34, no. 4, pp. 1354–1359, 2016.

[213] N. I. Landy, S. Sajuyigbe, J. J. Mock, D. R. Smith, and W. J. Padilla, "Perfect metamaterial absorber," *Physical Review Letters*, vol. 100, no. 20, pp. 1–4, 2008.

[214] F. Ding, Y. Cui, X. Ge, Y. Jin, and S. He, "Ultra-broadband microwave metamaterial absorber," *Applied Physics Letters*, vol. 100, pp. 1–4, 2012.

[215] W. Li, T. L. Wu, W. Wang, P. C. Zhai, and J. G. Gua, "Broadband patterned magnetic microwave absorber," *Journal of Applied Physics*, vol. 16, pp. 1–7, 2014.

[216] D. Zhou, X. Huang, and Z. Du, "Analysis and design of multilayered broadband radar absorbing metamaterial using the 3-D printing technology-based method," *IEEE Antennas Wireless Propag. Lett.*, vol. 16, pp. 133–136, 2017.

[217] D. Schurig, J. J. Mock, B. J. Justice, S. A. Cummer, J. B. Pendry, A. F. Starr, and D. R. Smith, "Metamaterial electromagnetic cloak at microwave frequencies," *Science*, vol. 314, no. 5801, pp. 977–980, 2006.

[218] X. Liu, C. Li, K. Yao, X. Meng, and F. Li, "Invisibility cloaks modeled by anisotropic metamaterials based on inductor-capacitor networks," *IEEE Antennas Wireless Propag. Lett.*, vol. 8, pp. 1154–1157, 2009.

[219] M. Zedler and G. V. Eleftheriades, "Anisotropic transmission-line metamaterials for 2-d transformation optics applications," *Proc. IEEE*, vol. 99, no. 10, pp. 1634–1645, 2011.

[220] X. Wang, F. Chen, and E. Semouchkina, "Implementation of low scattering microwave cloaking by all-dielectric metamaterials," *IEEE Microw. Wireless Compon. Lett.*, vol. 23, no. 2, pp. 63–65, 2013.

[221] T. Nagayama and A. Sanada, "Planar distributed full-tensor anisotropic metamaterials for transformation electromagnetics," *IEEE Trans. Microw. Theory Tech.*, vol. 63, no. 12, pp. 3851–3861, 2015.

[222] G. A. Covic and J. T. Boys, "Inductive power transfer," *Proceedings of the IEEE*, vol. 101, no. 6, pp. 1276–1289, 2013.

[223] D. Brizi, S. Member, J. P. Stang, A. Monorchio, and G. Lazzi, "On the design of planar arrays of nonresonant coils for tunable wireless power transfer applications," *IEEE Trans. Microw. Theory Tech.*, vol. 68, no. 9, pp. 3814–3821, 2020.

[224] T. P. Duong and J.-W. Lee, "Experimental results of high-efficiency resonant coupling wireless power transfer using a variable coupling method," *IEEE Trans. Microw. Theory Tech.*, vol. 21, no. 8, pp. 442–444, 2011.

[225] J. Kim, H.-C. Son, K.-H. Kim, and Y.-J. Park, "Efficiency analysis of magnetic resonance wireless power transfer with intermediate resonant coil," *IEEE Trans. Antennas Propag.*, vol. 10, pp. 389–392, 2011.

[226] W. X. Zhong, C. K. Lee, and S. Y. R. Hui, "Wireless power domino-resonator systems with non-coaxial axes and circular structures," *IEEE Trans. Power Electron.*, vol. 27, no. 11, pp. 4750–4762, 2012.

[227] M. Song, P. Belov, and P. Kapitanova, "Wireless power transfer based on dielectric resonators with colossal permittivity," *Applied Physics Letters*, vol. 109, no. 223902, 2016.

[228] I.-G. Lee, N. Kim, I.-K. Cho, and I.-P. Hong, "Design of a mu-near-zero metamaterial for reducing the backward magnetic flux leakage of a wireless power transfer system," *IEICE Electronics Express*, vol. 15, no. 15, 2018.

[229] A. L. A. K. Ranaweera, T. S. Pham, H. N. Bui, V. Ngo, and J.-W. Lee, "An active metasurface for field-localizing wireless power transfer using dynamically reconfigurable cavities," *Scientific Reports*, vol. 9, no. 11735, 2019.

[230] H.-D. Lang and C. D. Sarris, "Optimization of wireless power transfer systems enhanced by passive elements and metasurfaces," *IEEE Trans. Antennas Propag.*, vol. 65, no. 10, pp. 5462–5474, 2017.

[231] L. Li, H. Liu, H. Zhang, and W. Xue, "Efficient wireless power transfer system integrating with metasurface for biological applications," *IEEE Trans. Ind. Electron.*, vol. 65, no. 4, pp. 3230–3239, 2018.

[232] S. Yu, H. Liu, and L. Li, "Design of near-field focused metasurface for high-efficient wireless power transfer with multifocus characteristics," *IEEE Trans. Ind. Electron.*, vol. 66, no. 5, pp. 3993–4002, 2019.

[233] D. Brizi, J. P. Stang, A. Monorchio, and G. Lazzi, "A compact magnetically dispersive surface for low-frequency wireless power transfer applications," *IEEE Trans. Antennas Propag.*, vol. 68, no. 3, pp. 1887–1895, 2020.

[234] Y. Zhao and E. Leelarasmee, "Controlling the resonances of indefinite materials for maximizing efficiency in wireless power transfer," in *International Electrical Engineering Congress*, Chonburi, Thailand, Mar. 2014.

[235] K. Sun, R. Fan, X. Zhang, Z. Zhang, Z. Shi, N. Wang, P. Xie, Z. Wang, G. Fan, H. Liu, C. Liu, T. Li, C. Yan, and Z. Guo, "An overview of metamaterials and their achievements in wireless power transfer," *Journal of Materials Chemistry C*, vol. 6, pp. 2925–2943, 2018.

[236] F. D. Sergey I. Bozhevolnyi, Patrice Genevet, *Metasurfaces: Physics and Applications*, 1st ed. Basel, Switzerland: Mdpi AG, 2018.

[237] C. L. Holloway, E. F. Kuester, J. A. Gordon, J. OHara, J. Booth, and D. R. Smith, "An overview of the theory and applications of metasurfaces: The two-dimensional equivalents of metamaterials," *IEEE Trans. Antennas Propag.*, vol. 54, no. 2, pp. 10–35, 2012.

[238] S. Maci, G. Minatti, M. Casaletti, and M. Bosiljevac, "Metasurfing: Addressing waves on impenetrable metasurfaces," *IEEE Antennas Wireless Propag. Lett.*, vol. 10, pp. 1499–1502, 2011.

[239] K. Achouri, M. A. Salem, and C. Caloz, "General metasurface synthesis based on susceptibility tensors," *IEEE Trans. Antennas Propag.*, vol. 54, no. 2, pp. 2977–2991, 2012.

[240] C. L. Holloway, E. F. Kuester, and A. Dienstfrey, "Characterizing metasurfaces/metafilms: The connection between surface susceptibilities and effective material properties," *IEEE Antennas Wireless Propag. Lett.*, vol. 10, pp. 1507–1511, 2011.

[241] J. P. S. Wong, A. Epstein, and G. V. Eleftheriades, "Reflectionless wide-angle refracting metasurfaces," *IEEE Antennas Wireless Propag. Lett.*, vol. 15, pp. 1293–1296, 2016.

[242] H.-H. Hsiao, C. H. Chu, and D. P. Tsai, "Fundamentals and applications of metasurfaces," *Small Methods*, vol. 1, p. 1600064, 2017.

[243] D. F. Sievenpiper, J. H. Schaffner, H. J. Song, R. Y. Loo, and G. Tangonan, "Two-dimensional beam steering using an electrically tunable impedance surface," *IEEE Trans. Antennas Propag.*, vol. 51, no. 10, pp. 2713–2722, 2003.

[244] G. Minatti, F. Caminita, E. Martini, M. Sabbadini, and S. Maci, "Synthesis of modulated-metasurface antennas with amplitude, phase, and polarization control," *IEEE Trans. Antennas Propag.*, vol. 64, no. 9, pp. 3907–3918, 2016.

[245] A. Monti, J. Soric, A. Alu, F. Bilotti, A. Toscano, and L. Vegni, "Overcoming mutual blockage between neighboring dipole antennas using a low-profile patterned metasurface," *IEEE Antennas Wireless Propag. Lett.*, vol. 11, pp. 1414–1417, 2012.

[246] D. Gonzalez-Ovejero, G. Minatti, G. Chattopadhyay, and S. Maci, "Multibeam by metasurface antennas," *IEEE Trans. Antennas Propag.*, vol. 65, no. 6, pp. 2923–2930, 2017.

[247] N. Yu, P. Genevet, F. Aieta, M. A. Kats, R. Blanchard, G. Aoust, J.-P. Tetienne, Z. Gaburro, and F. Capasso, "Flat optics: Controlling wavefronts with optical antenna metasurfaces," *IEEE J. Sel. Topics Quantum Electron.*, vol. 19, no. 3, p. 4700423, 2013.

[248] M. Bosiljevac, M. Casaletti, F. Caminita, Z. Sipus, and S. Maci, "Non-uniform metasurface luneburg lens antenna design," *IEEE Trans. Antennas Propag.*, vol. 60, no. 9, pp. 4065–4073, 2012.

[249] H. M. Bernety and A. B. Yakovlev, "Reduction of mutual coupling between neighboring strip dipole antennas using confocal elliptical metasurface cloaks," *IEEE Trans. Antennas Propag.*, vol. 63, no. 4, pp. 1554–1563, 2015.

[250] A. Monti, J. C. Soric, A. Alu, A. Toscano, and F. Bilotti, "Anisotropic mantle cloaks for TM and TE scattering reduction," *IEEE Trans. Antennas Propag.*, vol. 63, no. 4, pp. 1775–1787, 2015.

[251] A. Arbabi and A. Faraon, "Fundamental limits of ultrathin metasurfaces," *Scientific Reports*, vol. 58, p. 43722, 2017.

[252] A. A. Fathnan, A. E. Olk, and D. A. Powell, "Bandwidth limit and synthesis approach for single resonance ultrathin metasurfaces," *Journal of Physics D: Applied Physics*, vol. 53, p. 495304, 2020.

[253] G. Minatti, M. Faenzi, M. Sabbadini, and S. Maci, "Bandwidth of gain in metasurface antennas," *IEEE Trans. Antennas Propag.*, vol. 65, no. 6, pp. 2836–2842, 2017.

[254] G. V. Eleftheriades, A. K. Iyer, and P. C. Kremer, "Planar negative refractive index media using periodically L-C loaded transmission lines," *IEEE Trans. Microw. Theory Tech.*, vol. 50, no. 12, pp. 2702–2712, 2002.

[255] L. Liu, C. Caloz, C.-C. Chang, and T. Itoh, "Forward coupling phenomena between artificial left-handed transmission lines," *Journal Of Applied Physics*, vol. 92, no. 9, pp. 5560–5565, 2002.

[256] A. K. Iyer, P. C. Kremer, and G. V. Eleftheriades, "Experimental and theoretical verification of focusing in a large, periodically loaded transmission line negative refractive index metamaterial," *Optics Express*, vol. 11, no. 7, pp. 696–708, 2003.

[257] A. K. Iyer and G. V. Eleftheriades, "Volumetric layered transmission-line metamaterial exhibiting a negative refractive index," *Journal of the Optical Society of America B*, vol. 23, no. 3, pp. 553–570, 2006.

[258] A. Grbic and G. V. Eleftheriades, "Dispersion analysis of a microstrip-based negative refractive index periodic structure," *IEEE Microw. Wireless Compon. Lett.*, vol. 13, no. 4, pp. 155–157, 2003.

[259] ——, "Periodic analysis of a 2-D negative refractive index transmission line structure," *IEEE Trans. Antennas Propag.*, vol. 51, no. 10, pp. 2604–2611, 2003.

[260] F. Elek and G. V. Eleftheriades, "A two-dimensional uniplanar transmission-line metamaterial with a negative index of refraction," *New Journal of Physics*, vol. 7, pp. 163–180, 2005.

[261] A. Sanada, C. Caloz, and T. Itoh, "Planar distributed structures with negative refractive index," *IEEE Trans. Microw. Theory Tech.*, vol. 52, no. 4, pp. 1252–1263, 2004.

[262] R. Islam, M. Zedler, and G. V. Eleftheriades, "Modal analysis and wave propagation in finite 2D transmission-line metamaterials," *IEEE Trans. Antennas Propag.*, vol. 59, no. 5, pp. 1562–1570, 2011.

[263] A. Tavallaee and R. Abhari, "2-D characterisation of electromagnetic bandgap structures employed in power distribution networks," *IET Microwaves, Antennas, and Propagation*, vol. 1, no. 1, pp. 204–211, 2007.

[264] C. R. Paul, *Analysis of Multiconductor Transmission Lines*, 2nd ed. Hoboken, New Jersey, USA: John Wiley & Sons, Inc., 2008.

[265] J. A. B. Faria, *Multiconductor Transmission-Line Structures: Modal Analysis Techniques.* Hoboken, New Jersey, USA: John Wiley & Sons, Inc., 1993.

[266] F. Elek, "Theory and applications of multiconductor transmission line analysis for shielded Sievenpiper and related structures," Ph.D. dissertation, University of Toronto, 2011.

[267] R. Islam, "Theory and applications of microstrip/negative-refractive-index transmission line (MS/NRI-TL) coupled-line couplers," Ph.D. dissertation, University of Toronto, 2011.

[268] F. Elek and G. V. Eleftheriades, "Dispersion analysis of the shielded sievenpiper structure using multiconductor transmission-line theory," *IEEE Microw. Wireless Compon. Lett.*, vol. 14, no. 9, pp. 434–436, 2004.

[269] F. Bongard, J. Perruisseau-Carrier, and J. R. Mosig, "Enhanced periodic structure analysis based on a multiconductor transmission line model and application to metamaterials," *IEEE Trans. Microw. Theory Tech.*, vol. 57, no. 11, pp. 2715–2726, 2009.

[270] R. Islam and G. V. Eleftheriades, "On the independence of the excitation of complex modes in isotropic structures," *IEEE Trans. Antennas Propag.*, vol. 58, no. 5, pp. 1567–1578, 2010.

[271] K. Payandehjoo, A. Tavallaee, and R. Abhari, "Analysis of shielded electromagnetic bandgap structures using multiconductor transmission-line theory," *IEEE Trans. Adv. Packag.*, vol. 33, no. 1, pp. 236–245, 2010.

[272] S. Barth and A. K. Iyer, "A miniaturized uniplanar metamaterial-based EBG for parallel plate mode suppression," *IEEE Trans. Microw. Theory Tech.*, vol. 64, no. 4, pp. 1176–1185, 2016.

[273] M. Stickel, F. Elek, J. Zhu, and G. V. Eleftheriades, "Volumetric negative-refractive-index metamaterials based upon the shunt-node transmission-line configuration," *Journal of Applied Physics*, vol. 102, pp. 1–7, 2007.

[274] S. M. Rudolph and A. Grbic, "The design of broadband, volumetric NRI media using multiconductor transmission-line analysis," *IEEE Trans. Antennas Propag.*, vol. 58, no. 4, pp. 1144–1154, 2010.

[275] S. M. Rudolph, C. Pfeiffer, and A. Grbic, "Design and free-space measurements of broadband, low-loss negative-permeability and negative-index media," *IEEE Trans. Antennas Propag.*, vol. 59, no. 8, pp. 2989–2997, 2011.

[276] M. Selvanayagam and G. V. Eleftheriades, "Dual-polarized volumetric transmission-line metamaterials," *IEEE Trans. Antennas Propag.*, vol. 61, no. 5, pp. 2550–2560, 2013.

[277] M. Bagheriasl, O. Quevedo-Teruel, and G. Valerio, "Bloch analysis of artificial lines and surfaces exhibiting glide symmetry," *IEEE Trans. Microw. Theory Tech.*, vol. 67, no. 7, pp. 2618–2628, 2019.

[278] C. Caloz, C. H. Ahn, and T. Itoh, "Analysis 2D finite-size metamaterials by the transmission matrix method," in *Proceedings of the IEEE Antennas and Propagation Society International Symposium, Vol. 3B*, Washington, District of Columbia, Jul. 2005, pp. 2–5.

[279] J. A. B. Faria, "Nonuniqueness of modal transformations for multiconductor transmission line problems," *International Transactions on Electrical Energy Systems*, 2017.

[280] P. J. Nahin, *Oliver Heaviside*. New York, New York, USA: IEEE Press, 1988.

[281] R. A. Chipman, *Theory and Problems of Transmission Lines*. New York, New York, USA: McGrawHill, Inc., 1968.

[282] W. Thomson, "On the theory of the electric telegraph," *Proceedings of the Royal Society of London*, vol. 7, pp. 382–399, 1856.

[283] O. Heaviside, "On induction between parallel wires," *Journal of the Society of Telegraph Engineers*, vol. 9, no. 34, pp. 427–458, 1880.

[284] C. Donaghy-Spargo, "On heaviside's contributions to transmission line theory: waves, diffusion and energy flux," *Philosophical Transactions of the Royal Society A*, vol. 376, no. 2134, p. 20170457, 2018.

[285] O. Heaviside, "Electromagnetic induction and its propagation," in *Electrical Papers, Part 1.* London, UK: Macmillan and Co., 1892, pp. 429–560.

[286] G. Mie, "Electrische wellen an zwei parallelen drahten," *Annalen der Physik*, vol. 4, no. 2, pp. 201–249, 1900.

[287] S. A. Schelkunoff, "Conversion of maxwell's equations into generalized telegraphist's equations," *The Bell System Technical Journal*, vol. 34, no. 5, pp. 995–1043, 1955.

[288] A.-M. Ampere, *Memoire sur la Theorie Mathematique des Phenomenes Electro-Dynamiques Uniquement Deduite de L'experience*, 1st ed. Paris, France: Firmin Didot, 1827.

[289] J. C. Maxwell, "On physical lines of force," *The London, Edinburgh and Dublin Philosophical Magazine and Journal of Science*, vol. 90, pp. 11–23, 1861.

[290] M. Faraday, "Experimental researches in electricity," *Philosophical Transactions of the Royal Society*, vol. 122, pp. 125–162, 1832.

[291] S. A. Schelkunoff, "Impedance concept in wave guides," *Quarterly of Applied Mathematics*, vol. 2, no. 1, pp. 1–15, 1944.

[292] L. Carin and K. J. Webb, "Characteristic impedance of multilevel, multiconductor hybrid mode microstrip," *IEEE Trans. Magn.*, vol. 25, no. 4, pp. 2947–2949, 1989.

[293] D. F. Williams, "Multiconductor transmission line characterization," *IEEE Trans. Compon., Packag., Manuf. Technol. B*, vol. 20, no. 2, pp. 129–132, 1997.

[294] M. S. Alam, M. Koshiba, K. Hirayama, and Y. Hayashi, "Hybrid-mode analysis of multilayered and multiconductor transmission lines," *IEEE Trans. Microw. Theory Tech.*, vol. 45, no. 2, pp. 205–211, 1997.

[295] D. Williams, J. Rogers, and C. Holloway, "Multiconductor transmission-line characterization: Representations, approximations, and accuracy," *IEEE Trans. Microw. Theory Tech.*, vol. 47, no. 4, pp. 403–409, 1999.

[296] G. W. Slade and K. J. Webb, "Computation of characteristic impedance for multiple microstrip transmission lines using a vector finite element method," *IEEE Trans. Microw. Theory Tech.*, vol. 40, no. 1, pp. 34–40, 1992.

[297] V. Tripathi and H. Lee, "Spectral-domain computation of characteristic impedances and multiport parameters of multiple coupled microstrip lines," *IEEE Trans. Microw. Theory Tech.*, vol. 37, no. 1, pp. 215–221, 1989.

[298] S. A. Schelkunoff, "The impedance concept and its application to problems of reflection, refraction, shielding and power absorption," *The Bell System Technical Journal*, vol. 17, no. 1, pp. 17–48, 1938.

[299] J. R. Pierce, "A note on the transmission line equations in terms of impedance," *Bell System Technical Journal*, vol. 2, no. 22, pp. 263–265, 1943.

[300] N. K. Das, "A new theory of the characteristic impedance of general printed transmission lines applicable when power leakage exists," *IEEE Trans. Microw. Theory Tech.*, vol. 48, no. 7, pp. 1108–1117, 2000.

[301] F. Mesa and D. R. Jackson, "A novel approach for calculating the characteristic impedance of printed-circuit lines," *IEEE Microw. Wireless Compon. Lett.*, vol. 15, no. 4, pp. 283–285, 2005.

[302] W. J. Getsinger, "Microstrip dispersion model," *IEEE Trans. Microw. Theory Tech.*, vol. 21, no. 1, pp. 34–39, 1973.

[303] B. Bianco, L. Panini, M. Parodi, and S. Ridella, "Some considerations about the frequency dependence of the characteristic impedance of uniform microstrips," *IEEE Trans. Microw. Theory Tech.*, vol. 26, no. 3, pp. 182–185, 1978.

[304] W. J. Getsinger, "Microstrip characteristic impedance," *IEEE Trans. Microw. Theory Tech.*, vol. 27, no. 4, p. 293, 1979.

[305] ——, "Measurement and modeling of the apparent characteristic impedance of microstrip," *IEEE Trans. Microw. Theory Tech.*, vol. 31, no. 8, pp. 624–632, 1983.

[306] J. R. Brews, "Characteristic impedance of microstrip lines," *IEEE Trans. Microw. Theory Tech.*, vol. 35, no. 1, pp. 30–34, 1987.

[307] R. H. Jansen and N. H. L. Koster, "New aspects concerning the definition of microstrip characteristic impedance as a function of frequency," in *IEEE MTT-S International Microwave Symposium Digest*, Dallas, TX, USA, Jun. 1982.

[308] J. C. Rautio, "A new definition of characteristic impedance," in *IEEE MTT-S International Microwave Symposium Digest*, Boston, MA, USA, Jul. 1991.

[309] L. Zhu and K. Wu, "Revisiting characteristic impedance and its definition of microstrip line with a self-calibrated 3-d mom scheme," *IEEE Microw. Guided Wave Lett.*, vol. 8, no. 2, pp. 87–89, 1998.

[310] D. K. Cheng, *Field and Wave Electromagnetics*, 2nd ed. Boston, Massachusetts, USA: Addison-Wesley, 1992.

[311] J. L. Lagrange, "Solutions analytiques de quelques problemes sur les pyramides triangulaires," *Nouveaux memoires de l'Academie royale des sciences et belles-lettres de Berlin*, vol. 3, pp. 661–692, 1773.

[312] J. Stewart, *Calculus*, 5th ed. Belmont, CA, USA: Thomson Learning: Brooks/Cole, 2003.

[313] J. L. Lagrange, "Sur l'attraction des spheroides elliptiques," *Nouveaux mmoires de l'Acadmie royale des sciences et belles-lettres de Berlin*, vol. 3, pp. 619–658, 1773.

[314] C. F. Guass, "Theoria attractionis corporum sphaeroidicorum ellipticorum homogeneorum methodo nova tractata," *Werke*, vol. 1, pp. 1–22, 1863.

[315] H. von Helmholtz, *Die Lehre von den Tonempfindungen als physiologische Grundlage fr die Theorie der Musik*, 5th ed. Berlin, DE: F. Vieweg und sohn, 1896.

[316] S. E. Miller, "Coupled wave theory and waveguide applications," *The Bell System Technical Journal*, vol. 33, no. 3, pp. 661–719, 1954.

[317] J. R. Pierce, "Coupling modes of propagation," *Journal of Applied Physics*, vol. 25, no. 2, pp. 179–183, 1954.

[318] H. A. Haus and W. Huang, "Coupled-mode theory," *Proceedings of the IEEE*, vol. 79, no. 10, pp. 1505–1518, 1991.

[319] R. A. Horn and C. R. Johnson, *Matrix Analysis*, 2nd ed. Cambridge, UK: Cambridge University Press, 2013.

[320] H. Anton and C. Rorres, *Elementary Linear Algebra*, 9th ed. Hoboken, New Jersey, USA: John Wiley & Sons, Inc., 2005.

[321] A. M. Belyantsev and A. V. Gaponov, "Waves with complex propagation constants in coupled transmission lines without energy dissipation," *Radio Engineering and Electronic Physics*, vol. 9, pp. 980–988, 1964.

[322] P. J. B. Clarricoats and K. R. Slinn, "Complex modes of propagation in dielectric loaded circular waveguides," *Electronics Letters*, vol. 1, no. 5, pp. 145–146, 1965.

[323] ——, "Complex modes of propagation in dielectric loaded circular waveguides," *Electronics Letters*, vol. 1, no. 5, pp. 145–146, 1965.

[324] S. Laxpati and R. Mittra, "Energy considerations in open and closed waveguides," *IEEE Trans. Antennas Propag.*, vol. 13, no. 6, pp. 883–890, 1965.

[325] M. Mrozowski, *Guided Electromagnetic Waves*. UCLA Chicano, USA: Research Studies Press Ltd., 1997.

[326] T. Rozzi, L. Pierantoni, and M. Farina, "General constraints on the propagation of complex waves in closed lossless isotropic waveguides," *IEEE Trans. Microw. Theory Tech.*, vol. 46, no. 5, pp. 512–516, 1998.

[327] M. J. Freire, F. Mesa, and M. Horno, "Excitation of complex and backward mode on shielded lossless printed lines," *IEEE Trans. Microw. Theory Tech.*, vol. 46, no. 5, pp. 512–516, 1998.

[328] R. Islam and G. V. Eleftheriades, "On the independence of the excitation of complex modes in isotropic structures," *IEEE Trans. Antennas Propag.*, vol. 58, no. 5, pp. 1567–1578, 2010.

[329] F. Bloch, "Uber die quantenmechanik der elektronen in kristallgittern," *Zeitschrift fur Physik*, vol. 52, no. 7, pp. 555–600, 1928.

[330] A. H. Wilson, "The theory of electronic semi-conductors," *Proceedings Of The Royal Society Of London Series A-Containing Papers Of A Mathematical And Physical Character*, vol. 133, no. 822, pp. 458–491, 1931.

[331] L. Hoddeson, G. Bayrn, and M. Eckert, "The development of the quantum-mechanical electron theory of metals: 19281933," *Reviews of Modern Physics,*, vol. 59, no. 1, pp. 287–327, 1987.

[332] W. Thomson, "On peristaltic induction of electric currents," *Proceedings of the Royal Society of London*, vol. 8, pp. 121–132, 1857.

[333] O. Heaviside, "On induction between parallel wires," *Journal of the Society of Telegraph Engineers*, vol. 9, no. 34, pp. 427–452, 1880.

[334] H. Pleijel, *General Properties of a System of Parallel Conductors with Variable Constants*. Stockholm, Sweden: P. A. Norstedt and Soner, 1918.

[335] S. A. Levin, "Electromagnetic waves guided by parallel wires with particular reference to the effect of the earth," *Transactions of the American Institute of Electrical Engineers*, vol. 46, pp. 983–989, 1927.

[336] J. R. Carson, "The rigorous and approximate theories of electrical transmission along wires," *The Bell System Technical Journal*, vol. 7, no. 1, pp. 11–25, 1928.

[337] L. A. Pipes, "Matrix theory of multiconductor transmission lines," *The London, Edinburgh, and Dublin Philosophical Magazine and Journal of Science*, vol. 24, no. 159, pp. 97–113, 1937.

[338] ——, "Steady-state analysis of multiconductor transmission lines," *Journal of Applied Physics*, vol. 12, pp. 782–799, 1941.

[339] ——, "Direct computation of transmission matrices of electrical transmission lines: Part I," *Journal of the Franklin Institute*, vol. 281, no. 4, pp. 275–292, 1966.

[340] S. O. Rice, "Steady state solutions of transmission line equations," *Bell System Technical Journal*, vol. 20, no. 2, pp. 131–178, 1941.

[341] C. R. Paul, "Applications of multiconductor transmission line theory to the prediction of cable coupling," Rome Air Development Center, Air Force Systems Command, Griffiss Air Forces Base, New York, USA, Tech. Rep. RADC-TR-76-1O1, April 1976.

[342] J. W. Strutt, *Theory of Sound*, 1st ed. London, UK: MacMillan and Co., 1877.

[343] T. K. Caughey and M. E. J. O'Kelly, "Classical normal modes in damped linear dynamic systems," *Journal of Applied Mechanics*, vol. 32, pp. 583–588, 1965.

[344] J. He and Z. F. Fu, *Modal Analysis*, 1st ed. Woburn, Massachusetts, USA: Butterworth-Heinemann, 2001.

[345] S. S. Rao, *Mechanical Vibrations*, 4th ed. Upper Saddle River, New Jersey, USA: Pearson Prentice Hall, 2005.

[346] S. Adhikari, "Calculation of derivative of complex modes using classical normal modes," *Computers and Structures*, vol. 77, pp. 625–633, 2000.

[347] K. A. Foss, "Coordinates which uncouple the equations of motion of damped linear systems," Office of Naval Research, Arlington, VA, USA, Tech. Rep., 1956.

[348] B. J. A. Faria and B. J. F. da Silva, "Irregular eigenvalues in the analysis of multimodal propagation," in *Proceedings of the 8th Power Systems Computation Conference*, Helsinki, Finland, Aug. 1984, pp. 760–764.

[349] ——, "Wave propagation in polyphase transmission lines a general solution to include cases where ordinary modal theory fails," *IEEE Trans. Power Del.*, vol. 1, no. 2, pp. 182–189, 1986.

[350] C. R. Paul, "Decoupling the multiconductor transmission line equations," *IEEE Trans. Microw. Theory Tech.*, vol. 44, no. 8, pp. 1429–1440, 1996.

[351] G. T. Lei, G. W. Pan, and B. K. Gilbert, "Examination, clarification and simplification of modal decoupling method for multiconductor transmission lines," *IEEE Trans. Microw. Theory Tech.*, vol. 43, no. 9, pp. 2090–2100, 1995.

[352] D. F. Williams, L. A. Hayden, and R. B. Marks, "A complete multimode equivalent-circuit theory for electrical design," *Journal of Research of the National Institute of Standards and Technology*, vol. 102, no. 4, pp. 405–423, 1997.

[353] B. D. Milovanovic, A. Marincic, and N. S. Doncov, "Invention of pupins periodically distributed inductance coils to allow for long-distance telephone transmission," in *IEEE History of Telecommunications Conference*, Paris, France, Sep. 2008, pp. 152–159.

[354] M. I. Pupin, "Propagation of long electrical waves," *Transactions of the American Institute of Electrical Engineers*, vol. 16, pp. 91–142, 1899.

[355] W. S. Aldrich and G. W. Redfield, "Performance of an artificial forty-mile transmission line," *Transactions of the American Institute of Electrical Engineers*, vol. 17, pp. 339–360, 1901.

[356] J. H. Cunningham, "Design, construction and test of an artificial transmission line," *Transactions of the American Institute of Electrical Engineers*, vol. 40, no. 1, pp. 245–256, 1911.

[357] C. E. Magnusson and S. R. Burbank, "An artificial transmission line with adjustable line constants," *Transactions of the American Institute of Electrical Engineers*, vol. 35, no. 2, pp. 1137–1153, 1916.

[358] F. S. Dellenbaugh, "Artificial transmission lines with distributed constants," *Journal of the American Institute of Electrical Engineers*, vol. 42, no. 12, pp. 1293–1296, 1923.

[359] L. Brillouin, *Wave Propagation in Periodic Strctures.* New York, New York, USA: McGrawHill, Inc., 1946.

[360] ——, *Wave Propagation in Periodic Strctures.* New York, New York, USA: McGrawHill, Inc., 1946.

[361] E. A. N. Whitehead, "The theory of parallel-plate media for microwave lenses," *Proceedings of the IEE - Part III: Radio and Communication Engineering*, vol. 95, no. 52, pp. 133–140, 1951.

[362] W. M. Sharpless, "Artificial dielectrics for microwaves," *Proceedings of the IRE*, vol. 39, no. 11, pp. 1389–1393, 1951.

[363] P. B. Johns and R. L. Beurle, "Numerical solution of 2-dimensional scattering problems using a transmission-line matrix," *Proceedings of the Institution of Electrical Engineers*, vol. 118, no. 9, pp. 1203–1208, 1971.

[364] E. Yablonovitch, "Inhibited spontaneous emission in solid-state physics and electronics," *Physical Review Letters*, vol. 58, no. 20, pp. 2059–2062, 1987.

[365] ——, "Photonic band-gap structures," *Journal of the Optical Society of America B*, vol. 10, no. 2, pp. 283–295, 1993.

[366] E. Yablonovitch and T. J. Gmitter, "Photonic band structure: The face-centered-cubic case employing nonspherical atoms," *Physical Review Letters*, vol. 67, no. 17, pp. 2295–2298, 1991.

[367] F. Yang and Y. Rahmat-Samii, *Electromagnetic Bandgap Structures in Antenna Engineering*, 1st ed. Cambridge, United Kingdom: Cambridge University Press, 2009.

[368] M. Abegaonkar, L. Kurra, and S. K. Koul, *Printed Resonant Periodic Structures And Their Applications*, 1st ed. Boca Raton, FL, USA: Taylor & Francis Group, 2017.

[369] S. John, "Strong localization of photons in certain disordered dielectric superlattices," *Physical Review Letters*, vol. 58, p. 24862489, 1987.

[370] H. Y. D. Yang, "Finite difference analysis of 2-D photonic crystals," *IEEE Trans. Microw. Theory Tech.*, vol. 44, no. 12, pp. 2688–2695, 1996.

[371] V. Radisic, Y. Qian, R. Coccioli, and T. Itoh, "Novel 2-D photonic bandgap structure for microstrip lines," *IEEE Microw. Guided Wave Lett.*, vol. 8, no. 2, pp. 69–71, 1998.

[372] T.-L. Wu and S.-T. Chen, "A photonic crystal power/ground layer for eliminating simultaneously switching noise in high-speed circuit," *IEEE Trans. Microw. Theory Tech.*, vol. 54, no. 8, pp. 3398–3406, 2006.

[373] Y. Zhao and D. R. Grischkowsky, "2-D terahertz metallic photonic crystals in parallel-plate waveguides," *IEEE Trans. Microw. Theory Tech.*, vol. 55, no. 4, pp. 656–663, 2007.

[374] C. Caloz and T. Itoh, "Application of the transmission line theory of left-handed (LH) materials to the realization of a microstrip "LH line"," in *Proceedings of the IEEE International Symposium on Antennas and Propagation*, San Antonio, TX, USA, Jun. 2002, pp. 412–415.

[375] Y. Kasahara, H. Toyao, and E. Hankui, "Compact and multiband electromagnetic bandgap structures with adjustable bandgaps derived from branched open-circuit lines," *IEEE Trans. Microw. Theory Tech.*, vol. 65, no. 7, pp. 2330–2340, 2017.

[376] D. Sievenpiper, L. Zhang, R. F. J. Broas, N. G. Alexopolous, and E. Yablonovitch, "High-impedance electromagnetic surfaces with a forbidden frequency band," *IEEE Trans. Microw. Theory Tech.*, vol. 47, no. 11, pp. 2059–2074, 1999.

[377] F. Yang, K. Ma, Y. Qian, and T. Itoh, "A uniplanar compact photonic-bandgap (UC-PBG) structure and its applications for microwave circuits," *IEEE Trans. Microw. Theory Tech.*, vol. 47, no. 8, pp. 1509–1514, 1999.

[378] R. Coccioli, F.-R. Yang, K.-P. Ma, and T. Itoh, "Aperture-coupled patch antenna on UC-PBG substrate," *IEEE Trans. Microw. Theory Tech.*, vol. 47, no. 11, pp. 2123–2130, 1999.

[379] R. Gonzalo, P. de Maagt, and M. Sorolla, "Enhanced patch-antenna performance by suppressing surface waves using photonic-bandgap substrates," *IEEE Trans. Microw. Theory Tech.*, vol. 47, no. 11, pp. 2131–2138, 1999.

[380] R. Abhari and G. V. Eleftheriades, "Metallo-dielectric electromagnetic bandgap structures for suppression and isolation of the parallel-plate noise in high-speed circuits," *IEEE Trans. Microw. Theory Tech.*, vol. 51, no. 6, pp. 1629–1639, 2003.

[381] S. Barth, "Theory and applications of a uniplanar transmission-line metamaterial-inspired electromagnetic bandgap structure," Master's thesis, University of Alberta, 2015.

[382] B. P. Smyth, S. Barth, J. A. Brown, and A. K. Iyer, "The MTM-EBG: A fully uniplanar, printable, and embedded solution for multi-band functionality in microstrip devices and antennas," in *Proceedings of the USNC-URSI National Radio Science Meeting*, San Diego, CA, USA, May 2019.

[383] F. Yang, K. Ma, Y. Qian, and T. Itoh, "A uniplanar compact photonic-bandgap (UC-PBG) structure and its applications for microwave circuits," *IEEE Trans. Microw. Theory Tech.*, vol. 47, no. 8, pp. 1509–1514, 1999.

[384] F.-R. Yang, K.-P. Ma, Y. Qian, and T. Itoh, "A novel TEM waveguide using uniplanar compact photonic-bandgap (UC-PBG) structure," *IEEE Trans. Microw. Theory Tech.*, vol. 47, no. 11, pp. 2092–2098, 1999.

[385] R. Coccioli, F.-R. Yang, K.-P. Ma, and T. Itoh, "Aperture-coupled patch antenna on UC-PBG substrate," *IEEE Trans. Microw. Theory Tech.*, vol. 47, no. 11, pp. 2123–2130, 1999.

[386] D. J. Kern, D. H. Werner, A. Monorchio, L. Lanuzza, and M. J. Wilhelm, "The design synthesis of multiband artificial magnetic conductors using high impedance frequency selective surfaces," *IEEE Trans. Antennas Propag.*, vol. 53, no. 1, pp. 8–17, 2005.

[387] A. E. I. Lamminen, A. R. Vimpari, and J. Sily, "UC-EBG on LTCC for 60-ghz frequency band antenna applications," *IEEE Trans. Antennas Propag.*, vol. 57, no. 10, pp. 2904–2912, 2009.

[388] B. P. Smyth and A. K. Iyer, "Compact tri-band microstrip stub filter using embedded MTM-EBGs," in *IEEE International Symposium on Antennas and Propagation and USNC/URSI Radio Science Meeting*, Boston, MA, Jul. 2018, pp. 163–164.

[389] J. A. Brown and A. K. Iyer, "Mechanically tunable MTM-EBG-based bandstop filter," in *14th European Conference on Antennas and Propagation (EuCAP)*, Copenhagen, Denmark, Mar. 2020.

[390] J. A. Brown, S. Barth, B. P. Smyth, and A. K. Iyer, "Compact mechanically tunable microstrip bandstop filter with constant absolute bandwidth using an embedded metamaterial-based EBG," *IEEE Trans. Microw. Theory Tech.*, vol. 68, no. 10, pp. 4369–4380, 2020.

[391] D. M. Pozar, *Microwave Engineering*, 3rd ed. Hoboken, New Jersey, USA: John Wiley & Sons, Inc., 2005.

[392] C. Fabry and A. Perot, "Theorie et applications d'une nouvelle methode de spectroscopie interferentielle," *Annales de chimie et de physique*, vol. 16, no. 7, pp. 115–144, 1899.

[393] A. Perot and C. Fabry, "On the application of interference phenomena to the solution of various problems of spectroscopy and metrology," *Astrophysical Journal*, vol. 9, p. 87, 1899.

[394] N. Ismail, C. C. Kores, D. Geskus, and M. Pollnau, "On the application of interference phenomena to the solution of various problems of spectroscopy and metrology," *Optics Express*, vol. 24, no. 15, pp. 16 366–16 389, 2016.

[395] S. Barth and A. K. Iyer, "A novel scaling process for the computation of multiconductor transmission-line modal properties using the basis invariance of total current and power," *IEEE Access*, vol. 8, 2020.

[396] F.-Y. Chang, "Transient analysis of lossless coupled transmission lines in a nonhomogeneous dielectric medium," *IEEE Trans. Microw. Theory Tech.*, vol. 18, no. 9, pp. 616–626, 1970.

[397] F. Grassi, Y. Yang, X. Wu, G. Spadacini, and S. A. Pignari, "On mode conversion in geometrically unbalanced differential lines and its analogy with crosstalk," *IEEE Trans. Electromagn. Compat.*, vol. 57, no. 2, pp. 283–291, 2015.

[398] C. L. Fortescue, "Method of symmetrical co-ordinates applied to the solution of polyphase networks," in *34th Annual Convention of the American Institute of Electrical Engineers*, Atlantic City, New Jersey, USA, Jun. 1918.

[399] W. C. Duesterhoeft, M. W. Schulz, and E. Clarke, "Determination of instantaneous currents and voltages by means of alpha, beta, and zero components," *Transactions of the American Institute of Electrical Engineers*, vol. 70, no. 2, pp. 1248–1255, 1951.

[400] J. D. Glover, M. S. Sarma, and T. J. Overbye, *Oliver Heaviside*, 4th ed. Toronto, Ontario, Canada: Thomson Learning, 2008.

[401] H. Carlin, "The scattering matrix in network theory," *IRE Transactions on Circuit Theory*, vol. 3, no. 2, pp. 88–97, 1956.

[402] K. Kurokawa, "Power waves and the scattering matrix," *IEEE Trans. Microw. Theory Tech.*, vol. 13, no. 2, pp. 194–202, 1965.

[403] S. Amakawa, "Scattered reflections on scattering parameters - demystifying complex-referenced S parameters," *IEICE Transactions on Eectronics*, vol. E99C, no. 10, pp. 1100–1111, 2016.

[404] J. G. F. Francis, "The QR transformation, i," *The Computer Journal*, vol. 4, no. 3, pp. 265–271, 1961.

[405] V. N. Kublanovskaya, "On some algorithms for the solution of the complete eigenvalue problem," *USSR Computational Mathematics and Mathematical Physics*, vol. 1, no. 3, p. 637657, 1963.

[406] A. Bravais, "Memoire sur les systemes formes par les points distribues regulierement sur un plan ou dans l'espace," *Journal de l'Ecole polytechnique*, vol. 19, p. 1128, 1850.

[407] C. Kittel, *Introduction to Solid State Physics*, 7th ed. New York, New York, USA: John Wiley & Sons, 1996.

[408] E. V. Haynsworth, "On the schur complement," *Basel Mathematical Notes*, vol. 20, p. 17, 1968.

[409] F. Zhang, *The Schur Complement and Its Applications*, vol. First.

[410] J. D. F. Richard L. Burden, *Numerical Analysis*, vol. Ninth.

[411] M. K. Larisa Beilina, Evgenii Karchevskii, *Numerical Linear Algebra: Theory and Applications*, vol. First.

[412] G. Rote, *Division-Free Algorithms for the Determinant and the Pfaffian: Algebraic and Combinatorial Approaches*. Berlin, DE: Springer, 2001, pp. 119–135.

[413] F. L. Gall, "Faster algorithms for rectangular matrix multiplication," in *Proceedings of the 53rd Annual IEEE Symposium on Foundations of Computer Science*, New Brunswick, NJ, USA, Oct. 2012, p. 514523.

[414] V. Strassen, "Gaussian elimination is not optimal," *Numerische Mathematik*, vol. 13, p. 354356, 1969.

[415] D. Coppersmith and S. Winograd, "Matrix multiplication via arithmetic progressions," *Journal of Symbolic Computation*, vol. 9, no. 3, p. 251, 1990.

[416] G. Guennebaud, B. Jacob *et al.* Eigen v3. Accessed: 25 February 2021. [Online]. Available: https://eigen.tuxfamily.org

[417] E. Allen, J. Burns, D. Gillam, J. Hill, and V. Shubov, "The impact of finite precision arithmetic and sensitivity on the numerical solution of partial differential equations," *Mathematical and Computer Modelling*, vol. 35, pp. 1165–1196, 2002.

[418] P. Holoborodko. Computing eigenvalues in extended precision. Accessed: 4 July 2021. [Online]. Available: https://www.advanpix.com/2011/10/12/multiprecision-computation-eigenvalues-eigenvectors/

[419] Xcode. Accessed: 25 February 2021. [Online]. Available: https://developer.apple.com/xcode/

[420] S. Barth and A. K. Iyer, "A compact MTM-EBG-enabled common-mode filter without a defected ground," in *Proceedings of the IEEE International Symposium on Antennas and Propagation and North American Radio Science Meeting*, Montreal, QC, Canada, Jul. 2020, pp. 801–802.

[421] Official U.S. government information about the global positioning system (GPS) and related topics. Accessed: 15 June 2015. [Online]. Available: http://www.gps.gov/applications/

[422] "Global positioning system standard positioning service signal specification," United States of America Department of Defence, Tech. Rep., 1995, accessed: 15 June 2015. [Online]. Available: http://www.gps.gov/technical/ps/1995-SPS-signal-specification.pdf

[423] K.-K. M. Cheng and F.-L. Wong, "A novel approach to the design and implementation of dual-band compact planar 90° branch-line coupler," *IEEE Trans. Microw. Theory Tech.*, vol. 52, no. 11, pp. 2458–2463, 2004.

[424] S. Y. Zheng, S. H. Yeung, W. S. Chan, K. F. Man, S. H. Leung, and Q. Xue, "Dual-band rectangular patch hybrid coupler," *IEEE Trans. Microw. Theory Tech.*, vol. 56, no. 7, pp. 1721–1728, 2008.

[425] H. Kim, B. Lee, and M.-J. Park, "Dual-band branch-line coupler with port extensions," *IEEE Trans. Microw. Theory Tech.*, vol. 58, no. 3, pp. 651–655, 2010.

[426] H. Zhang and K. J. Chen, "A stub tapped branch-line coupler for dual-band operations," *IEEE Microw. Wireless Compon. Lett.*, vol. 17, no. 2, pp. 106–108, 2007.

[427] C.-L. Hsu, J.-T. Kuo, , and C.-W. Chang, "Miniaturized dual-band hybrid couplers with arbitrary power division ratios," *IEEE Trans. Microw. Theory Tech.*, vol. 57, no. 1, pp. 149–156, 2009.

[428] M.-J. Park and B. Lee, "Dual-band, cross coupled branch line coupler," *IEEE Microw. Wireless Compon. Lett.*, vol. 15, no. 10, pp. 655–657, 2005.

[429] K.-K. M. Cheng and F.-L. Wong, "A novel rat race coupler design for dual-band applications," *IEEE Microw. Wireless Compon. Lett.*, vol. 15, no. 8, pp. 521–523, 2005.

[430] L. K. Yeung, "A compact dual-band 90° coupler with coupled-line sections," *IEEE Trans. Microw. Theory Tech.*, vol. 59, no. 9, pp. 2227–2232, 2011.

[431] X. Wang, W.-Y. Yin, and K.-L. Wu, "A dual-band coupled-line coupler with an arbitrary coupling coefficient," *IEEE Trans. Microw. Theory Tech.*, vol. 60, no. 4, pp. 945–951, 2012.

[432] L.-S. Wu, B. Xia, W.-Y. Yin, and J. Mao, "Collaborative design of a new dual-bandpass 180° hybrid coupler," *IEEE Trans. Microw. Theory Tech.*, vol. 61, no. 3, pp. 1053–1066, 2013.

[433] "Ro3010 laminates," Rogers Corporation, Tech. Rep., 2019, accessed: 27 February 2021. [Online]. Available: https://rogerscorp.com/advanced-connectivity-solutions/ro3000-series-laminates/ro3010-laminates

[434] (2015) Protolaser U3. Accessed: 27 February 2021. [Online]. Available: http://www.lpkfusa.com/datasheets/prototyping/317-lpkf-protolaser-u3.pdf

[435] (2021) N5244A PNA-X microwave network analyzer, 43.5 GHz. Accessed: 27 February 2021. [Online]. Available: https://www.keysight.com/en/pdx-x201767-pn-N5244A/pna-x-microwave-network-analyzer-435-ghz

[436] "IEEE Standard for Low-Voltage Differential Signals (LVDS) for Scalable Coherent Interface (SCI)," *IEEE Std 1596.3-1996.*

[437] W.-T. Liu, C.-H. Tsai, T.-W. Han, and T.-L. Wu, "An embedded common-mode suppression filter for ghz differential signals using periodic defected ground plane," *IEEE Microw. Wireless Compon. Lett.*, vol. 18, no. 4, pp. 248–250, 2008.

[438] F. de Paulis, M. Cracraft, D. D. Febo, M. H. Nisanci, S. Connor, B. Archambeault, and A. Orlandi, "EBG-based common-mode microstrip and stripline filters: Experimental investigation of performances and crosstalk," *IEEE Trans. Electromagn. Compat.*, vol. 57, no. 7, pp. 996–1004, 2015.

[439] P. Velez, J. Bonache, and F. Martn, "Differential microstrip lines with common-mode suppression based on electromagnetic band-gaps (EBGs)," *IEEE Antennas Wireless Propag. Lett.*, vol. 14, pp. 40–43, 2015.

[440] M. Kim, "Periodically corrugated reference planes for common-mode noise suppression in high-speed differential signals," *IEEE Trans. Electromagn. Compat.*, vol. 58, no. 2, pp. 619–622, 2016.

[441] "Ro3003 laminates," Rogers Corporation, Tech. Rep., 2019, accessed: 28 February 2021. [Online]. Available: https://rogerscorp.com/advanced-connectivity-solutions/ro3000-series-laminates/ro3003-laminates

[442] W. Kim and B. Lee, "Modelling and design of 2D UC-PBG structure using transmission line theory," in *IEEE Antennas and Propagation Society International Symposium on Antennas and Propagation*, San Antonio, TX, Jun. 2002, pp. 780–783.

[443] B.-G. Lin, Q.-R. Zheng, and N.-C. Yuan, "A novel planar PBG structure for size reduction," *IEEE Microw. Wireless Compon. Lett.*, vol. 16, no. 5, pp. 269–271, 2006.

[444] M. F. Abedin, M. Z. Azad, and M. Ali, "Wideband smaller unit-cell planar EBG structures and their application," *IEEE Trans. Antennas Propag.*, vol. 56, no. 3, pp. 903–908, 2008.

[445] P.-Q. Lin, J. Liang, Y.-S. Zeng, and H.-M. Zhang, "A novel compact and wide-band uni-planar EBG structure," *Progress In Electromagnetics Research C*, vol. 1, pp. 37–43, 2008.

[446] P. Chen, X. Yang, C. Chen, and Y. Zhao, "A novel uni-planar compact EBG structure," *Progress In Electromagnetics Research Letters*, vol. 45, pp. 31–34, 2014.

[447] P. B. Johns, "A symmetrical condensed node for the TLM method," *IEEE Trans. Microw. Theory Tech.*, vol. 35, no. 4, pp. 370–377, 1987.

[448] J. C. Maxwell, "A dynamical theory of the electromagnetic field," *Philosophical Transactions of the Royal Society of London*, vol. 155, pp. 459–512, 1865.

[449] J. D. Jackson and L. B. Okun, "Historical roots of gauge invariance," *Reviews of Modern Physics*, vol. 73, no. 3, pp. 663–680, 2001.

Appendix A

Comments on the Requirements for Decoupling the TEM Wave Equations

Consider the TEM wave equations of (2.1). Wave equations are generally assumed to possess such a form, which in the case of TEM electromagnetic waves requires that the electric fields $\vec{E}$ and magnetic fields $\vec{H}$ are completely decoupled from each other – that is, the wave equation of the electric field (2.1a) does not depend on the magnetic field, and vice-versa for the wave equation of the magnetic field (2.1b). Decoupled wave equations imply certain properties of Maxwell's equations, and may be derived from Ampere's Law (2.3a) and Faraday's Law (2.3b). For example, taking the curl of each of (2.3) yields:

$$\vec{\nabla} \times \vec{\nabla} \times \vec{H} = \vec{\nabla} \times \left([\sigma]\, \vec{E} + \frac{\partial}{\partial \tau} \left([\epsilon]\, \vec{E} \right) \right) \tag{A.1a}$$

$$\vec{\nabla} \times \vec{\nabla} \times \vec{E} = -\vec{\nabla} \times \left(\frac{\partial}{\partial \tau} \left([\mu]\, \vec{H} \right) \right) \tag{A.1b}$$

For simplicity, assume that the media are source-free and isotropic (but still generally inhomogeneous). Then,

$$\nabla^2 \vec{H} = -\vec{\nabla} \times \left(\sigma \vec{E} + \frac{\partial}{\partial \tau} \left(\epsilon \vec{E} \right) \right) = -\vec{\nabla} \times \left(\sigma \vec{E} \right) - \vec{\nabla} \times \left(\left(\frac{\partial}{\partial \tau} \epsilon \right) \vec{E} \right) - \vec{\nabla} \times \left(\epsilon \left(\frac{\partial}{\partial \tau} \vec{E} \right) \right) \tag{A.2a}$$

$$\nabla^2 \vec{E} = \vec{\nabla} \times \left(\frac{\partial}{\partial \tau} \left(\mu \vec{H} \right) \right) = \vec{\nabla} \times \left(\left(\frac{\partial}{\partial \tau} \mu \right) \vec{H} \right) + \vec{\nabla} \times \left(\mu \left(\frac{\partial}{\partial \tau} \vec{H} \right) \right) \tag{A.2b}$$

A vector identity [16] is used which allows the expansion of the curl of the position-dependent products:

$$\vec{\nabla} \times \left(a \vec{F} \right) = a \left(\vec{\nabla} \times \vec{F} \right) + \left(\left(\vec{\nabla} a \right) \times \vec{F} \right) \tag{A.3}$$

The curls on the right-hand sides of (A.2) may be expanded to:

$$\begin{gathered} -\nabla^2\vec{H} = \\ \sigma\left(\vec{\nabla}\times\vec{E}\right)+\left(\left(\vec{\nabla}\sigma\right)\times\vec{E}\right) \\ +\left(\frac{\partial}{\partial\tau}\epsilon\right)\left(\vec{\nabla}\times\vec{E}\right)+\left(\left(\vec{\nabla}\left(\frac{\partial}{\partial\tau}\epsilon\right)\right)\times\vec{E}\right) \\ +\epsilon\left(\vec{\nabla}\times\left(\frac{\partial}{\partial\tau}\vec{E}\right)\right)+\left(\left(\vec{\nabla}\epsilon\right)\times\left(\frac{\partial}{\partial\tau}\vec{E}\right)\right) \end{gathered} \tag{A.4a}$$

$$\begin{gathered} \nabla^2\vec{E} = \\ +\left(\frac{\partial}{\partial\tau}\mu\right)\left(\vec{\nabla}\times\vec{H}\right)+\left(\left(\vec{\nabla}\left(\frac{\partial}{\partial\tau}\mu\right)\right)\times\vec{H}\right) \\ +\mu\left(\vec{\nabla}\times\left(\frac{\partial}{\partial\tau}\vec{H}\right)\right)+\left(\left(\vec{\nabla}\mu\right)\times\left(\frac{\partial}{\partial\tau}\vec{H}\right)\right) \end{gathered} \tag{A.4b}$$

It is critical to observe that Equations (A.4) may only be decoupled if various assumptions hold. Decoupling in the sense of these equations means that one may replace $\vec{\nabla}\times\vec{E}$ with some function of $\vec{H}$, and $\vec{\nabla}\times\vec{H}$ with some function of $\vec{E}$, as given by the general forms of Ampere's and Faraday's laws (2.3). Terms such as $\vec{\nabla}\times\left(\epsilon\vec{E}\right)$ or $\vec{\nabla}\times\left(\mu\vec{H}\right)$ preclude decoupling of the equations, since there exist no substitutes for these terms in the case of inhomogeneous materials. It may be observed that there is only one of these curl-of-fields terms ($\vec{\nabla}\times\vec{E}$ or $\vec{\nabla}\times\vec{H}$) per equation, such that the others must be reduced or zeroed if the equations are to be diagonalizable. Firstly, the simplest terms to zero are the gradients of the material parameters – i.e., $\vec{\nabla}a=\vec{0}$ (the materials are assumed to be homogeneous). Secondly, either the time derivative of the materials must be zero ($\frac{\partial}{\partial\tau}a=0$), or the time-derivative must be location-invariant ($\vec{\nabla}\left(\frac{\partial}{\partial\tau}a\right)=\frac{\partial}{\partial\tau}\left(\vec{\nabla}a\right)$) in addition to being homogeneous. Thirdly, either the time derivative of the fields must be zero ($\frac{\partial}{\partial\tau}\vec{F}=\vec{0}$), or the time-derivative of the fields must be spatially invariant ($\vec{\nabla}\times\left(\frac{\partial}{\partial\tau}\vec{F}\right)=\frac{\partial}{\partial\tau}\left(\vec{\nabla}\times\vec{F}\right)$). Under these conditions, the wave equations are decoupled.

Then, an *anisotropic*, inhomogeneous material may be considered. The curl of the product of such a material's matrix $[A]$ with a vector $\vec{F}$ is expressed as:

$$\vec{\nabla}\times\left([A]\cdot\vec{F}\right) \tag{A.5}$$

For simplicity, the curl operator may be expressed as a non-commuting matrix $[\nabla\times]$, where

$$\vec{\nabla}\times\vec{F}=[\nabla\times]\cdot\vec{F} \tag{A.6}$$

Such that

$$\vec{\nabla}\times\left([A]\cdot\vec{F}\right)=[\nabla\times]\left([A]\cdot\vec{F}\right) \tag{A.7}$$

In Cartesian coordinates, this matrix may be expressed as:

$$[\nabla\times] = \begin{bmatrix} 0 & -\frac{\partial}{\partial z} & \frac{\partial}{\partial y} \\ \frac{\partial}{\partial z} & 0 & -\frac{\partial}{\partial x} \\ -\frac{\partial}{\partial y} & \frac{\partial}{\partial x} & 0 \end{bmatrix} \tag{A.8}$$

Such that:

$$[\nabla\times]\cdot\vec{F} = \begin{bmatrix} \frac{\partial}{\partial y}F_z - \frac{\partial}{\partial z}F_y \\ \frac{\partial}{\partial z}F_x - \frac{\partial}{\partial x}F_z \\ \frac{\partial}{\partial x}F_y - \frac{\partial}{\partial y}F_x \end{bmatrix} \tag{A.9}$$

Inserting a time derivative into (A.7) as present in Faraday's and Ampere's laws yields:

$$[\nabla\times]\frac{\partial}{\partial\tau}\left([A]\cdot\vec{F}\right) = [\nabla\times]\left(\frac{\partial}{\partial\tau}[A]\right)\cdot\vec{F} + [\nabla\times][A]\cdot\left(\frac{\partial}{\partial\tau}\vec{F}\right) =$$

$$\begin{bmatrix} 0 & -\frac{\partial}{\partial z} & \frac{\partial}{\partial y} \\ \frac{\partial}{\partial z} & 0 & -\frac{\partial}{\partial x} \\ -\frac{\partial}{\partial y} & \frac{\partial}{\partial x} & 0 \end{bmatrix} \begin{bmatrix} \left(\frac{\partial}{\partial\tau}A_{xx}\right)F_x + \left(\frac{\partial}{\partial\tau}A_{xy}\right)F_y + \left(\frac{\partial}{\partial\tau}A_{xz}\right)F_z \\ \left(\frac{\partial}{\partial\tau}A_{yx}\right)F_x + \left(\frac{\partial}{\partial\tau}A_{yy}\right)F_y + \left(\frac{\partial}{\partial\tau}A_{yz}\right)F_z \\ \left(\frac{\partial}{\partial\tau}A_{zx}\right)F_x + \left(\frac{\partial}{\partial\tau}A_{zy}\right)F_y + \left(\frac{\partial}{\partial\tau}A_{zz}\right)F_z \end{bmatrix} + \begin{bmatrix} 0 & -\frac{\partial}{\partial z} & \frac{\partial}{\partial y} \\ \frac{\partial}{\partial z} & 0 & -\frac{\partial}{\partial x} \\ -\frac{\partial}{\partial y} & \frac{\partial}{\partial x} & 0 \end{bmatrix} \begin{bmatrix} \frac{\partial}{\partial\tau}A_{xx}\frac{\partial}{\partial\tau}F_x + \frac{\partial}{\partial\tau}A_{xy}\frac{\partial}{\partial\tau}F_y + \frac{\partial}{\partial\tau}A_{xz}\frac{\partial}{\partial\tau}F_z \\ \frac{\partial}{\partial\tau}A_{yx}\frac{\partial}{\partial\tau}F_x + \frac{\partial}{\partial\tau}A_{yy}\frac{\partial}{\partial\tau}F_y + \frac{\partial}{\partial\tau}A_{yz}\frac{\partial}{\partial\tau}F_z \\ \frac{\partial}{\partial\tau}A_{zx}\frac{\partial}{\partial\tau}F_x + \frac{\partial}{\partial\tau}A_{zy}\frac{\partial}{\partial\tau}F_y + \frac{\partial}{\partial\tau}A_{zz}\frac{\partial}{\partial\tau}F_z \end{bmatrix}$$

$$= \begin{bmatrix} \frac{\partial}{\partial y}\left(\left(\frac{\partial}{\partial\tau}A_{zx}\right)F_x\right) + \frac{\partial}{\partial y}\left(\left(\frac{\partial}{\partial\tau}A_{zy}\right)F_y\right) + \frac{\partial}{\partial y}\left(\left(\frac{\partial}{\partial\tau}A_{zz}\right)F_z\right) - \frac{\partial}{\partial z}\left(\left(\frac{\partial}{\partial\tau}A_{yx}\right)F_x\right) - \frac{\partial}{\partial z}\left(\left(\frac{\partial}{\partial\tau}A_{yy}\right)F_y\right) - \frac{\partial}{\partial z}\left(\left(\frac{\partial}{\partial\tau}A_{yz}\right)F_z\right) \\ \frac{\partial}{\partial z}\left(\left(\frac{\partial}{\partial\tau}A_{xx}\right)F_x\right) + \frac{\partial}{\partial z}\left(\left(\frac{\partial}{\partial\tau}A_{xy}\right)F_y\right) + \frac{\partial}{\partial z}\left(\left(\frac{\partial}{\partial\tau}A_{xz}\right)F_z\right) - \frac{\partial}{\partial x}\left(\left(\frac{\partial}{\partial\tau}A_{zx}\right)F_x\right) - \frac{\partial}{\partial x}\left(\left(\frac{\partial}{\partial\tau}A_{zy}\right)F_y\right) - \frac{\partial}{\partial x}\left(\left(\frac{\partial}{\partial\tau}A_{zz}\right)F_z\right) \\ \frac{\partial}{\partial x}\left(\left(\frac{\partial}{\partial\tau}A_{yx}\right)F_x\right) + \frac{\partial}{\partial x}\left(\left(\frac{\partial}{\partial\tau}A_{yy}\right)F_y\right) + \frac{\partial}{\partial x}\left(\left(\frac{\partial}{\partial\tau}A_{yz}\right)F_z\right) - \frac{\partial}{\partial y}\left(\left(\frac{\partial}{\partial\tau}A_{xx}\right)F_x\right) - \frac{\partial}{\partial y}\left(\left(\frac{\partial}{\partial\tau}A_{xy}\right)F_y\right) - \frac{\partial}{\partial y}\left(\left(\frac{\partial}{\partial\tau}A_{xz}\right)F_z\right) \end{bmatrix}$$

$$+ \begin{bmatrix} \frac{\partial}{\partial y}\left(A_{zx}\frac{\partial}{\partial\tau}F_x\right) + \frac{\partial}{\partial y}\left(A_{zy}\frac{\partial}{\partial\tau}F_y\right) + \frac{\partial}{\partial y}\left(A_{zz}\frac{\partial}{\partial\tau}F_z\right) - \frac{\partial}{\partial z}\left(A_{yx}\frac{\partial}{\partial\tau}F_x\right) - \frac{\partial}{\partial z}\left(A_{yy}\frac{\partial}{\partial\tau}F_y\right) - \frac{\partial}{\partial z}\left(A_{yz}\frac{\partial}{\partial\tau}F_z\right) \\ \frac{\partial}{\partial z}\left(A_{xx}\frac{\partial}{\partial\tau}F_x\right) + \frac{\partial}{\partial z}\left(A_{xy}\frac{\partial}{\partial\tau}F_y\right) + \frac{\partial}{\partial z}\left(A_{xz}\frac{\partial}{\partial\tau}F_z\right) - \frac{\partial}{\partial x}\left(A_{zx}\frac{\partial}{\partial\tau}F_x\right) - \frac{\partial}{\partial x}\left(A_{zy}\frac{\partial}{\partial\tau}F_y\right) - \frac{\partial}{\partial x}\left(A_{zz}\frac{\partial}{\partial\tau}F_z\right) \\ \frac{\partial}{\partial x}\left(A_{yx}\frac{\partial}{\partial\tau}F_x\right) + \frac{\partial}{\partial x}\left(A_{yy}\frac{\partial}{\partial\tau}F_y\right) + \frac{\partial}{\partial x}\left(A_{yz}\frac{\partial}{\partial\tau}F_z\right) - \frac{\partial}{\partial y}\left(A_{xx}\frac{\partial}{\partial\tau}F_x\right) - \frac{\partial}{\partial y}\left(A_{xy}\frac{\partial}{\partial\tau}F_y\right) - \frac{\partial}{\partial y}\left(A_{xz}\frac{\partial}{\partial\tau}F_z\right) \end{bmatrix} =$$

$$\begin{bmatrix} \left(\frac{\partial}{\partial y}\left(\frac{\partial}{\partial\tau}A_{zx}\right)\right)F_x + \left(\frac{\partial}{\partial y}\left(\frac{\partial}{\partial\tau}A_{zy}\right)\right)F_y + \left(\frac{\partial}{\partial y}\left(\frac{\partial}{\partial\tau}A_{zz}\right)\right)F_z - \left(\frac{\partial}{\partial z}\left(\frac{\partial}{\partial\tau}A_{yx}\right)\right)F_x - \left(\frac{\partial}{\partial z}\left(\frac{\partial}{\partial\tau}A_{yy}\right)\right)F_y - \left(\frac{\partial}{\partial z}\left(\frac{\partial}{\partial\tau}A_{yz}\right)\right)F_z \\ \left(\frac{\partial}{\partial z}\left(\frac{\partial}{\partial\tau}A_{xx}\right)\right)F_x + \left(\frac{\partial}{\partial z}\left(\frac{\partial}{\partial\tau}A_{xy}\right)\right)F_y + \left(\frac{\partial}{\partial z}\left(\frac{\partial}{\partial\tau}A_{xz}\right)\right)F_z - \left(\frac{\partial}{\partial x}\left(\frac{\partial}{\partial\tau}A_{zx}\right)\right)F_x - \left(\frac{\partial}{\partial x}\left(\frac{\partial}{\partial\tau}A_{zy}\right)\right)F_y - \left(\frac{\partial}{\partial x}\left(\frac{\partial}{\partial\tau}A_{zz}\right)\right)F_z \\ \left(\frac{\partial}{\partial x}\left(\frac{\partial}{\partial\tau}A_{yx}\right)\right)F_x + \left(\frac{\partial}{\partial x}\left(\frac{\partial}{\partial\tau}A_{yy}\right)\right)F_y + \left(\frac{\partial}{\partial x}\left(\frac{\partial}{\partial\tau}A_{yz}\right)\right)F_z - \left(\frac{\partial}{\partial y}\left(\frac{\partial}{\partial\tau}A_{xx}\right)\right)F_x - \left(\frac{\partial}{\partial y}\left(\frac{\partial}{\partial\tau}A_{xy}\right)\right)F_y - \left(\frac{\partial}{\partial y}\left(\frac{\partial}{\partial\tau}A_{xz}\right)\right)F_z \end{bmatrix}$$

$$+ \begin{bmatrix} \left(\frac{\partial}{\partial\tau}A_{zx}\right)\left(\frac{\partial}{\partial y}F_x\right) + \left(\frac{\partial}{\partial\tau}A_{zy}\right)\left(\frac{\partial}{\partial y}F_y\right) + \left(\frac{\partial}{\partial\tau}A_{zz}\right)\left(\frac{\partial}{\partial y}F_z\right) - \left(\frac{\partial}{\partial\tau}A_{yx}\right)\left(\frac{\partial}{\partial z}F_x\right) - \left(\frac{\partial}{\partial\tau}A_{yy}\right)\left(\frac{\partial}{\partial z}F_y\right) - \left(\frac{\partial}{\partial\tau}A_{yz}\right)\left(\frac{\partial}{\partial z}F_z\right) \\ \left(\frac{\partial}{\partial\tau}A_{xx}\right)\left(\frac{\partial}{\partial z}F_x\right) + \left(\frac{\partial}{\partial\tau}A_{xy}\right)\left(\frac{\partial}{\partial z}F_y\right) + \left(\frac{\partial}{\partial\tau}A_{xz}\right)\left(\frac{\partial}{\partial z}F_z\right) - \left(\frac{\partial}{\partial\tau}A_{zx}\right)\left(\frac{\partial}{\partial x}F_x\right) - \left(\frac{\partial}{\partial\tau}A_{zy}\right)\left(\frac{\partial}{\partial x}F_y\right) - \left(\frac{\partial}{\partial\tau}A_{zz}\right)\left(\frac{\partial}{\partial x}F_z\right) \\ \left(\frac{\partial}{\partial\tau}A_{yx}\right)\left(\frac{\partial}{\partial x}F_x\right) + \left(\frac{\partial}{\partial\tau}A_{yy}\right)\left(\frac{\partial}{\partial x}F_y\right) + \left(\frac{\partial}{\partial\tau}A_{yz}\right)\left(\frac{\partial}{\partial x}F_z\right) - \left(\frac{\partial}{\partial\tau}A_{xx}\right)\left(\frac{\partial}{\partial y}F_x\right) - \left(\frac{\partial}{\partial\tau}A_{xy}\right)\left(\frac{\partial}{\partial y}F_y\right) - \left(\frac{\partial}{\partial\tau}A_{xz}\right)\left(\frac{\partial}{\partial y}F_z\right) \end{bmatrix}$$

$$+ \begin{bmatrix} \left(\frac{\partial}{\partial y}A_{zx}\right)\left(\frac{\partial}{\partial\tau}F_x\right) + \left(\frac{\partial}{\partial y}A_{zy}\right)\left(\frac{\partial}{\partial\tau}F_y\right) + \left(\frac{\partial}{\partial y}A_{zz}\right)\left(\frac{\partial}{\partial\tau}F_z\right) - \left(\frac{\partial}{\partial z}A_{yx}\right)\left(\frac{\partial}{\partial\tau}F_x\right) - \left(\frac{\partial}{\partial z}A_{yy}\right)\left(\frac{\partial}{\partial\tau}F_y\right) - \left(\frac{\partial}{\partial z}A_{yz}\right)\left(\frac{\partial}{\partial\tau}F_z\right) \\ \left(\frac{\partial}{\partial z}A_{xx}\right)\left(\frac{\partial}{\partial\tau}F_x\right) + \left(\frac{\partial}{\partial z}A_{xy}\right)\left(\frac{\partial}{\partial\tau}F_y\right) + \left(\frac{\partial}{\partial z}A_{xz}\right)\left(\frac{\partial}{\partial\tau}F_z\right) - \left(\frac{\partial}{\partial x}A_{zx}\right)\left(\frac{\partial}{\partial\tau}F_x\right) - \left(\frac{\partial}{\partial x}A_{zy}\right)\left(\frac{\partial}{\partial\tau}F_y\right) - \left(\frac{\partial}{\partial x}A_{zz}\right)\left(\frac{\partial}{\partial\tau}F_z\right) \\ \left(\frac{\partial}{\partial x}A_{yx}\right)\left(\frac{\partial}{\partial\tau}F_x\right) + \left(\frac{\partial}{\partial x}A_{yy}\right)\left(\frac{\partial}{\partial\tau}F_y\right) + \left(\frac{\partial}{\partial x}A_{yz}\right)\left(\frac{\partial}{\partial\tau}F_z\right) - \left(\frac{\partial}{\partial y}A_{xx}\right)\left(\frac{\partial}{\partial\tau}F_x\right) - \left(\frac{\partial}{\partial y}A_{xy}\right)\left(\frac{\partial}{\partial\tau}F_y\right) - \left(\frac{\partial}{\partial y}A_{xz}\right)\left(\frac{\partial}{\partial\tau}F_z\right) \end{bmatrix}$$

$$+ \begin{bmatrix} A_{zx}\frac{\partial}{\partial y}\left(\frac{\partial}{\partial\tau}F_x\right) + A_{zy}\frac{\partial}{\partial y}\left(\frac{\partial}{\partial\tau}F_y\right) + A_{zz}\frac{\partial}{\partial y}\left(\frac{\partial}{\partial\tau}F_z\right) - A_{yx}\frac{\partial}{\partial z}\left(\frac{\partial}{\partial\tau}F_x\right) - A_{yy}\frac{\partial}{\partial z}\left(\frac{\partial}{\partial\tau}F_y\right) - A_{yz}\frac{\partial}{\partial z}\left(\frac{\partial}{\partial\tau}F_z\right) \\ A_{xx}\frac{\partial}{\partial z}\left(\frac{\partial}{\partial\tau}F_x\right) + A_{xy}\frac{\partial}{\partial z}\left(\frac{\partial}{\partial\tau}F_y\right) + A_{xz}\frac{\partial}{\partial z}\left(\frac{\partial}{\partial\tau}F_z\right) - A_{zx}\frac{\partial}{\partial x}\left(\frac{\partial}{\partial\tau}F_x\right) - A_{zy}\frac{\partial}{\partial x}\left(\frac{\partial}{\partial\tau}F_y\right) - A_{zz}\frac{\partial}{\partial x}\left(\frac{\partial}{\partial\tau}F_z\right) \\ A_{yx}\frac{\partial}{\partial x}\left(\frac{\partial}{\partial\tau}F_x\right) + A_{yy}\frac{\partial}{\partial x}\left(\frac{\partial}{\partial\tau}F_y\right) + A_{yz}\frac{\partial}{\partial x}\left(\frac{\partial}{\partial\tau}F_z\right) - A_{xx}\frac{\partial}{\partial y}\left(\frac{\partial}{\partial\tau}F_x\right) - A_{xy}\frac{\partial}{\partial y}\left(\frac{\partial}{\partial\tau}F_y\right) - A_{xz}\frac{\partial}{\partial y}\left(\frac{\partial}{\partial\tau}F_z\right) \end{bmatrix} \tag{A.10}$$

Equation (A.10) ultimately consists of four terms, each of which is a vector with three entries. It may

be noted that:

$$[\nabla\times]\,[A] = \begin{bmatrix} 0 & -\frac{\partial}{\partial z} & \frac{\partial}{\partial y} \\ \frac{\partial}{\partial z} & 0 & -\frac{\partial}{\partial x} \\ -\frac{\partial}{\partial y} & \frac{\partial}{\partial x} & 0 \end{bmatrix} \begin{bmatrix} A_{xx}\, A_{xy}\, A_{xz} \\ A_{yx}\, A_{yy}\, A_{yz} \\ A_{zx}\, A_{zy}\, A_{zz} \end{bmatrix} = \begin{bmatrix} \left(\frac{\partial}{\partial y}A_{zx} - \frac{\partial}{\partial z}A_{yx}\right) & \left(\frac{\partial}{\partial y}A_{zy} - \frac{\partial}{\partial z}A_{yy}\right) & \left(\frac{\partial}{\partial y}A_{zz} - \frac{\partial}{\partial z}A_{yz}\right) \\ \left(\frac{\partial}{\partial z}A_{xx} - \frac{\partial}{\partial x}A_{zx}\right) & \left(\frac{\partial}{\partial z}A_{xy} - \frac{\partial}{\partial x}A_{zy}\right) & \left(\frac{\partial}{\partial z}A_{xz} - \frac{\partial}{\partial x}A_{zz}\right) \\ \left(\frac{\partial}{\partial x}A_{yx} - \frac{\partial}{\partial y}A_{xx}\right) & \left(\frac{\partial}{\partial x}A_{yy} - \frac{\partial}{\partial y}A_{xy}\right) & \left(\frac{\partial}{\partial x}A_{yz} - \frac{\partial}{\partial y}A_{xz}\right) \end{bmatrix} \tag{A.11}$$

such that the first term of the right-hand side of (A.10) may be expressed as $[\nabla\times]\left(\frac{\partial}{\partial\tau}[A]\right)\cdot\vec{F}$, while the third term may be expressed as $[\nabla\times][A]\cdot\left(\frac{\partial}{\partial\tau}\vec{F}\right)$. Since both of these terms must be zero, it may be concluded that $[\nabla\times]\left(\frac{\partial}{\partial\tau}[A]\right) = [0]$ and $[\nabla\times][A] = [0]$. Clearly, the first term is held if the time derivative of the the material's matrix $[A]$ is homogeneous. However, it could also hold under the pathological case that:

$$\begin{bmatrix} 0 & 0 & \frac{\partial}{\partial y} \\ \frac{\partial}{\partial z} & 0 & 0 \\ 0 & \frac{\partial}{\partial x} & 0 \end{bmatrix} \left(\frac{\partial}{\partial\tau}\begin{bmatrix} A_{xx}\, A_{xy}\, A_{xz} \\ A_{yx}\, A_{yy}\, A_{yz} \\ A_{zx}\, A_{zy}\, A_{zz} \end{bmatrix}\right)\cdot\vec{F} = \begin{bmatrix} 0 & \frac{\partial}{\partial z} & 0 \\ 0 & 0 & \frac{\partial}{\partial x} \\ \frac{\partial}{\partial y} & 0 & 0 \end{bmatrix} \left(\frac{\partial}{\partial\tau}\begin{bmatrix} A_{xx}\, A_{xy}\, A_{xz} \\ A_{yx}\, A_{yy}\, A_{yz} \\ A_{zx}\, A_{zy}\, A_{zz} \end{bmatrix}\right)\cdot\vec{F} \tag{A.12}$$

Similarly, the second is held if the material parameter's matrix is homogeneous, or if a similar pathological case holds:

$$\begin{bmatrix} 0 & 0 & \frac{\partial}{\partial y} \\ \frac{\partial}{\partial z} & 0 & 0 \\ 0 & \frac{\partial}{\partial x} & 0 \end{bmatrix} \begin{bmatrix} A_{xx}\, A_{xy}\, A_{xz} \\ A_{yx}\, A_{yy}\, A_{yz} \\ A_{zx}\, A_{zy}\, A_{zz} \end{bmatrix}\cdot\frac{\partial}{\partial\tau}\vec{F} = \begin{bmatrix} 0 & \frac{\partial}{\partial z} & 0 \\ 0 & 0 & \frac{\partial}{\partial x} \\ \frac{\partial}{\partial y} & 0 & 0 \end{bmatrix} \begin{bmatrix} A_{xx}\, A_{xy}\, A_{xz} \\ A_{yx}\, A_{yy}\, A_{yz} \\ A_{zx}\, A_{zy}\, A_{zz} \end{bmatrix}\cdot\frac{\partial}{\partial\tau}\vec{F} \tag{A.13}$$

The second and fourth terms of (A.10) are less straightforward. Clearly, both are somehow related to $[\nabla\times]\cdot\vec{F}$ or $[\nabla\times]\cdot\left(\frac{\partial}{\partial\tau}\vec{F}\right)$, but it is not readily apparent how so. Functions $\digamma$ are being sought, where the terms may be represented as $\digamma\left(\frac{\partial}{\partial\tau}[A]\right)[\nabla\times]\cdot\vec{F}$ and $\digamma\left([A]\right)[\nabla\times]\cdot\left(\frac{\partial}{\partial\tau}\vec{F}\right)$, but the current consensus appears to be that such a process is either unknown, or impossible to specify. Therefore, the only analytical route left which with to decouple the TEM wave equations appears to be to assume that the media are both homogeneous and isotropic.

In summary, it appears that in order for (decoupled) TEM waves to propagate in a given medium, that medium must be source-free, homogeneous, and anisotropic.

Appendix B

Magnetic Potential in Transmission-Line Modes

Vector magnetic potential ($\vec{A}$) is indirectly defined from electric and magnetic fields as [16, 310]:

$$\vec{E} = -\vec{\nabla}\Phi_E - \frac{\partial}{\partial t}\vec{A} \tag{B.1a}$$

$$\vec{H} = [\mu]^{-1}\,\vec{\nabla} \times \vec{A} \tag{B.1b}$$

Since (B.1b) also specifies that $\vec{A}$ is proportional to $\vec{H}$, it must be the case that the two share the same sources: currents. In this case, the divergence of $\vec{A}$ outside of the conductors (where there are no longitudinally-directed currents) may be specified using the Coulomb gauge [448, 449]:

$$\vec{\nabla} \cdot \vec{A} = 0 \tag{B.2}$$

A *scalar* magnetic potential Φ_M between the conductors may then be defined as:

$$\Phi_M = \vec{A} \cdot \hat{l} \tag{B.3}$$

The gradient of (B.3) is then defined as:

$$\nabla\Phi_M = \nabla\left(\vec{A} \cdot \hat{l}\right) \tag{B.4}$$

Equation (B.4) my be expanded through invoking the vector identity [16]:

$$\nabla\left(\vec{F} \cdot \vec{G}\right) = \left(\vec{F} \cdot \vec{\nabla}\right)\vec{G} + \left(\vec{G} \cdot \vec{\nabla}\right)\vec{F} + \vec{F} \times \left(\vec{\nabla} \times \vec{G}\right) + \vec{G} \times \left(\vec{\nabla} \times \vec{F}\right) \tag{B.5}$$

Invoking (B.2) and noting that $\left(\vec{A} \cdot \vec{\nabla}\right)\hat{l} = \vec{0}$ and $\vec{A} \times \left(\vec{\nabla} \times \hat{l}\right) = \vec{0}$:

$$\nabla\Phi_M = \frac{\partial}{\partial \vec{l}}\vec{A} + \left(\vec{\nabla} \times \vec{A}\right) \times \hat{l} \tag{B.6}$$

Integrating in the transverse plane yields:

$$-\int_0^1 (\nabla\Phi_M)\cdot d\vec{r} = -\int_0^1 \left(\left(\vec{\nabla}\times\vec{A}\right)\times\hat{l}\right)\cdot d\vec{r} \tag{B.7}$$

The left may be reduced by invoking the fundamental theorem of calculus for line integrals (Gradient theorem), which states [312]:

$$\int_0^1 (\nabla\phi(\vec{r}))\cdot d\vec{r} = \phi(1)-\phi(0) \tag{B.8}$$

By taking conductor 0 as the potential's reference:

$$\Phi_M = -\int_0^1 \left(\left(\vec{\nabla}\times\vec{A}\right)\times\hat{l}\right)\cdot d\vec{r} \tag{B.9}$$

Once again invoking (B.1b), and since the curl of $\vec{A}$ must be in the transverse plane:

$$\Phi_M = -\int_0^1 \left(\left([\mu]\,\vec{H}\right)\times\hat{l}\right)\cdot d\vec{r} \tag{B.10}$$

Of course, (B.9) only holds if the potential gradient $\nabla\Phi_M$ is conservative; the stipulations of this criterion are given in Section 2.1.3.

Appendix C

Derivation of Multi-Modal Scattering Parameters in Generalized Networks

In keeping with the notation of section 2.3.2, the terminal-domain voltage-based scattering parameters $[S_T]$ of a general network is expressed as [391]:

$$\vec{V}_T^- = [S_T]\,\vec{V}_T^+ \tag{C.1}$$

Expanding this notation to any number of ports N (with each port indicated by n) and, where each port contains $m\,(n)$ terminals yields:

$$\begin{bmatrix} \vec{V}_{T_0}^- \\ \vec{V}_{T_1}^- \\ \vec{V}_{T_2}^- \\ \vdots \\ \vec{V}_{T_{(N-1)}}^- \end{bmatrix} = [S_T] \begin{bmatrix} \vec{V}_{T_0}^+ \\ \vec{V}_{T_1}^+ \\ \vec{V}_{T_2}^+ \\ \vdots \\ \vec{V}_{T_{(N-1)}}^+ \end{bmatrix} \tag{C.2}$$

Invoking the change of bases from the terminal to modal domains (2.74), where

$$\vec{V}_{T_n}^{\pm} = [T_{V_n}]\,\vec{V}_{M_n}^{\pm} \tag{C.3}$$

where the subscript M_n is used to indicated the modal-domain properties at port n. Inserting (C.3) into (C.2) and re-arranging gives:

$$\begin{bmatrix} \vec{V}_{M_0}^- \\ \vec{V}_{M_1}^- \\ \vec{V}_{M_2}^- \\ \vdots \\ \vec{V}_{M_{(N-1)}}^- \end{bmatrix} = \begin{bmatrix} [T_{V_0}]^{-1} & [0] & [0] & \dots & [0] \\ [0] & [T_{V_1}]^{-1} & [0] & \dots & [0] \\ [0] & [0] & [T_{V_2}]^{-1} & \dots & [0] \\ \vdots & \vdots & \vdots & \ddots & \vdots \\ [0] & [0] & [0] & \dots & \left[T_{V_{(N-1)}}\right]^{-1} \end{bmatrix} [S_T] \begin{bmatrix} [T_{V_0}] & [0] & [0] & \dots & [0] \\ [0] & [T_{V_1}] & [0] & \dots & [0] \\ [0] & [0] & [T_{V_2}] & \dots & [0] \\ \vdots & \vdots & \vdots & \ddots & \vdots \\ [0] & [0] & [0] & \dots & \left[T_{V_{(N-1)}}\right] \end{bmatrix} \begin{bmatrix} \vec{V}_{M_0}^+ \\ \vec{V}_{M_1}^+ \\ \vec{V}_{M_2}^+ \\ \vdots \\ \vec{V}_{M_{(N-1)}}^+ \end{bmatrix} \tag{C.4}$$

The inner terms are defined as the modal-domain scattering parameters, such that:

$$[S_M] = \begin{bmatrix} [T_{V_0}]^{-1} & [0] & [0] & \dots & [0] \\ [0] & [T_{V_1}]^{-1} & [0] & \dots & [0] \\ [0] & [0] & [T_{V_2}]^{-1} & \dots & [0] \\ \vdots & \vdots & \vdots & \ddots & \vdots \\ [0] & [0] & [0] & \dots & \left[T_{V_{(N-1)}}\right]^{-1} \end{bmatrix} [S_T] \begin{bmatrix} [T_{V_0}] & [0] & [0] & \dots & [0] \\ [0] & [T_{V_1}] & [0] & \dots & [0] \\ [0] & [0] & [T_{V_2}] & \dots & [0] \\ \vdots & \vdots & \vdots & \ddots & \vdots \\ [0] & [0] & [0] & \dots & \left[T_{V_{(N-1)}}\right] \end{bmatrix} \tag{C.5}$$

Of course, this process may be applied to any change of basis of the voltage vectors, not only the terminal and modal domains.

Appendix D

Modal Properties Determination Process Details

Following the process with which to determine the current scaling coefficients $\left[a^I\right]$ in section 3.1.3 it becomes apparent that, due to the fact that information regarding the currents on the reference conductor is typically omitted from the determination of the eigenvectors via (2.70b), a workaround is required since in general only one of (3.16) will hold. This is true since the current on the reference conductor will either be positively directed, negatively directed, or possess zero magnitude. In this case, one of the sets will be smaller than the other, such that the scale factor a^I_{mm} may be expressed as.

$$a^I_{mm} = max\left(\left(\sum_{n=0}^{n<N}\left(\left[T_I^{+z}\right]\vec{\delta}_m\right)\right)^{-1}, \left(\sum_{n=0}^{n<N}\left(\left[T_I^{-z}\right]\vec{\delta}_m\right)\right)^{-1}\right) \tag{D.1}$$

The pseudocode Algorithm 1 is proposed to implement this solution, where all scalar or matrix values are assumed to be of a complex, floating-point type, unless they are indices (in which case they are integer values). This algorithm has an outermost loop which iterates over each column m, corresponding to a given mode. The inner loop has four main processes: in order of operation, the positive and negative sums are computed, and the larger sum is selected and evaluated. The column's a^I_{mm} is then multiplied by the inverse of the sum. Lastly, once the complete $\left[a^I\right]$ matrix (which is diagonal) has been calculated for all columns, the scaled $[T_I]$ can be calculated, and utilizing the power equality (3.4), $[T_V]$ is calculated directly. Both scaled matrices are then returned.

Algorithm 1 $[T_V]$ and $[T_I]$ Scaling Procedure

procedure ScaleTvTi($[T_V], [T_I]$)
  $[a] \leftarrow [I]$ ▷ Initialize $[a]$ with identity
  for `Each Column` m **do**
    $NegSum \leftarrow 0$
    $PosSum \leftarrow 0$
    $LargerSum \leftarrow 0$
    for `Each Row` n **do**
      $b \leftarrow \Re\{T_I(n,m) \times a(m,m)\}$
      if $b \leq 0$ **then**
        $NegSum \leftarrow NegSum - b$
      else
        $PosSum \leftarrow PosSum + b$
      end if
    end for
    if $NegSum \geq PosSum$ **then**
      $LargerSum \leftarrow NegSum$
    else
      $LargerSum \leftarrow PosSum$
    end if
    $a(m,m) \leftarrow a(m,m) \div LargerSum$
  end for
  $[T_I] \leftarrow [T_I] \times [a]$
  $[T_V] \leftarrow [T_I]^{-1^*}$
  return $([T_V], [T_I])$
end procedure

Appendix E

Determining Modal Properties From Fields

Understanding the numerical process of solving modes is key to understanding why some processes can directly determine all modal properties, while other cannot. For example: why can a waveport analysis in HFSS determine modal characteristic impedances without any scaling, whereas the analytical processes of section 2.3 requires scaling to yield correct values?

Although the exact processes used by HFSS are not publicly available, the technical notes in its documentation do provide some insight. To start, the waveport eigenmode solver in HFSS solves the electric fields of various modes on its surface ($\vec{E}_m\left(\vec{t}\right)$) via the eigenmode equation:

$$\vec{\nabla} \times \left(\frac{1}{\mu_r} \left(\vec{\nabla} \times \vec{E}_m\left(\vec{t}\right) \right) e^{-\gamma_m \vec{l}} \right) = k_0^2 \epsilon_r \vec{E}_m\left(\vec{t}\right) e^{-\gamma_m \vec{l}} \tag{E.1}$$

where the modal fields are the eigenvectors, the modal propagation constants are γ_m and $k_0^2 = \frac{\omega^2}{c^2}$ are the eigenvalues. It is not readily clear how the propagation constants γ_m are solved simultaneous with the fields, but regardless the documentation states that they are (it could also be assumed that waveport exists at a location $l = 0$, removing the need to solve these values). The fields $\vec{E}_m$ are scaled by some arbitrary value, which may be set by the user. Under the assumption of linear media, the corresponding modal magnetic fields $\vec{H}_m$ may be readily determined, since the geometry, material properties, and other relevant information are known. These magnetic fields will inherit the scaling factors of the electric fields. Then, by integrating $\vec{\nabla}_t \times \vec{H}_m$ over the area of the waveport the modal current I_M may be determined, and by integrating $\vec{E}_m \times \vec{H}_m$ over the area of the waveport, the modal power P_M may be determined. Then, modal properties such as characteristic impedance may de determined though equations such as [291–293]:

$$Z_{cM} = \frac{P_M}{I_M^2} \tag{E.2}$$

in which the scaling factors will cancel. On the contrary, the solution of modal characteristic impedances via the processes of section 2.3 follow a different method. Firstly, assuming the per-unit-length terminal-domain admittance and impedance matrices $[Y_t]$ and $[Z_t]$ are known, (2.59b) and (2.60b) may be combined

to yield the eigenmode expression (considerring a forward-travelling wave):

$$\gamma_M^2 \vec{I}_T^+ = [Y_T]\,[Z_T]\,\vec{I}_T^+ \tag{E.3}$$

which may be solved to yield γ_M, the propagation constant of each solved mode, along with the current distribution on the terminals $\vec{I}_T$ for each solved mode. The currents $\vec{I}_T$ are again scaled by any arbitrary quantity. Equation (2.57b) may then be integrated with (2.60a) to yield (again for a forward-travelling wave):

$$\vec{V}_T^+ = -\gamma_M^{-1}\,[Z]\,\vec{I}_T^+ \tag{E.4}$$

in which the voltages also inherit the scaling factors. However, unlike with the fields in HFSS, there does not appear to exist any method by which characteristic impedance may be computed (defining it as $Z_{cM} = V_M^+/I_M^+$) – noting that the (vector) terminal currents $\vec{I}_T^+$ may be converted to the (scalar) modal equivalent value I_M^+ as outline below.

While total modal power P_M is straightforward to compute, modal current I_M is somewhat awkward to work with, since especially in MTL systems, the currents are distributed over multiple conductors, and the modal current that is being sought is in fact the *loop* current of the mode. However, this may be remedied through observing that the modal loop current is precisely half of the total sum of the absolute values of each of the individual terminal-domain currents (making use of Postulate 1). A process for the determination of modal voltages from MTL fields does not appear to be available.

Of course, since various properties are extracted from modal simulations, the eigenvectors of these simulations (electric and magnetic fields, in the case of HFSS) are arbitrarily scaled. As such, the extracted currents must be correctly scaled as discussed in section 3.1 in order for them to bear meaning.

Appendix F

Conversion of M-Parameters To/From Other Parameters

M-Parameters are very flexible in their conversion to/from other types of parameters. In order to efficiently be transformed, it is useful to sort the columns of $[M]$ to define a pair of auxiliary matrices:

$$[M] = [[M_V] \ [M_I]] \tag{F.1}$$

where $[M_V]$ contains the columns corresponding to all of the voltage vectors, and $[M_I]$ contains the columns corresponding with all of the current vectors. That is:

$$[M_V]\,\vec{V} + [M_I]\,\vec{I} = \vec{0} \tag{F.2}$$

Then, the following derivations may be made:

F.1 S-Parameters

At each port, the voltages and currents on each non-reference conductors are described as a superposition of the ingoing $(+)$ and outgoing $(-)$ waves:

$$\vec{V} = \vec{V}^{+} + \vec{V}^{-} \tag{F.3a}$$

$$\vec{I} = \vec{I}^{+} + \vec{I}^{-} \tag{F.3b}$$

Inserting (F.3) into (F.2) gives:

$$[M_V]\left(\vec{V}^{+} + \vec{V}^{-}\right) + [M_I]\left(\vec{I}^{+} + \vec{I}^{-}\right) = \vec{0} \tag{F.4}$$

If $[Z_N]$ describes the relationships between $\vec{V}^{+}$, $\vec{I}^{+}$, $\vec{V}^{-}$, and $\vec{I}^{-}$ in a reciprocal network, where:

$$\vec{V}^{+} = [Z_N]\,\vec{I}^{+} \tag{F.5a}$$

$$\vec{V}^- = -\left[Z_N\right]\vec{I}^- \tag{F.5b}$$

then (F.4) may be expressed as:

$$\left[M_V\right]\left(\vec{V}^+ + \vec{V}^-\right) + \left[M_I\right]\left[Z_N\right]^{-1}\left(\vec{V}^+ - \vec{V}^-\right) = \vec{0} \tag{F.6}$$

Which may be re-arranged to give:

$$\left(\left[M_V\right] + \left[M_I\right]\left[Z_N\right]^{-1}\right)\vec{V}^+ + \left(\left[M_V\right] - \left[M_I\right]\left[Z_N\right]^{-1}\right)\vec{V}^- = \vec{0} \tag{F.7}$$

Which, in turn, may be expressed as:

$$\vec{V}^- = \left(\left[M_I\right]\left[Z_N\right]^{-1} - \left[M_V\right]\right)^{-1}\left(\left[M_I\right]\left[Z_N\right]^{-1} + \left[M_V\right]\right)\vec{V}^+ \tag{F.8}$$

Factoring out $[Z_N]$:

$$\vec{V}^- = \left[Z_N\right]\left(\left[M_I\right] - \left[M_V\right]\left[Z_N\right]\right)^{-1}\left(\left[M_I\right] + \left[M_V\right]\left[Z_N\right]\right)\left[Z_N\right]^{-1}\vec{V}^+ \tag{F.9}$$

Comparison with (3.39) yields:

$$\left[S\right] = \left[Z_N\right]\left(\left[M_I\right] - \left[M_V\right]\left[Z_N\right]\right)^{-1}\left(\left[M_I\right] + \left[M_V\right]\left[Z_N\right]\right)\left[Z_N\right]^{-1} \tag{F.10}$$

which is the resulting transformation. The reverse may be accomplished – that is, the transformation of $[S]$ to $[M]$ may be accomplished by first inserting (F.3a) into (F.4), as well as utilizing (F.3b) and (F.5) gives

$$\vec{V} = \left(\left[I\right] + \left[S\right]\right)\vec{V}^+ \tag{F.11a}$$

$$\vec{I} = \left[Z_N\right]^{-1}\left(\left[I\right] - \left[S\right]\right)\left[Z_N\right]\vec{I}^+ \tag{F.11b}$$

Equations (F.11) may be re-arranged to:

$$\vec{V}^+ = \left(\left[I\right] + \left[S\right]\right)^{-1}\vec{V} \tag{F.12a}$$

$$\vec{I}^+ = \left[Z_N\right]^{-1}\left(\left[I\right] - \left[S\right]\right)^{-1}\left[Z_N\right]\vec{I} \tag{F.12b}$$

Resubstituting (F.12) back into both sides of (F.5a) gives:

$$\left(\left[I\right] + \left[S\right]\right)^{-1}\vec{V} + \left(\left[S\right] - \left[I\right]\right)^{-1}\left[Z_N\right]\vec{I} = \vec{0} \tag{F.13}$$

Comparing (F.13) with (F.2) indicates that:

$$\left[M_V\right] = \left(\left[S\right] + \left[I\right]\right)^{-1} \tag{F.14a}$$

$$\left[M_I\right] = \left(\left[S\right] - \left[I\right]\right)^{-1}\left[Z_N\right] \tag{F.14b}$$

F.2 $ABCD$-Parameters

To transform M-Parameters into the more common $ABCD$-Parameters, firstly the matrix $[M]$ is partitioned as:

$$\begin{bmatrix} [M_{11}]\,[M_{12}]\,[M_{13}]\,[M_{14}] \\ [M_{21}]\,[M_{22}]\,[M_{23}]\,[M_{24}] \end{bmatrix} \begin{bmatrix} \vec{V}_1 \\ \vec{I}_1 \\ \vec{V}_2 \\ \vec{I}_2 \end{bmatrix} = \vec{0} \tag{F.15}$$

Equation (F.15) may be re-arranged to:

$$\begin{bmatrix} [M_{11}]\,[M_{12}] \\ [M_{21}]\,[M_{22}] \end{bmatrix} \begin{bmatrix} \vec{V}_1 \\ \vec{I}_1 \end{bmatrix} + \begin{bmatrix} [M_{13}]\,[M_{14}] \\ [M_{23}]\,[M_{24}] \end{bmatrix} \begin{bmatrix} \vec{V}_2 \\ \vec{I}_2 \end{bmatrix} = \vec{0} \tag{F.16}$$

and further to:

$$\begin{bmatrix} \vec{V}_1 \\ \vec{I}_1 \end{bmatrix} = - \begin{bmatrix} [M_{11}]\,[M_{12}] \\ [M_{21}]\,[M_{22}] \end{bmatrix}^{-1} \begin{bmatrix} [M_{13}]\,[M_{14}] \\ [M_{23}]\,[M_{24}] \end{bmatrix} \begin{bmatrix} \vec{V}_2 \\ \vec{I}_2 \end{bmatrix} \tag{F.17}$$

Then, to accommodate the fact that in the definition of $ABCD$-Parameters, the current at port 2 flows *outwards* from the port, the current coefficients are negated:

$$\begin{bmatrix} \vec{V}_1 \\ \vec{I}_1 \end{bmatrix} = - \begin{bmatrix} [M_{11}]\,[M_{12}] \\ [M_{21}]\,[M_{22}] \end{bmatrix}^{-1} \begin{bmatrix} [M_{13}]\,[M_{14}] \\ [M_{23}]\,[M_{24}] \end{bmatrix} \begin{bmatrix} [I] & [0] \\ [0] & -[I] \end{bmatrix} \begin{bmatrix} \vec{V}_2 \\ -\vec{I}_2 \end{bmatrix} \tag{F.18}$$

Comparing (F.18) with (3.40):

$$\begin{bmatrix} [A]\,[B] \\ [C]\,[D] \end{bmatrix} = - \begin{bmatrix} [M_{11}]\,[M_{12}] \\ [M_{21}]\,[M_{22}] \end{bmatrix}^{-1} \begin{bmatrix} [M_{13}]\,[M_{14}] \\ [M_{23}]\,[M_{24}] \end{bmatrix} \begin{bmatrix} [I] & [0] \\ [0] & -[I] \end{bmatrix} \tag{F.19}$$

The inversion of the submatrix of $[M]$ is handled though first diagonalizing it; this processes is discussed in detail in section 3.2.4.

Conversion from $ABCD$-Parameters back to M-Parameters may be accomplished by re-arranging (3.40) to:

$$- \begin{bmatrix} [I]\,[0] \\ [0]\,[I] \end{bmatrix} \begin{bmatrix} \vec{V}_1 \\ \vec{I}_1 \end{bmatrix} + \begin{bmatrix} [A]\,[B] \\ [C]\,[D] \end{bmatrix} \begin{bmatrix} [I] & [0] \\ [0] & -[I] \end{bmatrix} \begin{bmatrix} \vec{V}_2 \\ \vec{I}_2 \end{bmatrix} = \vec{0} \tag{F.20}$$

The vectors of (F.20) may be combined, such that the equation may be expressed as:

$$\begin{bmatrix} -[I] & [0] & [A] & -[B] \\ [0] & -[I] & [C] & -[D] \end{bmatrix} \begin{bmatrix} \vec{V}_1 \\ \vec{I}_1 \\ \vec{V}_2 \\ \vec{I}_2 \end{bmatrix} = \vec{0} \tag{F.21}$$

Negating both sides of (F.21) yields the matrix $[M]$ of:

$$\begin{bmatrix} [M_{11}] & [M_{12}] & [M_{13}] & [M_{14}] \\ [M_{21}] & [M_{22}] & [M_{23}] & [M_{24}] \end{bmatrix} = \begin{bmatrix} [I] & [0] & -[A] & [B] \\ [0] & [I] & -[C] & [D] \end{bmatrix} \tag{F.22}$$

F.3 Y-Parameters

To transform M-Parameters into Y-Parameters, (F.2) may be re-arranged to:

$$\vec{I} = -[M_I]^{-1}[M_V]\vec{I} \tag{F.23}$$

where comparison with (3.41) yields:

$$[Y] = -[M_I]^{-1}[M_V] \tag{F.24}$$

Converting Y-Parameters back to M-Parameters may be accomplishes by noting that (F.2) may be expressed as

$$-[Y]\vec{V} + [I]\vec{I} = \vec{0} \tag{F.25}$$

Equation (F.25) indicates that

$$[M_V] = -[Y] \tag{F.26a}$$

$$[M_I] = [I] \tag{F.26b}$$

F.4 Z-Parameters

To transform M-Parameters into Z-Parameters, (F.2) may be re-arranged to:

$$\vec{V} = -[M_V]^{-1}[M_I]\vec{I} \tag{F.27}$$

where comparison with (3.42) yields:

$$[Z] = -[M_V]^{-1}[M_I] \tag{F.28}$$

Converting Z-Parameters back to M-Parameters may be accomplishes by noting that (F.2) may be expressed as

$$[I]\vec{V} - [Z]\vec{I} = \vec{0} \tag{F.29}$$

Equation (F.29) indicates that

$$[M_V] = [I] \tag{F.30a}$$

$$[M_I] = -[Z] \tag{F.30b}$$